Universidad de Valladolid

ESCUELA DE INGENIERÍAS INDUSTRIALES

DPTO. DE INGENIERÍA DE SISTEMAS Y AUTOMÁTICA

TESIS DOCTORAL:

NON-LINEAR MODEL PREDICTIVE CONTROL FOR COOLING STRINGS OF SUPERCONDUCTING MAGNETS USING SUPERFLUID HELIUM

Presentada por Rafal Noga para optar al grado de doctor por la Universidad de Valladolid

Dirigida por:
Prof. Dr. César de Prada Moraga
Dr. Enrique Blanco Viñuela

Non-linear Model Predictive Control for cooling strings of superconducting magnets using superfluid helium

Rafał Noga

Department of Systems Engineering and Automatic Control
University of Valladolid

This dissertation is submitted for the degree of
Doctor of Philosophy

Supervisors:
Prof. César de Prada Moraga
University of Valladolid

Dr. Enrique Blanco Viñuela
CERN, the European Organization for Nuclear Research

November 2015

Moim kochającym Rodzicom. (To my loving Parents.)

Declaration

I hereby declare that except where specific reference is made to the work of others, the contents of this dissertation are original and have not been submitted in whole or in part for consideration for any other degree or qualification in this, or any other university. This dissertation is my own work and contains nothing which is the outcome of work done in collaboration with others, except as specified in the text and Acknowledgements.

Rafał Noga
November 2015

Acknowledgements

The long period of work on the challenging industrial project presented in this thesis was full of joy and happiness accompanied by intense learning, professional development and cultural discoveries thanks to the support provided to me by my family, supervisors, colleagues, friends and institutions, to whom I am greatly thankful and specially to:

- Prof. Cesar de Prada, Enrique Blanco and Juan Casas who supervised my work at CERN and at University of Valladolid,
- Prof. Toshiyuki Ohtsuka my teacher and supervisor at Osaka University,
- Serge Claudet, Gérard Ferlin, Krzysztof Brodziński and other members of the LHC cryogenic operation, who supervised my experimental work at the LHC,
- Daniel Sarabia, Miguel Rodriguez, Elena Gomez, Benjamin Bradu, Jacques Rochez, William Boot, Piotr Golonka, Hervé Milcent, Silvia Izquierdo, Andrzej Dworak, Axel Voitier, Philippe Lebrun, Marutani-san, my Japanese Host Family, administration stuff at University of Valladolid, CERN and Osaka University for their knowledge and support,
- Agnieszka Priebe, Dominika Dobrowolska, Anna Noga and Ryszard Noga for their love and support at home.

Abstract

In each of eight arcs of the 27 km circumference Large Hadron Collider (LHC), 2.5 km long strings of super-conducting magnets are cooled with superfluid Helium II at 1.9 K. The temperature stabilisation is a challenging control problem due to complex non-linear dynamics of the magnets temperature and presence of multiple operational constraints. Strong non-linearities and variable dead-times of the dynamics originate at strongly heat-flux dependent effective heat conductivity of superfluid that varies three orders of magnitude over the range of possible operational conditions. In order to improve the temperature stabilisation, a proof of concept on-line economic output-feedback Non-linear Model Predictive Controller (NMPC) is presented in this thesis. The controller is based on a novel complex first-principles distributed-parameters numerical model of the temperature dynamics over a 214 m long sub-sector of the LHC that is characterized by very low computational cost of simulation needed in real-time optimization based advanced process control. I present a thorough analysis of the thermo-hydraulic physical processes governing the temperature dynamics, reviewing the related R&D work. The analysis explains the key characteristics of the temperature dynamics and has been the starting point for development of the model and the control strategy. Experimental setups used to identify dynamics and model parameters of the unique superfluid cryogenic system are also described. Through the thesis, I highlight the practical methods used to achieve real-time feasibility of the controller, including: 1) approximations, handling of stiffness and algebraic equations in modelling and simulation, 2) application of Hybrid Luenberger Observer - Moving Horizon Estimation approach enabling output feedback control at very low computing cost, 3) parametrisation of the optimized variables trajectories that strongly reduces the number of optimized variables, 4) approximation of the original non-linear optimization problem with inequality constraints using one with box inequality constraints that is much easier to solve and 5) application of a single step Quasi-Newton solver to the specific box-constrained optimization problem that is repeatedly solved in an optimization-based controller. Two NMPC configurations are presented stabilizing the magnets temperature over a 214 m long LHC sub-sector: 1) using two control valves as manipulates variables, experimentally tested at the LHC, and 2) manipulating the two valves and 12 electric heaters, tested in simulations. Both setups are real-time feasible and exhibit excellent robust performance in wide range of

operating conditions, thus validating both the distributed-parameters model and the on-line output-feedback NMPC based on a complex first-principles model.

Resumen

En cada uno de los ocho arcos del Gran Colisionador de Hadrones (LHC) de 27 km de circunferencia, largas cadenas de imánes superconductores de 2.5 km se enfrian con helio II superfluido a 1.9 K. La estabilización de la temperatura es un problema de control retador debido a complejas dinámicas no lineales de la temperatura de los imanes y la presencia de múltiples restricciones operativas. No-linealidades fuertes y tiempos muertos variables de la dinámica se originan en la conductividad de calor eficaz de superfluido dependiendo fuertemente de flujo de calor y pueden variar hasta tres órdenes de magnitud dentro de la gama de posibles condiciones operativas. Con el fin de mejorar la estabilización de la temperatura, se ha realiado una demostración con un Controlador Predictivo No-lineal económico (NMPC) con retroalimentación de salida que se presenta en esta tesis. El controlador se basa en un modelo numerico de primeros principios y de parámetros distribuidos, novedoso y complejo, para la dinámica de la temperatura en un subsector del LHC de 214 m de largo. El modelo se caracteriza por el muy bajo costo computacional de la simulación, necesario en control de procesos avanzado basado en optimización en tiempo real. Se presenta un análisis exhaustivo de los procesos físicos termo-hidráulicos que rigen la dinámica de temperatura, incluido la revisión de programas de I+D relacionados. El análisis explica las principales características de la dinámica de temperatura y ha sido el punto de partida para el desarrollo del modelo y la estrategia de control. También se describen las configuraciones experimentales utilizadas para identificar la dinámica y los parámetros del modelo de este sistema criogénico superfluido único. A través de la tesis, destaco los métodos prácticos utilizados para lograr la factibilidad de tiempo real del controlador, incluyendo: 1) aproximaciones, manejo de rigidez y ecuaciones algebraicas en el modelado y simulación, 2) la aplicación del estimador de estado híbrido Luenberger Observer - Mover Horizonte Estimación que permite el control de retroalimentación de salida a un costo muy bajo de computación, 3) parametrización de las trayectorias de variables optimizadas que reduce significamente el número de variables optimizados, 4) la aproximación del problema de optimización no-lineal original con restricciones de desigualdad usando uno con restricciones de desigualdad tipo caja que es mucho más fácil de resolver y 5) la aplicación de un solo paso de un método Quasi-Newton para el problema de optimización con restricciones tipo caja específico que se resuelve repetidamente en un controlador basado en la optimización.

Se presentan dos configuraciones NMPC para la estabilización de la temperatura de los imanes sobre un sub-sector del LHC de 214 m de largo: 1) que manipula dos válvulas de control, probado experimentalmente en el LHC, y 2) que manipula las dos válvulas y 12 calentadores eléctricos, probado en simulaciones. Ambas configuraciones son factibles en tiempo real y presentan un excelente funcionamiento robusto en amplia gama de condiciones de operación, validando así tanto el modelo de parámetros distribuidos y el NMPC en linea con realimentación de salida basado en un modelo complejo de primeros principios.

Table of contents

List of figures

List of tables

Nomenclature

Roman Symbols

A	cross-section area
C	Thermal conductance
c	Specific heat
D	Diameter
F	superfluid helium thermal conductivity function
g	The gravitational acceleration of the Earth
h	specific enthalpy or heat transfer coefficient
I	electric current
J	cost functional to be minimized
k	heat conductivity
L	length or cost function to be minimized
l	level
M	Mass
N	Number of discretization intervals
P	perimeter or system parameter vector
q	heat transfer rate
r	radius

SE Standard Error

T Temperature

t Time

x Spatial position along magnet string

U Mean flow velocity or system input vector

v velocity

W mass flow rate

X dynamics system state variable vector

Greek Symbols

χ vapor quality

λ Lambda point, liquid-superfluid phase transition

Subscripts

$'$ at boundary between discrete intervals or temporary integration variable

b at Bayonet Heat Exchanger

c at Control Valve or cooling

f at Feeding Pipe

$f2bs$ from feeding pipe to superfluid in exchanger

$f2bv$ from feeding pipe to vapor in exchanger

fb at assembly of heat exchanger tube enclosing feeding pipe

h at Helium Bath or hydraulic

$h2bs$ from bath to superfluid in exchanger

$h2bv$ from bath to vapor in exchanger

he of helium

i inner or index

in at inlet or upstream

K Kapitza

l heat load

o outer

out at outlet or downstream

p at Phase Separator

pl at Plug

r at 1.8 K refrigerator

s saturated or of (in contact) with superfluid He II

sp Set Point

th thermal

v of (in contact) with vapor or at constant volume (used with specific heat)

Acronyms / Abbreviations

C/GMRES Continuation/Generalized Minimal Residual Method

CERN European Organization for Nuclear Research

CV Control Valve

EH Electrical Heater for Cryogenics

FT Flowmeter

LT Level Transducer

PT Pressure Transducer

TT Temperature Transducer

CV Control Valve

DAE Differential Algebraic Equations

EH Electric Heater

He I liquid helium

He II superfluid helium

LHC Large Hadron Collider

LMPC Linear Model Predictive Control

LT Level Transducer

MBD Model-Based Design

MB LHC module housing Main Bending Dipole Magnets

MHE Moving Horizon Estimation

NMPC Non-linear Model Predictive Control

ODE Ordinary Differential Equations

PDE Partial Differential Equations

PI Proportional-Integral (controller)

PT Pressure Transducer

SCADA Supervisory Control and Data Acquisition

SHCC Superfluid Helium Cryogenic Circuit

SSS Short Straight Section (LHC module)

TT Temperature Transducer

Chapter 1

Introduction

This chapter provides motivation, goals, contributions and layout of this thesis.

1.1 CERN and the LHC

The European Organization for Nuclear Research, known as CERN, is an international organization that operates the world's largest particle physics laboratory, also referred as CERN. In the laboratory, interactions between particles are studied, putting new light on fundamental questions concerning e.g. the origin of mass, presence of extra dimensions in the Universe, the dark matter, existence of the magnetic monopole, predictions of the Standard Model, biological effects of antiprotons or properties of antimatter, quark-gluon plasma, cosmic rays and vacuum. The experiments at CERN are performed using particle accelerators, particle detectors and massive computing power. *Accelerators* boost beams of particles to high kinetic energies. Then, the particles are collided with each other or with stationary targets and other particles are produced in the process. *Detectors* are used to record traces of particles produced in the collisions. The computers are then used to analyze the traces in order to calculate the properties of the particles that left them and then using the properties they analyze the interactions between the particles (CERN Press Office (2013)).

The 27 km circumference Large Hadron Collider (LHC), presented in the Fig. 1.1, is the largest and most powerful particle accelerator and collider at CERN and in the World (Brüning et al. (2004); Evans and Bryant (2008)). Since 2009, two beams of particles are accelerated in opposite directions and then circulate in the LHC for many hours. The beams are guided separately and they cross only at four interaction points where some of of the particles collide. In the head-on collisions, a part of their kinetic energy E is transformed into mass of new particles m, produced in the process, according to the Einstein's formula $E = m\,c^2$, with the speed of light in vacuum c. Among the particles produced this way, are rare instable

or antimatter particles that cannot simply be observed otherwise as they do not survive long enough in our environment. The results of the collisions produced at the LHC are analyzed by 6 particle detectors, also called the LHC experiments, including the two largest: the CMS experiment that weights approx 14'000 tonnes and the largest scientific instrument ever built - the 44 m long ATLAS experiment. The Worldwide LHC Computing Grid is used to store, distribute and analyse the 30 Petabytes (30 million Gigabytes) of data annually generated by the Large Hadron Collider. By accelerating particles to the world record energy level of 4 TeV, the LHC has enabled production of the approx. 125 GeV/c2 massive Higgs Boson, leading to its ground breaking discovery in July 2012. This discovery confirmed the theory describing the Brout-Englert-Higgs (BEH) mechanism, explaining the the origin of the mass of subatomic particles and thus the existence of the Higgs field.

The record energy levels have been reached by: 1) using hadrons as particles being accelerated and 2) superconducting magnets cooled with superfluid helium (He II) to guide them around the ring. Hadrons have significantly higher mass than leptons accelerated in the LHC predecessor - the 27-kilometer circumference Large Electron-Positron (LEP) collider and thus emit much less synchrotron radiation, which has limited the power of LEP to 0.209 TeV (CERN (2013)). In the LHC, the value of maximal energy of hadrons being accelerated is limited to 7 TeV by the maximal value of the centripetal force that keeps the particles on the orbit. The Lorentz force is provided by a total number of 1232 8.33 T strong superconducting dipole

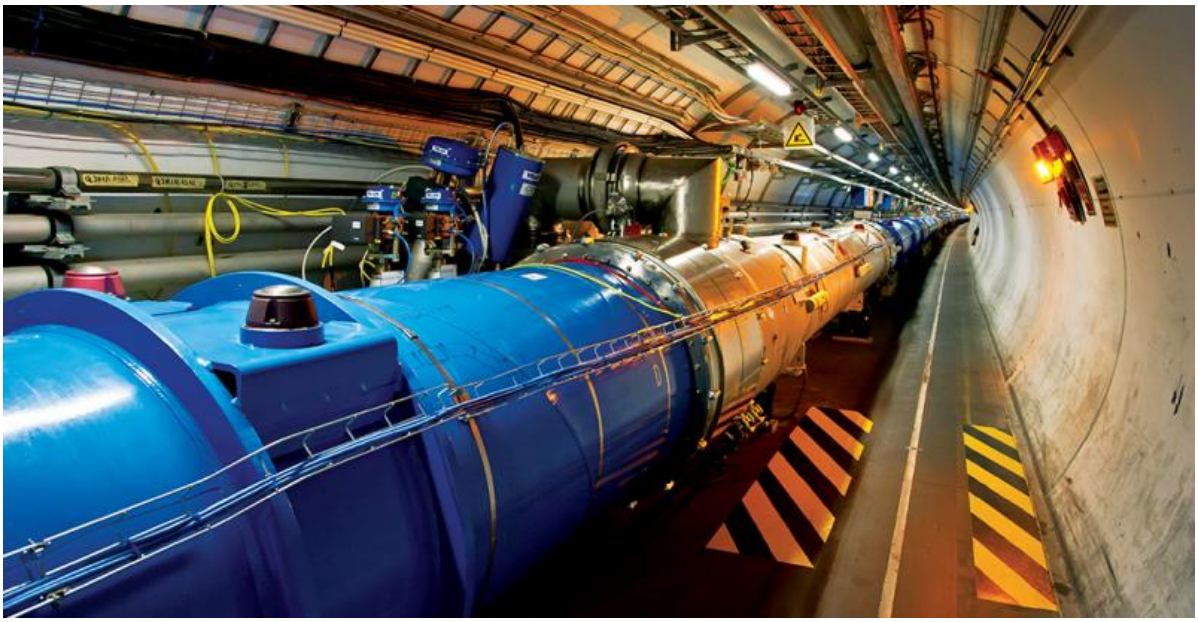

Fig. 1.1 The LHC in the tunnel. Image source: CERN.

electromagnets. Altogether some 10'000 superconducting magnets are used in the LHC to guide and focus particles.

1.2 Cooling superconductors using superfluid

Superconductivity is a phenomenon of zero electrical resistance and expulsion of magnetic fields occurring in certain materials at values of temperature, current density and intensity of magnetic field inferior than critical ones. At sufficiently low temperatures, no resistive heating occurs in zero-resistance superconducting devices that can work at very high current densities enabling design of powerful, compact and precise components. Thus, superconductivity is the key LHC technology widely applied radio frequency cavities and magnets that accelerate and steering particles, respectively. However, at temperatures above the critical, superconductor is in normal-conducting state characterized by significant electrical resistivity. If the resistive transition from superconducting to normal-conducting state happens when strong current flows in superconducting coils, *quench* occurs that is an intensive heat generation due to the discharge of high energy stored in the magnet's magnetic field at the cables resistance. The LHC Magnet Quench Protection System helps to dissipate the energy over large volumes and thus protects the magnets from being damaged during quench. However, few hours time are needed to re-cool magnets after a quench, before the LHC operation may be restarted.

The critical values of the temperature, electric current density and magnetic field intensity are related to each other and depend on the type of the material. Windings of the main LHC magnets are made of some 7600 km of superconducting, 22 mm^2 cross-section area, NbTi cables that carry currents up to 13 kA. NbTi is the industrial superconduction alloy widely used due to its excellent electrical and mechanical properties. Lowering the operational temperature of the NbTi superconducting magnets at the LHC to only 1.9 K (-271 °C), being the temperature of superfluid helium, allowed to increase the critical values for the two other parameters and thus: 1) boost their performance to 8.4 T and 2) increase the current carrying capacity of the superconductor, minimizing the the amount of material needed and hence: the size of the magnets that must fit in the existing tunnel and capital costs. In the main LHC superconducting magnets, at presence of nominal magnetic field and current densities, the NbTi critical temperature is equal to 3.3 K.

Some 80 tons of superfluid helium (He II) are used in the Superfluid Helium Cryogenic Circuit (SHCC) stabilizing at 1.9 K the temperature of 37'000 tons of equipment. Helium is the only coolant available at such very low temperatures, because it is the only substance flowing in these extreme conditions while all other are solid. Moreover, at $T_\lambda = 2.17$ K[1] helium 4

[1] This temperature is lower then in that in the outer space equal to 2.7 K!

undergoes a phase transition between liquid He I and superfluid He II. He II, available below this temperature, is the perfect coolant, characterized by a number of extraordinary physical properties including: very high apparent heat conductivity, vanishing viscosity for capillary flow and relatively high specific heat[2]. The apparent thermal conductivity of He II may be many orders of magnitude higher than that of high purity copper, however it varies strongly in function of temperature and its gradient, approaching infinity as the gradient vanishes. Cooling with superfluid is summarized in Lebrun and Tavian (2014).

The tandem of superfluidity and superconductivity have also been used in other large scale projects, including: 1) superconducting magnets are in condensed-matter physics, nuclear magnetic resonance, magnetic confinement fusion and circular particle accelerators and colliders, see Claudet (1993, 2005); Lebrun and Tavian (2002); Tavian (2000) for details and references, and 2) high-frequency superconducting devices, such as acceleration cavities, as described in Claudet (2005); Lebrun and Tavian (2002) and references herein. Also the successor of the LHC - the International Linear Collider (ILC) will apply this technology (Casas-Cubillos et al. (2007); IEC (2013)).

1.3 Temperature stabilization of long strings of LHC superconducting magnets

The temperature stabilisation of long strings of superconducting magnets cooled using superfluid helium is a challenging control problem due to complex non-linear dynamics of the magnets temperatures and presence of operational constraints. In fact the cooling with superfluid may only be used to keep the magnets temperature in a very narrow range between approx. 1.8 K ($-271.35\,^{\circ}$C) and 2.1 K ($-271.05\,^{\circ}$C), see Figure 1.2. The critical temperature of superconductor is at 3.1 K, at inner layer of a LHC dipole and at magnetic filed intensity of 8.65 T (Burnod et al. (1994)).

Heat conductivity of superfluid is strongly heat flux dependent, resulting in the controlled temperature dynamics that is highly non-linear in response to manipulation of the control valve that throttles the coolant mass flow rate and thus the cooling power delivered to the magnets. This means that the way the temperature is affected by the valve manipulation depends on the operating point of the system, defined mainly by the valves positions, heat loads into the magnets and the magnets temperature distribution along the LHC. Saturation effects are an example of very strong non-linearities, where the control input has significantly reduced impact on the controlled variables. Non-linearities are common property among various systems to be

[2] Specific heat of other materials vanishes at temperature approaches 0 K.

controlled and they effects are negligible as long as the operational conditions of a non-linear system do not vary too much. However, in case of the temperature dynamics, the non-linearity is pronounced because the operating point moves significantly during significant transient phases and due to heat load perturbations occurring during stable operation.

Moreover the dynamics is non-self-regulating - it is unstable and the system needs a controller in order for the temperature to maintain a stable value. Then, the dynamics exhibits varying dead-times, meaning that a delay occurs between the valve manipulation and its effect on the magnets temperature. Inverse response is also pronounced in some conditions, meaning that the effect of control action may be initially reverse to the the expected and only after some time, the main effect of the action takes over - this is confusing for human operators and also for simple control algorithms. Additionally, strong couplings exist between process variables that propagate the effect of the control actions over large number of other variables, making the effect of control actions even more difficult to predict. Moreover, multiple operational constraints on manipulated and controlled variables must be respected during the cooling circuit

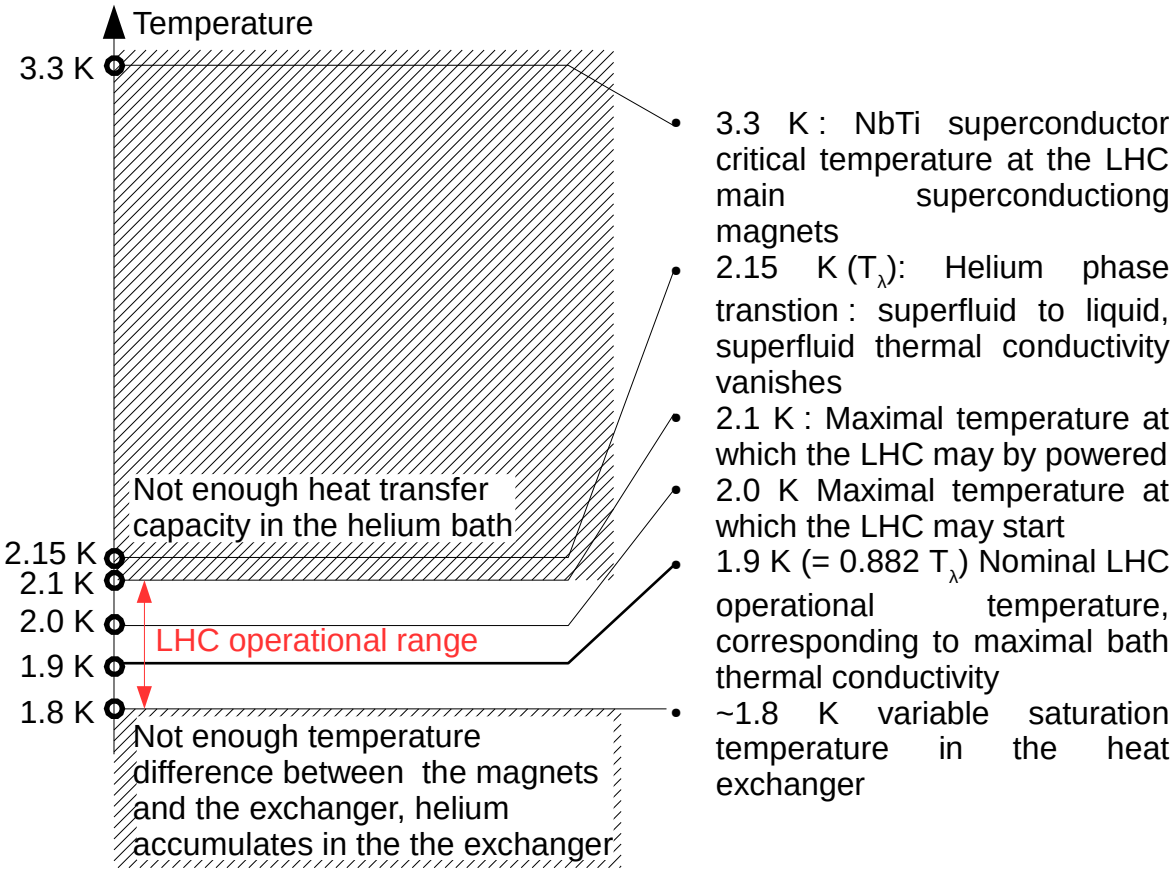

Fig. 1.2 LHC operational range.

operation. Finally, instrumentation is installed sparsely due to the size of the machine and presence of increased radiation levels in the LHC tunnel.

The Proportional-Integral (PI) controllers are workhorse in many industries. They are simple linear controllers, that calculate the the value of a single manipulated variable based on an error between a measured variable, closely related to the controlled variable, and a set-point. The reason for the succes of linear controllers even in case of strongly nonlinear systems operated at given conditions, is that each non-linear system may be approximated as linear one in close vicinity of an operational point, however the further away form the operational point system operates and/or the more non-linear its dynamics, the stronger is the deviation between the approximation and the actual dynamics and the quality of linear approximation degrades. Complex control architectures are frequently found in industry, where many PI controllers are interconnected often using additional logic in order to realize complex control goals.

At the LHC, many independent PI controllers are currently used to stabilize the magnets temperature, manipulating the control valves. An interlock system and a heating power management layers are added, that allows to handle the most important operational constraints. The system performs sufficiently well during stable operation at nominal conditions, however its performance is poor during transients, when occasional interlock system and/or manual intervention is needed to avoid constraints violation. The mains reason for the poor performance is the complex non-linear system dynamics, that cannot be sufficiently well addressed by a simple linear controller that doesn't handle at all the non-linearities nor the strong couplings between variables and handles other aspects of the dynamics like the dead times and inverse response through a conservative tuning - compromising the performance of closed loop temperature stabilisation.

Improvement of the control during transient cool-down phase, means faster cool-down and thus higher LHC availability for beam and lower the need for manual intervention and thus the operators workload. During the stable operation, a better control means lower variation of the controlled temperatures and decreased cost of system operation by operating closer to the constraints related to the minimal cooling power that are currently handled by the heaters power management system. Reducing the heaters power to the minimum allowing for safe operation within constraints, is motivated by the fact that some 20 kW of refrigeration power at 1.8 K are installed in the machine, which corresponds to electric power consumption of some 20 MW as the coefficient of performance is very small due to small Carnot cycle efficiency at 1.8 K and irreversible processes.

1.4 Non-linear Model Predictive Control of LHC magnets temperature

Non-linear Model Predictive Control (NMPC) is a feedback control technique where trajectories of manipulated variables are repeatedly optimized over a finite future time horizon using a non-linear model of system dynamics, available measurements and estimates and reference trajectories for controlled variables, as introduced by Findeisen and Allgöwer (2002). The advanced control techniques directly address the non-linear dynamics, complex interactions between process variables and operational constraints. This allows to reduce the variation of the controlled variables and shift the operational point closer to the constraints and thus increase the safety and efficiency of operation.

However, the NMPC is a state feedback technique, meaning that current values of internal model variables must be known to use the controller. Thus, NMPC needs an observer or estimator that provides the values based on the measured system variables. In fact, the estimation may be much more difficult than the control, because of higher number of estimated variables and complex relations between them and the measured outputs. Moving Horizon Estimation (MHE) is a estimation technique where trajectories of unknown states and perturbations are repeatedly optimized over a finite past time horizon using a non-linear model of system dynamics and available measurements described by Michalska and Mayne (1995). MHE may use the same model and optimization algorithms as the NMPC, the only difference being the formulation of the optimization problem.

In both, the MHE and NMPC, the total computational complexity of the model simulation and numerical solvers used in the optimizations must allow for its real-time feasibility - speed of calculation of the estimated states and inputs and manipulated inputs must match the spead of the controlled system dynamics evolution. Thus, both techniques rely on availability of system models enabling fast simulation and efficient numerical solvers for the underlying non-linear optimization problem with inequality and equality constraints. Large progress has been done in recent years in development of computing cost effective non-linear optimization methods tailored for the advanced control applications.

However, the effort needed to develop a non-linear model suitable for NMPC has been the main obstacle in the development of NMPC applications, including an advanced controller for the LHC magnets temperature stabilisation. The application of the non-linear MPC is much less widespread than that of the linear MPC, using simple linear models whose parameters may be identified much easier than those of complex non-linear models. This also makes the maintenance more difficult as the controlled systems dynamics do evolve over time and the models should be maintained. Moreover, computational cost of simulation of non-linear models

is much higher than that of simple linear models and thus may easily render the simulation based optimisation real-time infeasible - prohibiting its application in NMPC.

Most importantly, frequently the effort of development of a complex non-linear controller and its maintenance is not justified by the expected improvement of the system closed loop performance, further limiting the number of existing NMPC applications. In case of the LHC magnets temperature, this dynamics has been unknown until 2008 when the machine has been cooled down to the operational temperature at 1.9 K for the first time in history. The LHC is the first machine ever build where long strings of superconducting magnets are cooled using superfluid on this scale. However, a series of LHC prototypes have been built and tested from 1996 to 2003, including the longest 106.9 m long String 2 Phase 3 using pre-series LHC components. The temperature dynamics at his prototype has been strongly non-linear, exhibiting variable dead times and strong inverse response, all justifying the effort to develop an NMPC. The actual dynamics at the LHC is much less complex at nominal operational conditions, however is becomes similar to that of the prototypes at higher heat loads or during large transient phases.

1.5 Models and simulations in other applications

Model-Based Design (MBD) is a methodology applied in development of complex systems, including control systems and embedded software. This design aproach extensively uses system models instead of real systems in order to reduce the design related cost and time. Model-Based Design comprises following steps: 1) modeling a plant, 2) analyzing and synthesizing a controller for the plant, 3) simulating the plant and controller, including Software in the Loop (SIL) simulations where the system model is used to simulate the hardware and the tested software can be executed under simulated input conditions and 4) integrating all these phases by deploying the controller and performing Hardware in the Loop (HIL) simulations, where the plant model is executed in the real-time and the simulator emulates the electrical properties of sensors and actuators, providing an electrical interface allowing to exchange signals between the model and the control hardware under test.

MBD enables integration of development and validation of the software that is crucial for the efficient development of high-quality control software. Since approximate models may be developed even before a system is actually built, the model-based development of the control system may begin early, in parallel with the plant construction, enabling early detection of bugs and design flaws and thus saving time and money because debugging at later stages of system development is more expensive, e.g. once the system has been physically built. Simulations may be executed much faster than real-time system variables evolution and thus significantly

accelerate the development. The purely software testing and validation environment may be reconfigured much faster and at much smaller cost than those involving hardware used at later stages of control system development. External debuggers, such as Microsoft Visual Studio, can be used for step-by-step code evaluation. Moreover, model simulation may be used for dimensioning, optimization, failure simulation and validation. The reaction of the system to certain faults can in some cases be investigated only in the simulated environment due to safety hazards or due to the costs of assembly destruction.

In case of the LHC croygenics, models enabled simulations of the LHC magnets cool down and warm up processes between ambient and cryogenic temperatures (Liu et al. (2003, 2004)). Bradu (2010) has developed models of various cryogenic installations at CERN, including the complete LHC cryogenic installation supplying helium to the LHC magnets cooling. He successfully used the models to develop new control strategies for the 4.5 K refrigerators of the LHC.

System simulation, using first principles models contributes significantly to the operation of an industrial process. Models enable development of soft sensors, also called virtual instrumentation providing estimates and visualization of system states and parameters that cannot be measured directly. A system model represents the designer knowledge that may integrated into advanced controllers or estimators to achieve advanced controls functionality. A simple example is a Kalman-filter where the knowledge represented as linear model allows to: 1) optimize the measurements filtering or 2) translate the measured values into the values of non-measured variables of interest, or 3) combine multiple measurements to obtain higher quality estimates of the variables of interest.

Virtual flow meters - soft sensors used to provide actual values of mass flowrates without the need of installing actual instrumentation are widely used at the LHC cryogenics to monitor and control the helium flows around the system (Arpaia et al. (2015); Ödlund (2007)).

Providing additional and reference information about process, models also enable self-diagnostics, fault-detection and safety-shutdown. Simulations enable prediction of plant behavior in the future, that are widely used used for operator training and optimization of operating conditions. Simulation based operators training allows to safely train atypical and dangerous situations, improving the operator response in case of real situations and thus improving the system operation safety and availability.

The models and simulation of cryogenic installations at CERN developed by Bradu (2010) have been integrated into a process simulator enabling operator training.

1.6 Goals

The goal of the thesis is twofold. First, it aims to **advance the state of the art in the super-fluid cryogenic process development and control** by providing a model of the temperature dynamics of the LHC superconducting magnets cooled with superfluid helium that enables further developments of model and simulation based applications for this process, including the NMPC and completing of the LHC cryogenic installation simulation. Moreover, the thesis provides a proof of concept real-time output-feedback NMPC for the magnets temperature stabilization in the LHC arcs, developed based on the model. The second goal is to **advance the state of the art in real-time output-feedback NMPC** by developing a thorough approach comprising modelling, simulation and real-time non-linear optimization enabling application of output feedback NMPC based on complex first principles models.

1.7 Contributions

The goals of the thesis are achieved based on 1) the work of other researchers in various fields, including control theory, numerical methods, thermo-hydraulics and super-fluid helium dynamics and 2) the specific contributions described in this this thesis, listed below.

A complete approach to development of Output-feedback on-line NMPC based on relatively complex first-principles models is presented in Chapters 6 and 7 and by Noga et al. (2015). It enables application of non-linear predictive control and Moving Horizon Estimation to complex, large scale systems described using distributed parameters models with stiff dynamics that are characterized by high computational cost of simulation. The approach includes: 1) widespread use of approximation, handling of stiffness and algebraic equations in modelling and simulation, 2) application of Hybrid Luenberger Observer - Moving Horizon Estimation, 3) parametrisation of the optimized variables trajectories, 4) approximation of a non-linear optimization problem with inequality constraints using one with box inequality constraints and 5) application of a single step Quasi-Newton solver to the approximated optimization problem.

Proof of concept, output-feedback NMPC application to the magnets temperature stabilization in an SHCC sub-sector at the LHC, using the innovative MHE-LO state estimator, presented in Chapter 7 and by Noga et al. (2015), has been developed following the approach, implemented in C, simulated in MATLAB and experimentally implemented and tested at the LHC using WinCC OA (previously Siemens SIMATIC WinCC Open Architecture) SCADA. The control objectives have been defined, acknowledging the importance of distributed parameter nature of the circuit and the saturation temperature in the heat exchanger and

the important role of the constraints on the helium supply mass flow rate. The NMPC has demonstrated real-time feasibility and excellent robust experimental performance.

Detailed, first-principles, thermo-hydraulic, distributed-parameters, numerical model of the temperature dynamics at the LHC, having 262 states has been developed, see Chapter 6. It implements the modelling approach minimizing the computational cost of its simulation and thus enabled the development of the real-time optimization based controller. The model is built upon the **results of a wide R&D programs related to the LHC cryogenics, that are reviewed** in the same chapter.

Large amount of unique empirical data has been collected during the model identification and validation tests, demonstrating various aspects of the non-linear circuit dynamics and the related operational challenges. The experiments cover wide operational range, far beyond typical operational conditions.

Methodology for identification and validation experiments tailored for of the highly non-linear circuit dynamics operated under constraints has been developed and implemented to collect the data. The experiments were automated using custom-developed SCADA panels, enabling precise and repeatable execution of complex and lengthy experiments at all of the eight LHC sectors.

Detailed analysis of the processes behind the circuit dynamics at the LHC has been performed based on the experimental and model simulation data and is presented in Chapter 5. The analysis provides an unique insight into behaviour of internal circuit variables in wide range of operational conditions and explaining complex interactions between them, leading to the acknowledgement of the critical role of small-diameter helium feeding pipe in development of the inverse response, variable dead times and probably also the thermo-hydraulic instabilities characterizing the magnet temperature dynamics.

An unexpected phenomenon: high frequency instabilities of the helium temperatures of magnets and at the control valve has been discovered and described.

1.8 Outline

This dissertation is organized in 9 chapters. Chapter 1 provides the context, motivation, formulation and contributions of the thesis. Chapters 2, 4 and 3 provide the background and detailed motivation, describing the superfluid helium cryogenic circuit, the first principles modelling methodology and tools and the key components of the NMPC control, respectively. Chapter 2 also provides analysis of the circuit dynamics that is a starting point for: 1) the modelling process, allowing to identify the key aspects of the circuit dynamics to be reproduced and allowable simplifications and 2) the development of the controller specification. Chapter 5

provides a detailed description of the modelling process starting with identification and analysis of the physical processes behind the dynamics, followed by their mathematical description and leading to numerical models of the dynamics characterized by low computing cost, presented on Chapter 6. The results of the R&D programs related to various cryogenic circuit components are reviewed and enhanced with new analysis performed using the model and the LHC experimental data. Chapter 7 describes the advanced controller for the process, composed of the the MHE-LO and the NMPC, starting with the definition of the control goals, followed by their formulation as optimization problem and development of real-time solver. Large number of simulation studies is presented. Chapter 8 describes the proof of concept controller implementation and simulation and experimental results. Finally, Chapter 9 concludes the paper an gives an outlook.

1.9 Summary of publications

Other publication related to this research project and partially covering the topics of this thesis are listed here. The final NMPC/MHE setup tested at the LHC and presented in this thesis has been summed up in the conference papers (Noga et al. (2014)) and (Noga et al. (2015)), with the latter paper focusing on the modelling and optimization approach that lead to the real time feasibility of the controller. An early NMPC setup with a simplified model with 10 dynamic states and using Continuation/Generalized Minimal Residual Method (C/GMRES) method and automatic code generation environment AutoGenU that has been unsuccessfully tested at the LHC and not covered in this thesis is presented in the conference papers (Noga et al. (2011)) and (Noga et al. (2010)). Some ideas of semi-automatic code generation and evaluation of the first order optimality condition for the stiff, distributed parameter system are discussed in the conference paper (Noga and Ohtsuka (2011)). The first distributed parameter model for the SHCC version used at the LHC, acknowledging the importance of the feeding pipe has been presented in my Master's Thesis (Noga (2007)).

Chapter 2

Introduction to superfluid helium cryogenics at the LHC

The Superfluid Helium Cryogenic Circuit (SHCC) provides cooling and stabilizes the magnets temperature. It is introduced in this chapter and the challenges related to the magnets temperature stabilisation are presented in detail.

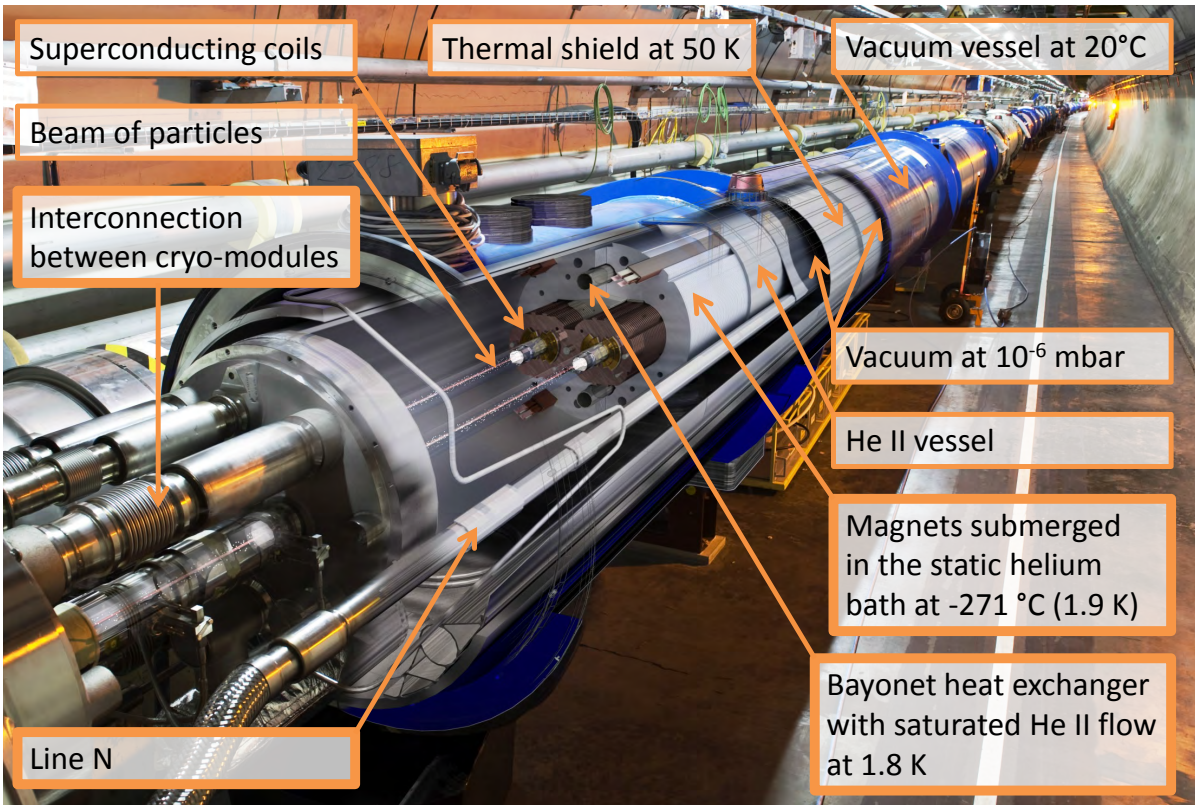

Fig. 2.1 The LHC in its tunnel and section through a cryo-dipole. Source of image: CERN

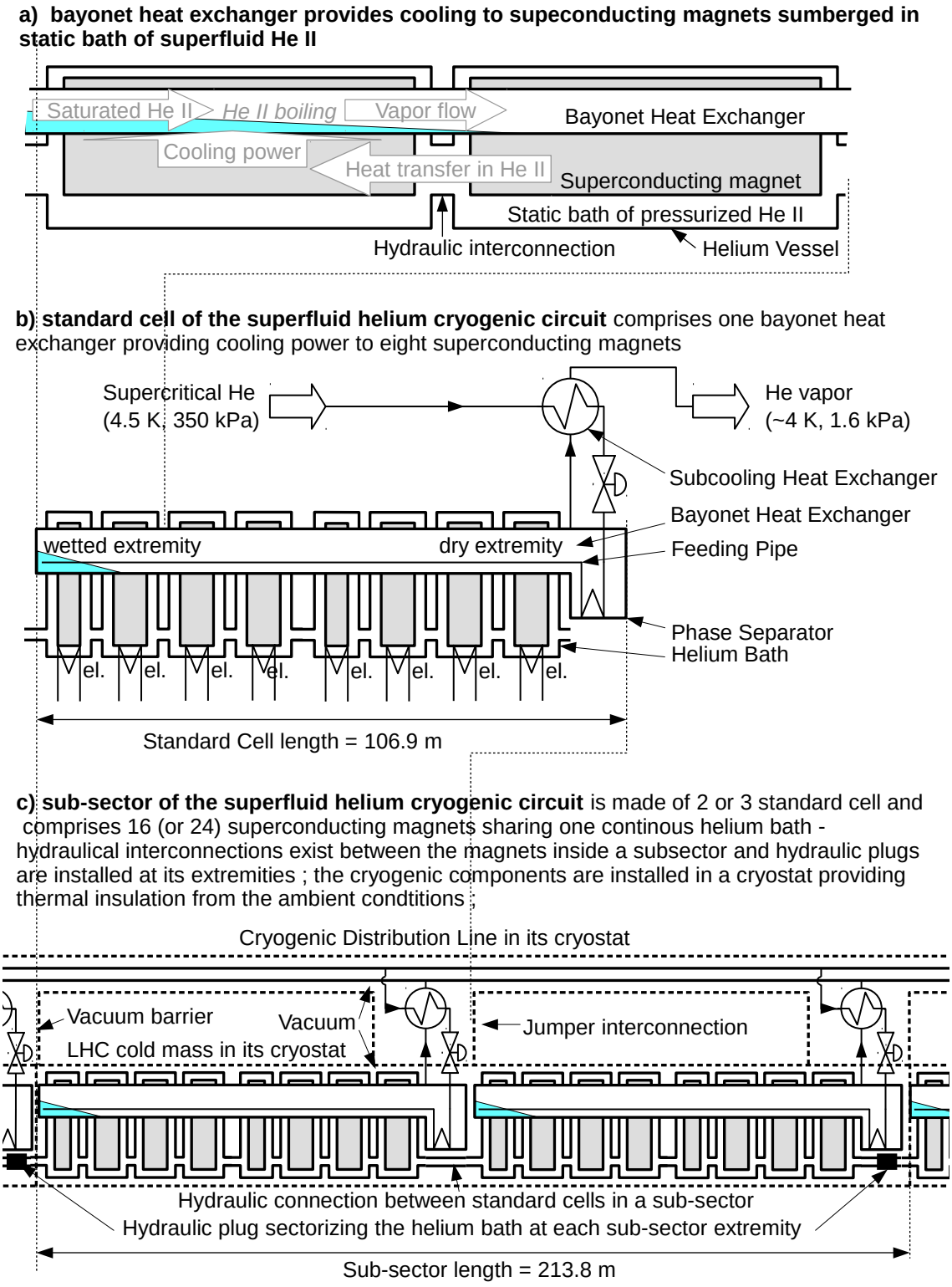

Fig. 2.2 Superfluid Helium Cryogenic Circuit at the LHC.

2.1 Layout and principle of operation

Design of the SHCC, also known as the 1.8 K Cooling Loop, is based on the novel concept of a bayonet heat exchanger, integrated into a static bath of pressurized He II together with the cooled superconducting magnet coils, see Figs. 2.1 and 2.2 (Bézaguet et al. (1993); Lebrun et al. (1997)).

Supercritical helium at 5 K, 400 kPa, (Fig. 2.3) is supplied from a refrigerator, through a 3 km long distribution line to 23, *106.9 m long standard cells of the circuit*, distributed along a 2.5 km long arc of the LHC, see Fig. 2.8. Then, at each cell, this helium is sub-cooled, throttled at a control valve and the resulting two-phase helium is feed through an over 100 m long, 10 mm inner diameter pipe into a larger 54 mm inner diameter, over 100 m long tube of the bayonet heat exchanger. Very low pressure of 1.6 kPa is maintained in the heat exchanger tube, forcing the He II flowing inside to boil at 1.8 K, taking away the heat transferred from the bath. The created vapor is sucked away through the phase separator, the sub-cooling heat exchanger and the distribution line back to the refrigerator.

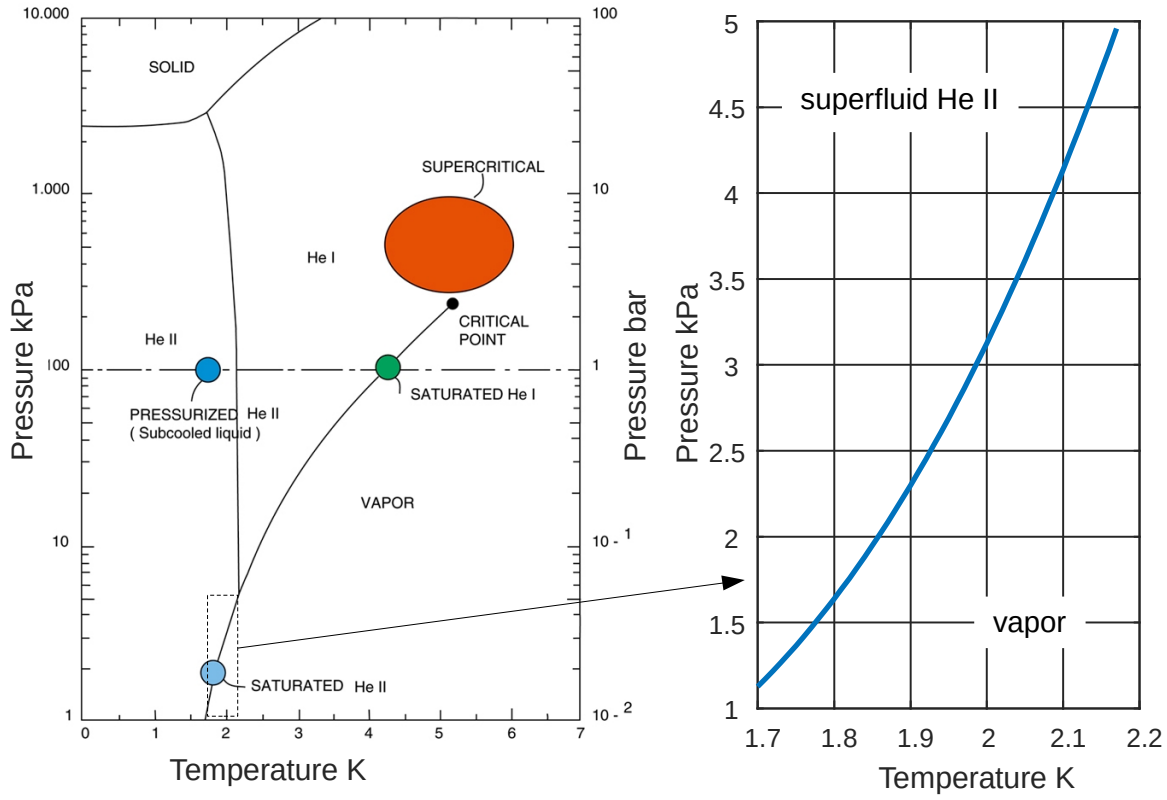

Fig. 2.3 Phase diagram of helium. Source: CERN.

The role of the helium bath is 1) to provide thermal connection between the superconducting magnets' windings and the wetted zone of the partially wetted bayonet heat exchanger, 2) to thermally stabilize the windings temperature and 3) to thermally buffer transient heat produced during current ramp or discharge or loss of superconductivity in the superconducting magnets. This is done efficiently by exploiting the extraordinary physical properties of He II: zero viscosity for capillary flow, relatively high specific heat capacity and very high apparent thermal conductivity.

The bath is shared by 2 or 3 standard cells composing a sub-sector that stretches over 213.8 m or 320.7 m, respectively. One bayonet heat exchanger per standard cell is installed, running through 6 cryo-dipoles and 2 Short-Straight-Sections (SSS) housing 8 main superconducting magnets. The basic repetitive magnetic segment of the LHC arc is the 53.4-m long half-cell composed of three cryo-dipoles followed by an SSS. Each cryo-dipole consists of one main LHC superconducting two-in-one 8.4 T bending dipole magnet integrated into a 15 m long cryostat. The 5.4 m long cryostat of the SSS houses various magnets and instrumentation including main focusing/defocusing quadrupole.

The LHC cryostats consist of a cold mass maintained at 1.9 K surrounded by actively cooled aluminum thermal shield operating at 60 K, covered by 30 layers of multi-layers insulation blankets, and vacuum vessel, see Figures 2.1, 2.4 and 2.5. Additional cooling loop at 20 K is used to intercept the heat generated by the particles at the beam screen. The SSS and cryo-dipoles are interconnected along the arc, creating one long cryostat. As mentioned before, every 106.9 m, the arc cryostat is is linked to the distribution line each via a jumper interconnection installed at the SSS. The arc cryostat is sectorized by means of hydraulic plugs placed each 214 m to sectorize the helium bath and vacuum barriers placed each 228 m to sectorize the insulation vacuum. This allows to cool down or warm-up only small stretches of the arc cryostat in only about 8 days, as compared to 24 days necessary for the full arc.

The role of the cryostat is to limit to minimum the amount of heat entering the low temperature level of 1.9 K. For the detailed description of various aspects of the LHC cryostats please refer to Lebrun and Tavian (2002) and Poncet and Parma (2007). Due to the First and Second law of thermodynamics, the coefficient of performance (COP) for a refrigeration system that moves heat from low temperature T_{cold} to high temperature T_{hot} cannot be better then the Carnot cycle efficiency $COP_{ideal} = T_{\text{cold}}/(T_{\text{hot}} - T_{\text{cold}})$. Thus, the Carnot cycle efficiency approaches 0 as the low temperature approaches 0 K, thus in any cryogenic system heat entering the low temperature level should be limited to the minimum. In case of the LHC, with $T_{\text{hot}} = 293\ K$ and $T_{\text{cold}} = 1.8\ K$, the $COP_{ideal} = 0.006$, which means that 1 W provided to the refrigeration system may at most produce 0.006 W of refrigeration power at 1.8 K - in ideal case. A real mixed-compression 1.8 K refrigeration cycle achieves a Coefficient of performance

(COP) of about 0.0011 (Claudet et al. (2004)), thus 900 W of electric power are needed to provide 1 W of refrigeration power at 1.8 K.

2.2 Refrigeration and helium distribution at the LHC

The superfluid cryogenic circuit in the LHC arcs is a part of the powerful LHC helium cryogenic system, see Figs. 2.6 and 2.7. The LHC magnets are located approx. 100 m underground in a 27 km circumference tunnel inherited after previous accelerator, the Large Electron-Positron Collider (LEP). The tunnel is composed of 8 arcs separated by 8 straight sections (Evans and Bryant (2008)). At eight points, in the middle of each straight section, caverns house the LHC experiments, built at the interaction points were particles collide, and other equipment and shafts provide a connection to the surface. The LHC is subdivided into 8 3.3 km long machine sectors, limited by the eight main access points and each comprising one machine arc. The

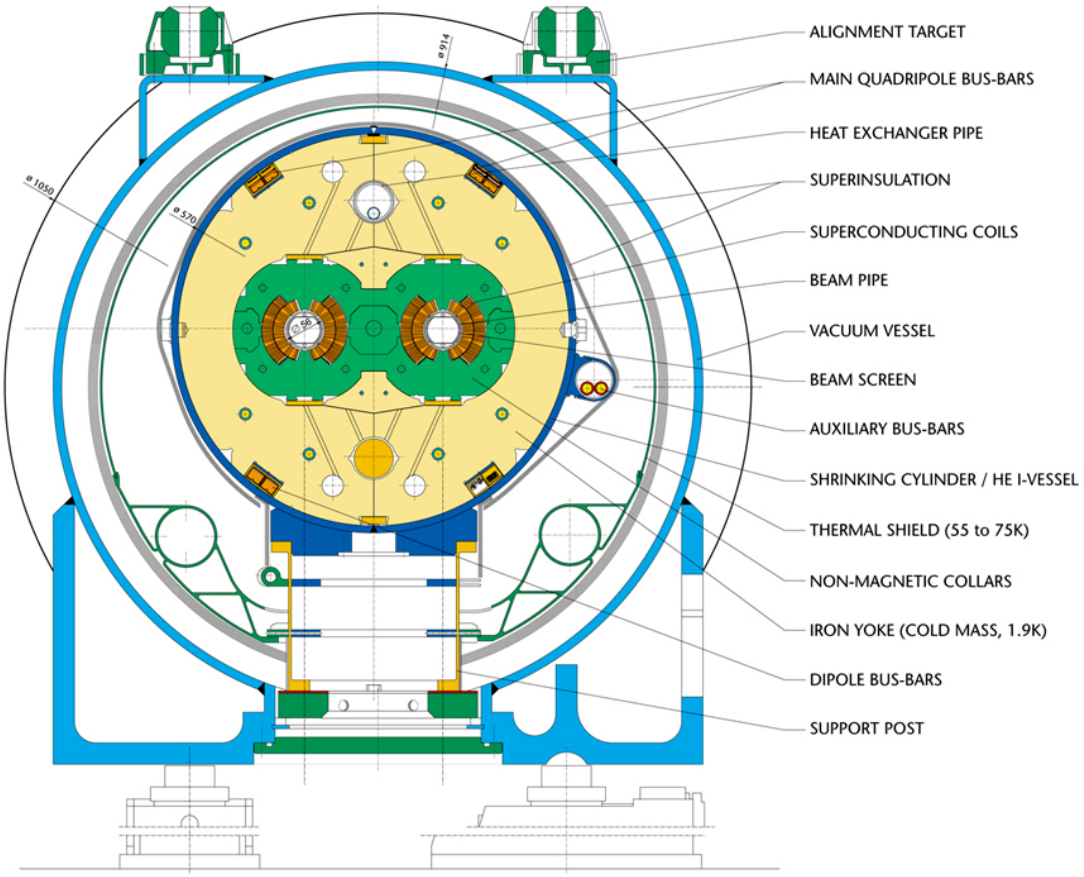

Fig. 2.4 Cryodipole cross-section. Image source: CERN.

plane comprising the tunnel is inclined at 1.4 %, thus the inclination of the tunnel varies from -1.4 % to 1.4 %.

Besides in the arcs, the superfluid helium cooling loops are present in other parts od the machine. The dispersion suppressor is made of four special half-cells with two dipoles and one quadrupole and placed just outside the arc. These superconducting magnets are cooled using cells very similar to that in the arc. Inner Triplets are focusing quadrupole magnets located close to the interaction regions, where the particles are collided. The inner triplet are exposed to much higher heat loads than other magnets, thus the layout of the corresponding cooling circuit is similar but re-dimensioned.

In the LHC, cryogenic refrigeration is lumped in five "islands" serving the adjacent sectors. Each of eight large LHC refrigerators provide 18 kW refrigeration power at 4.5 K using the Claude cycle. A refrigerator is composed of a compressor station and a cold box housing the heat exchangers and expanders, see Fig. 2.8. Supercritical (compressible liquid) helium produced at the 4.5 K refrigerators is distributed via the distribution line to the magnets distributed along a sector. Each of those 4.5 K refrigerators, feeds one 1.8 K refrigerator providing 2.4 kW at 1.8 K. The 1.8 K unit pumps via the distribution line the very low pressure helium vapor leaving the magnets, compressing it above the atmospheric pressure. The compressed helium is then recovered by the 4.5 K refrigerator, as described by Lebrun and Tavian (2002).

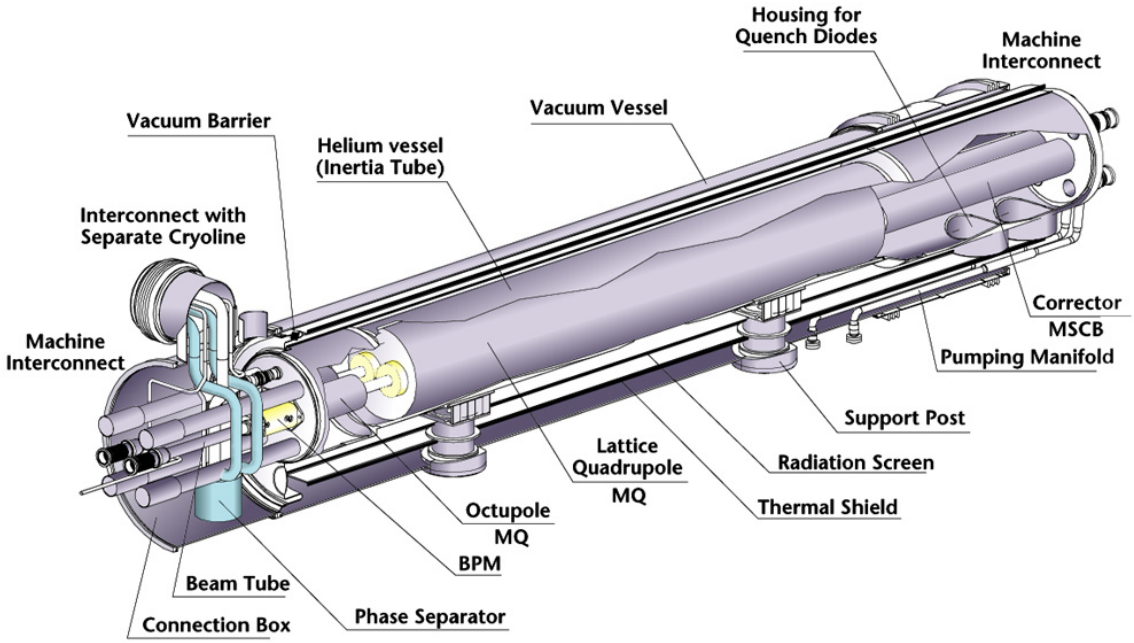

Fig. 2.5 Short Straight Section 3-D cross-section. Source: CERN.

Claude cycle is used in all refrigerators using helium as working fluid. The cycle is a combination of multiple Brayton cycles and Joule-Thompson (JT) expansion stage. In JT process the temperature of a gas or liquid changes when it is forced through a valve or porous plug while kept insulated so that no heat is exchanged with the environment. At

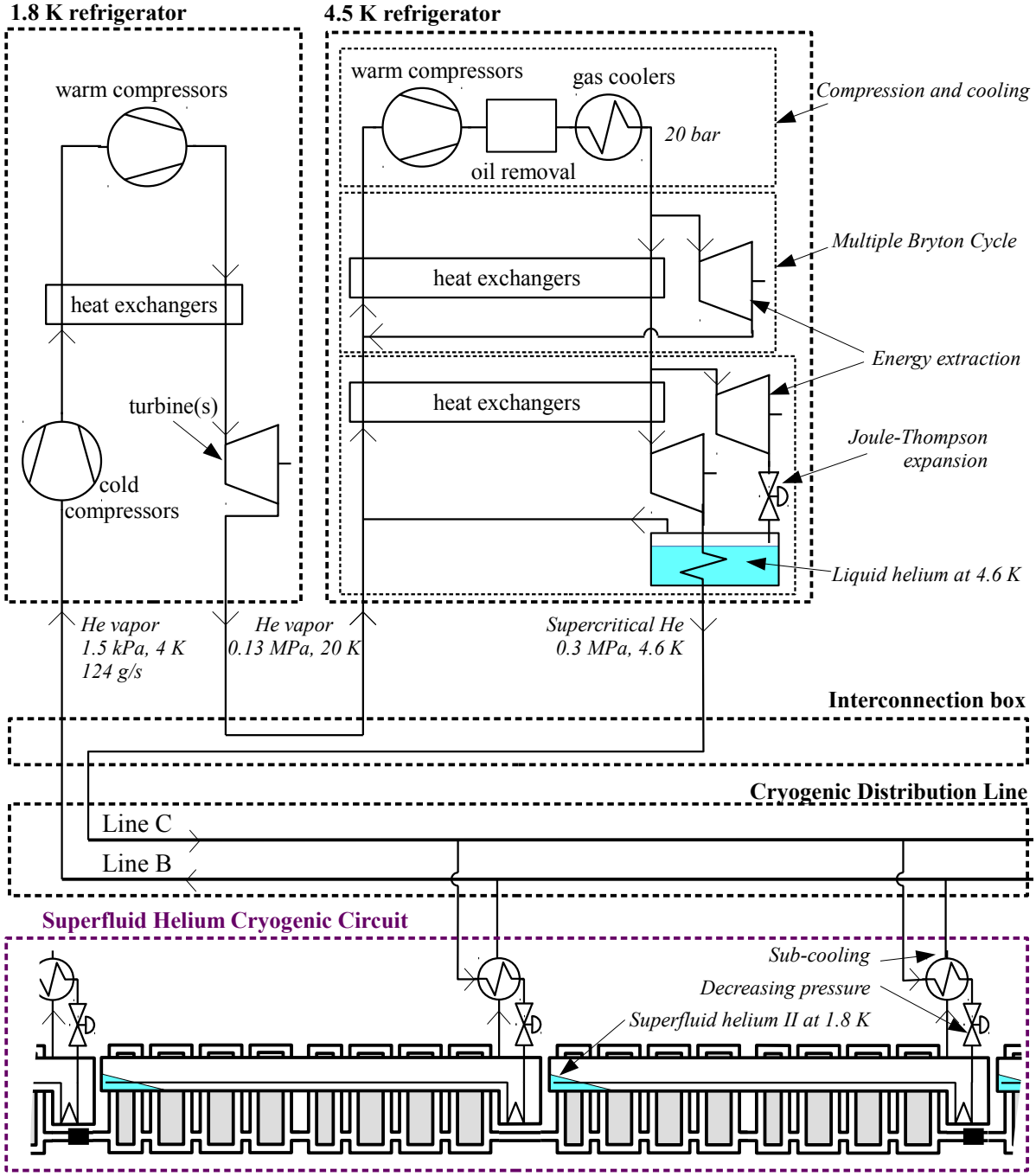

Fig. 2.6 LHC 1.8 K refrigeration.

room temperature, all gases except hydrogen, helium and neon cool upon expansion by the Joule-Thomson process. For helium to cool upon expansion, it must be first pre-cooled to temperatures below 45 K, which is realised using multiple, typically two, Bryton cycles. In the Bryton cycle, helium is first compressed at ambient temperature, than heat is removed from the helium using heat exchangers and work is extracted using expansion machines (turbines).

The 1.8 K refrigerator, works with "mixed" compression cycle where the very-low-pressure gaseous helium is first pumped at low temperature, when it is dense, using three or four stages of cold hydrodynamic compressors operating at cryogenic temperatures. Than, high compression stage is performed by warm sub-atmospheric volumetric compressors. This configuration enables compression with high pressure ratio exceeding 80, from 1.6 kPa to 100 kPa, while maintaining high dynamic range of refrigeration power qual to 3. The dynamic range is comprised between the minimal mass flow rate of helium vapor at 1.5 kPa on machine standby equal to 41.5 g/s and the installed capacity of 124 g/s. The reason for this is that with subatmospheric compressors having volumetric characteristics, the pressure at the outlet of the cold compressors decreases linearly with the flow-rate, thus keeping the working point fixed in the operating field (Lebrun and Tavian (2002)).

2.3 Instrumentation and process data logging

Instrumentation installed at the superfluid circuit provides measurements of actual system parameters and allows to influence them by manipulating other process parameters.

At each standard cell, one equal-percentage cryogenic control valve produced by Velan throttles the mass flow rate of helium entering the feeding pipe controlling the cooling power

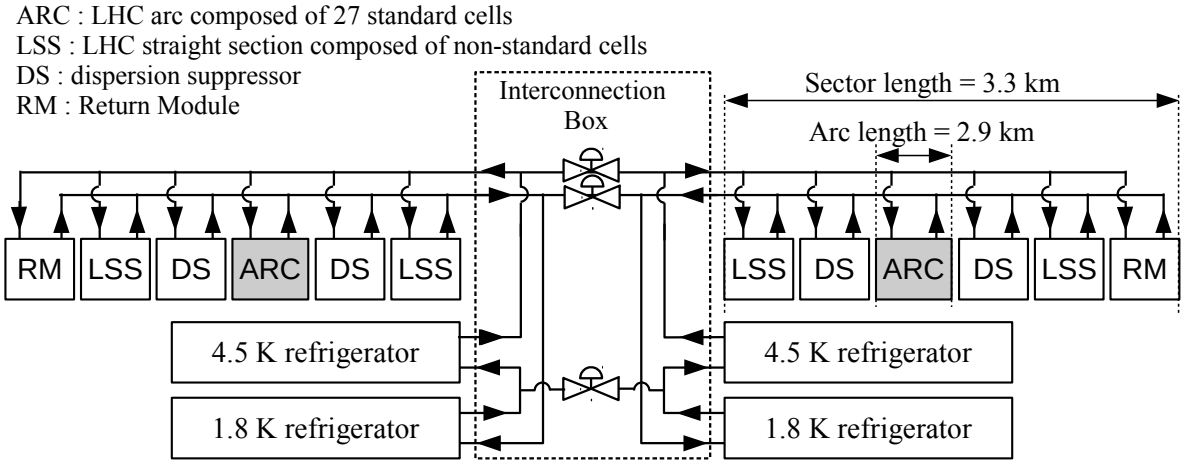

Fig. 2.7 LHC helium distribution related to the Superfluid Helium Cryogenic Circuit.

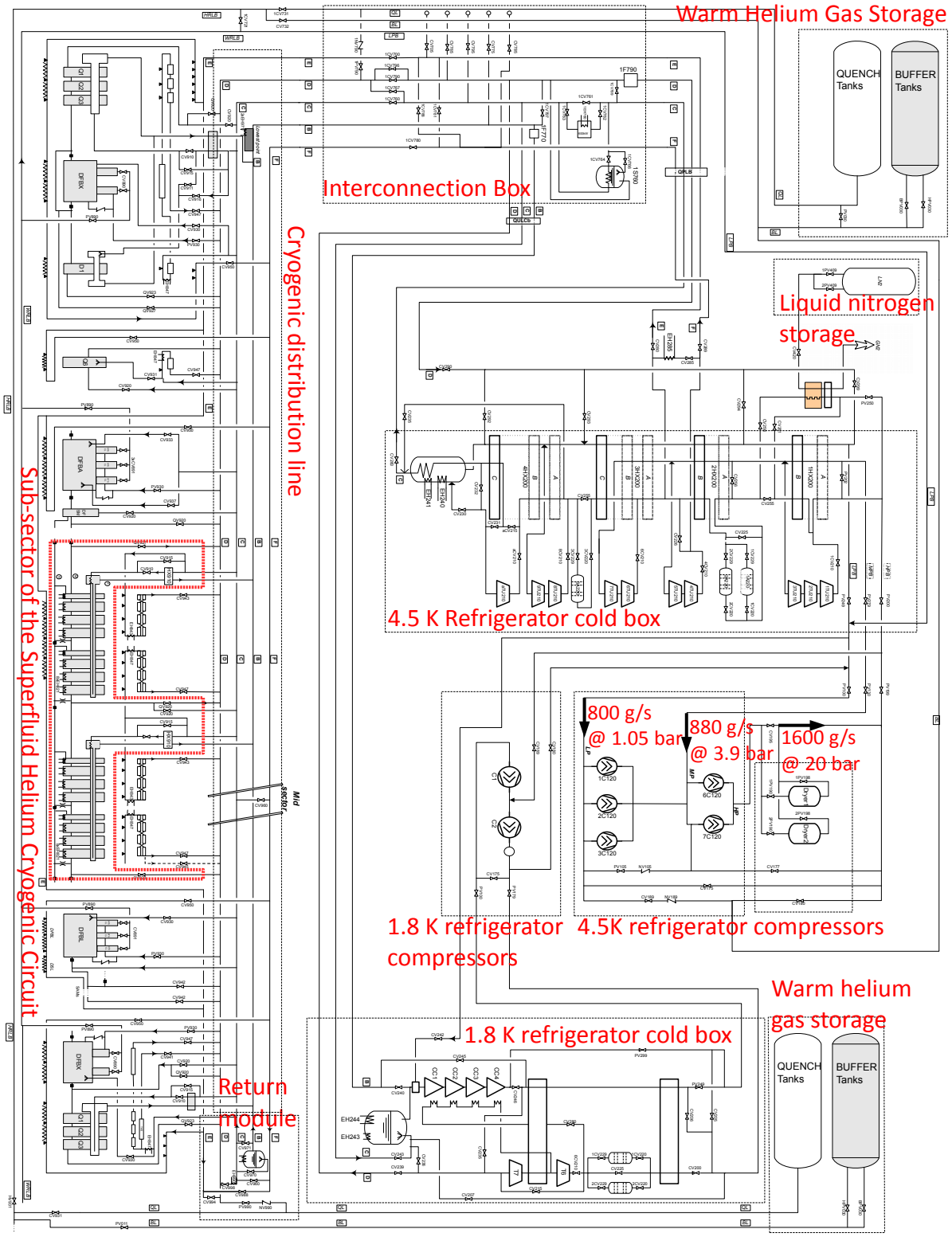

Fig. 2.8 LHC Cryogenics: Process Flow Diagram for sector 8-1. Source: CERN.

of the corresponding bayonet heat exchanger, see Fig. 2.13. The maximal valve capacity lies at approx. 20 g/s. The mass flow rate at the valve is calculated by a virtual flow meter, see Fig. 2.13c, based in upstream and downstream conditions at the valve.

The power of the 1.8 K refrigerator is kept in operational range using cryogenic electric heaters installed at most magnets. The heaters are also used to speed up the magnets warm up. Each heater has a maximal power of 25 W that can be precisely controlled and is submerged in the bath at positions indicated in Fig. 2.9.

Temperature at each of the main superconducting magnets is measured using one cryogenic thermometer, see Figure 2.9 that represents the helium bath in scale. The CERNOX™(Ceramic Nitride-Oxide) is a thin film resistance temperature sensor commercialized by M/s Lakeshore Cryotronics, Inc. It has operational range from below 0.3 K to 420 K, high sensitivity, excellent short-term and long-term stability, small physical size, fast thermal response and small calibration shifts when exposed to magnetic fields or ionizing radiation. Long term stability after 5.8 years has been assessed as a function of temperature: 1) at temperature of 1.4 K, the mean deviation was + 0.05 mK and 2) at 4.2K temperature the mean deviation observed was -0.17 K. CERNOX sensors are insensitive to radiation. The mean calibration shift was +1mK after tests where they were irradiated at 1.8 K with neutrons to total fluences of 3 10^{14}

a) SSS and Cryodipole, respecting the scale

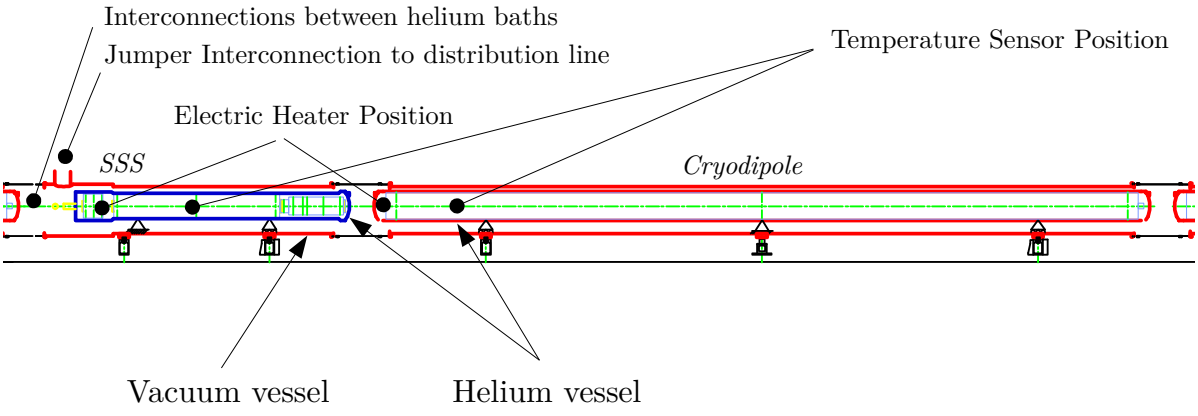

b) helium vessels in a standard cell, respecting the scale

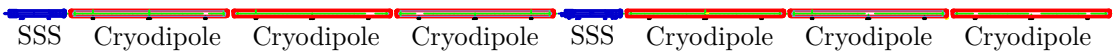

Fig. 2.9 Instrumentation localisation. Drawing source: CERN.

n/cm2 to 1 10^{15} n/cm2 (Balle et al. (2007); Prashant and Bangalore (2004). At each standard cell the temperature of helium entering the control valve after subcooling is mesured. At each sub-sector, the temperature of supercritical helium in header C and that of low pressure gas in the Line B are measured. The level helium in phase separators at each standard cell are measured using special devices where the resistance of superconducting filament is measured to obtain corresponding helium level, as the part of filament submerged in the He II is in a superconducting state and has no resistance. The quality of this measurement doesn't need to be high, as the phase separator should be empty during normal operation. The pressure of supercritical helium in header C is measured at each sub-sector, however the very low pressure of vapour in the header B is measured exclusively at the cold compressor station of the 1.8 K refrigerator.

The bias of measurements provided by the thermometers installed in the helium bath has been estimated based on the fact that due to the very high thermal conductivity of superfluid helium, the temperature along the bath is uniform while it warms up slowly at stand-by heat loads when no cooling power is provided nor electric heaters are turned on. This tact has been used to calibrate the thermometers and calculate the standard error

$$SE_{TT_h} = 7.3707 \times 10^{-4} \text{ K} \tag{2.1}$$

based on population of 96 thermometers present in the 6 sub-sectors that have been extensively tested '19L2', '23L3', '23L4', '27L6', '27L7' and '23L8', see Figure 2.10.

The measured process data is filtered using dead-band to reduce the number of samples and then it is permanently stored. The process data used in the thesis is the logged data accessed via TIMBER with 10 s sampling time with the REPEAT interpolation mode and then the data is filtered using dedicated PERL scripts, starting with removal of the repeated values resulting

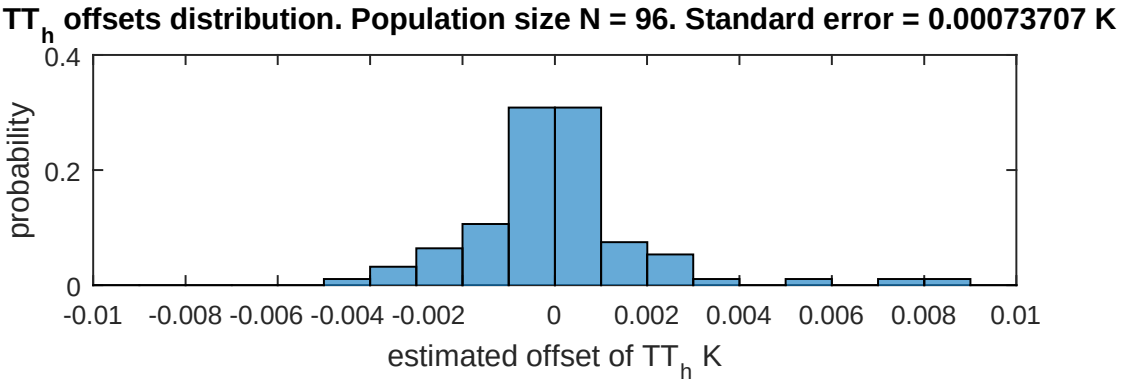

Fig. 2.10 TT_h offset distribution.

in data presented in Figure 2.11 and then interpolating and re-sampling all process data to a common time grid. Two interpolation techniques are used, one for slowly changing variables, see Figure 2.11a and another for fast changing variables presented in Figure 2.11c.

2.4 Control system architechture

The LHC cryogenics control system assures optimal and safe operation of the cryogenic system, by manipulating process variables based on actual values of other measured process variables and providing the information about current system condition to the human operators. As described by Gomes et al. (2008), the process automation for the cryogenic system around the LHC circumference is based on 16 high-end S7-400 Programmable Logic Controllers (PLC) with 500 ms cycle, each running 250 control loops, 500 alarms and interlocks, and a phase sequencer. Spread along 27 km and under ionizing radiation, 15 000 cryogenic sensors and actuators are accessed through industrial field networks. The fieldbuses allow for considerable simplification in cabling and maintenance, comparing to point-to-point connections and offering offer the capability of remote diagnosis and configuration. Profibus (1.5 Mbit/s) is used for the command and feedback of valves and some heaters. WorldFIP® (1 Mbit/s) gives access to data from sensors of temperature, pressure, level and from electrical heaters. The WorldFIP-PLC communication gateway is provided by dedicated Front-End Computers. In each sector, there are 2 PLCs, eight WorldFIP®network segments and five Profibus network segments, see Fig. 2.12. Due to the high level of ionizing radiation in the LHC tunnel, if possible, equipment has been installed in radiation-protected areas outside the tunnel. Large part of the front-end electronics, like high precision signal conditioners for the cryogenic thermometers, that installed in the tunnel has been designed at CERN. Siemens developed a version of their Profibus “intelligent” valve positioner where the radiation sensitive electronics is split from the cryogenic valve pneumatic actuator installed in the tunnel.

The man-machine interface is based on two SCADA systems (Supervisory Control and Data Acquisition), built with Siemens SIMATIC WinCC Open Architecture®: CRYO-SCADA, used by the operators and Cryogenic Instrumentation Expert Tool (CIET) used by the control experts to remotely monitor, configure, parameterize, and reset the WorldFIP read-out channels. Data-servers hosted in the CERN Control Center (CCC) are used to run the SCADA systems. CCC is the main control room at CERN, corresponding to operation of multiple particle accelerators and electricity and water installations at all CERN sites. The CERN secured Ethernet Technical Network is used for the communication between the PLCs, the Front-End Computers, the SCADA, and with other systems.

Δt is time interval, and Δ CV and Δ TT are measured value intervals between subsequent data samples

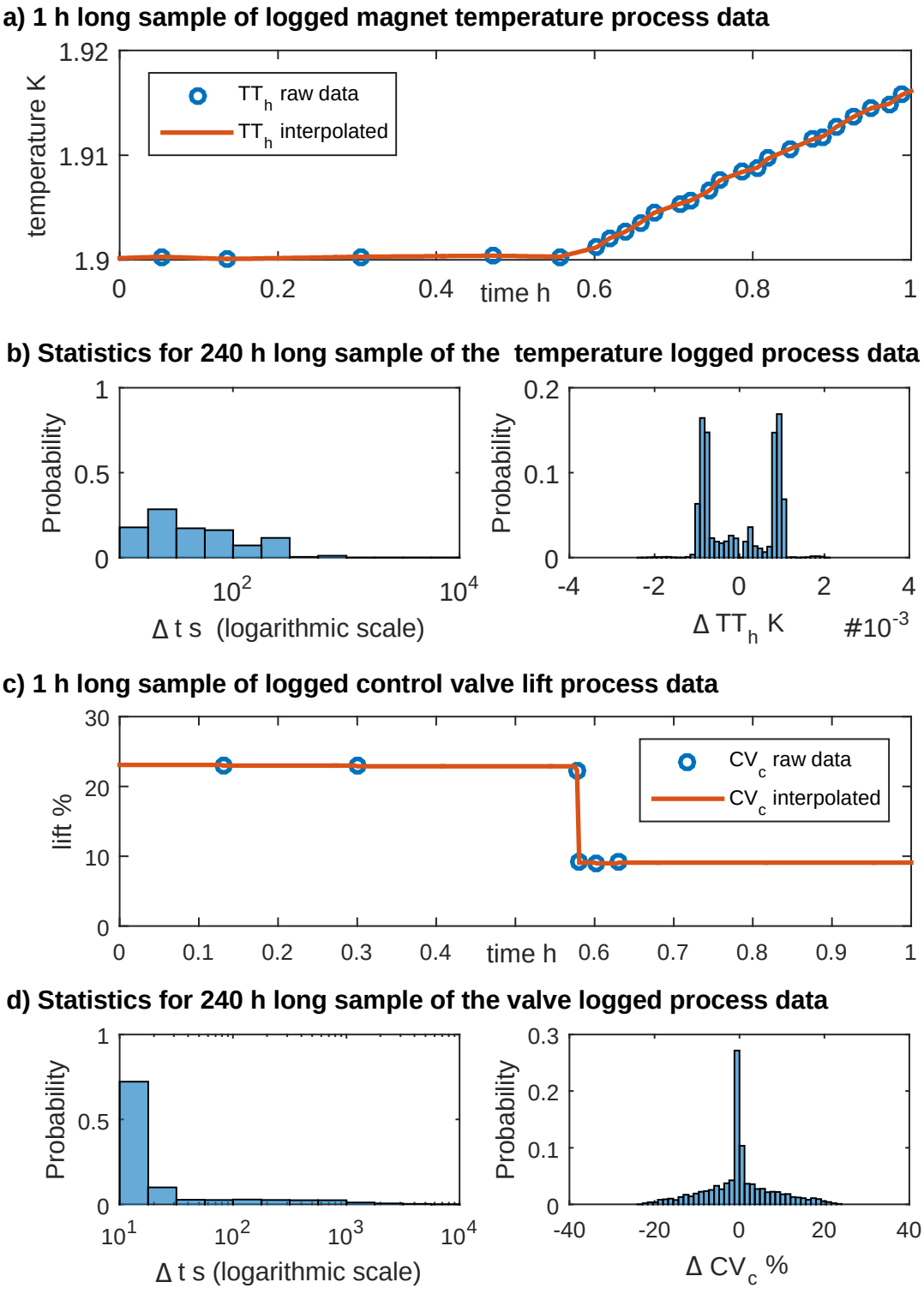

Fig. 2.11 Properties of logged LHC process data used in this work.

Several databases are the knowledge source for manufacturing, installation and test of the front-end hardware and for the automated software production. Those are: a) The LHC Layout DB managing the information on all LHC equipment topology, and logical or physical relationships; b) the CERN Engineering and Equipment Data Management System concerning all engineering documents and equipment information; c) Manufacturing and Test Folder used to store and track individual equipment data, like calibration data; d) Thermbase dedicated to individual data of all thermometers in the LHC; e) Controls Layout database providing an interface between Manufacturing and Test Folder, LHC Layout database and Thermbase.

The control software for FEC, PLC, CIET, and SCADA is mostly based on the CERN UNICOS framework (UNified Industrial COntrol System), which provides methodology, components, and tools to design and program industrial control systems. In the framework, the information from various databases is used to generate specifications for hardware configuration for the PLCs and Profibus front-end and for code generators that create the memory assignment for PLCs and SCADA, the PLC source code, the code for the PLC-SCADA communication middleware. This allows for rapid prototyping of the control system while minimizing human intervention and error sources. The source code of a single PLC typically contains 250 000 lines of Structured Control Language.

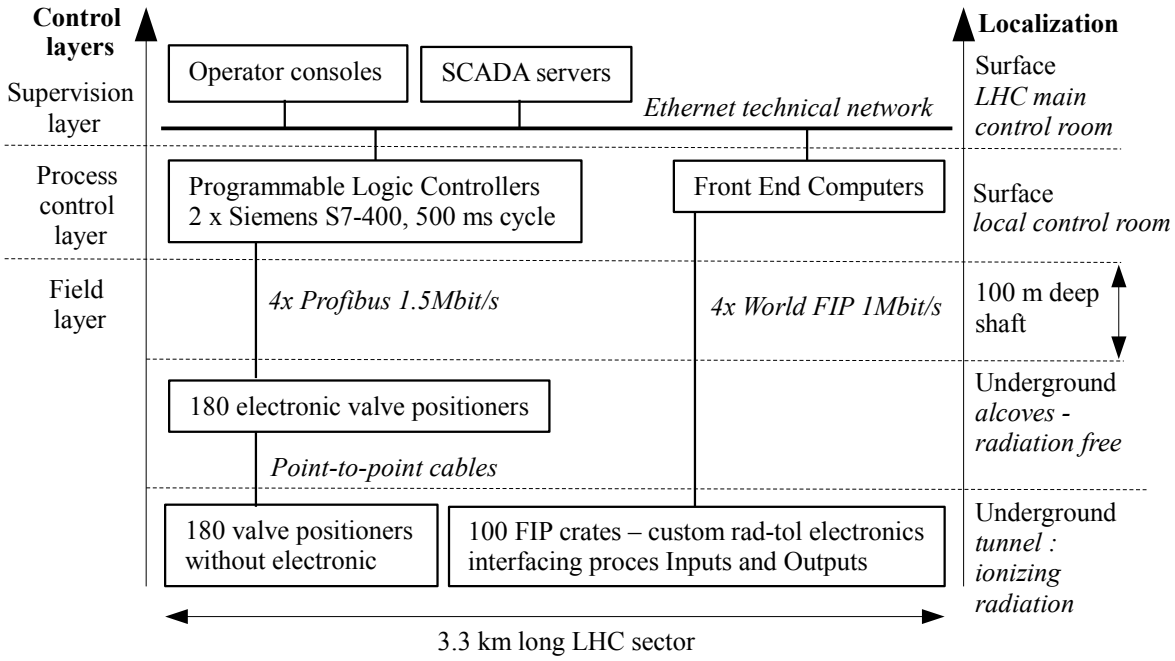

Fig. 2.12 Cryogenics control system architecture in the LHC tunnel.

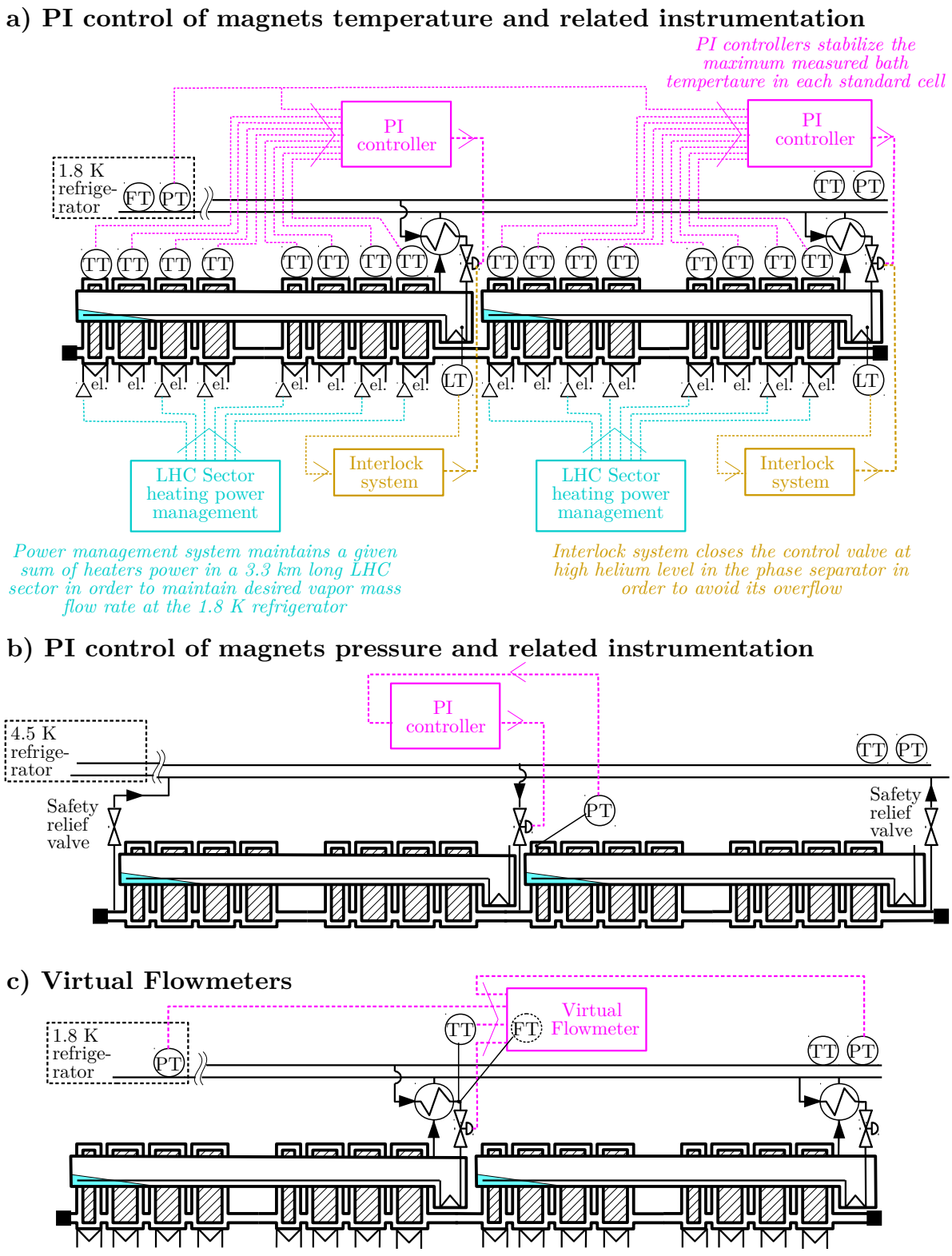

Fig. 2.13 Principal control loops, virtual flowmeters and related instrumentation.

2.5 Operation and magnets temperature dynamics

Figure 2.14a shows an LHC sub-sector during stable operation with particle beam energy of 3.5 TeV, when strongest perturbations to the measured magnets temperatures $T_{TT,h}$ occur during ramping up and down of the magnets current I_{dipole}. The maximal magnets temperature in each of the two standard cells is regulated using a PI controller manipulating the valve lift x_c, see Figure 2.13a. The 16 magnets temperatures are level while the close loop dynamics is very slow, with approx. 10 h of time needed to stabilize the temperature at the set-point $T_{sp} = 1.9\ K$. We notice that one valve tends to close due to strong thermal couplings between the cells sharing common helium bath. The lowest valve position is constrained in order to maintain the helium flow thermalizing it. Moreover, in some LHC arcs, electric heaters introduce additional heat into the bath $q_{EH,h}$ to keep vapor mass flow rate at the refrigerator above the minimal allowed value. The phase separators at the exchanger outlet are empty during normal operation as indicated by the measured levels of helium $l_{LT,p}$.

During LHC operation, superfluid in the bath is pressurized to enhance its heat transfer capabilities in comparison to saturated superfluid. The bath pressure p_h is regulated to stay in range

$$125\ \text{kPa} < p_h(t) < 165\ \text{kPa} \tag{2.2}$$

by another PI control loop manipulating a filling valve, see Fig. 2.13b. The preessure varies over time as 1) superfluid density changes with the bath temperature and volume of the helium vessel is constant and 2) due to superfluid vanishing viscosity, micro-leaks from the bath occur at rates in order of 1% of mass per month, e.g. through the safety relief valves as measured by Dufay et al. (1999). Thus bath is refilled automatically in case that the bath pressure drops under a ceratin level, Since He II leaks from the helium vessel into the surrounding it vacuum vessel, vacuum pump work continuously to maintain the insulation vacuum. The bath has to be kept pressurized and the pressure is controlled.

Figure 2.14b presents the operation of an LHC sub-sector while the very low pressure is degraded and lost. When the pressure measured at the refrigerator rises, the corresponding unmeasured helium saturation temperature in the heat exchanger increases. The set-point must be kept above the this saturation temperature in order to avoid coolant accumulation in the phase separator. The margin of approx. 0.1 K kept between the saturation temperature at the refrigerator and the set-point takes into account an unknown pressure drop in the distribution line. If the maximal temperature in an LHC arc exceeds 2.1 K, the magnets powering is not permitted, see Figure 1.2. When it rises above $T_\lambda\,(p_h = 130\ \text{kPa}) = 2.16\text{K}$, superfluidity is lost and pronounced temperature gradients appear. A cool-down phase starts when the pressure is recovered and is characterized by significant bath temperature gradients. The PI performance

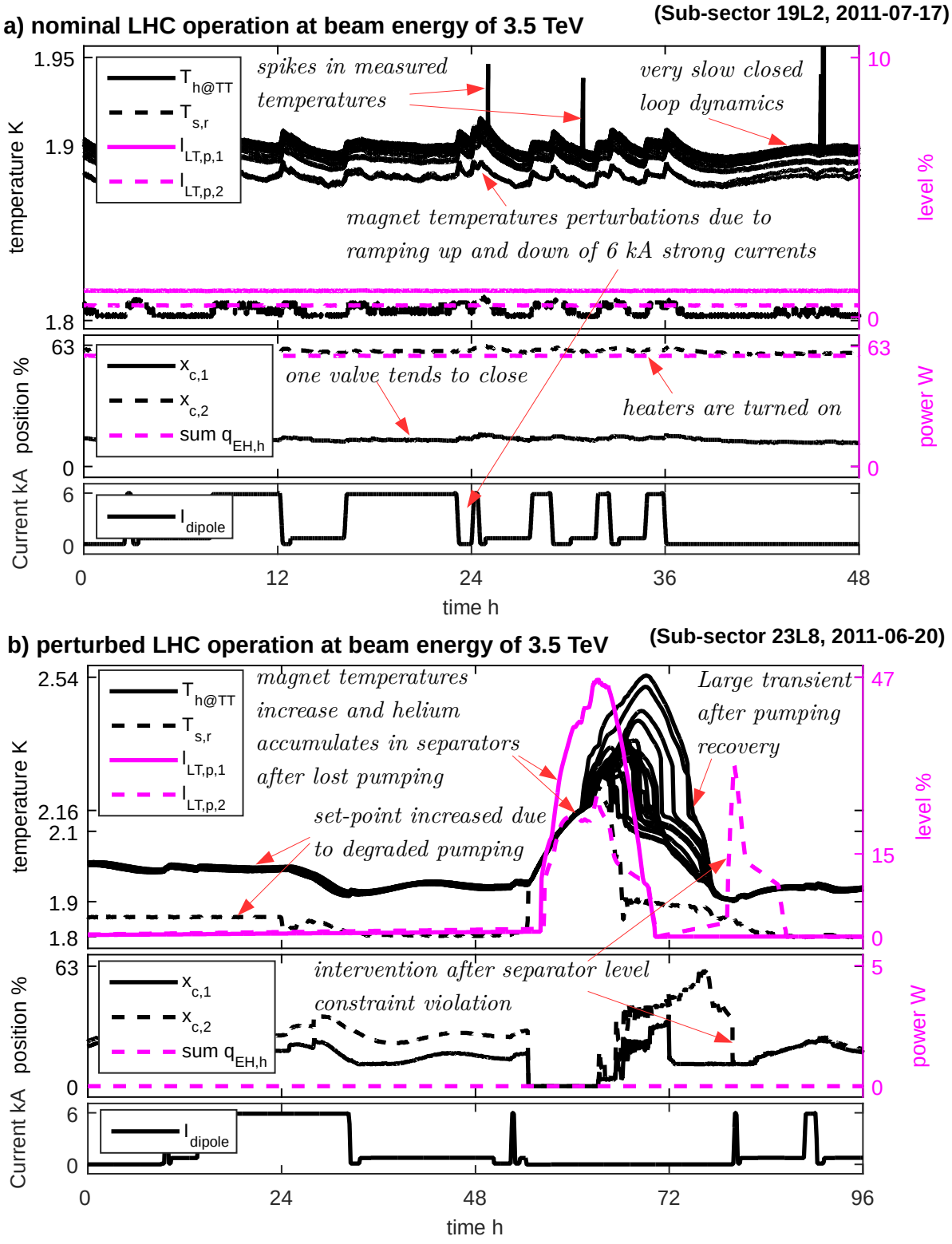

Fig. 2.14 LHC operation

during the transient is poor, occasionally forcing the interlock system or the operator to adjust the control valves position in order to accelerate the cool-down or respect the refrigerator constraints on maximal vapor mass flow rates and its rate of change or to avoid overflowing of the phase separators.

Figure 2.15 presents the magnets temperature dynamics during two identification tests at different levels of static heat loads into the bath, corresponding to the LHC stand-by and approx. to its double, respectively. During the identification tests electric heaters were used to imitate the additional heat loads. We observe that non-negligible temperature gradients appear along the 214 m long bath when the cooling power or the heat loads increase. The temperature dynamics changes drastically with increasing gradients and valve lifts: inverse response and dead-times that are hardly visible at lowest heat heat loads, dominate the dynamics at higher temperature gradients. Moreover, the dynamics depends on amplitude and direction of the control valve movements and cell's position.

The conclusion is that the dynamics is strongly non-linear, because the characteristics of magnet temperature response to valve manipulation varies strongly in function of the operational conditions and amplitude and sign of input excitation. Moreover, magnets temperature dynamics varies strongly along the bath and thus the distributed nature of the temperature dynamics is non-negligible even at lowest heat loads if more cooling power is applied. The heat load, having strong impact on the dynamics and thus defining the operational point, can rapidly change as it depends on the qualities of the cryostat insulation vacuum and particles' beam.

2.6 Modelling of the dynamics and advanced process control

Since early 1990's, dynamic models of the SHCC prototypes have been developed at CERN for purpose of system analysis, simulation and control system development (Andersen (2002); Blanco (2001); Casas and Van Weelderen (1993); Cyvoct et al. (1991); Flemsaeter (1995); Flemsaeter et al. (1998); Flemseater (2000)). Motivated by variable dead-time and strong inverse response of the non-linear temperature dynamics at the 30 m long LHC prototypes, NMPC and MHE have been developed using a first-principles, lumped parameter model of the dynamics, having 2 state variables, and an off-the-shelf optimization procedure (Blanco (2001); Blanco et al. (2009)). The first model of the SHCC version used at the LHC was the distributed-parameters model of the full-scale prototype of the *106.9 m long standard cell of the LHC* (Noga (2007)).

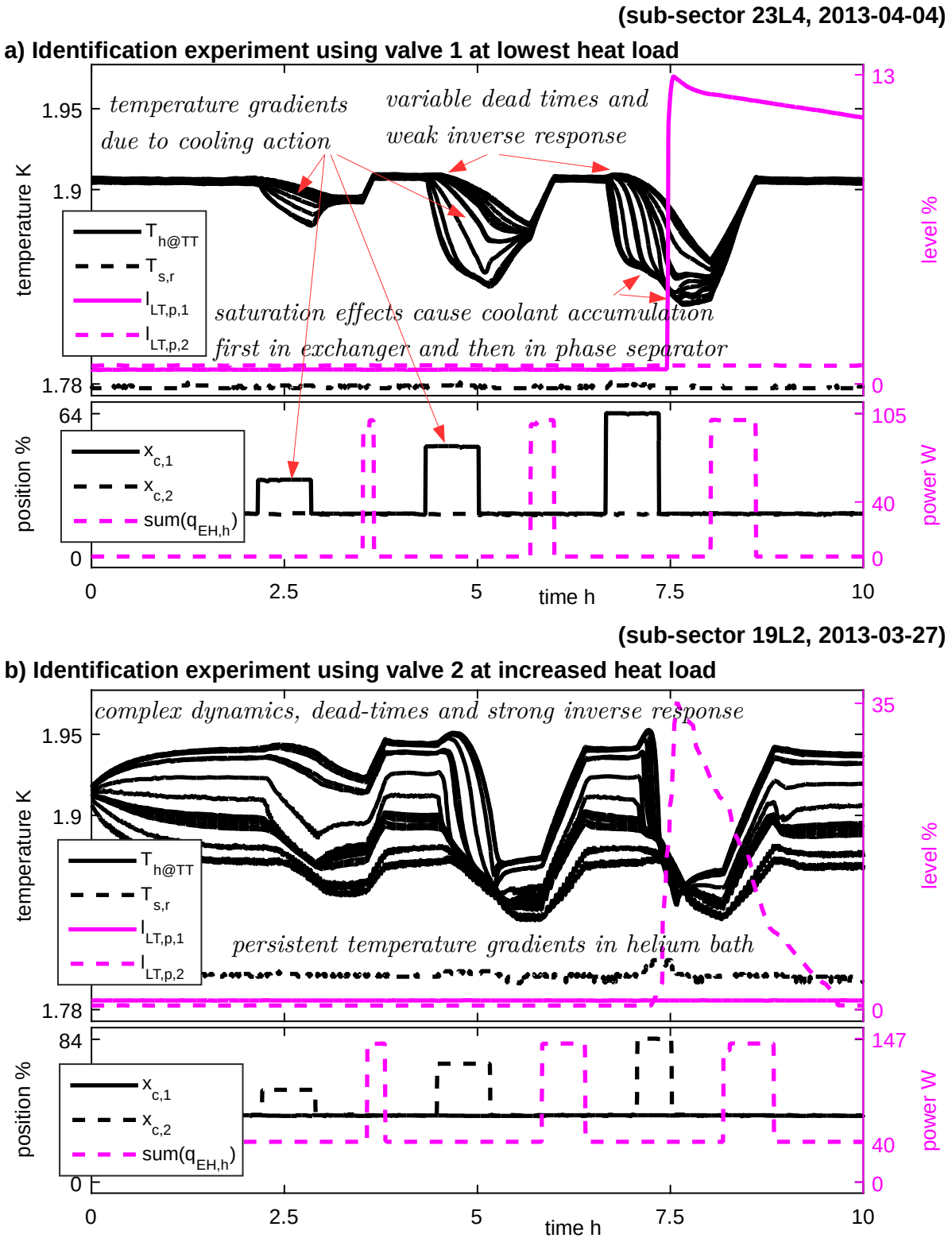

Fig. 2.15 LHC identification experiments.

Then, a distributed-parameters model of the temperature dynamics at a *214-m long sub-sector* of the SHCC at the LHC, having 10 states, has been used in the first version of NMPC and MHE unsuccessfully tested at the LHC, proving that real-time feasibility may be achieved with a more complex, distributed parameters model if a tailored optimization algorithm is applied (Noga et al. (2011)). Fortunately, the LHC magnets temperature dynamics is less challenging that in the prototypes - especially the inverse response is much less pronounced at nominal operational conditions and a PI controller is able to handle the dynamics during stable operation if tuned sufficiently conservatively to avoid excitation of non-linear aspects of the dynamics and respect the constraints on the coolant supply. Nevertheless, improved magnet temperature control has a direct impact on the LHC availability for operation and thus has a strong economic impact.

Chapter 3

Introduction to Non-linear Model Predictive Control

This chapter introduces basic background knowledge related to context, classification, formulation and solution of Non-linear Model Predictive Control problems.

3.1 NMPC as optimal feedback control

Feedback occurs when outputs of a system influence in inputs, creating a closed feedback loop. Feedback is extensively used in many areas of application to modify the system behaviour. Negative and positive feedback exist, that have stabilizing and destabilizing effect of the system, respectively. The stabilizing negative feedback is widely applied in control engineering in order to improve the behaviour of controlled system variables, e.g. the difference between actual and desired output, called the error signal, is applied as feedback to the input of the system, to bring the actual output closer to the reference.

Optimal control deals with the problem of finding a control input for a given system such that a certain optimality criterion is achieved. The criterion is typically expressed as finding a minimum of a cost functional or maximum of a performance functional. The typical optimal control problem has the form

$$\text{minimize } J = \phi(x(t+T)) + \int_t^{t+T} L(x(t'), u(t'))\,\mathrm{d}t', \tag{3.1}$$

subject to equality constraints corresponding to system dynamics and initial state x_0

$$\mathrm{d}x/\mathrm{d}t = f(x(t), u(t)),\ x(t=0) = x_0 \tag{3.2}$$

and an arbitrary vector-valued functions $E(x(t),u(t))$ and $I(x(t),u(t))$

$$E(x(t),u(t)) = 0,\ I(x(t),u(t)) \leq 0. \tag{3.3}$$

Optimal control problems are generally nonlinear and therefore, generally do not have analytic solutions and thus must be solved numerically.

3.1.1 Linear-Quadratic Regulator

In the special case of an unconstrained optimal control problem with linear model of system dynamics

$$\mathrm{d}x/\mathrm{d}t = A\,x(t) + B\,u(t),\ x(t=0) = x_0, \tag{3.4}$$

quadratic cost functional J

$$\text{minimize } J = \int_t^{t+T} x(t')^T\ Q\,x(t') + u(t')^T\ R\,u(t'))\,\mathrm{d}t',\ Q \geq 0,\ R > 0 \tag{3.5}$$

and no constraints, an analytic solution may be derived by solving a Riccati equation even for the case when the horizon length T is infinite. The solution has a feedback form

$$u(t) = K\,x(t) \tag{3.6}$$

and may be implemented as Linear Quadratic Regulator (LQR), providing optimal control for an unconstrained infinite horizon problem. LQR efficiently handles complex interactions between system variables in case of systems with multiple inputs and multiple outputs.

3.1.2 Linear Model Predictive Control

If the previous case with linear model, Eq. (3.4) and quadratic cost functional Eq. (3.5) is enhanced by taking into account presence of linear constraints

$$M\,x(t) + N\,u(t) + O \leq 0. \tag{3.7}$$

then the control law is non-linear and no general feedback form solution exist.

Linear Model Predictive Control (LMPC) approach provides optimal feedback control in this case by repeatedly solving the open loop optimization problem over a finite future time horizon, updating the initial conditions of the optimization problem using current system states in order to implement the feedback. The the convex quadratic programming problem found in the LMPC, is relatively easy to solve comparing to the general optimisation problem. Moreover,

a piecewise linear state feedback solution exists for LMPC problems, applied in Explicit Model Predictive Control. The LMPC is widely used in multiple industries as the control method that efficiently handles multivariable systems operated under constraints (Qin and Badgwell (2003)).

3.1.3 Non-linear Model Predictive Control

Non-linear Model Predictive Control (NMPC) is an extension of the feedback implementation approach used on MPC to a general non-linear constrained optimal control problem Eq. 3.1. NMPC is a feedback control technique where trajectories of manipulated variables (MVs) are repeatedly optimized over a finite future time horizon using: a) a non-linear model of system dynamics, b) measurements and estimates of system states and inputs, c) reference trajectories for controlled variables and d) knowledge about system constraints (Findeisen and Allgöwer (2002)). The NMPC, also known as Receding Horizon Control (RHC), is a powerful tool that directly addresses non-linear dynamics, complex interactions between process variables and operational constraints. Thus, it allows to meet complex control goals in case of nonlinear process operated in a wide range of conditions, e.g. polymerization reaction processes (Seki et al. (2001)). The couplings between process variables in multi-input-multi-output (MIMO) systems are directly handled by the NMPC, including cases where tuning and decoupling of the traditional PID controller is difficult. Thus in the process industry, the NMPC application provides a number of advantages, like saving resources and energy, increasing production capacity, reducing operators' load, and improving product quality, see Kano and Ogawa (2010).

In practice, application of NMPC may be expensive because it is difficult to build a non-linear model of a system. This makes the benefits of applications of NMPC questionable in cases where the performance of less advanced control systems supported with operators' suitable manual intervention is acceptable (Kano and Ogawa (2010)). Since NMPC involves solving a non-linear optimization problem, it requires special attention to ensure (local) convergence and real-time feasibility. This technique also asks for a special training of the operators and engineers and maintenance load may be higher if the models must be adjusted due to altering of system behaviour over time (ageing).

3.2 Output-feedback NMPC and optimal estimation

Optimal controllers are state feedback techniques and thus current values of system states and inputs must be provided first. However, in most practical problems, measurements of state

variables are not directly available and estimates are used instead that are provided by a state estimator.

Estimators can also be used independently. A soft-sensor, or a virtual sensor, is a software estimator that uses available knowledge about system variables and system model to provide measurements of the process variable(s) of interest when: 1) hardware sensors are unavailable or unsuitable or 2) data fusion from multiple sensors provides cheaper or more accurate measurements 3) redundant measurements are needed to improve fault-tolerance, provide fault-detection capability or monitor performance of other sensors.

Kalman filtering, also known as linear quadratic estimation (LQE), is an algorithm where a quadratic unconstrained optimisation problem, dual to the LQR controller, is solved in order to optimize the trajectories of the unknown estimated variables based on a linear system model and available measurements of system outputs and states.

Extended Kalman filter (EKF) is the nonlinear version of the Kalman filter which linearizes the nonlinear system model around current state estimate. The EKF is considered as standard in the theory of nonlinear state estimation, navigation systems and GPS.

Moving Horizon Estimation (MHE) is an estimation technique where past trajectories of unknown states and perturbations are repeatedly optimized over a finite past time horizon using a non-linear model of system dynamics and available measurements (Michalska and Mayne (1995), Rao et al. (2001)). Thus the approach used in MHE is similar to that used in NMPC and MHE may be used to provide the soft-sensor estimation functionality in case of challenging non-linear system taking into account non-linear constraints on estimated variables. Moreover, both NMPC and MHE may share the same model and optimization solver and they differ in the formulation of the optimization problems.

3.3 Economic NMPC

In a basic optimal control problem the goal is to minimize deviation of the controlled variable from a reference trajectory or a fixed steady-state set-point. However, in case of complex systems, the reference trajectory of the set-point must be optimized too, to optimize the global plant performance. The steady-state optimization of the reference is performed by the Real-Time Optimization (RTO) at a slow rate and only when the process is in a steady-state.

This approach has a number of drawbacks. The static models used in the RTO and the dynamic models used in the optimal control are different and due to the discrepancies between the models, in particular different steady-state gains, the set-points calculated from RTO are often inconsistent and unreachable for the controller. Moreover, since the RTO is executed much less frequently than controller, the optimization in RTO layer is inevitably delayed.

Finally if the process is operated over a wide range of conditions, a fixed model identified at a steady-state is usually not sufficient to cover the whole operating range, see Huang (2010) for more details and references.

NMPC has the advantages that the non-linear model is valid over a wider range of operating conditions and can be used for both the optimal control and the the RTO. This enables extension of NMPC to the Dynamic Real-Time Optimization (DRTO) or Economic NMPC (eNMPC) that is an advanced version of NMPC optimizes overall system performance taking into account multiple criteria, far beyond the basic deviation of the controlled variable from a set-point. Thus, the economic dynamic optimization problem optimizes simultaneously the system closed loop dynamics and its global performance. Since the optimization is performed much more frequently than the traditional steady-state optimization, the disturbances with a favorable impact on the profit can also be exploited efficiently.

However, due to more complex tradeoffs represented in the minimized cost functional in the eNMPC, its tuning is more complicated than that of basic NMPC formulation. Moreover, in case of optimization over a finite-horizon, the optimized trajectories may be attracted to a constant path and finally move away from the constant path at the end of the horizon. The turnpike, related to the inexact representation of the effects of the control actions after the finite horizon, is a characteristic property of the economic optimization problem with finite-horizon and has been introduced and studied in the economics literature before (Carlson et al. (1991), Würth et al. (2009)).

3.4 Stability

Assuring closed loop stability is a key goal of each control system. There are two notions of stability widely considered: 1) the nominal stability and 2) the robust stability. In case of non-linear systems, Lyapunov stability conditions may be used to evaluate the stability, but in practice Lyapunov functions needed in the process are very difficult to find. Moreover, in case of a non-linear output-feedback control, a system composed of a stable state non-linear estimator and stable non-linear controller is not necessarily stable.

For the model based advanced control methods, in general, very long horizons provide stable control but lead to high computational costs. Two methods are used to improve the closed-loop system stability using shorter horizons: 1) introducing a terminal constraint, (that is not applicable to the eNMPC) or, 2) introducing a terminal cost approximating the value of the cost functional corresponding to the time beyond the horizon, as proposed by Chen and Allgöwer (1998). Stability of the real-time optimization based controllers may be also

deteriorated by the delays due to the finite time needed to numerically solve the optimisation problems.

3.5 Models

In general, the dynamic models used in the model-based control techniques may be 1) data-driven black-box models, where parameters of arbitrary models are optimized to match the observed system dynamics or 2) system knowledge based first-principles models, describing the physical processes behind the model dynamics. In practice, the first-principles models are rather "grey-box" models where the the processes are partially described and 1) some of the model parameters are optimized to minimize the modelling errors or 2) the whole processes that are less well known or mode difficult to model or needed to be simplified, are modelled using the black-box approach.

Black-box models max have smaller state space than corresponding first-principles models and thus may have lower computational cost of simulation. Besides of the higher number of dynamic variables, the first-principle dynamic models usually involve differential algebraic equations (DAE) introducing significant computational complexity to the model simulation. Linear black-box models are widely used and their relatively straight-forward development is one of the reasons behind a widespread use of the LMPC.

In case of non-linear models, parameters of black-box models are much difficult to identify as the modelled dynamics may vary strongly at various operating points and thus large amount of system process data covering the whole operational range is needed. In this case of non-linear first-principles models, implementing the knowledge about system dynamics allow to actually reduce the number of model parameters to be optimized and thus greatly facilitates the identification of a non-linear model.

3.6 Solving NMPC optimization problem

Moving Horizon Estimation and Model Predictive Control are advanced control techniques that use 1) a model of system dynamics, 2) knowledge about operational conditions and 3) real-time optimization to provide estimation and controls functionalities. Both techniques rely on solving a non-linear optimization problems with inequality and equality constraints. The optimization is repeated continuously over time using updated measurements/estimates, which provides the feedback. The choice of the optimization strategy is strongly affected by the fact that the solution of an open loop optimal control problem is repeated continuously and in real-time,

implying that 1) speed of optimization must much the real system dynamics evolution and 2) the sub-sequent solutions of the optimization evolve slowly.

3.6.1 Direct vs. Indirect Methods

In order to solve a non-linear optimal open loop problem, the indirect methods or variational methods apply "optimize then discretize" strategy, by starting with solving the specific optimization problem involving system dynamics based on calculus of variations and the Pontryagins Maximum Principle, and then discretizing and solving numerically the optimality conditions in order to solve the optimized variables. C/GMRES by Ohtsuka (2004) is an example of this approach.

The direct methods, start with parametrization of the control problem that transforms the dynamic optimization problem it a standard static non-linear optimization problem that is then solved using one of many non-linear optimization solver that are reviewed by Leyffer and Mahajan (2010). The state and/or control trajectories are parameterized using an appropriate functions transforming the cost functional into a cost function. Then, the parameters of the function approximations are treated as optimization variables.

3.6.2 Explicit, on-line and mixed NMPC

The computational cost of an on-line optimization of a NMPC control update can be too high to much for the optimization to match the real system dynamics evolution and thus to reach realise the real-time feasibility of NMPC. In order to reduce the on-line computational burden, Explicit NMPC uses multi-parametric Nonlinear Programming (mp-NLP) to pre-compute off-line a sub-optimal piece-wise linear controller, where various linear feedback control laws are used in different regions if partitioned state space, Grancharova et al. (2007) provides the details and references.

3.6.3 Discretization of the optimized trajectories

Since the optimized finite-time trajectories of inputs and optionally states (and eventually co-states in indirect methods only) are described as real-valued functions, they consist of infinite number of points and thus the optimisation problem is infinite dimensional. Discretisation using a finite number of parameters and basis functions is widely used to covert the original infinite dimensional problem into a finite-dimensional one that can be solved numerically. E.g.

an optimized input trajectory may be expressed as

$$u(t) = \sum_{i=1}^{N} \sigma_i(t)\, u_i^*(t) \tag{3.8}$$

using N parameters $u_i^*(t)$, and N basis functions $\sigma_i(t)$.

3.6.4 Model simulation - solving the system dynamics

Since the cost functional is a functional of state variables trajectories they must be evaluated too. Thus the model must be simulated - it's dynamics must be integrated. There are three widely used approaches to this problem: single shooting, multiple shooting and collocation method.

Single shooting

The single shooting method is based on the observation that given the initial state and input variables trajectories over the horizon, the modelled dynamics may be simply integrated over the horizon. Thus, the state variables need not to be optimized as they are found as solution of the simple initial value problem. The main drawback of this method is that in case of unstable systems the trajectory may run away over the horizon rendering the optimization impossible.

Multiple shooting

Multiple shooting allows to overcome the drawback of the single shooting by subdividing the simulation horizon into a number of shorter sub-intervals and thus limiting the risk of a runaway of the state variables. This is achieved at a price of adding: 1) the initial states at the sub-intervals into to set of optimized variables and 2) constraints assuring continuity of the state variables trajectories between the intervals.

Collocation method

The two methods just mentioned, are sequential methods where the the optimization of the manipulated variables was effectively separated from the integration of the state dynamics in order to reduce the number of optimized variables. The collocation method is a simultaneous solution strategy, where the state variables trajectories are parameterized and the parameters are included into the set of the optimized variables and the system dynamics is a part of the optimization problem constraints. Thud in this method, the manipulated variables and the state variables are optimized simultaneously.

3.7 Non-Linear Programming with constraints

Non-Linear Programming (NLP) is the process of solving non-linear optimization problems with inequality and equality constraints. A generic non-linear program (NLP) has the form

$$\min_{x \in \mathbb{R}^{n_x}} \{J(x) : \; E(x) = 0, \; I(x) \leq 0\} \tag{3.9}$$

with the scalar cost function $J(x) : \mathbb{R}^{n_x} \to \mathbb{R}^1$, the equality constraint vector-valued function $E(x) : \mathbb{R}^{n_x} \to \mathbb{R}^{n_E}$ and the inequality constraint vector-valued function $I(x) : \mathbb{R}^{n_x} \to \mathbb{R}^{n_I}$.

3.7.1 First order necessary optimality conditions

Any local minimizing solution x^* of the optimization problem must satisfy the necessary optimality conditions - the Karush-Kuhn-Tucker (KKT) conditions Kuhn and Tucker (1951):

$$\nabla_x \left(J(x^*) + \lambda^{*T} \, E(x^*) + \mu^{*T} \, I(x^*) \right) = 0, \tag{3.10a}$$

$$E(x^*) = 0, \tag{3.10b}$$

$$[I(x^*)]_i \, [\mu^*]_i = 0, \; i = 0, \ldots, n_I, \tag{3.10c}$$

$$I(x^*) \leq 0 \tag{3.10d}$$

$$\text{and } \mu^* \geq 0, \tag{3.10e}$$

with vectors of Lagrange multipliers $\lambda^* \in \mathbb{R}^{n_E}$ and $\mu^* \in \mathbb{R}^{n_I}$. An i-th element of μ^* and vector-valued function $I(x^*)$ are noted as $[\mu^*]_i$ and $[I(x^*)]_i$ respectively. In case of a convex problem, the conditions are also sufficient conditions for a global optimum.

3.7.2 Handling the inequality constraints

The Newton's method cannot be applied directly to the system of non-linear equations Eqs. (3.10a)-(3.10c) due to presence of the inequalities Eqs. (3.10d) and (3.10e) and the related product form (3.10c). Application of the Newton's method is possible only after the original problem with inequality constraints has been transformed into a non-linear program with equality constraints. There are three mainstream approaches to the NLP with inequality constraints, which do this transformation Diehl et al. (2009):

- the active set method, where the inequality constraints are subdivided into to two sets: one of active constrains $[I(x^*)]_i = 0$ that can be treated as equality constraints and anther of inactive constraints $[I(x^*)]_i < 0$ that do not affect the solution and thus can be neglected, the active set must be updated continuously during the solution process,

- the interior point method Waltz et al. (2006), where the inequality constraints are replaced by barrier functions added to the cost function, so that the excessive cost associated with approaching the limits of the feasible region defined by the inequality constraints keeps the solution in this region, the barrier should evolve during the solution to assure good convergence and accuracy of solution,

- the slack variable method used in Continuation/GMRES Ohtsuka (2004) where the inequality constraints are transformed into equality constraints using additional slack variables; in order to obtain a well posed problem, the slack variables must enter into the cost function, which makes the formulation similar to the interior point method.

Active set method

The Active Set approach is based on the observation that if an inequality constraint is not active, i.e. smaller than zero, then it does not influence the optimal solution and can be neglected. In case that it is equal to zero and the corresponding Lagrange multiplier is positive, it is active and it can be treated as all the other equality constraints. Thus the set of active and violated inequality constraints

$$\mathscr{A}(I(x)) = \{i | [I(x)]_i \geq 0 \text{ and } [\mu]_i > 0\} \tag{3.11}$$

and the corresponding vector-valued function of active constrains

$$I_A(x) \text{ is composed by } [I]_i, i \in \mathscr{A} \tag{3.12}$$

with Lagrange multipliers

$$\mu_A(x) \text{ composed by } [\mu]_i, i \in \mathscr{A} \tag{3.13}$$

are continuously updated. The resulting non-linear program with equality constraints

$$\min_{x \in \mathbb{R}^{n_x}} \{J(x) : \ E(x) = 0, \ I_A(x) = 0\}, \tag{3.14}$$

with $I_A(x) : \mathbb{R}^{n_x} \to \mathbb{R}^{n_{I_A}}$, $0 \leq n_{I_A} \leq n_I$, that is reformulated using Lagrange multipliers λ_A as

$$\min_{x, \ \lambda, \ \mu_A} \ J(x) + \lambda^T \ E(x) + \mu_A^T \ I_A(x). \tag{3.15}$$

The first order necessary optimality condition for this problem is

$$F_{AS}(X_{AS}^*) = 0, \tag{3.16}$$

with

$$F_{AS}(X^*_{AS}) = \begin{bmatrix} \frac{\partial}{\partial x}\left(\mathscr{L}_{AS}(x^*, \lambda^*, \mu^*_A)\right) \\ E(x^*) \\ I_A(x^*) \end{bmatrix} \tag{3.17}$$

with the Lagrangian function

$$\mathscr{L}_{AS}(x^*, \lambda^*, \mu^*_A) = J(x^*) + \lambda^{*T}\, E(x^*) + \mu^{*T}_A\, I_A(x^*) \tag{3.18}$$

and is solved for

$$X^*_{AS} = \begin{bmatrix} x^* \\ \lambda^* \\ \mu^*_A \end{bmatrix} \tag{3.19}$$

using a Newton-type method, with update of the active set at each iteration.

Interior point method

In the interior point approach, the inequality constraints are replaced by barrier functions integrated into the cost function. The barrier function has form $-\log(-[I(x)]_i)$ and tends towards infinity as the constraint function $[I(x)]_i$ approaches zero. This approximation converts the original problem (3.9) into a non-linear program with equality constraints in the form

$$\min_{x \in \mathbb{R}^{n_x}} \left\{ J(x) - a \sum_{i=1}^{n_I} \log(-[I(x)]_i) :\ E(x) = 0 \right\}. \tag{3.20}$$

However, due to possible numerical problems related to rank deficiency in the linear equation corresponding to this formulation, another formulation is widely used, involving the vector of slack variables $s \in \mathbb{R}^{n_I}$, $s > 0$:

$$\min_{x \in \mathbb{R}^{n_x}} \left\{ J(x) - a \sum_{i=1}^{n_I} \log(s]_i) :\ E(x) = 0,\ I(x) + s = 0 \right\}. \tag{3.21}$$

After reformulation using Lagrange multipliers and with the Lagrangian function

$$\mathscr{L}_{IP}(x, \lambda, \mu, s) = J(x) - a \sum_{i=1}^{n_I} \log(s]_i) + \lambda^T\, E(x) + \mu\ (I(x) + s) \tag{3.22}$$

the corresponding first order necessary optimality condition is

$$F_{IP}(X^*_{IP}) = 0, \tag{3.23}$$

with

$$F_{IP}(X^*_{IP}) = \begin{bmatrix} \frac{\partial}{\partial x}\mathscr{L}_{IP}(x^*,\lambda^*,\mu^*,s^*) \\ E(x^*) \\ I(x)+s \\ [\mu^*]_1 \;\; [s]_1 - a \\ \vdots \\ [\mu^*]_{n_I} \;\; [s]_{n_I} - a \end{bmatrix}. \tag{3.24}$$

and is solved for

$$X^*_{IP} = \begin{bmatrix} x^* \\ \lambda^* \\ \mu^* \\ s^* \end{bmatrix} \tag{3.25}$$

using a Newton-type method, and the value of parameter a is decreased during optimization to achieve a compromise between the convergence rate and the solution accuracy. This is inconvenient in case where optimization with a single step Newton is used. Single iteration per control update is enough in real-time control applications, where optimization is performed continuously over time and the solution is suppose to evolve slowly over time - the solution property has been exploited in the Continuation/GMRES method Ohtsuka (2004).

Slack variable method

In the slack variable method Ohtsuka (2004), the inequality constraints are converted into equality constraints using slack variables $s \in \mathbb{R}^{n_I}$. A non-negative function of the slack variables is introduced into the original problem formulation (3.9). Moreover, the slack variable must appear in the objective function, similarly as in the IP method, in order to avoid singularities at $s_i = 0$ Seguchi and Ohtsuka (2003). The corresponding non-linear program with equality constraints has the form

$$\min_{x\in\mathbb{R}^{n_x}} \left\{ J(x) + a \sum_{i=1}^{n_I} [s]_i : \; E(x) = 0, \; [I(x)]_i + [s]_i^2 = 0, \; i = 0,\ldots,n_I \right\}. \tag{3.26}$$

Using the Lagrangian function

$$\mathscr{L}_{SV}(x,\lambda,\mu,s) = J(x) + a \sum_{i=1}^{n_I} [s]_i + \lambda^T \, E(x) + \sum_{i=1}^{n_I} [\mu]_i \, \left([I(x)]_i + [s]_i^2 \right) \tag{3.27}$$

the corresponding optimality condition is

$$F_{SV}(X^*_{SV}) = 0, \tag{3.28}$$

with

$$F_{SV}(X^*_{SV}) = \begin{bmatrix} \frac{\partial}{\partial x}\mathscr{L}_{SV}(x^*, \lambda^*, \mu^*, s^*) \\ E(x^*) \\ [I(x)]_1 + [s^*]_1^2 \\ \vdots \\ [I(x)]_{n_I} + [s^*]_{n_I}^2 \\ 2\ [\mu^*]_1\ [s^*]_1 - a \\ \vdots \\ 2\ [\mu^*]_{n_I}\ [s^*]_{n_I} - a \end{bmatrix} \tag{3.29}$$

and is solved for

$$X^*_{SV} = \begin{bmatrix} x^* \\ \lambda^* \\ \mu^* \\ s^* \end{bmatrix} \tag{3.30}$$

The similarity between this formulation and that of the Interior Point method is clearly visible. Both methods contain the product expression $[\mu^*]_{n_I}\ [s^*]_{n_I}$.

Geometry of the product term

The choice of method for the non-linear programming has strong impact on the conditioning of the linear equation for the Newton's step. Among the Active Set, the Interior Point and the Slack Variable methods, the Active Set method has the best conditioning. The reason for the deteriorated conditioning in the other two methods, even in case of the simple example presented, is the presence of the product term having "zero gradient" zones, where its gradients vanish. Those gradients enter into the linear equation, and their values are strongly reduced as the solution enters the problematic zone, resulting in deteriorating conditioning. The geometric aspects of the Active Set equivalent method illustrate the superior conditioning of the Active Set method. Good conditioning makes Active Set approach suitable for non-linear programming implementations where the linear equation is solved using an iterative solver like GMRES. The reason for this is that in case of iterative solvers a direct link exists between the conditioning and the minimal computational cost necessary to obtain a good approximation to the exact solution.

3.8 Iterative methods for non-linear optimization

Numerical methods for non-linear optimization problems are iterative - a new approximated solution is calculated based on a current approximated solution and the process is repeated until an iteration is accepted as the solution. The iterative methods for optimization can be classified into two categories: line search methods and trust region methods. Line search algorithms for optimization, first calculates a search direction for each iteration and then searches along this direction to find a better solution. The sequence is reversed in a trust region algorithm, where the trust region is defined first that limits the maximal length of the update step and then the solution update is found within that region, see the monograph by Conn et al. (2000).

In the Newton's method for solving the non-linear optimization problem, the Jacobian vector of first derivatives and the Hessian matrix of second derivatives of the cost function to be minimized must be provided. The derivatives may be calculated by hand only in the simplest cases. For more complex functions, automatic differentiation may be used that breaks down computer code used to calculate a function value evaluating elementary arithmetic operations and perform the function differentiation by chain rule. A similar approach is symbolic differentiation, where the chain rule is applied to the algebraic expression of the function to be differentiated. The differentiation methods just mentioned may only be used on smooth functions and the size of the code produced using the chain rule may be large for very complex functions. Another possibility is application of finite differencing to numerically calculate approximate derivatives.

Quasi-Newton methods avoid using second order derivatives of the minimized function by replacing it with secant approximations calculated based on the first derivatives of the cost function. Those methods are widely used because they converge faster than steepest descent method and are cheaper to compute per iteration than Newton's method. A widely used approximation is the Broyden–Fletcher–Goldfarb–Shanno (BFGS) algorithm.

Chapter 4

Introduction to first principles modelling and numerical simulation

In this section we discuss the motivation for and the key aspects of the first-principles modelling approach applied to distributed parameters systems, like the superfluid helium cryogenic circuit.

4.1 First-Principle Versus Data-Driven Models

A first principles model of a physical quantity implements the laws of physics governing that quantity. In case of non-linear models, first-principles models offer a number of advantages over data-driven black-box models. One big advantage is that since their structure corresponds to that of the modelled system, one may expect the first-principle models may be valid outside of the range covered by the process data used in the model development. In contrast, the data-driven models are valid only in the range covered by the process data used in their development and thus the data-driven models for complex non-linear systems would need very large sets of process identification data, that may be prohibitively large. Thus the set of the identification process data needed to develop an application-specific first-principles model are in general smaller than those needed to develop a black-box model. The main disadvantage of first principles model, is the time and skill required to develop them.

4.2 Conservation laws

The description of the modelled dynamics is based on formulation of the conservation laws, see White (1998) for reference. Since 1-D Finite Volume discretization approach is widely used in

the model, in the following sub-section I review the laws in the integral form suitable for 1-D finite volume.

4.2.1 The Reynolds transport theorem

The integral form is based on the Reynolds transport theorem that relates the dynamics of a system property P_{syst} with the dynamics of that property P within a specific region. Here, the system is a finite volume occupying the region. In 1-D the theorem has the form

$$\mathrm{d}/\mathrm{d}t(P_{syst}) = \mathrm{d}/\mathrm{d}t(\int_{FV} \mathrm{d}P/\mathrm{d}m\ \rho\ \mathrm{d}V) + (\mathrm{d}P/\mathrm{d}m\ \rho\ A\ U)_{out} - (\mathrm{d}P/\mathrm{d}m\ \rho\ A\ U)_{in} \tag{4.1}$$

here the three terms on the right hand side are, respectively, the rate of change of P within the finite volume, and the fluxes of P passing out of and into the volume. The form is suitable for our system, in which the density of the two phase flow varies and the finite volume occupied by He II is deformable in case of the He II-vapor two phase flow in the bayonet heat exchanger.

4.2.2 Mass conservation

Substituting the property P by the mass m in the Eq. 4.1, we obtain the mass conservation law in the integral form

$$0 = \mathrm{d}/\mathrm{d}t(m_{syst}) = \mathrm{d}/\mathrm{d}t(\int_{FV} \rho\ \mathrm{d}V) + (\rho\ A\ U)_{out} - (\rho\ A\ U)_{in}. \tag{4.2}$$

4.2.3 Linear momentum conservation

Substituting the property P by the linear momentum mU in the Eq. (4.1), we obtain the mass conservation law in the integral form

$$\sum F = \mathrm{d}/\mathrm{d}t(m\ U)_{syst} = \mathrm{d}/\mathrm{d}t(\int_{FV} U\ \rho\ \mathrm{d}V) + (\rho\ A\ U^2)_{out} - (\rho\ A\ U^2)_{in}, \tag{4.3}$$

with $\sum F$ including all the forces acting on the finite volume. This can be rewritten by substituting

$$U = W/\rho\ A \tag{4.4}$$

with the mass flow rate W as

$$\sum F = \mathrm{d}/\mathrm{d}t(m\ U)_{syst} = \mathrm{d}/\mathrm{d}t(\int_{FV} U\ \rho\ \mathrm{d}V) + (W\ U)_{out} - (W\ U)_{in}. \tag{4.5}$$

This representation is based on assumption that the velocities are uniformly distributed in the flows, that introduces negligible errors only in turbulent flows, present in this model. For laminar flows, that are not considered here, a momentum-flux correction factor must be used. Moreover, it is valid for an inertial reference frame, thus we neglect the influence of the Coriolis effect.

4.2.4 Energy conservation

Substituting the property P by the energy E in the Eq. (4.1), we obtain the energy conservation law in the integral form

$$\begin{aligned} \mathrm{d}Q/\mathrm{d}t - \mathrm{d}\hat{W}/\mathrm{d}t = \mathrm{d}/\mathrm{d}t(E_{syst}) = \\ \mathrm{d}/\mathrm{d}t(\int_{FV} \mathrm{d}E/\mathrm{d}m\ \rho\ \mathrm{d}V) + (\mathrm{d}E/\mathrm{d}m\ \rho\ A\ U)_{out} - (\mathrm{d}E/\mathrm{d}m\ \rho\ A\ U)_{in} \end{aligned} \quad (4.6)$$

where positive Q denotes the heat added to the system and positive $\hat{W}$ denotes work done by the system. In the following we consider three components of the energy,

$$E = E_{int} + 1/2\ m\ U^2\ + m\ g\ y, \quad (4.7)$$

the internal, kinetic and potential energy. I neglect all components of the work therm $\hat{W}$ but the work done by pressure at the control surfaces,

$$\mathrm{d}\hat{W}_p/\mathrm{d}t = \int p\ U_{in}\ \mathrm{d}A \quad (4.8)$$

because there are no moving parts in the circuit and the work due to viscous stresses is negligible. The positive flow velocity U_{in} corresponds to flow into the finite volume. After this simplifications and using enthalpy

$$h = U/m + p/\rho \quad (4.9)$$

we obtain the form of the energy conservation law widely used in this thesis

$$\begin{aligned} \mathrm{d}Q/\mathrm{d}t = \\ \mathrm{d}/\mathrm{d}t(\int_{FV} \mathrm{d}E/\mathrm{d}m\ \rho\ \mathrm{d}V) + (h + 1/2\ U^2 + g\ y)_{out}\ W_{out} - (h + 1/2\ U^2 + g\ y)_{in}\ W_{in}. \end{aligned} \quad (4.10)$$

4.3 Empirical formulas

Unfortunately, many physical processes are still not precisely described by theoretical formulas and thus empirical data and engineering correlations are used to describe them. This is valid of He II properties including the counter-flow heat transfer, pressure drops, flow regime transitions, pressure drops and heat transfer in turbulent two phase flow, Kapitza conductance and many other key physical processes governing the circuit dynamics. Thus, the model is a first principles model in the sense that it is describes the macroscopic processes using the available descriptions and it does not precisely explains the physics behind them.

4.4 Distributed Parameters Systems and Partial Differential Equations

A system of Partial Differential Equations (PDEs) describes the distributed variables dynamics at an infinite number of continuously distributed points in space and time and thus the system has an infinite number of degrees of freedom and the dimension of the equations' solution is infinite. In order to numerically solve PDEs, we lower the number of degrees of freedom to a finite number. One possibility to do this is through spatial and temporal discretization. The spatial discretization, transforms the infinite-dimensional PDE into a set of finite number of Ordinary Differential Equations (ODEs) describing dynamics of a finite number of variables that may correspond to values at a given point in space or to average value over an interval, etc.

Three commonly used spatial discretization methods are the finite element method (FEM), finite volume method (FVM) and finite difference method (FDM). In model describing the conservation laws, the finite volume approach providing the most intuitive interpretation is preferred. In this approach, the continuous spatial domain is subdivided into a finite number of intervals, or volumes, and the modeled variable is treated as lumped, representing average value of the distributed variable, in each finite volume.

A useful concept closely related to the distributed parameter systems is linear density that is the measure of a quantity of any characteristic value per unit of length. Linear mass density and linear heat load density (the amount of heat load per unit length) are two examples used in science and engineering, that freqently apprear in the cryogenics system analysis and modelling. The term linear density is most often used when describing the characteristics of one-dimensional objects, although linear density can also be used to describe the density of a three-dimensional quantity along one particular dimension. Just as density is most often used to mean mass density, the term linear density likewise often refers to linear mass density.

However, this is only one example of a linear density, as any quantity can be measured in terms of its value along one dimension.

4.5 Dynamic systems and Ordinary Differential Equations

The model simulation is the solving of the ODEs describing the model dynamics in order to obtain the trajectories of the process variables that are time integrals of their dynamics. In order to numerically solve, integrate, the ODE over the simulated time horizon, the continuous time is discretized into a finite number of discrete time intervals that are delimited by time points, called time steps. The states, outputs and the system dynamics are successively evaluated at the time points, from the simulation start time to the finish time. The interval between the time points is the size or length of the time steps. Decreasing the step size increases the temporal resolution and generally improves accuracy of the results while increasing the number of the simulation steps and thus the computational cost of simulation.

A number of numerical methods exists to solve ODEs, that can be divided into various categories. *Fixed-step* solvers use predefined, constant value of the length of the time intervals between time steps. This is in contrast to *variable-step* solvers that vary the length during the simulation trying to speed up simulation by keeping the step length at the maximal value that satisfies the accuracy requirements, at the cost of additional computing burden, comparing to fixed-step solvers that need no error control mechanism. The *order of solver* is an important parameter stating how fast the simulation error grows with respect to the increasing step size. In a n-order method, the local error (error per step) is proportional to the $n+1$ power of the step size, and the global error (error at a given time) is proportional to the n power of the step size. Thus higher order solvers tend to provide more precision with exception of very coarse time discretization. The numerical dynamics integration can be *implicit or explicit*. Explicit calculation of the dynamic evolution is straight-forward but it converges only at lengths of the time discretization intervals below a certain value defined by the fastest mode of the simulated dynamics. Implicit calculations of the dynamic evolution provide greater stability but involve solution of a set of algebraic equations at every time step using a Newton-like method and thus are much more complex and computationally expensive.

4.5.1 Stiff dynamics

Stiff dynamics is one described by an ODEs set including variables that evolve at very different time scales - some much faster than the others. The problem with the stiffness is that the simulation horizon length is defined by the slowest variables and the length of the maximal

time step of the dynamics integration is limited by the fastest, thus forcing the numerical solver to integrate with large number of steps - at high computational cost. Explicit solvers are not suitable for stiff systems because their maximal allowable time step is limited to assure convergence. This is not the case for implicit solvers, designed specifically for solving stiff problems. Thus the stiffness strongly increases the computational cost of solving an ODE, that is the system simulation, because it calls for computationally complex implicit solvers.

4.6 Constrained dynamic systems and Differential Algebraic Equations

Algebraic equations frequently appear in the description of the physical processes that are modelled. They originate at simplifications of description of the modeled processes, including neglecting of some very fast system dynamics, e.g. that related to pressure propagation, that are modelled as instantaneous change. The steady-state solution of the original fast ODE's replaces the original ODE's describing the fast dynamics and the corresponding model equations do not contain any derivatives and thus are purely algebraic and not differential. Often, they involve many model variables, resulting in complex "algebraic loops" in modelled dependencies propagations.

Presence of the algebraic equations in the system's model is equivalent to system dynamics being described by a set of differential algebraic equations (DAEs). DAEs contain equations that involve independent and dynamic variables but no derivatives of the dynamic variables that. DAEs are significantly more difficult to solve numerically than ODEs. Proper solution of a DAE consists of two parts, first the search for consistent initial values and second the computation of a trajectory of dynamics variables. Typically, iterative Newton's method method is used to continuously solve the algebraic equations along with the solution of the differential equations. This significantly slows down the model simulation and in some cases the Newton's method may not converge without a good initial guess for the algebraic states.

4.7 Tools

A number of software tools and programming languages may be used to develop models, simulate (solve) them and present results of the simulation. The software provides Integrated Development Environment (IDE), libraries of models of frequently used components and numerical solvers that greatly facilitate model development and simulation. Model and simulation implementation using bare programming languages may be much more complicated

than using software packages, but this approach may allow models better optimized for a given application as the modeler has much more freedom. Lets review some tools that may be used for thermo-hydraulic processes simulations.

MATLAB is a numerical computing environment and programming language. A proprietary programming language developed by MathWorks, MATLAB allows matrix manipulations, plotting of functions and data, implementation of algorithms, creation of user interfaces, and interfacing with programs written in other languages, including C, C++, Java, Fortran and Python. An additional package, Simulink, adds graphical multi-domain simulation and model-based design for dynamic and embedded systems. MATLAB does not provide tools for direct modelling and simulation of systems described by PDEs, however, it may simulate the ODEs obtained after manual spatial discretisation performed by the programmer.

Python is a widely used general-purpose, high-level programming language. Python supports multiple programming paradigms, including object-oriented, imperative and functional programming or procedural styles. It features a dynamic type system and automatic memory management and has a large and comprehensive standard library. The Python programming language was not initially designed for numerical computing, but attracted the attention of the scientific/engineering community early on and a number of extensions have been developed. NumPy is an extension to the Python programming language, adding support for large, multi-dimensional arrays and matrices, along with a large library of high-level mathematical functions to operate on these arrays. Using NumPy in Python gives functionality comparable to MATLAB since they are both interpreted, and they both allow the user to write fast programs as long as most operations work on arrays or matrices instead of scalars. In comparison, MATLAB boasts a large number of additional toolboxes, notably Simulink; whereas NumPy is intrinsically integrated with Python, a more modern, complete, and open source programming language. Moreover, complementary Python packages are available. SciPy contains modules for optimization, linear algebra, integration, interpolation, special functions, FFT, signal and image processing, ODE solvers and other tasks common in science and engineering. SciPy is a library that adds more MATLAB-like functionality and Matplotlib is a plotting package that provides MATLAB-like plotting functionality.

EcosimPro is a modeling and simulation tool for modeling 0D or 1D multidisciplinary continuous-discrete systems and any kind of system based on differential-algebraic equations (DAE) and discrete events. EcosimPro has been designed to carry out steady and transient studies, as an optimization and design tool that helps the engineer to improve any kind of system modeled with equations (0D and 1D). It also provides a highly intuitive graphics environment that facilitates its use in creating physical models based on schematic views.

COMSOL Multiphysics is a finite element analysis, solver and Simulation software for various physics and engineering applications involving distributed parameters systems, especially coupled phenomena, or multiphysics. A solution of a model involving the PDE using FEM typically involves relatively fine spatial demonetisation steps and thus the computing cost of solution is too high for real time simulation based optimization.

C is a general-purpose, imperative computer programming language, supporting structured programming, lexical variable scope and recursion, while a static type system prevents many unintended operations. By design, C provides constructs that map efficiently to typical machine instructions, and therefore it has found lasting use in performance optimized applications that had formerly been coded in assembly language.

4.8 Discussion

First principles modelling involves formulation of mathematical equations describing the modelled process behaviour and their numerical solution. The type of the equations to be solved is related to the properties of the modelled system and simulation approach chosen. A large number of tools for modelling and simulation is available, however none of them is dedicated to development of models characterised by reduced computing cost, sacrificing the simulation accuracy. However, a highly efficient programming language like C, may be used to implement model and simulation from scratch. A model that may be optimized for low computational cost of simulations as needed in the advanced control applications.

Chapter 5

Analysis of temperature dynamics of long strings of LHC magnets

This chapter provides detailed analysis of the processes shaping temperature dynamics of long strings of the LHC superconducting magnets cooled with superfluid.

5.1 Purpose, approach and validity

The purpose of the temperature dynamics analysis presented in this chapter is to identify the principal physical processes that govern the magnets temperature dynamics. Mathematical description of the processes provides a foundation for development of first principles models of the temperature dynamics. Moreover, understanding of the processes is the key development of an efficient advanced control strategy.

In case of complex first-principles models, the analysis allows to optimally choose the extent to which the different processed are represented in the model. This choice, representing trade-off between computing cost of the model simulation and the simulation accuracy, enables development of complex models characterized by computing cost sufficiently low to enable real-time optimization based advanced control applications like the MHE and NMPC. Here, "real-time" means that the optimization is performed at a rate that matches that of the real control system.

The approach to the analysis is iterative, because how strong the impact must be to be considered as "non-negligible" is decided based on the performance of numerical models and advanced controllers developed based on the analysis. Thus the analysis and modelling that follows are strongly linked. The iterative process starts with analysis of principal processes chosen based on analysis of the experimental process data. This initial analysis enables

development of the simplest models that are then simulated using input variables corresponding to the experimental data enabling direct comparison between the simulated and actual process dynamics. Any discrepancies between the two indicate modelling errors, i.e. missing or inadequately represented processes.

Performance of a model to be used in a model based advanced control application is one of the factors defining the performance of the application itself. Thus, insufficient model performance is a legitimate reason the preform another "analyse-model-simulate-validate" iteration, where deeper system analysis, followed by more detailed model development, simulation and assessment of the simulation results against the experimental process data. The choice of the experimental data that exhibits the effects of the analyzed processes on the modelled dynamics is thus crucial for successful analysis and modelling.

The validity of the analysis is largely imposed by the desired detail level of the model and validity range of the model based controller, the former being the reason for using 1-D distributed parameters description and the latter corresponding to full range of operational conditions with superfluid helium. Thus initially the analysis is constrained to the magnets temperature T_m range

$$T_{s,b,min} = 1.77 \text{ K} \leq T_m \leq T_\lambda = 2.16 \text{ K}, \tag{5.1}$$

where the value of minimal temperature of saturated helium in the heat exchanger $T_{s,b,min} = 1.77$ K corresponds to pressure of 1400 Pa, the lowest provided by the 1.8 K refrigerator, and defines the lowest possible temperature of the source of cooling power. The bath pressure range is defined by inequality (2.2). However, as the analysis the processes progresses, the validity range of the model and thus that of the controller are refined.

5.2 Temperature dynamics of the superfluid helium bath

The temperature dynamics of magnets submerged in a static bath of superfluid helium should be the same as temperature dynamics of the bath. There reasons for this assumption are that 1) superfluid helium has zero viscosity for capillary flow and thus permeates deep into the magnets structure providing very good thermal contact between the bath and magnet components and 2) 98.3 % of total thermal energy of the cold mass kept at 1.9 K is accumulated in the helium bath because specific heat of other materials vanishes at this extremely low operating temperature, as calculated by Maglioni and Parma (2010).

This may be counter-intuitive taking into account that mass of the helium bath stretching over a 214 m long sub-sector is estimated to be approx. 875 kg (Section 5.2.3) while the cold mass of other magnet components sums up to approx. 300'000 kg (Maglioni and Parma (2008)). The cold mass includes NbTi superconducting coils and busbars, non-magnetic stainless steel

force-retaining collar, iron yoke, stainless steel cryogenic piping and copper heat exchanger tube, all surrounded by a 570 mm diameter stainless steel shrinking cylinder being also the He II vessel, presented in Figures 2.4, 2.1 and 2.5. As calculated by Maglioni and Parma (2008), it is the steel that stores the remaining 1.7 % in the cold mass thermal energy.

5.2.1 Energy conservation

The helium bath temperature dynamics is derived from the energy conservation in the bath, describing the balance of heat transfers and work done at the bath. The heat transfers may be divided with respect to their direction into 1) heat loads flowing into the bath cooling power and 2) those flowing in the opposite direction representing the cooling power provided to the bath, their sums represented as q_l and q_c, respectively.

Dynamics of average bath temperature

If the temperature gradients along the bath are negligible, the distributed magnets temperature dynamics is identical to the dynamics of average bath temperature $\tilde{T}_h(t)$ that at time t is expressed using single ODE

$$\mathrm{d}\tilde{T}_h(t)/\mathrm{d}t = \sum q/\left(c_{v,h}\, M_h\right), \tag{5.2}$$

with specific heat of helium at constant volume $c_{v,h}$, the mass of helium bath M_h and the sum of all heat transfers into and from the bath

$$\sum q = q_l - q_c. \tag{5.3}$$

Dynamics of distributed bath temperature

In order to describe the temperature gradients along the bath that seem to have important impact on the magnets temperature dynamics, as observed during the identification tests, the dynamics of distributed bath temperature is formulated as a 1-D PDE. The 1-D formulation is desired for low complexity and is justified by the large ratio between the length and the diameter of the bath equal to approx. 400.

The helium bath is static and any convection, both in the inclined helium vessel and in the loop created by the vessel connected each 54 m through a capillary to the line N running along the helium vessel, should be negligible due to extremely small temperature gradients in He II. The temperature dynamics of the part of the helium inside the line N has been measured to be different than that inside the helium vessel. However, at minimum cross-section of the line

N free for helium equal to 82 mm^2 (Kowalczyk et al. (2000)), thus the corresponding helium mass in the line N is approx. 2.5 kg, being 0.3 % of helium bath and thus the heat transfers between the vessel and line N due to this additional dynamics are negligible.

Thus, assuming that helium doesn't move in the bath the temperature dynamics over the helium bath length L_h may be formulated taking into account divergence of longitudinal heat transfer rate in He II $\nabla \cdot q_s(x,t)$,

$$\partial T_h(x,t)/\partial t = \left(\partial q_l/\partial x - \partial q_c/\partial x - \nabla \cdot q_s\right) / \left(c_{v,h}\, \mathrm{d}M_h/\mathrm{d}x\right),\ 0 < x < L_h \tag{5.4}$$

with linear densities of the sum of heat loads into the bath $\partial q_l/\partial x(x,t)$, of the total cooling power provided by the heat exchanger $\partial q_c/\partial x(x,t)$ an that of the helium mass $\mathrm{d}M_h/\mathrm{d}x(x)$. At the helium bath extremities, tight plugs cut off the heat transfer in He II, and the effects of a remaining heat transfer due to thermal conduction through the plug is negligible at small temperature differences occurring at He II temperatures. Thus, the boundary conditions at the bath extremities are of Von Neumann type:

$$0 = q_{pl} = C_{pl}\ \partial T_h(x,t)/\partial x,\ x = \{0, L_h\} \tag{5.5}$$

with the values of plug thermal conductance $C_{pl} = 0$ and thus the heat transfer rate through the plug $q_{pl} = 0$.

5.2.2 Specific heat of superfluid helium

The specific heat of superfluid helium at constant volume $c_{v,he}(T,p)$ that is a non-linear function of pressure p and temperature T in the initial validity range (Eq. 5.1). However, the pressure dependence gets pronounced only as helium temperature approaches the T_λ. Thus, further limiting the description validity validity to $T_h \leq 2.11$ K allows to express inverse of the specific heat using a simplified approximation neglecting the pressure dependence

$$1/c_{v,he} = 7.9936\ 10^{-3}\ T_h^{-5.7874} + 0.1230\ 10^{-3}\ (2.15 - T_h)^{0.5234}\ \text{kg K/J}. \tag{5.6}$$

that matches within 10% error the values from HEPAK in the refined validity range

$$1.77\ \text{K} < T_h(x,t) < 2.11\ \text{K}\ \&\ (2.2). \tag{5.7}$$

At pressure $p = 130$ kPa, the fit closely matches the values from HEPAK, that slightly differ from another fit presented by Van Sciver (2011): $1/c_{v,he} = 8.5\ 10^{-3}\ T_h^{-5.6}$ kg K/J, see Fig. 5.1.

5.2.3 Mass

The volumes of helium in the helium vessels of cryo-dipole and SSS have been measured before the cryostats have been installed at the LHC and average values are equal to $V_{MB,\text{measured}} = 0.348 \pm 0.019$ m^3 and $V_{\text{SSS,measured}} = 0.2166 \pm 0.0046$ m^3 respectively, as reported by Maglioni and Parma (2007). Thus the mass of helium present in 4 SSSs and 12 cryo-dipoles present in a 214 m long sub-sector

$$M_{h,MB+SSS,measured} = (4\, V_{\text{SSS,measured}} + 12\, V_{\text{MB,measured}})\, \rho_{h,h} = 746 \pm 37 \text{ kg} \tag{5.8}$$

with helium density in the bath at 1.9 K and 130 kPa

$$\rho_{h,h} = 147.84 \text{ kg/m}^3. \tag{5.9}$$

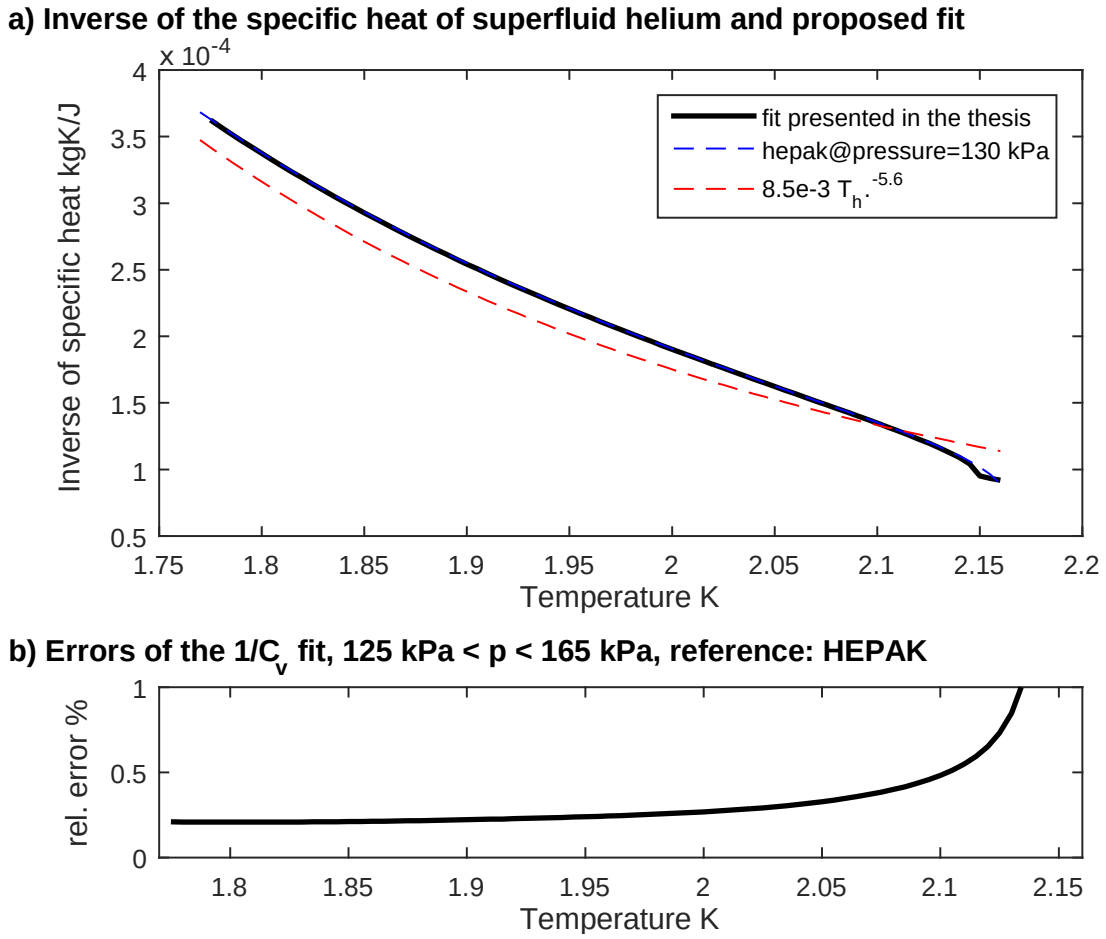

Fig. 5.1 Inverse of He II specific heat and its approximation. Please note that the lines corresponding to values form HEPAK cannot be differentiated from the approximation.

Similar values of helium volumes have also been calculated by Maglioni and Parma (2008) using geometry of the helium vessels to get their empty volume and then subtracting from this value the volumes of the magnets components it encloses (calculated using their mass and density of materials) has been subtracted, giving $V_{MB,calculated} = 0.3715 \pm 0.0084$ m3 and $V_{SSS,calculated} = 0.162 \pm 0.0018$ m^3. Thus the calculated mass of helium present in the vessels along a 214 m long sub-sector

$$M_{h,\mathrm{MB+SSS,calculated}} = (4\, V_{\mathrm{SSS,calculated}} + 12\, V_{\mathrm{MB,calculated}})\, \rho_{h,h} = 755 \pm 16 \text{ kg}. \tag{5.10}$$

The helium bath is fills not only the vessels, but also the line N and interconnections between the vessels. The mass of helium in the line N is negligible as discussed in Section 5.2.1. Total length of the interconnections over a sub-sector sums up to approx. 214 m - 4 5.355 m - 12 14.782 m = 15 m, and the interconnection free cross-section is equal to approx $9.9 \times 10\ -3$ m^2 (Nikitina et al. (2003)) thus the mass of helium present in this volume $M_{h,ic} \approx 22$ kg.

Another way to estimate the mass is to analyze its influence on the bath temperature dynamics. Experiments have been performed at the LHC cryogenic circuit by Maglioni and Parma (2010), where the coolant flow has been turned off and the bath temperature has started to rise due to static heat loads and after some time additional heat load has been introduced into the bath at a constant rate accelerating the warm up. Analysis of the time derivatives allowed to estimate the helium bath in a sub-sector to be

$$M_{h,\mathrm{experimental}} = 848 \pm 98 \text{ kg}. \tag{5.11}$$

It is impossible to identify small heat transfers in superfluid helium based on temperature measurements only due to very high heat conductivity of superfluid helium. Thus it is impossible to experimentally identify helium mass separately for each of the cryostat section after they have been installed at the LHC and share the helium bath.

Estimation of mass of the bath

In order to increase the precision of the helium mass estimation, at each standard cell under test I perform multiple experiments similar to that performed by Maglioni and Parma (2010), however I analyse the experiments using multiple linear regression - based on significantly higher number of data samples than used in their tests, see Figure 5.2. In the identification experiments electric heaters installed at the magnets have been used to induce magnets temperature variations at varying rate, while the control valves at the sub-sector under test were closed - no cooling was

was provided to the magnets, no helium was present in corresponding phase separators and magnet were not powered.

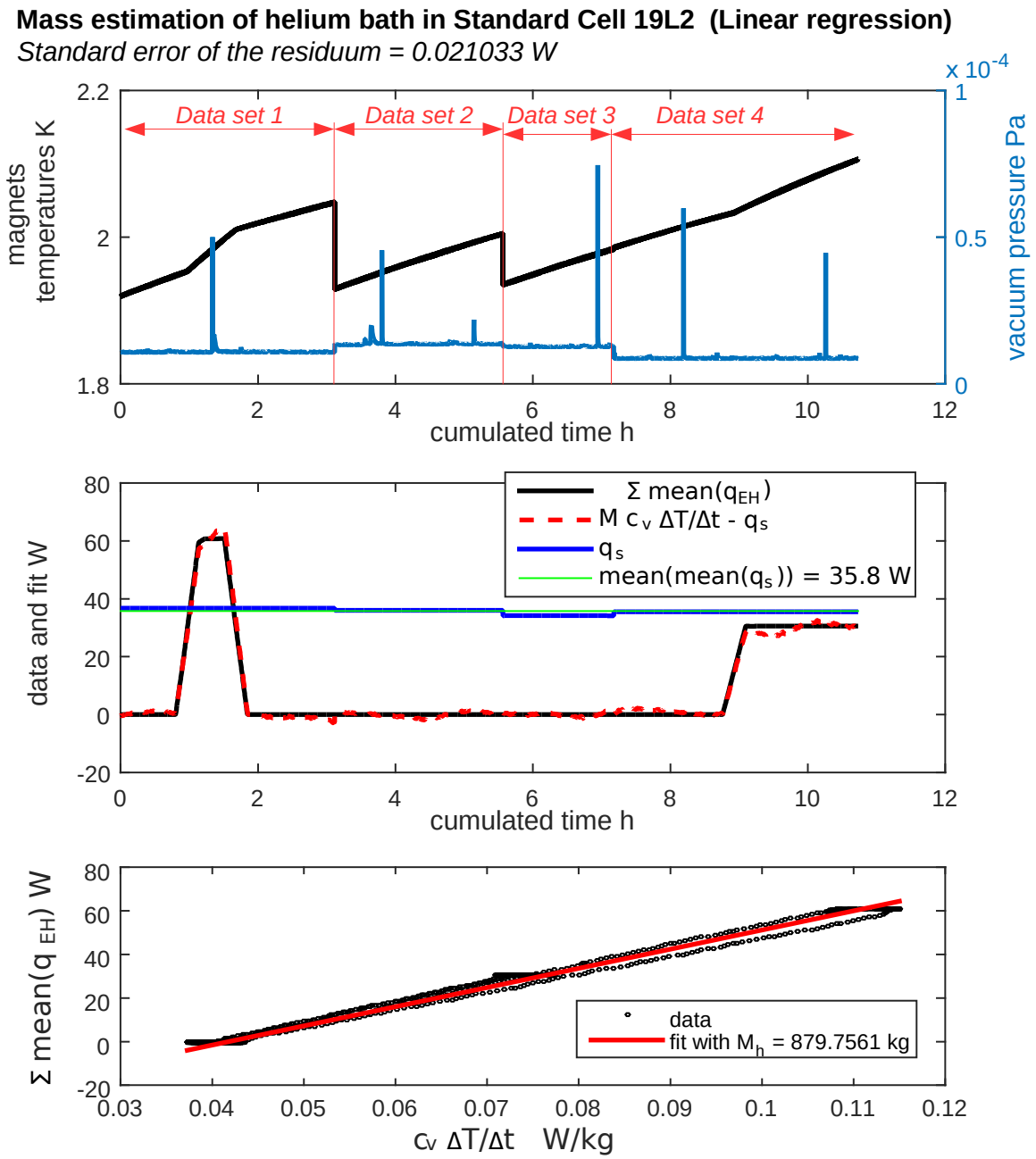

Fig. 5.2 Estimation of mass of helium bath.

The basis for the linear regression is the energy conservation equation with average helium temperature dynamics

$$c_{v,h}\ \left(\tilde{T}_h(t+\Delta t)-\tilde{T}_h(t+\Delta t)\right)/\Delta t\ M_h-\int_t^{t+\Delta t} q_{h,ls}\mathrm{d}t=\int_t^{t+\Delta t} q_{h,eh}\mathrm{d}t \qquad (5.12)$$

with the unknown parameters M_h and q_s and the time interval $\Delta t = 1200$ s. Data from multiple experiments are used in the regression, thus multiple values of q_s are optimized, one for each experiment. The results are presented in Table 5.1.

Due to the large amount of data used standard error of the residuum of the regression is negligible. Thus, the errors of the estimate parameters are bounded by systematic errors of the variables: specific heat $e_{c_{v,h}} = 3$ % (Arp and McCarty (1989)), temperature difference due to the dead-band filtering of logging data $e_{\Delta T_h} = 2\ 10^{-3}$ K. In the difference error, absolute temperature offsets compensate and I observed that non-linearities of sensor characteristics that do not cancel are negligibly small. Error of electric heaters power varies depending on the power output from 3% above 6 W per heater to 1.5% at the maximum output of 25 W. To simplify the errors analysis, I used the value of 4% of average heaters power during all the test at a cell. Actually, weighted regression should be performed as since the variance of $M_h\ C_v\ \Delta T/\Delta t$ is proportional to $\Delta T/\Delta t$ and C_v, however no weights are used to keep the multiple regression simpler. Moreover, since the tests have been performed during operation of the complex cryogenic circuit, the 95 % confidence intervals presented here should be regarded as the most optimistic, since it is very probable that some systematic errors have been missed in the analysis of the system where complex interactions between process variables exist. This is clearly visible in case of the static heat load that varies in function of residual pressure of insulation vacuum.

The estimated value of helium mass also contains a contribution corresponding to the heat capacity of stainless steel submerged in the bath, that has been neglected in the analysis. Thus the estimates are perfectly suited for models that also use the same assumption, however the actual physical amount of helium is overestimated by approx 1.7 %.

Sub-sector number	Estimated bath mass kg	Estimated static heat load W
19L2	870 ± 7.6	36.7, 36.0, 34.2, 35.5 ± 0.41
23L4	875.6 ± 8.1	31.9 ± 0.49
27L6	872.2 ± 4.7	36.7, 38.0, 35.6, 37.0, 33.6 ± 0.25
27L7	879.2 ± 5.5	32.3, 36.0, 33.4, 34.8 ± 0.29
23L8	875.1 ± 4.3	35.5, 35.6 ± 0.27

Table 5.1 Estimated helium bath mass and static heat load over a 214 m long sub-sector.

5.2.4 Counterflow heat transfer in superfluid helium

The heat transfer in superfluid helium is unique, extremely effective and strongly influenced by temperature, by its gradient and by channel geometry. This complex process, described in detail by Van Sciver (2011), is explained by the theory of two-fluid model that considers superfluid He II being a mixture of two interpenetrating components: normal and superfluid. The relative amount of the superfluid in the mixture increases from 0 to 100 % as the temperature decreases from T_λ, corresponding to the liquid-superfluid helium phase transition, to 0 K. The superfluid component has no viscosity and zero entropy, contrary to the normal component that is characterized by nonzero viscosity and nonzero entropy. Due to this fact, thermomechanical effect occurs where temperature difference ΔT in superfluid helium corresponds to pressure difference

$$\Delta p_s = \rho \; s \; \Delta T \tag{5.13}$$

with density ρ and entropy s. The pressure difference forces the non-zero entropy normal component to flow in the direction of decreasing temperature, thus carrying heat in this direction and forcing the superfluid component to flow in the opposite direction to replace it. This the counter-flow heat transfer mechanism is extremely effective and limited only by the friction between the two fluid components and the flow boundaries. However, the effective heat conductivity it highly heat flux and temperature dependent and it vanishes at the Lambda point.

Three regimes of the counterflow are distinguished: 1) laminar, 2) with normal component turbulence and 3) with superfluid component turbulence. At low heat fluxes the relative flows velocities are small and flows of both components are laminar and only small friction shear stress at the boundaries limits the counter-flow and thus the apparent superfluid thermal conductivity is large and geometry dependent. At higher heat fluxes, which occur in practical applications, turbulence appears in the superfluid and in the normal component that increased the friction between the components an at the boundaries. Mutual friction between the two components due superfluid turbulence limits the counter-flow heat exchange at higher heat fluxes, resulting in apparent superfluid heat conductivity that is geometry-independent and is a highly nonlinear in function of temperature and its gradient, see Fig. 5.4.

The onset of superfluid turbulence is related to the critical superfluid component velocity $v_{c,s}$ that depends on the channel diameter D. Among three relations presented by Van Sciver (2011), we have an approximate experimental correlation

$$v_{c,s} \approx 3.16 \times 10^{-3} \; D^{-1/4} \tag{5.14}$$

and the the theoretical formula by Feynmann

$$v_{c,s} = h/(\pi\, m_{he\,4}\, D)\ \ (log(4\, D/a_0) - 7/4)\,, \tag{5.15}$$

with the Planck constant $h = 6.626\ 10^{-34}$, mass of helium 4 molecule $m_{he\,4} = 4\ 1.66\ 10^{-27}$ kg and size of a vortex core $a0 \approx 10^{-9}$ m. The relation between the heat flux $\mathrm{d}q/\mathrm{d}A$ and the velocity of the superfluid component v_s

$$\mathrm{d}q/\mathrm{d}A = v_s\ s\ T\ \rho_s\ \rho/\rho_n, \tag{5.16}$$

with superfluid component, normal component and total densities ρ_s, ρ_n and ρ, respectively.

The helium bath at the LHC comprises a number of longitudinal channels in the cryostats and at the interconnections, having hydraulic diameters in the range 0.4 mm $< D_h <$ 49.3 mm. The maximal value corresponds to the interconnections between cryostats, calculated based

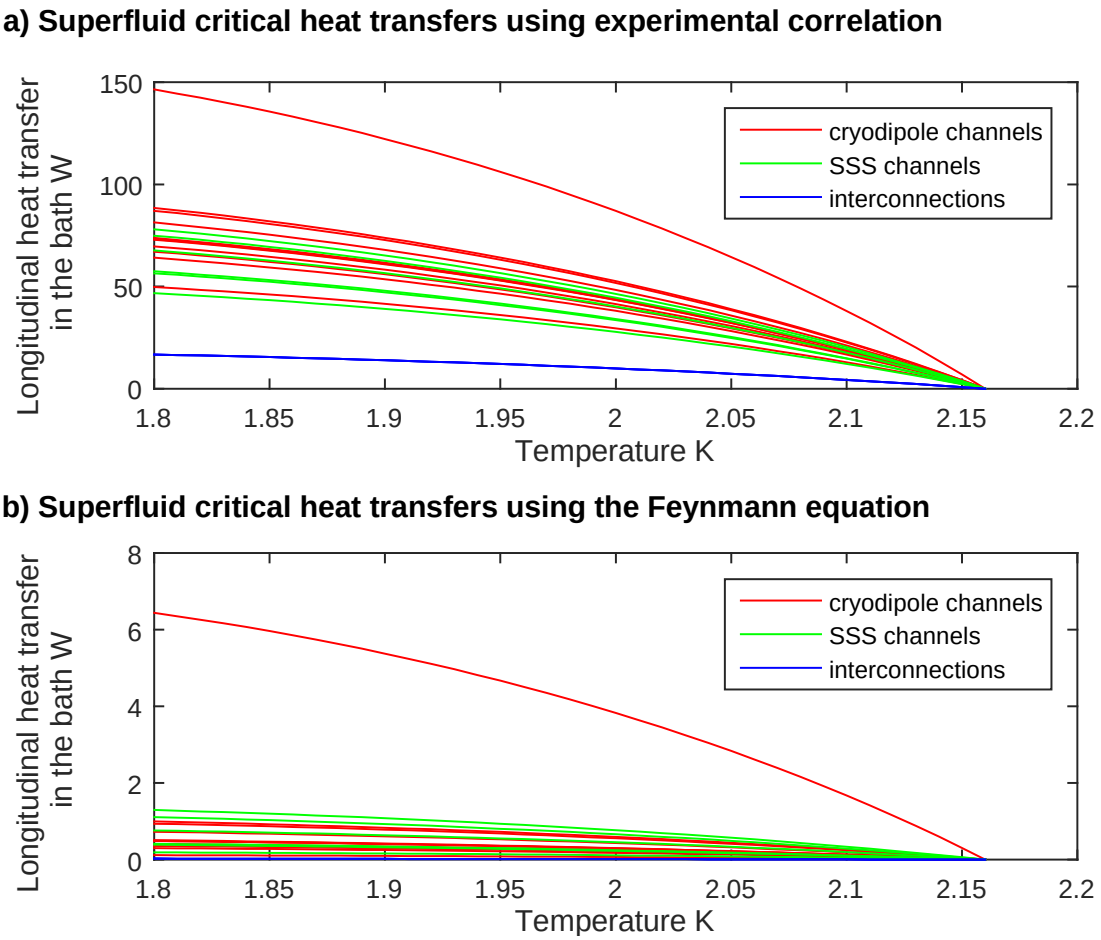

Fig. 5.3 Superfluid critical heat transfer at the LHC.

on the LHC technical drawing by Nikitina et al. (2003). Liu et al. (2003) have calculated the values inside the cryostats. Values of longitudinal heat transfer in the bath that correspond to the critical superfluid velocity in different channels are presented in Fig. 5.3. The relatively high values calculated using the experimental correlation, see the upper plot, indicate that the heat transfer in the bath should stay in the regime without superfluid turbulence, contrary to what is indicated by the values obtained using the Feynmann equation, presented in the lower plot. The scale of helium bath temperature gradients observed at the LHC clearly indicate that the superconducting turbulence is always present at heat transfers corresponding to measurable gradients, thus the theoretical formula seems to be more adequate. The analysis of the Reynolds number of the normal component flow indicates that this component is also turbulent, however friction due to this turbulence is much weaker that that related to the superfluid turbulence and thus its influence may be neglected.

Thus, the heat transfer in bath is limited by the mutual friction between normal and superfluid components due to the superfluid turbulence. An experimental correlation exists for 1-D channels where the heat flux

$$(\mathrm{d}q/\mathrm{d}A)_{h,s} = -F^{1/m}\ \mathrm{sgn}(\mathrm{d}T_h/\mathrm{d}x)\ |\mathrm{d}T_h/\mathrm{d}x|^{1/m} \tag{5.17}$$

expressed using the sign function sgn(), with pseudo conduction term $F(T,p)$ called superfluid Thermal Conductivity Function (Srinivasan and Hofmann (1985), Van Sciver (2011), Sato et al. (2005)). In the past, theoretical value of the power $m = 3$ that approximatively matches experimental results was widely used, including HEPAK. More recently, Sato et al. (2005) have measured He II properties in wide range of pressures and found better value

$$m = 3.4. \tag{5.18}$$

They have also prosed a fit to approximate the $F(T,p)$ with errors of smaller than 2 % for experimental data in the heat flux range from 10^4 W/m^2 to 2×10^4 W/m^2. This heat flux values are higher than what those corresponding to the LHC operation, see Fig. 5.4c. Based on this fit and neglecting the pressure dependence, at $p = 130$ kPa

$$F^{1/3.4}(T) = 2.2666\ 10^4 \left(1 + (t-0.882)^2 \sum_{n=0}^{9} \{a_n\ (t-1)^n\}\right)^{1/3.4},\ t = T/T_\lambda, \tag{5.19}$$

with $a_0 = -71.818$, $a_1 = 1.2172617\times10^3$, $a_2 = -1.4992321\times10^4$, $a_3 = -3.9491398\times10^5$, $a_4 = -2.9716249\times10^6$, $a_5 = -1.2716045\times10^7$, $a_6 = -3.8519949\times10^7$, $a_7 = -8.6644230\times10^7$,

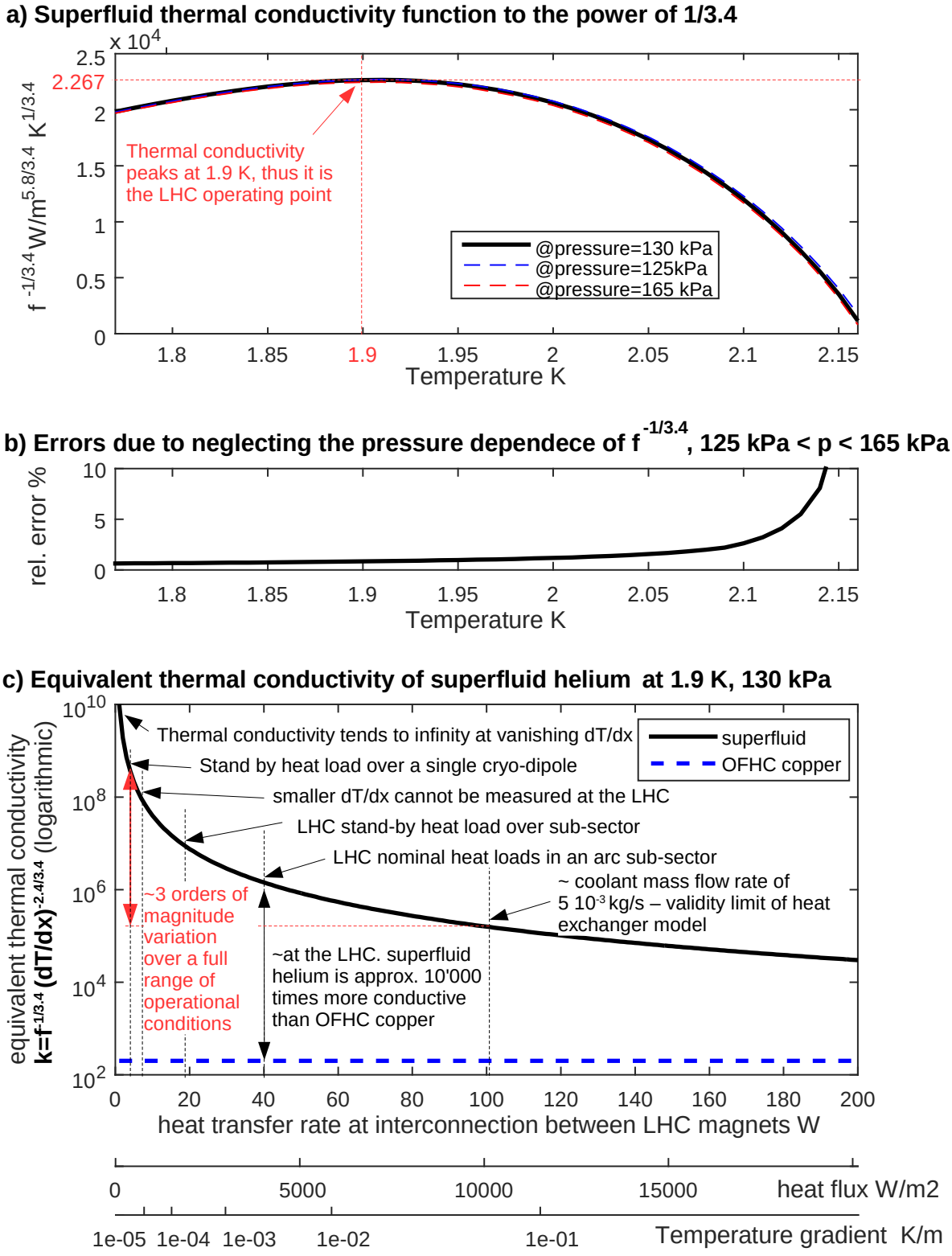

Fig. 5.4 Superfluid heat conductivity at the LHC.

$a_8 = -1.2501488 \times 10^8$, $a_9 = -8.1273591 \times 10^7$. This fit is presented in the Fig. 5.4a. Fig. 5.3b shows the errors introduced by neglecting the pressure dependence, in the pressure range corresponding to the LHC operational conditions, that are significant only as temperature approach the T_λ.

Using the distributed parameter model presented in this thesis, I have optimized the value of the parameter m, confirming that $m = 3.4$ produces the best agreement between the experimental results of the LHC identification and model simulation results. The value strongly influences the calculated heat transfers at very small heat fluxes, that occur during the LHC operation. Using the previously recommended value of $m = 3$ during investigation of the temperature drop over interconnections at the LHC prototype, Blanco, E (2003) found a correlation between the estimated cross-section area and the temperature gradient, suggesting that $x \neq 3$.

The apparent heat conductivity of superfluid helium

$$k_s = \mathrm{F}^{1/m} \, |\mathrm{d}T_h/\mathrm{d}x|^{1/m-1} \tag{5.20}$$

is found by rearranging the Eq. 5.17 into the familiar form

$$(\mathrm{d}q/\mathrm{d}A)_{h,s} = -k_s \, \mathrm{d}T_h/\mathrm{d}x. \tag{5.21}$$

Fig. 5.3c makes clear that the apparent thermal conductivity of superfluid helium in the regime with superfluid turbulence is extraordinary: from 3 to 6 orders of magnitude higher than that of OFHC copper. It strongly depends on the temperature gradient and varies by three orders of magnitude over the heat fluxes range corresponding to LHC operation. Fig. 5.3a demonstrates why the temperature 1.9 K at which the thermal conductivity is superfluid peaks has been chosen as the operational temperature for the superconducting magnets.

It is interesting to note that heat propagates in form of thermal waves in superfluid helium as a result of fluctuations in the local entropy. The speed of this propagation, called second sound because it is similar to sound propagation due to density fluctuations, is around 20 m/s between 1 and 2 K (Van Sciver (2011)), thus relatively high even taking into account the length of the LHC helium bath.

Finally, the longitudinal heat transfer in the bath $q_{h,h}$ is related to the heat flux through the effective bath cross-section for heat transfer A_h,

$$q_{h,s} = A_h \, (\mathrm{d}q/\mathrm{d}A)_{h,s}. \tag{5.22}$$

5.2.5 Effective bath cross-section for heat transfer

The effective bath cross-section for heat transfer varies along the bath length. At uniform sections of the bath it has been calculated based on size of helium channels in cryo-dipoles and SSSs by Liu et al. (2003) and at the interconnections by Nikitina et al. (2003). Average total cross-section of the helium bath may be estimated based on the helium mass distribution, total sub-sector mass estimated in this thesis in Section 5.2.3 and cryo-dipole and SSS volume measured by Maglioni and Parma (2007). The total value is the largest bound for the cross-section contributing into the longitudinal heat transfer as it comprises empty spaces that do not extend in the longitudinal direction and thus do not contribute into the heat transfer. The effective cross-sections, averaged over sections corresponding to the distributed model spatial discretization grid, are model parameters that have been optimized. The effective value in a cryo-dipole correspond to roughly 50 % of values calculated based dipole magnet geometry or measured volume, asking for some further investigation. All these values, corresponding to slightly different concepts, are presented in Table 5.2.

5.2.6 Heat loads

Heat loads into the helium bath have strong direct effect on the magnets temperature dynamics, due to the strong heat flux dependence of the apparent heat conductivity of superfluid helium. The heat loads have different sources but may be divided into two groups: static heat loads originating at ambient temperature and dynamic loads related to magnets powering and presence of particles beam, as described in this section and illustrated in Fig. 5.5 and Table 5.3.

Static heat loads

Static heat loads into are present while the magnets temperature is lower than ambient temperature, causing heat to leak into colder helium bath due to radiation and conduction. Refrigeration efficiency strongly decreases with decreasing temperature of point at which the cooling power is provided. Thus special care must be taken to reduce the heat loads at the lowest temperature

Type (Source)	Cross-section m^2			
	SSS	Cryo-dipole	interconnections	average
Effective (channels size)	0.0190	0.0249	0.0099	
Total (helium mass)				0.0277
Total (helium volume)	0.0405	0.0230		
Effective (model)		0.013	0.0145*, 0.0139**	

Table 5.2 Estimated helium bath cross-sections. *) MB-SSS, **) MB-MB and SSS-MB

a) crossection of the LHC cryostat (cryo-dipole)

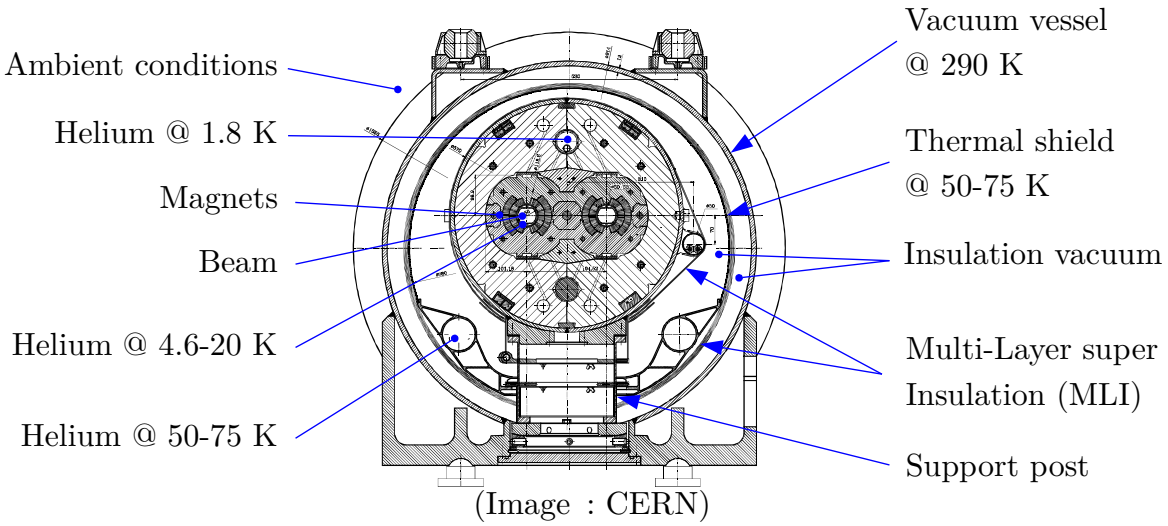

b) principal heat loads in 106.9 m long Standard Cell of the cryostat

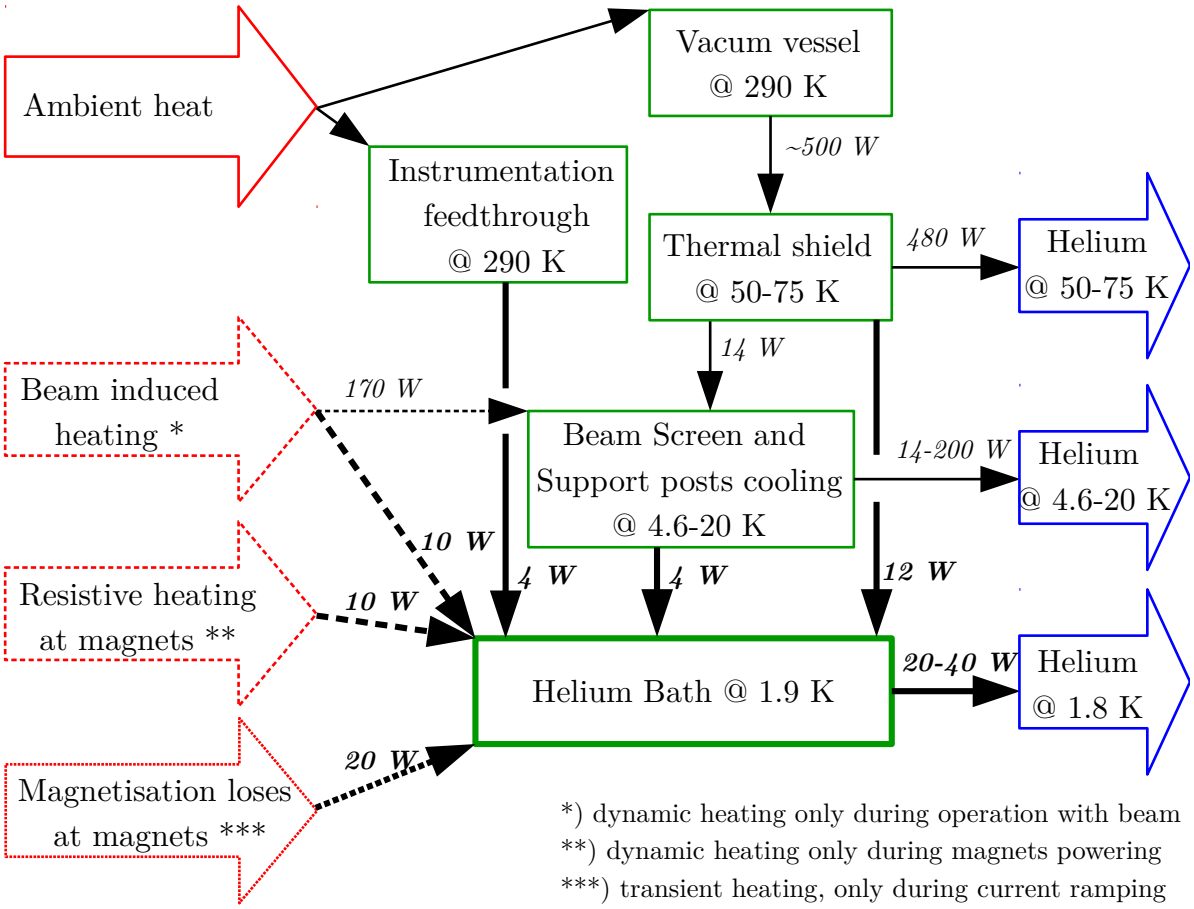

Fig. 5.5 Heat loads in a Standard Cell. Most values from Heat Load Working Group (2001).

Source of heat load	Heat load over a 214 m long sub-sector W			
	Static	Transient	Dynamic (Magnets)	Dynamic (Beam)
Static heat in-leaks:				
Radiative insulation	22.6			
Instrumentation Feedthrough	8.5			
Beam Screen	3.2			
Support posts	2.1			
Beam position monitor	1.21			
Dipole corrector feedthrough	1.1			
Beam vacuum feedthrough	0.84			
Longitudinal Vacuum Barrier	0.42			
Service Module	0.21			
Resistive heating:				
Eddy curents		80		
Busbars at interconnections			8.1	
Busbars within dipoles			8.0	
Busbars within SSS			3.4	
Auxilaries			1.2	
Beam induced:				
Synchrotron radiation				0.14
Mirror currents				0.22
Photoelectron deposition				1.9
Beam Gas Scattering				10.32
Random local losses				6.8
Sum design	40.2	80	20.7	19.38
Sum actual	**32-37**	**40**	**26** (Magnets+Beam)	

Table 5.3 Design and measured values of heat loads into helium bath over a 213.8 m long Sub-sector. Data source: Heat Load Working Group (2001), Ferlin et al. (2010), Tavian (2012) and Brüning et al. (2004).

levels. In order to reduce the static heat loads into the bath at 1.9 K, the magnets are placed inside the continuous arc cryostat that provides thermal insulation and interception of heat at higher temperature levels. Thus, it is the thermal performance of LHC cryostats, described by Lebrun and Tavian (2002), Bourcey et al. (2002) and Brunet et al. (1997), that defines the static heat load levels. Following discussion is based on a detailed analysis of thermal performance of the prototype LHC cryostat performed by Riddone (1997).

In the cryostat, the helium vessel is surrounded by a thermal shield cooled to 50-70 K that is exposed to the heat loads originating at 290 K corresponding to ambient temperature. The heat loads sum up to approx. 500 W per sub-sector and cooling with forced flow of supercritical helium at 50-70 K is provided to stabilize the shield temperature, and thus intercepting the heat

at 50-70 K. Similarly, the beam pipes confining the particles beam, are equipped with beam screen cooled with forced flow of supercritical helium at 5-20 K. Before entering the beam screens, the stream of helium at 4.5 K is used to cool the Glass Fiber Reinforced Epoxy posts supporting the helium vessels. 44 support posts are present over a 214 m long sub-sector, 2 per SSS and 3 per cryo-dipole.

The flows of helium intercepting heat is presented in Fig. 2.8. Thermalisation of various components is widely used to reduce the heat loads into the lowest temperature levels. The thermalisation is realized by thermally connecting these components to the actively cooled parts just mentioned.

Thanks to the heat interception, the exposition of the helium bath to the ambient temperatures of 290 K is greatly reduced, limited only to instrumentation feed-through. Thus the helium vessel is mainly exposed to the components that are much colder than the ambient temperature surrounding and thus are sources of much smaller heat loads into the bath, see Fig. 5.5. However, the temperature of these actively cooled components may vary over time and has strong impact on the value of the static heat loads into the bath, see Fig. 5.6b and c.

Insulation vacuum, confined by vacuum vessel surrounding the helium vessel and the thermal shield, largely reduces heat conduction into the bath. Moreover, the vessel is wrapped in 10 layers of Multi-Layer super Insulation (MLI) that allows to significantly reduce the heat transfer due to radiation originating at the warmer thermal shield. MLI is made of layers of 6 10^{-6} m thick polyethylene reflective films coated on each side with 400 øA of aluminium and interleaved with polyester spacer nets (Bourcey et al. (2002)). Heat transfer through the MLI insulation strongly depends on the vacuum pressure, decreasing as the residual pressure decreases. As presented in Fig. 5.6a, the heat load into the bath increases slowly with rising pressure at pressures below 10^{-2} Pa. Above this value the heat load dependence on the pressure is dramatic (Riddone (1997), Ekin (2006), Lebrun and Tavian (2002), Lebrun et al. (1992)). During nominal LHC operation, the residual pressure of insulating vacuum $p_{vac} \approx 10^{-4}$ Pa. Since He II leaks from the helium vessel into the surrounding it vacuum vessel, vacuum pump work continuously to maintain the insulation vacuum. Any perturbation to the pump action results in rising vacuum pressure and leads to significantly increased heat loads into the bath. The vacuum is sectorized using vacuum barriers installed at one SSS at extremity of each sub-sector.

The total static heat load in nominal operating conditions has been designed to be 40.4 W (Heat Load Working Group (2001)). The heat load has over a sub-sector have been measured at the LHC multiple times, independently of other variables by Maglioni and Parma (2008) and during estimation of the static heat loads, by Maglioni and Parma (2010) and myself, see

a) Insulating vacuum quality vs. heat load into the bath measured at the Cryostat Thermal Model, scaled to correspond to a 214 m long subsector

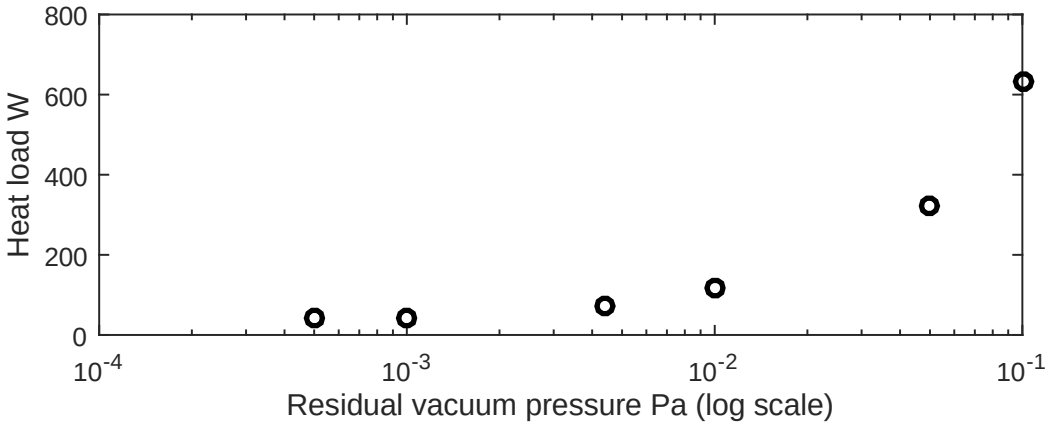

b) Thermal shield temperature vs. radiative heat load into the bath measured at the Cryostat Thermal Model, scaled to correspond to a 214 m long subsectorr

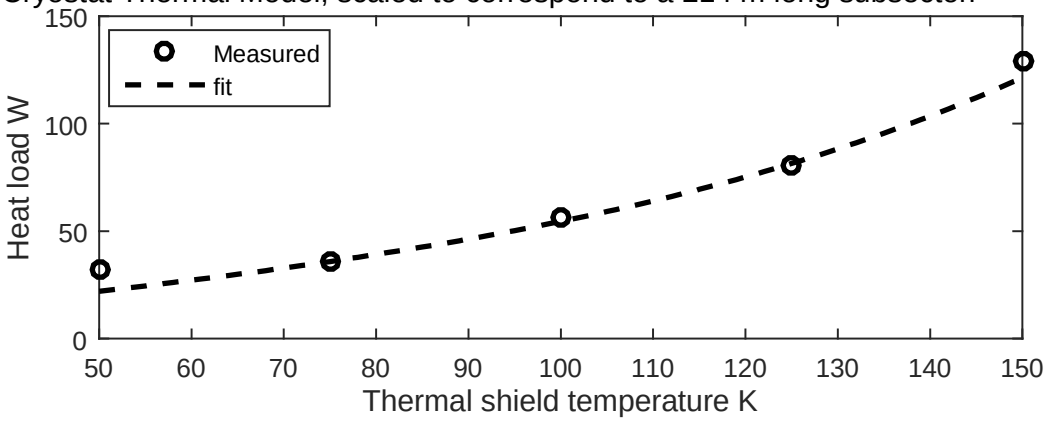

c) Heat intercept temperature vs. heat load through the support posts into the bath calculated for prototype dipole magnet cryostats, scaled to correspond to a 214 m long subsector

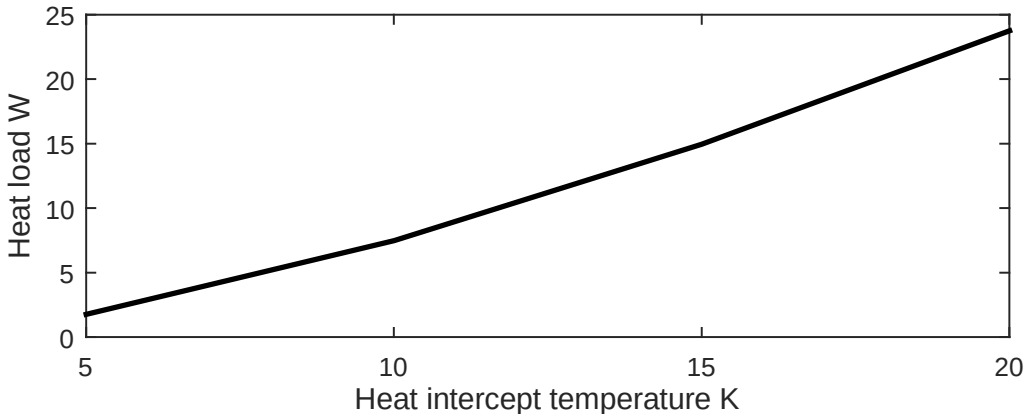

Fig. 5.6 Variation of static heat loads into the bath. Source of data: Riddone (1997)

Section 5.2.3. The values found for different sub-sectors fit into the range

$$32 \text{ W} \leq q_{h,ls} \leq 37 \text{ W}. \tag{5.23}$$

Due to strong dependence on vacuum quality and heat interception temperatures, the static heat load may significantly vary between sub-sectors and over time. The static heat load has been also evaluated for a whole LHC sector by Ferlin et al. (2010).

Most, sources of heat loads are equally distributed over length of a sub-sector, representing a repetitive structure of interconnected cryostats, except of the heat loads at the service module including the vacuum barrier and feed-troughs for pumping, current leads and instrumentation and jumper interconnection to the cryogenic distribution line, located at one sub-sector extremity.

Transient dynamic heat loads

Transient dynamic heat loads into the bath are present over limited periods of time during ramping up and down the magnets currents and during helium bath refilling. During current ramping of the main LHC magnets, heat is generated inside the magnet structure due to hystresis in the filaments, inter-filament coupling, inter-strand coupling and eddy currents developed in the superconducting cables and in the mechanical structure of the magnets. According to Brüning et al. (2004), raising the current to its nominal value of 13 kA in time period of 1200 s is expected to dissipate energy density of 480 J/m at main dipole, corresponding to heat load of approximately 80 W per sub-sector. The shape of the current ramp has been optimized with respect to the magnets field quality, see Burla et al. (1999).

During the LHC Run 1, shorter current ramp has been used because the LHC has been commissioned and used at lower than nominal value of the maximal magnets current. The transient hysteresis losses are proportional with the current intensity and the coupling losses are proportional to its rate of change over time (Flemseater (2000)). Thus we expect the observed heat loads to correspond well to initial part of the nominal ramping process. I have estimated the total transient heat loads over a sub-sector based on measured average bath temperature dynamics and using the bath energy equation,

$$q_{h,ldt} \approx 4.1 \, |dI/dt|. \tag{5.24}$$

with I being the average value of three currents flowing through 3 types of main superconducting LHC magnets, see Fig. 5.7.

It is interesting to note that in the case of a superconductor resistive transition or in an emergency, it is possible to ramp the full LHC current of 13 kA down to zero in 80 s, resulting

in an energy dissipation at rate of approximately 38 W/metre, that is 8.1 kW per sub-sector! In fact the mass of helium bath has been design to provide enough heat capacity to buffer those loads while keeping the bath temperature increase sufficiently low.

Bath is refilled with helium at 4.5 K and 350 kPa as a part of bath pressure control. This warmer helium entering the bath also represents transient heat loads into the bath. However the heat loads last very short periods of time and the refilling does not occur frequently during normal magnet operation.

Steady dynamic heat loads

Steady dynamic heat lads are generated in the bath during magnets powering and operation with beam and are present as long as the current flows in the magnets or particles are guided in the LHC. Tavian (2012) estimates that the loads are expected to sum up to 26 W over a sub-sector while operating the LHC very close to the nominal during the LHC Run 2 starting in 2015.

While the superconducting magnets are powered, resistive heating occurs at locations where superconducting cables are soldered together. The splices in are used to subdivide magnet coils into regions of different current density or to join magnets after installations. Although being superconducting at magnetic fields intensities below 0.3 T (Riddone (1997)), the solder 40 % lead and 60 % tin is resistive at the filed intensities up to 8.4 T corresponding to the

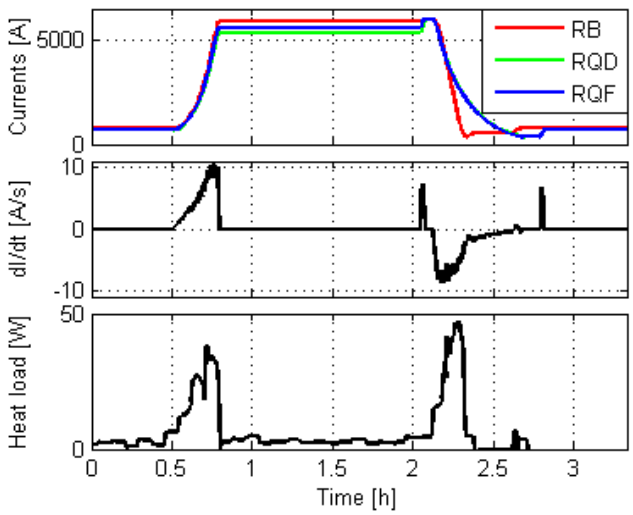

Fig. 5.7 Transient dynamic heat loads over a 214 m long sub-sector during current ramping at 6 kA. Three currents denoted as RB, RQF and RQD correspond to main LHC bending dipoles, focusing and defocusing quadrupoles, respectively.

LHC nominal operation and thus energy is dissipated in the solder while magnets are powered, generating heat.

While beam circulates in the LHC, it induces heat loads due to nuclear inelastic beam-gas scattering, synchrotron radiation and image current power. As presented in Fig. 5.5, most of the heat load is intercepted at the beam screen at 5-20 K, however some of the heat is generated inside the magnets and thus adds to the steady dynamic heat loads into the bath. The heat load strongly depends on the beam parameters such as energy and intensity, number and length of particles' bunches.

Discussion

The total design heat loads into the bath in an LHC sub-sector during nominal operation with beam, comprising static and steady dynamic heat loads, was 75.3 W. Based on the measurements performed during the LHC Run 1, the value has been updated to be approximatively equal 58-63 W during LHC Run 2. The heat loads vary among sub-sectors and over time in function of large number of parameters. The transient dynamic heat load of approx. 20 W was the strongest recurrent perturbation of the magnets temperature during Run 1.

5.3 Cooling power of the Bayonet Heat Exchanger

Two over 100 m long bayonet heat exchangers are submerged in the helium bath. In the exchanger tubes, two phase superfluid-vapor helium flows at very low pressure of 1.6 kPa, corresponding to helium saturation temperature of 1.8 K. Heat flows due to conduction from the warmer bath kept at 1.9 K, through the wall of the tube into the colder superfluid helium that boils at the saturation temperature of 1.8 K. Due to the boiling, the heat exchanger is only partially wetted and pure vapor is sucked out of the exchanger tube. While flowing inside the exchanger tube, the vapor that is initially saturated and then warms up due to contact with exchanger wall and with the feeding pipe placed inside the heat exchanger tube. Due to the heat transfer from the feeding pipe, the vapor may eventually become warmer than the bath around the dry exchanger extremity and the heat flow is reversed in this zone, from the exchanger to the helium bath, badly influencing the bath temperature dynamics.

5.3.1 Energy conservation

The cooling power of the heat exchanger based on the energy conservation

$$q_c(t) = W_{f,in}\, h_{f,in} - W_{b,out}\, h_{b,out} - \mathrm{d}H_{fb,he}/\mathrm{d}t - \mathrm{d}U_{fb,pipes}/\mathrm{d}t \tag{5.25}$$

with helium mass flow rate and its specific enthalpy at the inlet of the feeding pipe $W_{f,in}$ and $h_{f,in}$, respectively, helium mass flow rate and its enthalpy at the heat exchanger output $W_{b,out}$, $h_{b,out}$, respectively. $H_{fb,he}$ and $U_{fb,pipes}$ represents the total enthalpy of the helium and total internal energy of pipe walls present in the assembly of the exchanger enclosing the feeding pipe. Due to the vanishing heat capacity of metals, variation of the internal energy may be neglected. Mass o helium present in the assembly is very small compared with the mass of helium bath, however its dynamics may be much faster and thus needs deeper analysis.

The cooling power relies on the fact that the enthalpy of helium vapor stream leaving the exchanger is much higher than that if superfluid helium entering the feeding pipe. Strong saturation of magnet temperature dynamics observed at lower bath temperatures and at higher cooling power, originate at the fact that due to reduced temperature difference between the bath and heat exchanger, heat transfer through the exchanger wall is reduced, causing reduced helium boiling and thus vapor generation rate resulting in helium mass accumulation in the exchanger and reduced cooling power. Thus due to the accumulation, the mass flow rate at the heat exchanger output differs from that at the feeding pipe input, rendering the equation (5.25) inapplicable for the cooling power estimation. In this general case, the cooling power is calculated based on a fairly complicated energy conservation analysis of the two-phase helium flow, taking into account the dynamics of helium mass distribution in the heat exchanger tube and in the feeding pipe.

However, the special case when no visible saturation effects occur is frequently observed during the LHC operation at nominal conditions and in this case the dynamics of the helium mass may be neglected, enabling application of the Eq. (5.25) and thus significantly simplifying the calculation of the cooling power.

In this section, we start with the simple case neglecting the mass dynamics and then move to the detailed analysis of more general energy conservation taking into account the mass dynamics. The detailed analysis also allows to precisely analyze the operational conditions at which the no-saturation case is valid.

No-saturation case neglecting coolant mass dynamics

If helium mass and enthalpy dynamics in the feeding pipe and in the bayonet heat exchanger are negligible

$$W_{b,out} = W_{f,in} = W_c, \quad \mathrm{d}H_{fb,he}/\mathrm{d}t = 0, \tag{5.26}$$

with mass flow rate the control valve W_c and when the phase separators are empty, and no heat is intercepted at the phase separator as explained later in Section 5.8, then

$$h_{f,in} = h_c, \tag{5.27}$$

with the specific enthalpy of helium entering the control valve h_c. In those conditions, the energy conservation Eq. (5.25) becomes the useful simple lumped parameter description of the cooling power of the heat exchanger

$$q_c(t) = W_c\ (h_c - h_{b,out}) \tag{5.28}$$

with helium mass flow rate and its enthalpy at the control valve W_c and h_c respectively.

This equation is directly applicable to calculate the cooling power, because the approximate value of W_c is rather straight forward to calculate based on the measured valve lift and upstream temperature and pressure, see Section 5.5. The latter two measurements are sufficient to calculate h_c.

The helium enthalpy at the outlet $h_{b,\mathrm{out}}$ may be either calculated approximatively as that of the saturated helium vapor at pressure measured at the 1.8 K refrigerator, thus neglecting the vapor heating in the heat exchanger, or more precisely additionally taking into account the relations between the vapor temperature and the temperatures of the bath and at the control valve inlet, presented in Sections 5.3.7 and 5.6, respectively.

5.3.2 Heat transfer via tube wall of the heat exchanger

When the dynamics of helium mass accumulated in the feeding pipe and in the bayonet heat exchanger is not neglected

$$W_{b,out} \neq W_{f,in} \tag{5.29}$$

in general and thus $W_{b,out}$ is unknown and the Eq. (5.28) cannot be directly applied.

In this general case, the linear density of cooling power of the heat exchanger is a sum of heat transfers from the static He II bath, via the oxygen-free copper wall of the exchanger into superfluid He II q_{h2bs} and vapor q_{h2bv} in the two phase flow:

$$\partial q_c/\partial x = \partial q_{h2bs}/\partial x + \partial q_{h2bv}/\partial x, \text{ with} \tag{5.30}$$

$$\partial q_{h2bs}/\partial x = (T_h - T_s)\ \partial C_{th,h2bs}/\partial x \geq 0 \tag{5.31}$$

$$\partial q_{h2bv}/\partial x = (T_h - T_v)\ \partial C_{th,h2bv}/\partial x \tag{5.32}$$

with temperatures of the He II T_s and He vapor T_v, linear densities of the thermal conductances corresponding to the heat flows $\partial C_{th,h2bs}/\partial x$ and $\partial C_{th,h2bv}/\partial x$, respectively. The two phases are considered separately because the two phase flow phase flow is stratified, meaning that a clear boundary between the superfluid and vapor phases exist.

Please note that, the heat transfer from the helium bath to the He II $\partial q_{h2bs}/\partial x$ is approximatively non-negative, because the boiling superfluid helium in the heat exchanger may only receive heat from the bath and cannot be heat source when helium condensation and saturated superfluid helium temperature dynamics are negligible.

5.3.3 Geometry of the heat exchanger tube

The heat exchanger is composed of approx 106 m long, 58 mm outer diameter, 2.3 mm thick tube. Inside, at the bottom of the tube, the feeding pipe supplying helium is placed. The tube has 10 mm outer diameter and 1 mm thick wall, see Fig. 5.8.

Heat exchanger cross-section related variables

Variables related to the geometry of the heat exchanger are used later in the description of its cooling power and related two phase flows. For the stratified flow, the inner perimeter of heat exchanger tube wetted by the superfluid helium phase expressed in function of superfluid level

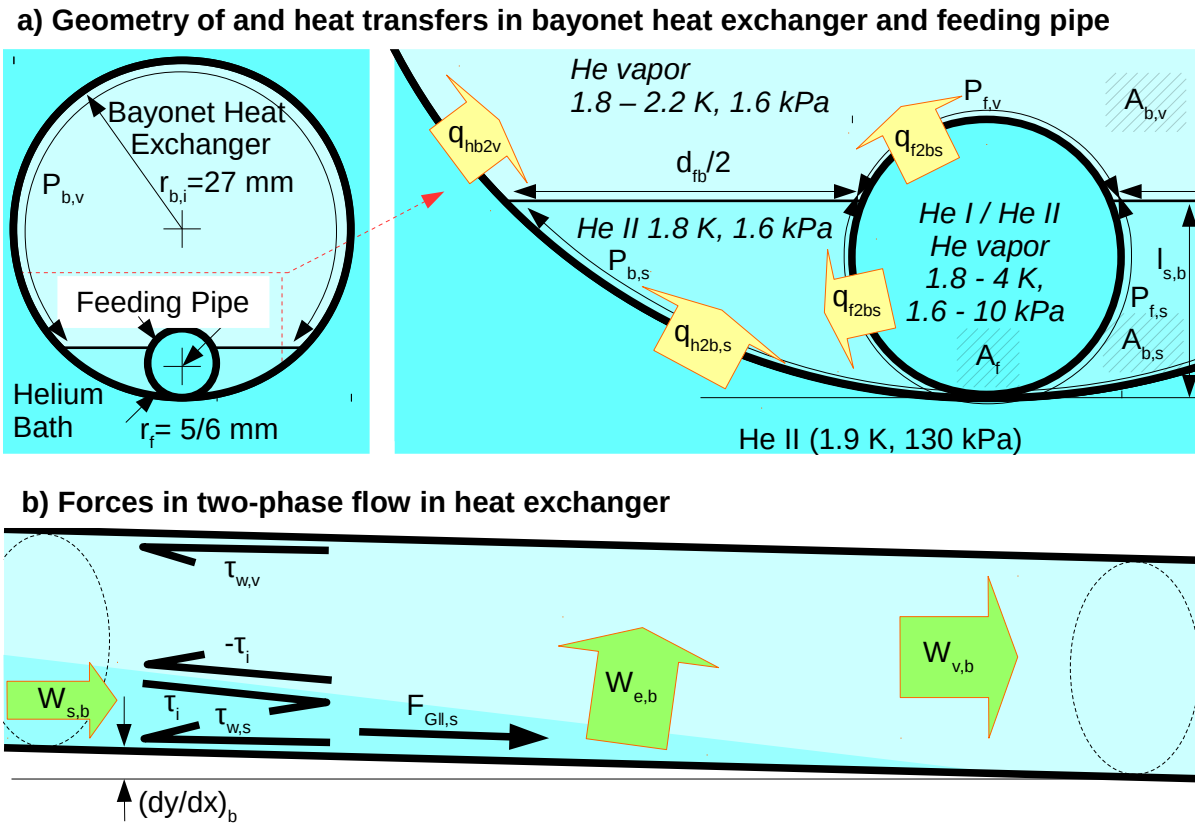

Fig. 5.8 Two-phase diabatic helium flow in the heat exchanger.

$l_{s,b}$

$$P_{b,s}(l_{s,b}) = 2\, r_{b,i}\ \arccos((r_{b,i} - l_{s,b})/r_{b,i}),\ 0 \le l_{s,b} \le 53.4\ \text{mm}, \tag{5.33}$$

with the inner radius of the tube $r_{b,i}$. Similarly, the outer perimeter of the feeding pipe wetted by the superfluid

$$P_{f,s}(l_{s,b}) = \begin{cases} 2\, r_{f,o}\ \arccos((r_{f,o} - l_{s,b})/r_{f,o}), & \text{if } 0 \le l_{s,b} \le 2\, r_{f,o} = 12\ \text{mm} \\ 2\, \pi\, r_{f,o}, & \text{if } l_{s,b} > 2\, r_{f,o} = 12\ \text{mm}, \end{cases} \tag{5.34}$$

The surface area of the heat exchanger cross-section occupied by superfluid phase

$$A_{s,b}(l_{s,b}) = r_{b,i}^2\ (\arccos(1 - l_{s,b}./r_{b,i}) - (1 - (1 - l_{s,b}./r_{b,i})^2)^{0.5}\ (1 - l_{s,b}/r_{b,i})) - A_{f,b}(l_{s,b}) \tag{5.35}$$

with the cross-section area of the heat exchanger tube occupied by feeding pipe

$$A_{f,b}(l_{s,b}) = \begin{cases} r_{f,o}^2\ (\arccos(1 - l_{s,b}/r_{f,o}) - (1 - (1 - l_{s,b}/r_{f,o})^2)^{0.5}\ (1 - l_{s,b}/r_{f,o})), \\ \quad \text{if } 0 \le l_{s,b} \le 2\, r_{f,o} \\ \pi\, r_{f,o}^2, \quad \text{if } l_{s,b} > 2\, r_{f,o} = 12\ \text{mm}, \end{cases} \tag{5.36}$$

Tunnel slope

The LHC tunnel plane is inclined

$$\mathrm{d}Z/\mathrm{d}X = -0.0140,\ \mathrm{d}Z/\mathrm{d}Y = 0.0012, \tag{5.37}$$

with coordinates X, Y and Z from Quesnel (1999). Thus, the tunnel slope varies along the LHC circumference

$$\mathrm{d}y_t/\mathrm{d}x = \mathrm{d}Z/\mathrm{d}x = \mathrm{d}Z/\mathrm{d}X\ \sin\alpha + \mathrm{d}Z/\mathrm{d}Y\ \cos\alpha, \tag{5.38}$$

with the angle α between the X-axis direction, center of the arc and the position x in the arc. Using coordinates of an arc endpoint (X_e, Y_e) and the center of the circle (X_c, Y_c)

$$\alpha = \arctan\left((Y_e - Y_c)\,/\,(X_e - X_c)\right) - x_0/r, \tag{5.39}$$

with the distance x_0 along the LHC arc from its endpoint to the SC (positive direction is clockwise looking from the center of the circle) and the arc radius $r = 3494$ m.

5.3.4 Thermal conductance of the heat exchanger

This section starts with analysis of the helium distribution in the heat exchanger and then provides description of the heat conductivity between the helium bath and the superfluid and vapor helium flowing in the heat exchanger. The tube has an outer diameter of 58 mm for 2.3 mm of wall thickness and it is made of oxygen free high-conductivity (OFHC) copper with 21 % cold work.

Two-phase flow regime

The bayonet heat exchanger is designed to operate as partially wetted with two phase diabatic co-current flow of He II and He vapor at approx. 1.6 kPa, 1.8 K. The exchanger tube is smooth, over 100 m long, 54 mm inner diameter and is slightly inclined following the geometry of the as the LHC tunnel contained in a plane inclined at 1.39 Thus the flow in the tube is almost horizontal, at small negative slope varying along the tunnel circumference as

$$-1.39\ \% \leq (\mathrm{d}y/\mathrm{d}x)_t \leq 0\ \% \tag{5.40}$$

see Figure 5.8 for details.

Superfluid helium distribution across the tube strongly depends on the vapor velocity. At small vapor mass flow rates $W_v, b \leq 7 \times 10^{-3}$ kg/s the flow is dominated by the gravity forces and superfluid phase stratifies at the bottom of the tube. Thus, in the stratified flow the two phases are separated from each other by a continuous interface, smooth or rippled by small waves, and the tube perimeter wetter by the He II is directly related to the tube cross-section area occupied by this phase. At higher vapor velocities (mass flow rates) increasing drag between the two phases creates large amplitude, irregular waves and droplets are entertained from the waves and are deposited at the wall or at the interface. This atomisation phenomenon increases the wetted perimeter and thus the heat transfer as explained and experimentally demonstrated by Tzotzi and Andritsos (2013)) for general two-phase flow and Rousset et al. (1998), Rousset et al. (1997) and Rousset et al. (1999) for the superfluid-vapor flow.

In the following, I limit the description to stratified flow without atomisation corresponding to the case of the small vapor velocities and neglect the case when the interface between the phases is not continuous.

Helium bath - superfluid helium phase

Linear density of thermal conductance of a sample of the heat exchanger tube completely filled with pressurized He II and submerged in bath of saturated He II has been measured by Camacho

et al. (1998) that stated that it strongly depends on the surface cleanliness of the sample, with the maximal value

$$\mathrm{d}C_{th,h2bs,full}/\mathrm{d}x \ @\ 1.9\ \mathrm{K} = 717\ \mathrm{W/K\ m}, \tag{5.41}$$

corresponding to linear density of thermal resistance

$$\mathrm{d}R_{th,h2bs,full}/\mathrm{d}x = \mathrm{d}/(1/C_{th,h2bs,full})/\mathrm{d}x = 1.39\ \mathrm{K/W\ m}. \tag{5.42}$$

The thermal resistance between helium inside and outside of the sample

$$R_{th,h2bs,full} = R_{th,K,i} + R_{th,Cu} + R_{th,K,o} \tag{5.43}$$

is a sum of very small the thermal resistance of the the copper wall

$$\mathrm{d}R_{th,Cu}/\mathrm{d}x = \ln(r_{b,o}/r_{b,i})/(2\ \pi\ \lambda_{Cu}) = 6.5757 \times 10^{-5}\ \mathrm{K/W\ m}. \tag{5.44}$$

and the Kapitza resistance at inner and outer perimeter of the tube wetted by He II $R_{th,K,i}$, $R_{th,K,o}$, respectively.

Kapitza resistance corresponds to a temperature discontinuity accompanying the heat transfer through liquid-solid interfaces or solid-solid interfaces. At small temperature differences $\Delta T \ll T$, the Kapitza resistance

$$R_{th,K,i} \approx 1/(a_K\ A\ T^n) \tag{5.45}$$

with the interface area A and values of Kapitza coefficient a_K and exponent n that strongly depend on surface cleanness and solid properties. For copper (Van Sciver (2011)),

$$n = 3, \quad 400\ \mathrm{W/m^2} \leq a_k \leq 900\ \mathrm{W/m^2}. \tag{5.46}$$

Analysis of the results for the exchanger sample provided by Camacho et al. (1998), confirmed the value of n, but lead to much higher maximal

$$a_K = 1244\ \mathrm{W/K^4 m^2}. \tag{5.47}$$

Camacho et al. (1998) suggest that cold work may be responsible for the higher value of a_K of the exchanger sample. This is why at cryogenic temperatures of 1.9 K, the Kapitza resistance dominates the thermal resistance between the helium bath and He II in the heat exchanger. Pressure dependence of the resistance is negligible at 2 K, see Van Sciver (2011).

During normal LHC operation, the whole outer perimeter of the tube is wetted, as in the investigated sample. However in case of stratified two-phase flow, only a fraction of inner perimeter of the heat exchanger $P_{b,s}$ is wetted, resulting in a non-trivial heat transfer pattern through the wall, see Figure 5.13. I was able to express the thermal conductivity of the tube with inner wetted perimeter

$$\mathrm{d}C_{th,h2bs}/\mathrm{d}x = 0.5\ P_{b,s}\ c_{P_{b,s}}(P_{b,s})\ C_K\ T_s^3. \tag{5.48}$$

taking into account two Kapitza resistances the heat pattern thanks to the correction factor $c_{P_{b,s}}(P_{b,s})$ presented in Fig. 5.9 and calculated based on simulation using 2-D model of the tube and Finite Element Method. In simulations, temperature dependence of the correction factor is negligible. Saturation temperature inside the heat exchanger $T_{s,b}$ is used for both, inner and outer wall temperatures because the tube conductance is so high that He II may penetrate into the tube exclusively at small temperature differences $T_h - T_{s,b}$, corresponding to small cooling power and thus small evaporation rates.

In case of stratified two-phase flow, the length of the inner perimeter of tube wetted by the superfluid helium $P_{b,s}(A_{b,s})$ is related through the tube geometry, see Fig. 5.8, to the cross-section of the tube occupied by the superfluid helium $A_{b,s}$ that is defined by the spatial distribution of He II mass along the length, described in next section.

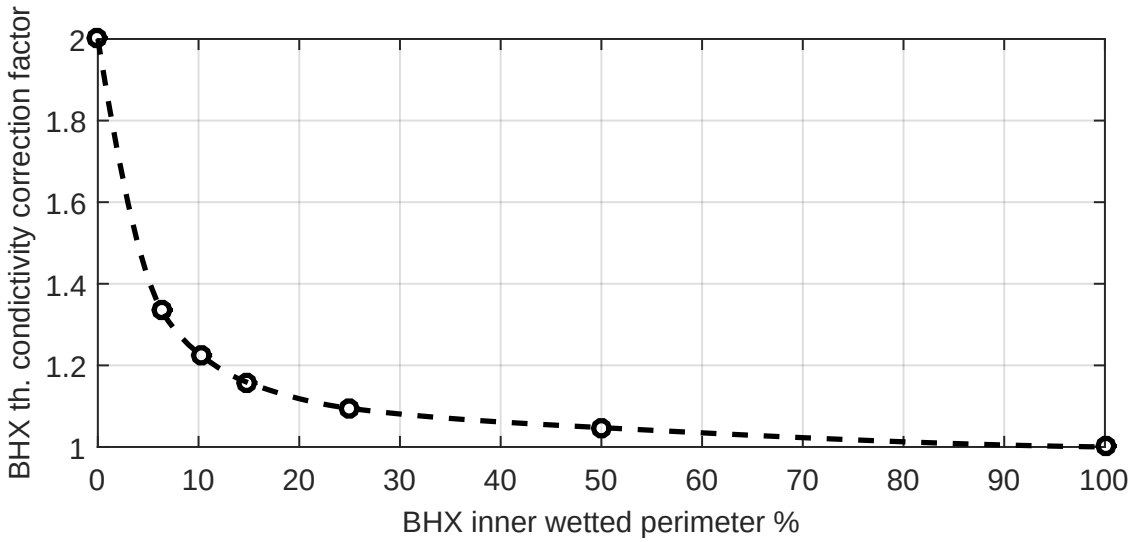

Fig. 5.9 Correction factor for thermal conductance of heat exchanger: value of 1, no correction, corresponds to fully wetted inner perimeter. At vanishing wetted inner perimeter only one Kapitza resistance at exchanger inner wall is limiting the flow, thus the conductance doubles and the value of correction factor is 2.

Helium bath - vapor phase

The thermal resistance between the superfluid helium in the bath and the helium vapor flowing in the heat exchanger

$$R_{th,h2bv} = R_{th,b,K,o} + R_{th,b,w} + R_{th,b,w2v}, \tag{5.49}$$

with the Kapitza resistance at the superfluid helium - outer heat exchanger wall interface in the bath and the wall thermal resistance mentioned in the precedent section. $R_{th,b,w2v}$ is the thermal resistance corresponding to heat transfer coefficient at the boundary between the helium vapor forced turbulent flow inside the exchanger tube and the inner wall.

The vapor flow properties are presented in the Fig. 5.10. The flow is turbulent in the whole range of mass flow rates and temperatures, and thus the heat conduction $C_{th,b,w2v} = 1/R_{th,b,w2v}$ at the wall-vapor boundary is defined by the bulk heat conductivity of helium vapor k_v scaled using the Nusselt number Nu_v and characteristic length represented by the hydraulic diameter

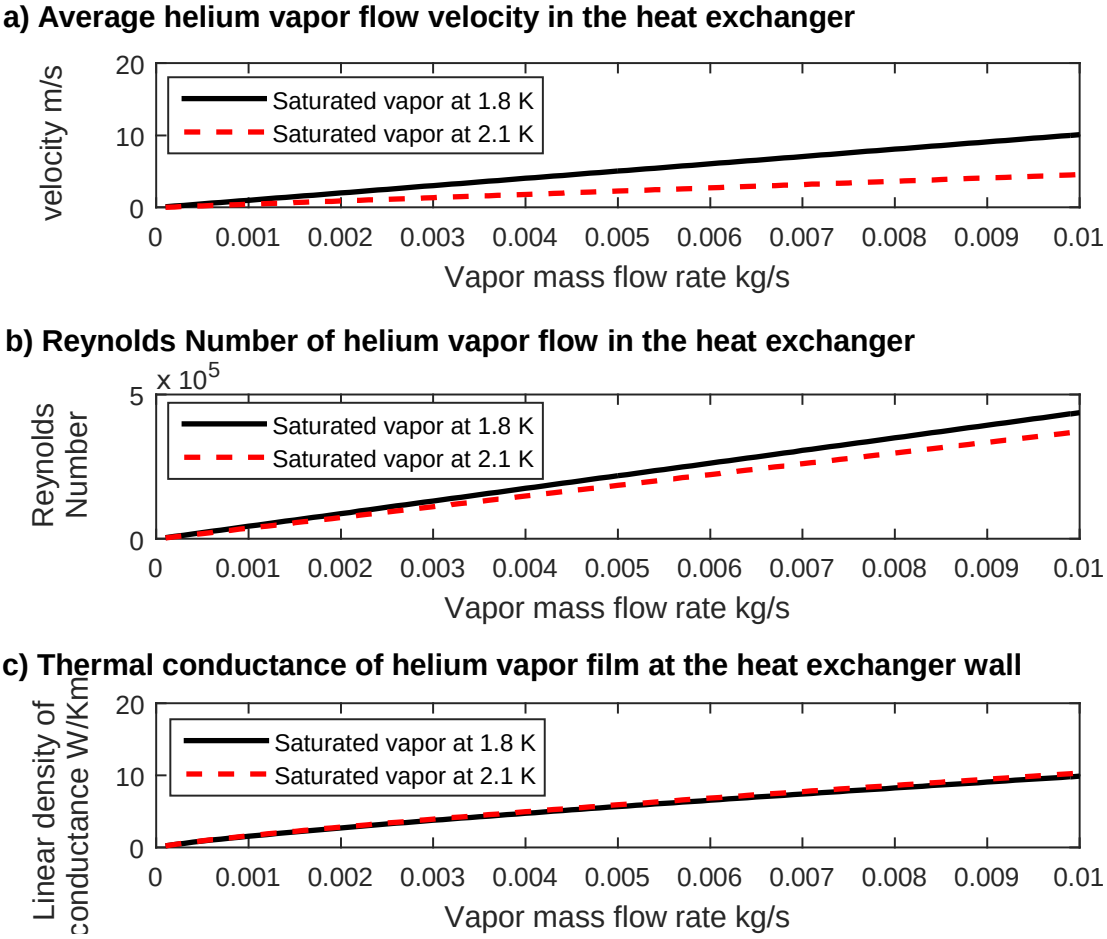

Fig. 5.10 Properties of vapor flow in the bayonet heat exchanger.

of the vapor flow $D_{h,b,v}$

$$\partial C_{th,b,w2v}/\partial x = h_{v,b}\, P_{b,v}, \tag{5.50}$$

with the heat exchanger tube perimeter that is in contact with the vapor flow

$$P_{b,v}(A_{b,s}) = P_{b,i} - P_{b,s}(A_{b,s}), \tag{5.51}$$

with the inner tube perimeter $P_{b,i}$.

The heat transfer coefficient for the forced turbulent vapor flow in the exchanger tube

$$h_{v,b} = k_v\, Nu_v/D_{h,b,v}. \tag{5.52}$$

Which correlation choose to describe the Nusslet number Nu_v is related to the Reynolds number and value of the Prandl number for saturated vapor at 1.8 K

$$Pr_v = c_{p,v,b}\, \mu_{v,b}/k_v = 0.77 \tag{5.53}$$

with the specific heat $c_{p,v,b}$ and dynamic viscosity $\mu_{v,b}$. Thus, I use the Dittus Boelter correlation to find the Nusselt number for forced convection

$$Nu_v = 0.023\, Re_v^{4/5}\, Pr_v^{2/5}, \tag{5.54}$$

resulting in values of the linear density of the heat conductivity at the boundary presented in Fig. 5.10c that are much smaller than that of the Kapitza conductance of the outer wall, studied in previous section,

$$\mathrm{d}(1/R_{th,b,K,o})/\mathrm{d}x \approx 2\ \mathrm{d}C_{th,b,full}/\mathrm{d}x = 1424\,\mathrm{W\ K^{-1}\ m^{-1}}. \tag{5.55}$$

Thus, the Kapitza conductance is negligible and

$$\partial C_{th,h2bv}/\partial x = \partial C_{th,b,w2v}/\partial x = h_{v,b}\, P_{b,v}, \tag{5.56}$$

with

$$h_{v,b} = 0.023\, \mu_v^{-2/5}\, c_p^{2/5}\, k_v^{3/5}\, A_{v,b}^{-4/5}\, D_{h,b,v}^{-1/5}\, W^{4/5}. \tag{5.57}$$

5.3.5 Superfluid mass distribution

Superfluid helium mass distribution has principal impact on the the cooling power distribution of the bayonet heat exchanger, through the wetted inner perimeter of the exchanger tube. The

mass distribution in the two phase, stratified, diabatic flow is governed by mass, momentum and energy conservation principles. In order to keep the level of description adequate for the purpose of development of a model that may be simulated at relatively low computing cost, I use a 1-D Saint Venant-type approach - a macroscopic approach based on engineering correlations suitable for implementation in a model discretized with large spatial step of few meters. Original Saint Venant equation describes open channel liquid flow and thus, I enhance them to take into account the interaction between the two helium phases flowing in the heat exchanger tube. Thus, full first-principles microscopic description of the flow based on Navier-Stokes equations with an appropriate turbulence models is out of scope of this work because it would need a much finer spatial discretization grid resulting in much higher computational cost of simulation, unsuitable for real-time optimization applications.

Mass conservation

The mass conservation along the He II flow is described by the 1-D PDE

$$\rho_s \, \partial A_{b,s}/\partial t(x,t) = \mathrm{d}W_{s,b}/\mathrm{d}x - \mathrm{d}W_{e,b}/\mathrm{d}x \tag{5.58}$$

with the heat exchanger cross-section area occupied by He II $A_{b,s}$, the divergence of the He II mass flow rate $\mathrm{d}W_{s,b}/\mathrm{d}x$ and linear density of the He II evaporation mass flow rate $\mathrm{d}W_{e,b}/\mathrm{d}x$.

The evaporation rate

$$\partial W_{e,b}/\partial x = (\partial q_e/\partial x)/\Delta_H \geq 0 \tag{5.59}$$

is proportional to the net evaporation heat input $q_e(x,t)$, found using energy conservation principle, described later. The evaporation rate is non-negative when condensation is neglected. The latent heat of evaporation of helium in the analysis validity range

$$\Delta_H = 23.4 \times 10^3 \text{ J/kg}. \tag{5.60}$$

Energy conservation

Superfluid helium in the bayonet heat exchanger is typically colder than the bath and thus heat continuously flows form the bath into the exchanger and maintains the superfluid helium saturated. In the helium flow, energy dissipation due to friction in the He II flow and net enthalpy transport of the flowing helium are negligible. Thus, the evaporation heat input

$$\partial q_e/\partial x = \partial q_{s,b}/\partial x + \partial q_{h2bs}/\partial x + \partial q_{f2bs}/\partial x \tag{5.61}$$

using static form of energy conservation because the temperature dynamics of saturated helium is negligible when the saturation temperature varies slowly.

The heat transfer from the bath into the superfluid q_{h2bs} have been calculated in this section. Heat transfer from helium flowing in the feeding pipe q_{f2bs} is described in Section 5.4. The 1-D divergence of the longitudinal heat transfer in the superfluid

$$\partial q_{s,b}/\partial x = 0 \tag{5.62}$$

because the longitudinal heat transfer is negligible due to very small gradients of the saturation temperature, velocity and cross-section area of the superfluid flow. Direct heat transfer between the feeding pipe and the heat exchanger pipe (Salerno (1983)) is also negligible at the very small temperature differences and vanishing contact area between them.

Momentum conservation

Van Sciver (2011) noted that turbulent flow of superfluid helium is similar to that of common viscous fluids. Thus the superfluid helium mass flow rate distribution along the heat exchanger tube is found using standard static momentum conservation,

$$\mathrm{d}F_{G,\parallel} - \mathrm{d}(\int pdA) - \mathrm{d}F_{b,w,s} + \mathrm{d}F_{v2s,b} - \mathrm{d}W_e\, U_{s,b} - \mathrm{d}(W_{s,b}\, U_{s,b}) = 0 \tag{5.63}$$

valid each point along the flow. This formulation is characteristic for the Saint-Venant approach suitable for low-computing cost implementation, introducing errors related to the the neglected forces corresponding to inertia of the flowing helium are small comparing to the gravity force driving the flow. The flow is driven by the component of the gravity force parallel to the slope

$$\mathrm{d}F_{G,\parallel} = -\mathrm{d}x\, A_{s,b}\, \rho_s\, g\, \mathrm{d}y_t/\mathrm{d}x, \tag{5.64}$$

with the tunnel slope $(\mathrm{d}y/\mathrm{d}x)_t$ being the small angles approximation

$$\mathrm{sin}\mathrm{d}y_t/\mathrm{d}x \approx \mathrm{d}y_t/\mathrm{d}x \tag{5.65}$$

and with the gravitational acceleration of the Earth g. The other component of the gravity force, perpendicular to the slope is responsible for build up of the hydrostatic pressure $p_{h,s}$ in the superfluid phase. Infinitesimal change along the flow direction of the total hydrostatic force at the superfluid flow cross-section

$$\mathrm{d}(\int p_{h,s}\mathrm{d}A_{b,s}) = \mathrm{d}p_b + \mathrm{d}(\int_0^{l_{s,b}} \rho\, g\, (l_{s,b} - l')\, d_b(l')\, \mathrm{d}l') \tag{5.66}$$

integrated in the vertical direction along the superfluid helium level $l_{s,b}$ and with chord d_b. $\tau_i\ S_{b,i}$ and $\tau_{ws}\ S_{b,s}$ are the shear stress at and perimeter of the interface at the vapor phase and at the both feeding pipe outer and heat exchanger inner walls, respectively and finally $W_{s,b}$, $U_{s,b}$ and W_e are mass flow rate and mean velocity of the superfluid flow and evaporation rate, respectively.

The sheer stress at the superfluid - vapor interface in the stratified wavy two-phase flow is described by an improved version of the Andritsos-Hanratty model developed by Tzotzi and Andritsos (2013). The model is based on the observation that four sub-regimes of the stratified gas-liquid flow in horizontal and slightly downward pipes exist: 1) a smooth region, occurring at very low gas and liquid velocities, where the gas-liquid interface is smooth, 2) a two-dimensional (2-D) wave region, where the interface is covered by small amplitude, short wavelength regular disturbances, 3) a wavy region with large amplitude, irregular waves, with a steep front and a gradually sloping back, also called roll waves or Kelvin-Helmholtz (K-H) waves and 4) the atomization region, where droplets or liquid filaments are torn off from the crests of the large-amplitude waves and deposited on the pipe wall that is out of the scope of the model. The transition between the regimes happens at the superficial flow velocity of vapor

$$U_{GS,2-D} = 1/1.95\ (\rho_s/\rho_w)^{0.1}\ (\rho_a/\rho_v)^{0.5}\ (\mu_s/\mu_w)^{0.35}\ \ln[0.8\ (\mu_s/\mu_w)^{0.2}/U_{LS}] \tag{5.67}$$

for the smooth-2-D wave transition and

$$U_{GS,K-H} = 1/0.65\ (\rho_s/\rho_w)^{0.5}\ (\rho_a/\rho_v)^{0.5}\ (\sigma_s/\sigma_w)^{0.33}\ \ln[1.39\ (\mu_w/\mu_s)^{0.15}/U_{LS}] \tag{5.68}$$

for the 2-D wave - K-H large amplitude wave transition, with superficial flow velocity of superfluid U_{LS}, densities of water ρ_w and air ρ_a, dynamic viscosity of water μ_w and surface tensions of superfluid σ_s and water σ_w. Superficial velocity is the one calculated as if just one phase was present in the pipe. Having determined the flow regime, the infinitesimal increment of force along the exchanger length

$$\mathrm{d}F_{v2s,b} = \tau_i\ S_i\ \mathrm{d}x, \tag{5.69}$$

with the interfacial shear stress

$$\tau_i = f_i\ \rho_v\ (U_v - U_l)^2/2 = f_i/f_v\ f_v\rho_v\ (U_v - U_l)^2/2, \tag{5.70}$$

where the friction coefficient at the interface

$$f_i/f_g = \begin{cases} 1 \quad \text{if } U_{GS} < U_{GS,2-D}, \\ 1 + 0.35\ (h/D)^{0.5}\ (U_{GS} - U_{GS,2-D}) \quad \text{if } U_{GS,2-D} \leq U_{GS} \leq U_{GS,K-H}, \\ 2\ (h/D\ \rho_l/\rho_w)^{0.1} + 4\ (h/D)^{0.5}\ (U_{GS} - U_{GS,K-H}) \quad \text{if } U_{GS} > U_{GS,K-H}, \end{cases} \tag{5.71}$$

is expressed in relation to that of the wall-vapor interface friction coefficient. The Blasius formula describes the friction coefficient of turbulent flow

$$f_v = 0.079\ Re_v^{-1/4}, \tag{5.72}$$

with the Reynolds number for the vapor phase flow

$$Re_v = \rho_v\ U_v\ D_{h,v}/\mu_v. \tag{5.73}$$

After substitutions

$$F_i/\Delta x = f_i/f_v\ S_i\ 0.079/2\ D_v^{-1/4}\ A_v^{1/4}\ \mu_v^{1/4}\ \rho_v\ W_v^{-1/4}\ (U_v - U_l)^2. \tag{5.74}$$

The shear force at the superfluid - wall interface

$$\mathrm{d}F_{b,w,s} = \tau_{b,w,s}\ S_{b,s}\ \mathrm{d}x, \tag{5.75}$$

with the sheer stress corresponding to the standard Darcy-Weisbach equation White (1998)

$$\tau_{b,w,s} = f_s\ \rho_s\ (U_{b,s})^2/2, \tag{5.76}$$

with the average superfluid phase velocity

$$U_{s,b} = W_{s,b}/(A_{b,s}\ \rho_s), \tag{5.77}$$

using the Blasius correlation for turbulent wall friction coefficient

$$f_{b,s} = 0.079\ Re_{b,s}^{-1/4}, \tag{5.78}$$

with the Reynolds number for the He II phase flow

$$Re_{b,s} = \rho_s\ U_{b,s}\ D_{h,b,s}/\mu_s. \tag{5.79}$$

Rearranging the substituting the above relation leads to allows the expression for superfluid mass flow rate in function of the shear force

$$W_{s,b} = (\mathrm{d}F_{b,w,s}/\mathrm{d}x\ 8/0.316\ \rho_s\ \mu_s^{-1/4}\ A_{s,b}^{7/4}\ D_{h,b,s}^{1/4}/S_{b,s})^{4/7}, \tag{5.80}$$

with the gradient of the friction shear force

$$\mathrm{d}F_{b,w,s}/\mathrm{d}x = \mathrm{d}F_{G,\|}/\mathrm{d}x - \mathrm{d}(\int pdA)/\mathrm{d}x + \mathrm{d}F_{v2s,b}/\mathrm{d}x - \mathrm{d}W_e/\mathrm{d}x\ U_{s,b} - \mathrm{d}(W_{s,b}\ U_{s,b})/\mathrm{d}x \tag{5.81}$$

with He II density $\rho_s = 145$ kg/m3, gravitational acceleration $g = 9.81$ m/s2 and $\mu_s = 0.13\ 10^{-5}$ Pa s, $d_h = 4A_s/P_s$ and W_s that stand for He II dynamic viscosity, hydraulic diameter and mass flow rate of He II.

Actually, the Reynolds number of the flow reach values just over the upper limit of the Blasius formula validity, see Fig. 5.12 but I prefer to use this simple formula instead of more complicated by Haaland at cost of eventual negligible errors.

The analysis of the forces magnitudes presented in the Figure 5.11 shows that the gravity force and wall shear stress dominate the flow, with the interfacial stress gaining importance at higher vapor mass flow rates. In this Fig., F_a represent the forced responsible for increase of the momentum flux.

Boundary conditions

At the heat exchanger inlet, the superfluid mass flow rate is equal to that at the outlet of the feeding pipe

$$W_{s,b}(x_{b,in},t) = W_{s,b,in}(t) = -(1-\chi_{f,out}(t))\ W_{f,out}(t) = -(1-\chi_f(x_{f,out},t))\ W_f(x_{f,out},t), \tag{5.82}$$

with the mass flow rate and vapor quality of the two phase flow at the feeding pipe outlet $W_{f,out}(t)$ and $\chi_{f,out}$, respectively. Assuming that only vapor can be sucked into the feeding pipe

$$W_{s,b}(x_{b,in},t) \geq 0. \tag{5.83}$$

Helium leaving the feeding pipe flows against the closed end of the exchanger tube, where it changes direction to opposite. Thus, it is difficult to asses the helium velocity at the boundary, since significant turbulence may be presents at the extremity.

At the heat exchanger outlet, no superfluid helium should appear since the heat exchanger is designed to work as partially wetted, however at very low temperature differences between the saturation temperature in the exchanger and the bath temperature helium may penetrate into

the exchanger and overflow at the open extremity into the phase separator. Thus, the boundary condition corresponds to free overfall where the mass flow rate is limited by the flow critical velocity in case of sub-critical flow, or the boundary condition has no effect on the upstream flow in case of super-critical flow.

The classic relation between the critical flow depth $l_{s,b,crit}$ and the critical superfluid helium mass flow rate $W_{b,s,crit}$

$$(\mathrm{d}A_{b,s}/\mathrm{d}l)_{b,s,crit}(l_{b,s,crit}) = g\, A_{b,s,crit}(l_{b,s,crit})\, \rho_s / W^2_{b,s,crit}. \tag{5.84}$$

If one evaluates this expression, neglecting the effect of the interfacial drag and assuming that the gravity force driving the flow is compensated by the wall shear force, then the flow is sub critical at slopes smaller than approx 0.0043 that corresponds to the distance stretching only over 5 subs-sectors from the zero-slope point. Thus at the LHC, the flow is sub-critical only in few sub-sectors and super-critical in all the rest. However, due to the large ratio between the

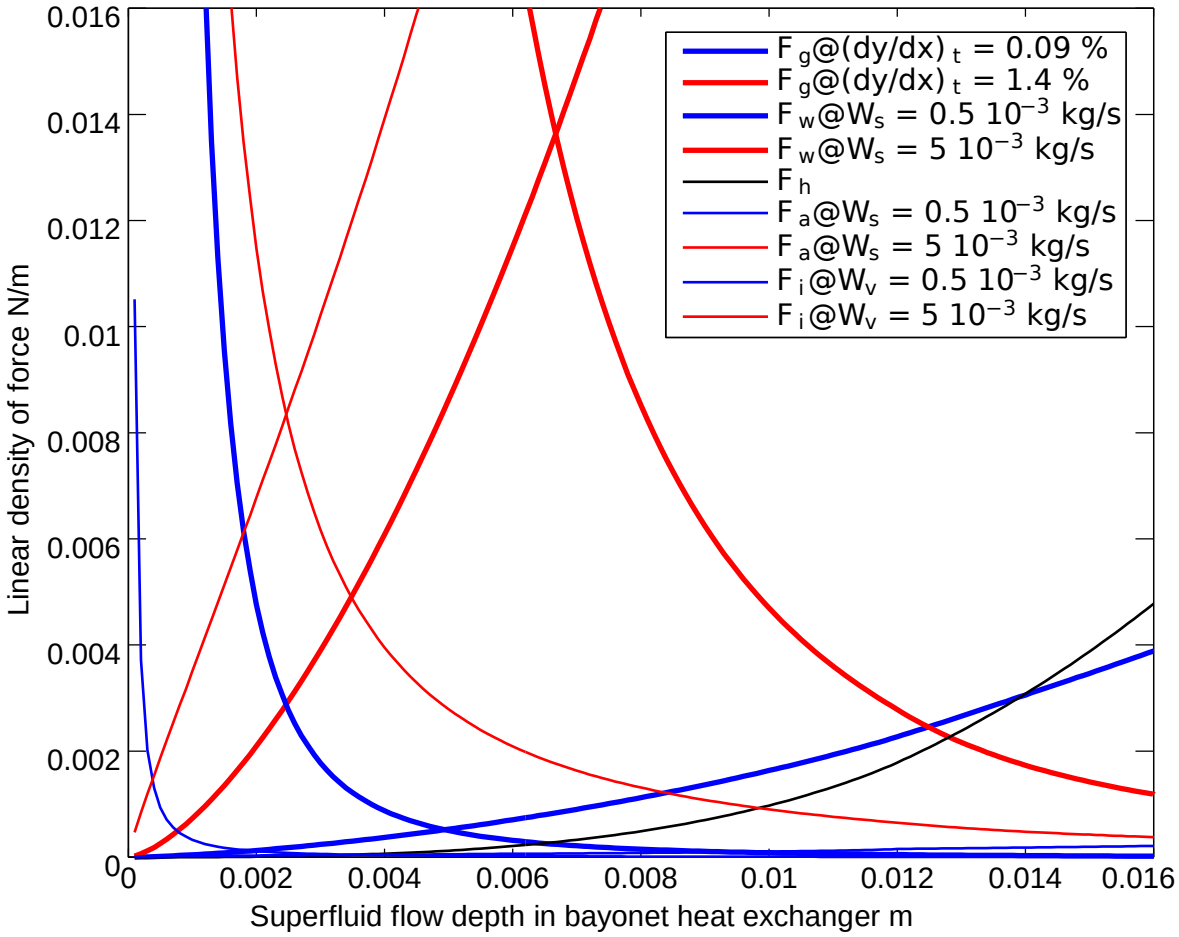

Fig. 5.11 Estimated forces in superfluid flow in the bayonet heat exchanger.

length and diameter of the heat exchanger, the boundary conditions affect the flow only over relatively small zones at the tube extremities and can be neglected if small spatial resolution of model description is used.

5.3.6 Superfluid helium temperature

Superfluid helium in the heat exchanger tube is saturated most of the time due to heat input from the helium bath. Thus, the helium temperature is the saturation temperature of helium

$$T_{s,b}(x,t) = T_{s,he}(p_b(x,t)) \tag{5.85}$$

at the vapor pressure in the exchanger.

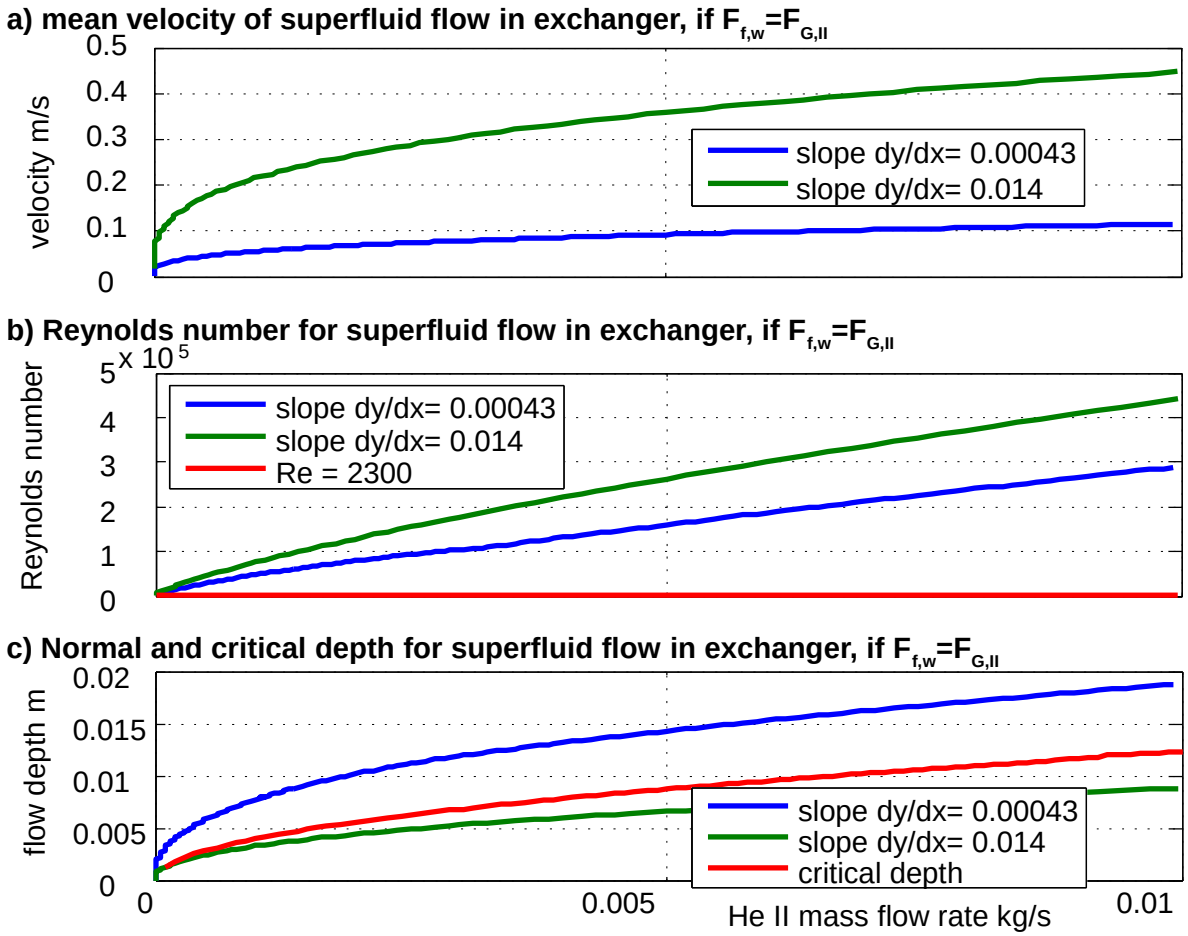

Fig. 5.12 Superfluid flow parameters in bayonet heat exchanger.

Vapor helium flow momentum conservation

The pressure distribution inside the heat exchanger tube $p_b(x,t)$ is defined by a static momentum and mass conservation in the vapor flow, since the very fast vapor pressure and mass dynamics on the magnets temperature dynamics are negligible. The static momentum conservation describes the balance between the sum of forces acting on the flow $\sum F_{v,b}$ and the momentum flux $(U\ W)_{v,b}$

$$\sum \mathrm{d}F_{v,b} + \mathrm{d}(U\ W)_{v,b} = 0 \tag{5.86}$$

where

$$\sum F_{v,b} = \mathrm{d}F_{g||,v,b} - \mathrm{d}F_{v2l,b} - \mathrm{d}F_{fw,v,b} - \mathrm{d}(p_b\ A_{v,b}) \tag{5.87}$$

with the gravity forces parallel to the wall $F_{g||,v,b}$, shear forces at the superfluid-vapor interface $F_{v2l,b}$, shear forces at the vapor-wall boundary $F_{fw,v,b}$ and the infinitesimal change along the flow direction of the total force at the vapor flow cross-section $\mathrm{d}(p_b\ A_{v,b})$ due to pressure gradient.

$$\mathrm{d}(U\ W)_{v,b} = \mathrm{d}(W_{v,b}\ U_{v,b}) - \mathrm{d}|W_e|\ U_{s,b}, \tag{5.88}$$

with the component of the gravity force parallel to the heat exchanger tube wall

$$\mathrm{d}F_{g||,v,b} = g\ \rho_v\ A_{v,b}\ \mathrm{d}y_b \tag{5.89}$$

and the friction force at the wall

$$\mathrm{d}F_{fw,v,b} = \tau_{fw,v,b}\ S_{v,b}\ \mathrm{d}x \tag{5.90}$$

with the shear stress

$$\tau_{fw,v,b} = f_{v,b}/2\ \rho_{v,b}\ U_{v,b}^2 \tag{5.91}$$

calculated the Darcy-Weisbach equation and Blasius correlation for the turbulent wall friction coeffcient (White (1998))

$$f_{b,v} = 0.079\ Re_{b,v}^{-1/4}, \tag{5.92}$$

with the Reynolds number for the He II phase flow

$$Re_{b,v} = \rho_v\ U_{b,v}\ D_{h,b,v}/\mu_v. \tag{5.93}$$

The average superfluid phase velocity

$$U_{v,b} = W_{v,b}/(A_{v,b}\ \rho_{v,b}) \tag{5.94}$$

and after substitution and rearranging the above equations we obtain the frictional shear force

$$\mathrm{d}F_{f,v,b} = 0.079/2\ \rho_{v,b}^{-1}\ \mu_{v,b}^{1/4}\ A_{v,b}^{-7/4}\ D_{h,v,b}^{-1/4}\ S_{b,v}\ W_{v,b}^{7/4}\mathrm{d}x. \tag{5.95}$$

Thus after rearranging the momentum equation, the pressure gradient

$$\mathrm{d}p_b/\mathrm{d}x = (\mathrm{d}F_{g||,v,b}/\mathrm{d}x - \mathrm{d}F_{v2l,b}/\mathrm{d}x - \mathrm{d}F_{fw,v,b}/\mathrm{d}x + \mathrm{d}(W_{v,b}^2/(A_{v,b}\ \rho_{v,b}))/\mathrm{d}x - \mathrm{d}W_e/\mathrm{d}x\ U_{s,b})/A_{v,b} \tag{5.96}$$

Using the chain rule, the saturation temperature gradient

$$\mathrm{d}T_{s,b}/\mathrm{d}x = \mathrm{d}T_{s,he}/\mathrm{d}p\ \mathrm{d}p_b/\mathrm{d}x \tag{5.97}$$

may be integrated starting from the boundary condition at the heat exchanger outlet $x_{b,out}$ in the negative x direction to find the saturation temperature profile inside the heat exchanger

$$T_{s,b}(x) = T_{s,he}(p_{b,out}) - \int_{x_{out}}^{x} \mathrm{d}T_{s,b}/\mathrm{d}x'(T_{s,b}(x'), W_{v,b}(x'))\ \mathrm{d}x'. \tag{5.98}$$

Helium vapor is sucked out the heat exchanger through the tube outlet, the phase separator, the sub-cooling heat exchanger, the jumper interconnection and the long distribution line back to the 1.8 K refrigerator. The pressure drop at the sub-cooling heat exchanger and the jumper interconnection are negligible, thus pressure at the heat exchanger outlet

$$p_{b,out}(t) = p_r(t) + \Delta p_{lb}(x,t) \tag{5.99}$$

is equal to pressure in the distribution line at a sub-sector, with the pressure measured at the refrigerator p_r and the unknown pressure drop along the cryogenic distribution line $\Delta p_{lb}(x,t)$ due to frictional losses and hydrostatic load. The 3 km long distribution line has much larger volume than the tube thus the pressure at the heat exchanger output represents a constant pressure boundary condition that is an important model input, that must me estimated. In following chapters, I present how the saturation pressure at exchanger outlet $T_{s,b,out}(p_{b,out})$ is estimated directly using a nonlinear, recursive, numerical filter based on the model and described in following chapters.

Vapor helium flow mass conservation

Vapor mass flow rate distribution along the heat exchanger is described by the static mass conservation in the flow

$$\mathrm{d}W_{v,b}/\mathrm{d}x = -\mathrm{d}W_{e,b}/\mathrm{d}x(T_{s,b}(x), T_h(x)) \tag{5.100}$$

with the boundary condition at the heat exchanger inlet

$$W_{v,b,in} = -W_{f,o} - W_{l,b,in}. \tag{5.101}$$

Integrating from the inlet in the positive x direction, we find the vapor mass flow rate distribution along the exchanger

$$W_{v,b}(x) = W_{v,b,in} + \int_{x_{in}}^{x} \mathrm{d}W_{v,b}/\mathrm{d}x'(T_{s,b}(x'), T_h(x'))\ \mathrm{d}x'. \tag{5.102}$$

Tho point boundary value problem

Thus the saturation temperature distribution bounded at the heat exchanger outlet, Eq. (5.98) and vapor mass flow rate distribution bounded at its inlet, Eq. (5.102), are strongly coupled and represent a challenging two point boundary value problem.

5.3.7 Helium vapor temperature

The temperature of helium vapor flowing in the heat exchanger may be higher than the saturation temperature, due to convection over zones with different saturation temperature and due to heat transfers into the vapor flow originating at the helium bath and at the helium flowing in the feeding pipe. As demonstrated by the models presented in this thesis, warm vapor flow near the heat exchanger outlet is the source of heat transfers into the bath causing the the inverse response of the magnets temperature dynamics.

Values of helium vapor temperature $T_{he,v}(h_v, p_v)$ in function of its specific enthalpy and pressure are available from HEPAK. Since pressure is related to the saturation temperature that has been already described, the temperature of the vapor flow in the exchanger is better expressed as

$$T_{v,b}(h_{v,b}, T_{s,b}) = T_{he,v}(h_{v,b}, p_{v,s}(T_{s,b})). \tag{5.103}$$

Energy conservation

The dynamics of the vapor flow enthalpy is described by the energy conservation

$$\partial h_{v,b}/\partial t = (\sum \partial q_{v,b}/\partial x - \partial(W_{v,b}\, h_{v,b})/\partial x + \partial(W_e/\partial x\, h_{sv,b}))/(A_{v,b}\, \rho_{v,b}) \tag{5.104}$$

with the enthalpy of saturated vapor $h_{sv,b}(T_{s,b})$. The total heat transfers into the vapor flow

$$\sum q_{v,b} = q_{h2bv} + q_{f2bv} \tag{5.105}$$

with heat transfers originating at the helium bath q_{h2bv} that has been already discussed and at the helium flow in the feeding pipe q_{f2bv} that will be described in the following section.

The boundary condition at the heat exchanger inlet

$$h_{v,b,in} = \begin{cases} h_{sv}(T_{s,b,in}), & \text{if } \chi_{f,out} < 1 \\ h_{f,out}, & \text{otherwise (pure vapor flow),} \end{cases} \tag{5.106}$$

with vapor quality and specific enthalpy of the two phase flow at the feeding pipe outlet $\chi_{f,out}$ and $h_{f,out}$, respectively.

5.4 Helium mass and temperature in Feeding Pipe

The feeding pipe, officially called helium supply header Y, is placed inside the heat exchanger tube. It feeds helium from the control valve, through the phase separator and the whole length of the heat exchanger, to its inlet, that is in fact a closed extremity opposite to the phase separator. Thanks to the feeding pipe, superfluid and vapor flow in the same direction in the heat exchanger and the two phase co-current flow has much better thermo-hydraulic behaviour than a counter-flow when the phases flow in opposite directions perturbed by the drag between them. Thus, the direction of helium flow inside the feeding pipe is opposite to the co-current flow in the heat exchanger tube. The two phase vapor-liquid and vapor-superfluid flow is horizontal at small positive inclination with absolute value varying along the LHC tunnel from 0 to 1.4 %. The pipe has 10 mm inner and 12 mm outer diameter and is approx. 106 m long.

5.4.1 Motivation

The feeding pipe seems to be irrelevant to the magnets temperature dynamics I found no previous work on modelling of the two phase flow in the feeding pipe. However, deeper analysis of the process data and of the magnets temperature dynamics leads to the conclusion

that it is the feeding pipe has a strong negative effect on the circuit dynamics introducing inverse response and dead-times because it participates in heat exchange with the rest of the system and allows for accumulation of significant quantities of helium, comparatively with the very small mass flow rates in the system. However, the importance of the pipe in the circuit has not been acknowledged previously and no research work on the subject exist.

Inverse response of the temperature dynamics

Inverse response of the magnets temperature dynamics is a phenomenon observed first at the LHC prototypes, when immediately after increasing the control valve lift and thus increasing the coolant mass flow rate in the bayonet heat exchanger, the magnets temperature started to rise, contrary to the intuition and only after some time the effects of the increased cooling power were visible. This dynamic, counterintuitive effect made automatic control of the temperature challenging and was the impulse for development of a series of advanced controllers for the temperature stabilisation, including those presented in the thesis. At the LHC, the inverse response was barely visible during typical operational conditions during the LHC Run 1 at reduced power. However, it was clearly visible during identification tests performed at the LHC when larger heat loads to the bath were realized.

In the past, the explanation for the inverse response of magnets temperature dynamics was that it is an effect of cooling power reduction due to increased pressure in the heat exchanger tube. However, in the partially wetted heat exchanger, there is no cooling power available at the heat exchanger outlet corresponding to location where the magnets temperature were raising the strongest during the inverse response. Thus, I have suggested that the bath heating by the feeding pipe is the cause for the inverse response of the magnets temperature dynamics because the magnets temperature raised at the bath extremity close to the feeding pipe inlet, where warmer helium is feed from the control valve. I have developed an largely oversimplified model of the feeding pipe heating that surprisingly well reproduced the inverse response (Noga (2007)).

In this section, I develop a true first principles model of the inverse response, where the warmer helium flow in the feeding pipe heats the vapor in the heat exchanger that passes the heat to the helium bath.

Dead times of the temperature dynamics

A important delay in order of few minutes between rapid opening of the control valve and the cooling action has been identified during the preliminary tests of an advanced controller leading to erratic action of the state estimator and its failed experimental validation, even though the

controller has been successfully testes in simulations, see Noga et al. (2011). The successful attempt to explain this phenomenon, was to link it with helium mass accumulation in the feeding pipe due to strongly varying vapor quality and thus density of the two phase flow in the pipe. Probably, this phenomenon was also the reason for excessively high values of optimized helium viscosity in my first model of in the LHC Prototype (Noga (2007)).

5.4.2 Two-phase flow regime

The two phase flow in the feeding pipe is not stratified due to the positive slope and very small diameter of the pipe. Thus I use the homogenous model that assumes the two phases move at the same velocity and thus the flow may be regarded as a flow of homogenous mixture of tho phases, characterized by average properties of the phases. The homogenous model has been successfully applied to liquid helium flows by Baudouy et al. (2013).

5.4.3 Mass flow rate distribution (mass conservation)

The mass conservation principle describes the mass flow rate W_f distribution along the feeding pipe

$$\mathrm{d}W_f/\mathrm{d}x = A_f \, \partial\rho_f(x,t)/\partial t \tag{5.107}$$

The boundary at the pipe inlet taking into account that the flow direction in the pipe is negative x direction

$$W_{f,in}(t) = -W_c(t). \tag{5.108}$$

The mass flow rate at the control valve W_c is not affected by the pressure drop in the pipe or other downstream conditions because the flow at the valve is choked, as described in Section 5.5.

The two phase flow density distribution

$$1/\rho_f(x,t) = 1/\rho_{l,f} + \chi_f(x,t)\ (1/\rho_{v,f}(x,t) - 1/\rho_{l,f}), \tag{5.109}$$

with approximatively constant density of liquid or superfluid $\rho_{l,f}$ and temperature and pressure dependent density of vapor helium in the pipe $\rho_{v,f}$. The vapor quality

$$\chi_f(x,t) = (h_f(x,t) - h_{s,f}(x,t))/\Delta_h \tag{5.110}$$

varies strongly in function of specific enthalpy distribution in the two-phase flow $h_f(x,t)$ and that of saturated liquid or superfluid $h_s(p_f(x,t))$ being a function of pressure distribution in the feeding pipe. The density distribution of the two phase flow and thus mass accumulated

in the pipe volume varies strongly in function of vapor quality. Variation of the mass, is the reason for differences between helium mass flow rates at the inlet and outlet of the feeding pipe, corresponding to that at the control valve and at the heat exchanger inlet, respectively.

5.4.4 Helium temperature

The temperature of the helium flowing inside the feeding pipe is equal either to helium saturation temperature $T_{s,he}(p_f(x,t))$ at pressure in the feeding pipe if two phases superfluid/liquid and vapor are coexisting at the considered location along the pipe or 2) helium temperature $T_{he}(h_f(x,t), p_f(x,t))$ at given enthalpy and pressure if only one phase superfluid/liquid or vapor is present:

$$T_f(x,t) = \begin{cases} T_{he}(h_f(x,t), p_f(x,t)), & \text{if } \chi_f(x,t) \in \{0,\ 1\} \text{ (single phase)} \\ T_{s,he}(p_f(x,t)) & \text{otherwise (two phase flow).} \end{cases} \tag{5.111}$$

Saturation temperature profile (momentum conservation)

Static formulation of momentum conservation principle describes the pressure and thus helium saturation temperature profile along the pipe

$$\sum \mathrm{d}F_f = \mathrm{d}(U_f\ W_f), \tag{5.112}$$

with the momentum flux $(U_f\ W_f)$ and sum of the non-negligible forces acting on the flow in the feeding pipe

$$\sum \mathrm{d}F_f = \mathrm{d}F_{f,g\|} + \mathrm{d}F_{fw,f} + \mathrm{d}p_f\ A_f, \tag{5.113}$$

with the gravitational force parallel to the pipe wall

$$\mathrm{d}F_{f,g\|} = -A_f\ \rho_f(x,t)\ g\ \mathrm{d}y_t, \tag{5.114}$$

the force acting over the fluid cross-section area due to pressure increment $\mathrm{d}p_f\ A_f$ and the frictional shear force at the wall

$$\mathrm{d}F_{fw,f} = \tau_{fw,f}\ S_{i,f}\ \mathrm{d}x \tag{5.115}$$

with the shear stress calculated using the Darcy-Weisbach equation

$$\tau_{fw,f} = f_{fw,f}/2\ \rho_f\ U_f^2, \tag{5.116}$$

with the Blasius correlation for the turbulent wall friction coefficient (White (1998))

$$f_{fw,f} = 0.079\, Re_f^{-1/4}, \tag{5.117}$$

with the Reynolds number for the homogenous two phase flow

$$Re_f = \rho_f\, U_f\, D_{h,f}/\mu_f. \tag{5.118}$$

The average dynamic viscosity of the homogenous flow (Collier (1972))

$$1/\mu_f = \chi_f/\mu_{v,f} + (1-\chi_f)/\mu_{sl,f}. \tag{5.119}$$

Using average flow velocity

$$U_f = W_f/(A_f\, \rho_f) \tag{5.120}$$

and after substitution and rearranging the above equations we obtain the frictional shear force at the wall

$$\mathrm{d}F_{fw,f} = 0.079/2\, \rho_f^{-1}\, \mu_f^{1/4}\, A_{i,f}^{-7/4}\, D_{h,f}^{-1/4}\, S_{i,f}\, \mathrm{d}x. \tag{5.121}$$

Thus after rearranging the momentum equation, the pressure gradient

$$\partial p_f/\partial x = \left(\partial F_{g\|,f}/\partial x - \partial F_{fw,f}/\partial x + \partial (W_f^2/(A_{i,f}\, \rho_f))/\partial x\right)/A_{i,f} \tag{5.122}$$

Using the chain rule, the saturation temperature gradient

$$\partial T_{s,f}/\partial x = \mathrm{d}T_{s,he}/\mathrm{d}p\; \partial p_f/\partial x \tag{5.123}$$

may be integrated starting from the boundary condition at the feeding pipe outlet

$$T_{s,f}(x_{out,f}) = T_{s,b}(x_{in,b}), \tag{5.124}$$

in the positive x direction to find the saturation temperature profile inside the heat exchanger

$$T_{s,f}(x) = T_{s,he}(p_f(x_{out,f})) + \int_{x_{out,f}}^{x} \partial T_{s,f}/\partial x'(T_{s,f}(x'), W_f(x'), h_f(x'))\, \mathrm{d}x'. \tag{5.125}$$

We see that the saturation temperature distribution, bounded at the pipe outlet, is closely coupled to distributions of the helium enthalpy and mass flow rate that are bounded at the pipe inlet. Thus, the Eqs. (5.125), (5.107) and (5.126) represent a complex two-point boundary value problem.

Helium enthalpy (energy conservation)

The energy conservation principle describes the helium enthalpy evolution along the feeding pipe

$$\partial h_f/\partial t = (-\partial(W_f\ h_f)/\partial x + \partial q_f\,(x,t)\,/\partial x - \partial q_{f2b,v}/\partial x - \partial q_{f2b,s}/\partial x)/(A_{v,b}\ \rho_v) \quad (5.126)$$

where 1-D divergence of longitudinal heat transfer rate in the superfluid/liquid-vapor flow $\partial q_f\,(x,t)\,/\partial x$ is negligible due to very small cross-section area.

The boundary condition imposed on the specific enthalpy od the flow at the inlet of the feeding pipe

$$h_f(x_{in,f},t) = \begin{cases} h_c(t), & \text{if } m_{l,p} < 0.2168 \text{ kg} \\ h_{sl}(T_{s,b}(x_{b,out},t)), & \text{otherwise} \end{cases} \quad (5.127)$$

that depends on the level of superfluid helium in the phase separator because section of the pipe placed inside the phase separator and thus if the level of saturated superfluid in the separator does not reach the feeding pipe, no heat exchange takes place over this section and enthalpy of helium entering the section of feeding pipe placed inside the heat exchanger is equal to that upstream of the control valve. However, at higher levels in the separator, the feeding pipe is in contact with the helium and due to the high conductance of the interface, the enthalpy is reduced to the level corresponding to temperature of saturated superfluid in the separator.

The heat transfer from the feeding pipe placed at the bottom of the heat exchanger tube, to the superfluid flowing in the exchanger

$$(\partial q/\partial x)_{f2bs} = \begin{cases} \partial C_{f2bs}/\partial x\ (T_f - T_{s,b}), & \text{if } T_f \geq T_{s,b} \\ 0, & \text{otherwise,} \end{cases} \quad (5.128)$$

thus again neglecting condensation and longitudinal heat transfers in superfluid helium flowing in the exchanger, leading to one directional heat transfer used principally (entirely) to evaporate superfluid in the heat exchanger.

Similarly, the heat transfer between the feeding pipe and the helium vapor in the exchanger

$$(\partial q/\partial x)_{f2bv} = \partial C_{f2bv}/\partial x\ (T_f - T_{v,b}). \quad (5.129)$$

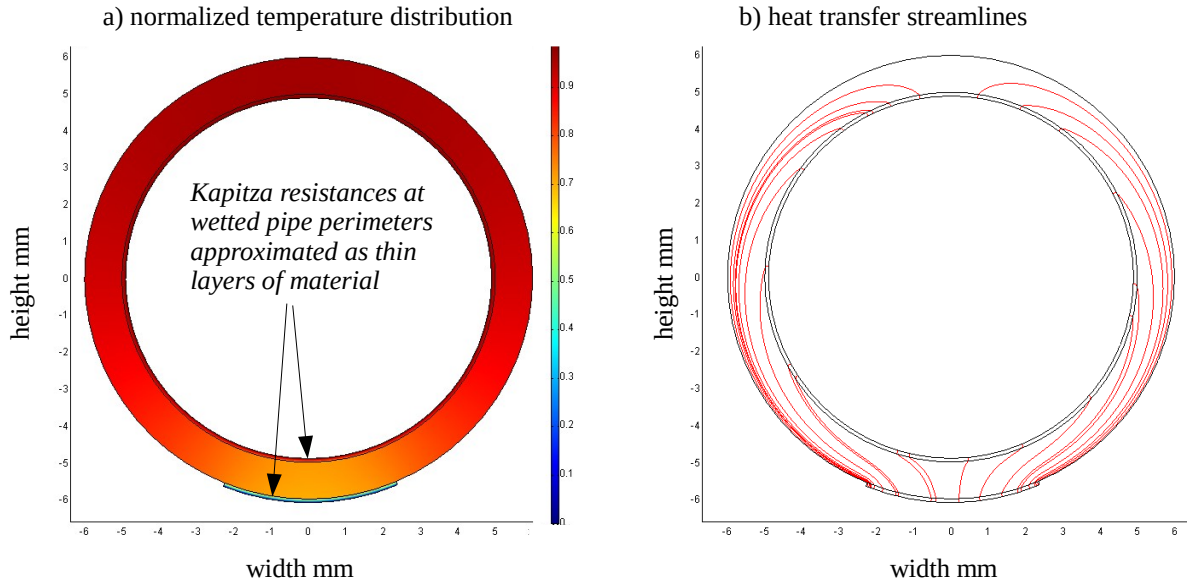

Fig. 5.13 Heat transfer pattern across feeding pipe wall. Inner pipe perimeter is fully wetted and only 12.5 % of outer perimeter is wetted in the presented case.

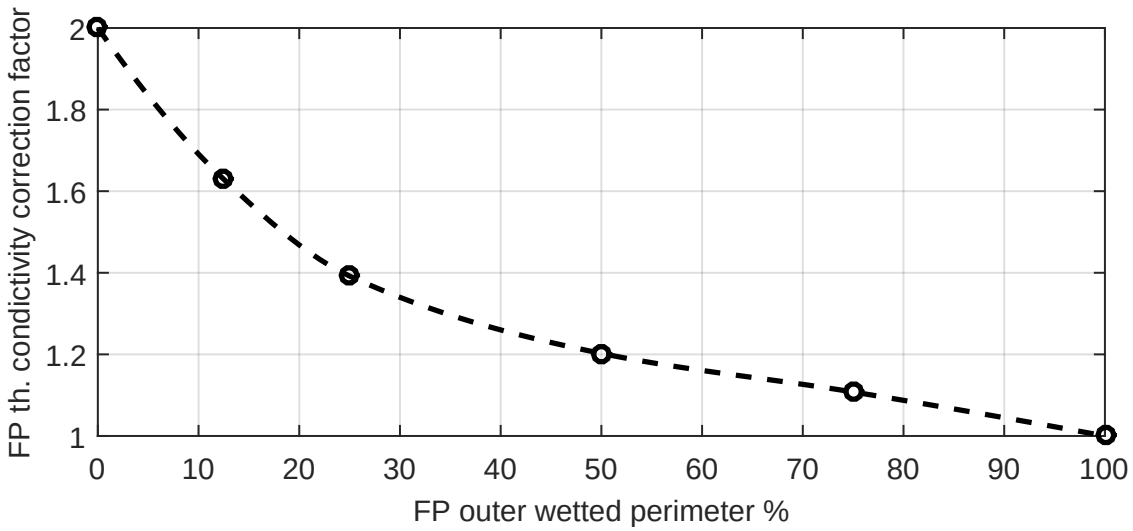

Fig. 5.14 Correction factor for thermal conductance of feeding pipe: value of 1, no correction, corresponds to fully wetted outer perimeter. At vanishing wetted outer perimeter only one Kapitza resistance at pipe outer wall is limiting the flow, thus the conductance doubles and the value of correction factor is 2.

5.4.5 Thermal conductance of feeding pipe

Between two phase flow in feeding pipe and superfluid flow in the heat exchanger

The thermal conductance between two phase flow in feeding pipe and superfluid flow in the heat exchanger is dominated by the Kapitza conductance in case when the flows on both sides contain superfluid characterized by very hight thermal conductivity. Assuming that at low vapor qualities, the inner pipe wall is fully wetted by the superfluid helium and the length of the outer wetted perimeter depends on the depth of helium flow in the exchanger tube, a complex heat transfer pattern is observed in the wall, that is taken into account through correction factor $c_{P_{f,o,s}}$ approximating the effects of a non-trivial heat flow pattern in the feeding pipe wall, see Figure 5.14, similar to that in the heat exchanger tube. Thus

$$\partial C_{f2b,s}/\partial x = c_{P_{f,o,s}}\, P_{f,o,s}\, h_{k,f}/2 \tag{5.130}$$

where $h_{K,f}/2$ corresponds to total heat transfer coefficient of two solid-liquid interfaces connected in series, with the Kapitza heat transfer coefficient

$$h_{K,f} = a_{K,f}\, T_{s,b}^3 \tag{5.131}$$

at the saturated helium temperature $T_{s,b}$, if the interface temperature difference on both sides of the feeding pipe wall is small, which should be the case due to very high thermal conductivity of copper.

Between two phase flow in feeding pipe and vapor flow in the heat exchanger

The thermal conductance between two phase flow in feeding pipe and vapor flow in the heat exchanger is dominated by the heat transfer coefficient of the forced turbulent vapor flow, in case when the flow inside the feeding pipe contains superfluid characterized by very hight thermal conductivity. However this is not the case at high vapor qualities or when helium temperature in the heat exchanger exceeds T_λ - this conditions are not covered by the following description and may be the reason for high value of one of the model parameters - the correction of turbulent vapor flow conductivity, see Section 6.6.

The vapor heat transfer coefficient $h_{v,b}$ is the same as for the heat transfer between the vapor in the exchanger and the bath, see Eq. 5.3.4, and thus the linear density of heat conductance

$$\partial C_{f2bv}/\partial x = h_{v,b}\, P_{o,v,f}\, (T_f - T_{v,b}); \tag{5.132}$$

with the outer perimeter of the feeding pipe in contact with vapor

$$P_{f,o,v} = P_{f,o} - P_{f,s}, \quad P_{f,o,v} \geq 0. \tag{5.133}$$

I do not investigate the corresponding correction of the complex heat pattern in the feeding pipe wall, because the heat transfer coefficients at both walls are now different and may may significantly depending on the vapor mass flow rate, thus developing reliable corrections factors is much more complicated. However, the wetted length is relatively short during typical operating conditions and thus, the complex patterns exist only over the corresponding short lengths.

5.5 Helium mass flow rate at the control valve

The control valve throttles the flow of sub-cooled helium into the the feeding pipe that allows to control the cooling power of the bayonet heat exchanger. During normal LHC operation, the mass flow rate is very small in order of 1-2 g/s, since 1g/s corresponds to approx. 20 W of cooling power. Helium is supplied to the valve from the cryogenic distribution line C, through the sub-cooling heat exchanger, where the helium is cooled against the vapor leaving the bayonet heat exchanger. During normal operation, the temperature of helium arriving at the valve depends on the sub-cooling and variation in in range $T_\lambda(p_{in}) = 2.17\ \mathrm{K} < T_c < 5\ \mathrm{K}$ has been observed. However, it can reach lower values below T_λ if there is enough superfluid He in the phase separator, or much higher up to 100 K if the helium flow was cut for a longer period of time, and thermalization was lost. The upstream pressure at the valve is almost constant in range $2.8\ 10^5\ \mathrm{Pa} < p_{JT,i} < 5\ 10^5\ \mathrm{Pa}$, equal to that in the distribution line, since the pressure drop in the super critical channel of the sub-cooling heat exchanger is very small $\Delta p_{HX,S} < 0.2\ 10^5$ Pa, see (Riddone et al. (2006)). The downstream pressure at the valve has been estimated to be in order of few kPa and is equal to the sum of pressure in the bayonet heat exchanger and the pressure drop over the length of the feeding pipe.

The valve is also called the Joule-Thompson (J-T) valve because it is used to lower helium gas temperature through expansion at higher operating temperatures that occur during the LHC initial cool down phase from ambient temperatures. However, nominal LHC operation the upstream helium flow consists of sub-cooled supercritical helium, that is a quasi-incompressible fluid characterized by positive Joule-Thompson coefficient. Thus the flow warms up during adiabatic expansion at the valve and the control valve does not work as a J-T valve at nominal operating conditions. In contrary, since

The very low downstream pressure at the valve is the reason why the flow at the valve is always choked, since the calculated maximum downstream pressure for choked flow is much higher - in the range 80 kPa - 220 kPa. Thus the pressure drop in the feeding pipe has no impact on the mass flow rate at the valve. The calculations used the condition for choked flow (IEC (1998))

$$p_c - p_{c,o} > F_L^2 \ (p_c - F_F \ p_v), \tag{5.134}$$

with the liquid critical pressure ratio factor $F_F = 0.96 - 0.28 \ p_v/p_{crit}$, the critical pressure $p_{crit} = 227 \ kPa$ and the vapor pressure at inlet temperature $p_v(T_c)$. The pressure recovery factor for the globe valve used $F_L = 0.87$. The norm suggest evaluation of the helium vapor pressure p_v at the upstream temperature T_c, however the helium property is highly temperature dependent and in order to take into account the temperature rise during helium expansion in the valve, the vapor pressure corresponding to saturated liquid helium having enthalpy equal to that of the upstream helium is used

$$p_v = p_{SL}(h = h_c), \ h_c = f(T_c, p_c). \tag{5.135}$$

Thus, the mass flow rate for the turbulent, choked flow does not depend on the downstream conditionsIEC (1998)

$$W_c = 2.78 \ 10^{-5} \ K_V \ F_l \ (\rho_c \ (p_c - F_F \ p_v))^{0.5}, \tag{5.136}$$

with upstream helium density ρ_c.

The control valve has equal-percentage characteristics, thus the flow coefficient should be

$$K_V = K_{VS} \ R^{(x_c - 1)}, \tag{5.137}$$

with valve lift, position, x_c and the valve parameters in the sub-sectors under test: saturation flow coefficient $K_{VS} = 0.11$ m3/h bar and a rangeability $R = 40$. However, model identification indicates that the installed characteristics may slightly deviate from the ideal by few percent and a calibration curve needs to be identified for each valve, see Fig. 5.15.

The valve cutoff position observed during LHC operation

$$x_c = 3.5 \pm 2 \ \%. \tag{5.138}$$

The mass flow rate through the valve, can be controlled in range limited from above by K_{VS}, calculated as being $W_{c,max} \approx 22 \ 10^{-3}$ kg/s, and from below due to limited valve rangeability $W_{c,min} \approx 0.6$ g/s.

Significant offset exists between real x_c and measured $x_{c,measured}$ positions of the valve clapet that appears due to temperature dilatation of valve components at cryogenic temperatures because the valve offset calibration is done at ambient temperature. Thus the real valve lift value is calculated using the correction Δx_c

$$x_c = x_{c,m} - \Delta x_c \tag{5.139}$$

corresponding to measured valve position at closed valve, identified separately for each valve and in the range

$$\Delta x_c = 9.5 \pm 1\%. \tag{5.140}$$

5.6 Subcooling Heat Exchanger

The helium stream entering the valve is sub-cooled in the Sub-cooling heat exchanger against the vapor leaving the bayonet heat exchanger. This improves the overall circuit efficiency and decreases the vapor quality of helium created during the expansion at the valve and in the

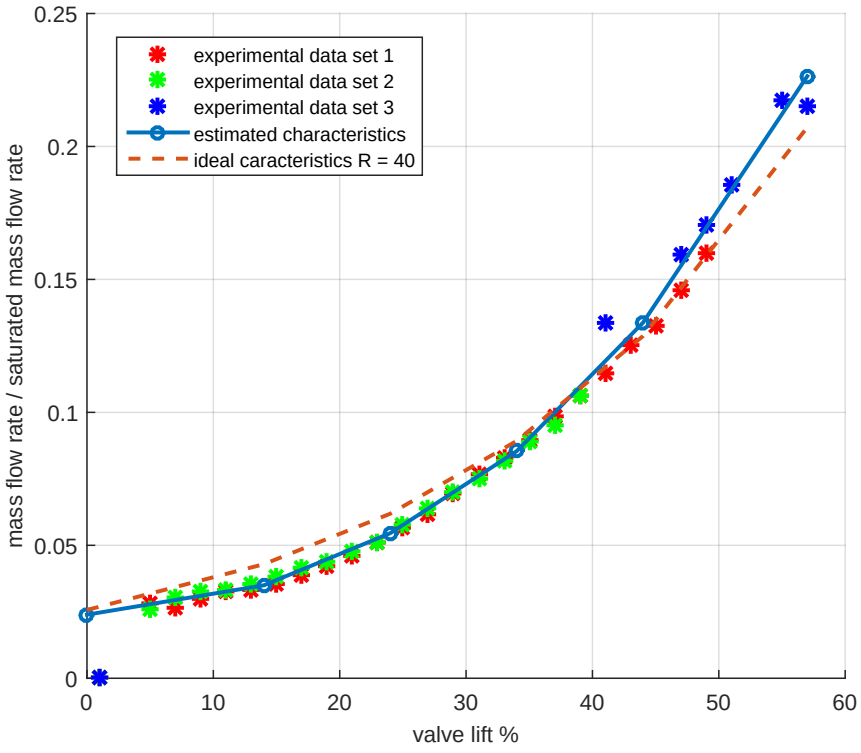

Fig. 5.15 Estimated and ideal valve characteristics

feeding pipe, decreasing the pressure drop. The temperature and pressure of the helium flow at the valve inlet is measured, thus its enthalpy can be directly calculated. When the valve is closed, the valve's inlet temperature rises up to 100K, due to heat loads. Due to the thermal capacity of sub-cooling heat exchanger, after the valve is opened again, time is needed in order to cool down the inlet stream temperature to its nominal temperature. During the transition, only warm vapor helium enters the bayonet heat exchanger thus not only no cooling power is provided, but the magnets are heated from the vapor. Thus the circuit dynamics changes significantly after long closures of the valve, that are avoided during the normal LHC operation.

5.7 Thermo-hydraulic oscillations

A pronounced oscillations of the valve inlet temperature, in range $T_\lambda @ 3bar = 2.17$ K $< T_{JT,in} < 3K$, and helium bath temperature at the wetted zone of heat exchanger have been observed, see figure 5.16. The onset and strength of this oscillation seems to be correlated with tunnel slope and magnets temperatures. The oscillation amplitude and frequency changes with the valve position and magnets temperature. The onset results in slightly reduced cooling power of heat exchanger at fixed control valve lift.

The temperature of the helium at the valve inlet and thus leaving the sub-cooling heat exchanger sub-cooling channel, may vary in function of the sub-cooling heat exchanger inlet temperature, that is quasi-invariant, or mass flow rate - the valve position is invariant, or in function of the vapor channel flow parameters like mass flow rate and inlet temperature, that are not measured.

Looking at the variations of helium bath temperature at the extremity at the wetted zone, close to the feeding pipe outlet, depicted in the figure, it seems that the temperature of the feeding pipe outlet flow is oscillating and periodically warm helium is deposited at the wetted zone. The thermo-hydraulic instability is understood and has not been modelled. One may expect that it originates at slug two phase flow in the feeding pipe or at the thermal conductivity of feeding pipe that varies strongly in function of temperature (very high for superfluid) and vapor quality.

5.8 Dynamics of helium level in phase separator

The circuit is designed to work with partially wetted heat exchanger, so that pure vapor flow leaves the exchanger and the phase separator remains empty. However, helium accumulates in the phase separator during overflow of the bayonet heat exchanger. Modelling of the He II level dynamics allows to deal with the constraints on the maximal helium level in the separator.

The heat transfer between helium in the pipe and that in the phase separator, see Eq. (5.127)

$$q_{f2p}(t) = \begin{cases} 0 & \text{if } m_{l,ps} < 0.2168 \\ W_c\ (h_c - h_{SL}(T_{s,b}(L,t))) & \text{otherwise.} \end{cases} \tag{5.141}$$

The He II mass dynamics in the separator is reflects the mass balance between helium overflowing the heat exchanger into the separator and that evaporating from the separator,

$$\mathrm{d}m/\mathrm{d}t_{l,p}(t) = W_{l,b}(L,t) - (q_{p,l} + q_{f2p})/\Delta_{h,He}, \tag{5.142}$$

taking into account the heat exchange with the feeding pipe q_{f2p} and a constant identified heat load into the separator

$$q_{p,l} = 0.2. \tag{5.143}$$

Helium level in the separator is related to the accumulated helium mass through the separator geometry

$$l_{s,p} = 50\ (1 + 0.5190\ (m_{s,p} - 1.3666) + 0.0602\ \tan(m_{s,p} - 1.3666)). \tag{5.144}$$

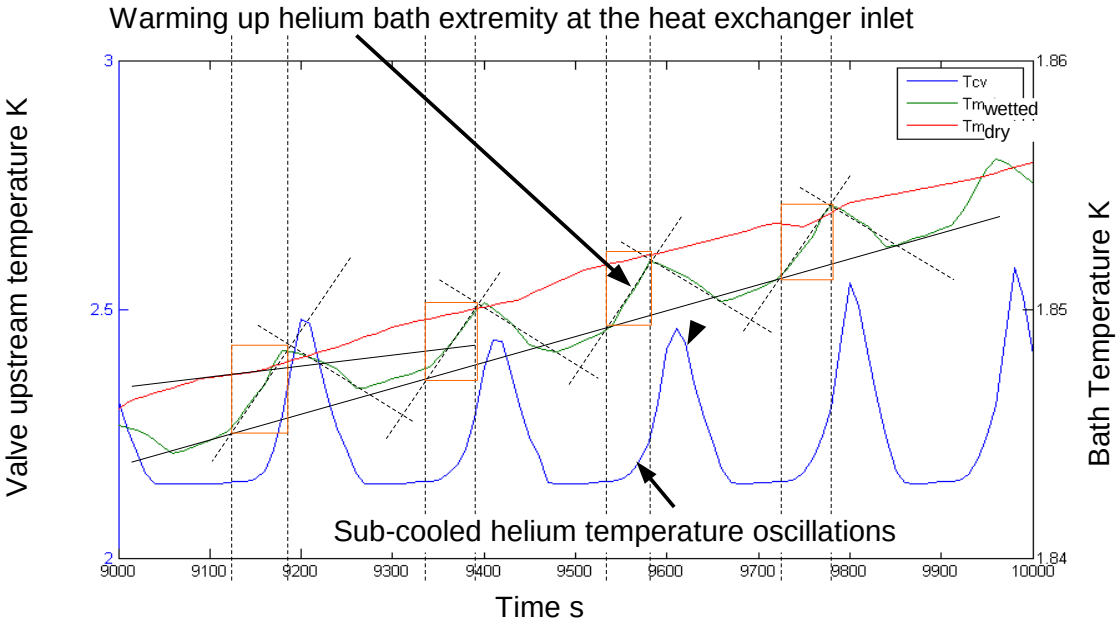

Fig. 5.16 Thermo-hydraulic oscillations at valve inlet and bath around wetted zone.

5.9 Discussion

I have presented description of the dynamic thermo-hydraulic processes that have non-negligible impact on the magnets temperature dynamics over a Sub-Sector from the perspective of a developer of a first principles model for a real-time optimization based advanced control application. The most of the process variables strongly vary along the length of a sub-sector and many are strongly coupled leading to a number of complex two-point boundary problems. Description of the heat transfers originating at the feeding pipe is limited to the case when superfluid is present in the pipe. However simulation results indicate that at high mass flow rates at the valve, the flow temperature may exceed the super-fluid - liquid phase transition temperature, see Fig. 6.14, and thus the description is incomplete.

Chapter 6

Numerical model of temperature dynamics of long strings of LHC magnets

6.1 Purpose, approach and validity

6.1.1 Hard constraint on computational cost of model simulation

The purpose of the model of the helium bath temperature dynamics at a 214 m long sub-sector of the LHC is to enable advanced control of the temperature based on online simulation and optimization, like MHE and NMPC. Thus, the computational cost of the model simulation is constrained by the time available for calculations of control update of the controller and thus the model itself must be simple enough to allow to achieve the real-time feasibility of the optimization. Here, "real-time" means that the optimization is performed at a rate that matches that of the real control system.

Many simulations using the model are performed in each step of the model-based optimization and thus the system dynamics must be simulated at a rate much faster than the real system, in order to enable the real-time optimization. In fact, it is the low combined computational cost of optimization algorithm and the simulations, that enables the real-time feasibility. Thus application of system-tailored, simplified optimization algorithms characterized by lower computing cost and careful model implementation allows me for a relatively complex model.

6.1.2 Model simplifications based on analysis of dynamics and control goals

The analysis of both the actual and simulated system dynamics, presented in previous chapter, is the key in the decision process about what physical processes and to which extent will be

represented in the model in order to capture all the key characteristics of the system dynamics with acceptable errors enabling high quality performance of advanced controls while keeping the model's computational complexity low enough to enable fast simulation needed in the real-time optimization.

The modelling approach and model validity range are chosen based on the analysis of the dynamics and the goals of the controller. As demonstrated in Section 2.5 and explained in previous chapter, the distributed nature of the 214 m long system and the unique properties of superfluid are the key factors behind the complex system dynamics and cannot be neglected. Thus a first-principles distributed-parameters model will be developed, where the helium bath temperature and other key variables, related to various helium mass and heat transfers, are represented as distributed along the system length.

The analysis of the magnets temperature dynamics indicates that: 1) helium penetration inside the heat exchanger is small in wide range operating conditions due to the very high thermal conductance of the heat exchanger wall and thus the section of the exchanger where superfluid and vapor co-exist is relatively short, allowing to neglect the interfacial frictional shear force between the phases and 2) heat transfer originating at the feeding pipe must be modelled in order to reproduce the inverse response observed at higher temperature gradients, 3) helium mass accumulation in the feeding pipe must be modelled to represent some of important modes of the magnet temperature dynamics.

6.1.3 Model inputs and outputs

Inputs and outputs of the model have been chosen as those that allow to realize the control strategy presented in following Chapter, based on the system analysis. The model outputs, corresponding to the cooling process controlled variables, are: 1) the distributed helium bath temperature, at the model discretization mesh $1.77\ \text{K} \leq T_h \leq 2.1\ \text{K},\ T_h \in \mathbb{R}^{28}$ and at the positions corresponding to the location of the thermometers $T_{h,@TT} \in \mathbb{R}^{16}$, 2) the superfluid He II levels in the phase separators $0\ \text{m} \leq l_p \leq 0.2\ \text{m},\ l_p \in \mathbb{R}^2$, 3) the superfluid He II mass flow rate at the heat exchanger outlets $0\ \text{kg/s} \leq W_{b,s}(L),\ W_{b,s}(L) \in \mathbb{R}^2$. The model inputs correspond to the system manipulated variables: 1) estimated helium mass flow rate at the control valves, closely related to the positions of the control valves $0\ \text{kg/s} \leq \hat{W}_c \leq 5\ 10^{-3}\ \text{kg/s},\ \hat{W}_c \in \mathbb{R}^2$ 2) power of the cryogenic electric heaters $0\ \text{W} \leq q_{h,EH} \leq 25\ \text{W},\ q_{h,EH} \in \mathbb{R}^{12}$, the key measured perturbations such as 3) enthalpy of helium at the control valves $h_c \in \mathbb{R}^2$, calculated using measured He temperature in the valves at the sub-sector and pressure in the line C at the sub-sector and the key unmeasured perturbations: 4) estimated pressure in the cryogenic distribution line B at the sub-sector, approx. equal to pressure at the outlet of the bayonet heat exchanger $1.77\ \text{K} \leq \hat{T}_{s,b}(L) \leq 2.1\ \text{K},\ \hat{T}_{s,b}(L) \in \mathbb{R}^2$ and 5) estimated linear density of heat

load into the helium bath $\mathrm{d}\hat{q}/\mathrm{d}x_{h,l} \in \mathbb{R}^1$. The fact that we do not include magnet currents as important measured perturbations is only due to the fact that the current feed-forward action is not implemented into the proof of concept setup because it was not meant to be tested at the LHC during magnets powering.

6.1.4 Model validity

The model validity range corresponds to the full LHC operational range with beam in a very wide range of heat loads and saturation temperatures in the heat exchanger. The lower bath and saturation temperature limit at 1.77 K corresponds to He saturation temperature at lowest pressure in the bayonet heat exchanger $p_{b,min} = 1.4$ kPa. An interlock system is programmed to dump the beam and switch off the current in the LHC magnets if the bath temperature rises over 2.1 K, see section 2.5. Regarding the two phase flow in the heat exchanger, I limit the model validity to the stratified flow without atomisation range to neglect the case when the interface between the phases is not continuous. I implement this approximatively by limiting the helium mass flow rates at the control valve

$$W_c \leq 5\ 10^{-3}\ \mathrm{kg/s} \tag{6.1}$$

that covers full range of typical operational conditions with He II. This limitation of the model validity range also decreases the numerical cost of simulation because speed of some dynamic modes related to the helium mass transfer is proportional to the helium mass flow rate and thus stiffness increases with the mass flow rates. Further limitation of model validity is due to the fact that neglects the important shear friction force at the superfluid-vapor interface in the heat exchanger. This simplification is applied based on the observation sections where superfluid and vapor coexist are fairly limited due to short wetted length of the heat exchanger at most operating conditions, also in case when weak saturation effects occur. Thus the model validity may be compromised due to this simplification when strong saturation effects occur, especially at higher vapor mass flow rates.

6.2 First-principles modelling at low computing cost

Low computational cost of the model simulation is the main design parameter of the model having the key impact on the modelling process. In the following, I discuss important issues that must be addressed during the modelling process in order to optimize the model for low computational speed of simulation.

6.2.1 1-D spatial discretization grid

The number of ODEs produced during spatial discretization of a PDE is defined by the number of the discretisation parameters, in our case the discretization points, that is affected by the the number of spatial dimensions modelled and the density of the discretization grid. Then, temporal discretisation transforms each infinite-dimensional ODE into a finite set of points in time at which the ODE's solution is calculated.

In order to lower the number of ODEs, one-dimension (1-D) representation of the system used in the distributed-parameters model. This simplification significantly reduces the computational complexity and is justified by large ratios between length and diameter of the circuit components: 214 m/0.57 m = 375 in case of the helium bath, 107 m/0.054 m = 2000 in case of the bayonet heat exchanger and 107/0.012= 9000 in case of the feeding pipe.

Three commonly used spatial discretization methods are the finite element method (FEM), finite volume method (FVM) and finite difference method (FDM). In the 1-D case, the three discretization methods are equivalent if first order approximations are used, the difference being the physical interpretation of the discrete variables. In model describing the conservation laws, the finite volume approach providing the most intuitive interpretation is preferred.

The number of the finite volumes, or spatial discretization steps, N_x is a very important parameter of the discretization, as its choice represents the trade off between the modelling errors and the computational complexity. As the number of the discretization points increases, the model precision increases too however also its computational cost of simulation increases significantly. The computing cost related to the solution of the ODE's increases with rising number of discretization points because: 1) the size of the ODE set rises and 2) the number of time steps needed for the system dynamics integration rises, if an explicit solution method is applied to the ODE's. The latter is related to the maximal time step length guarantying convergence of the ODEs numerical integration using explicit numerical method, that is inversely proportional to the N_x.

The value of $N_x = 28$ per length of 214 m long sub-sector of the circuit has been chosen as the one that: 1) represents excellent balance between the simulation errors and computing cost, 2) allows to adjust the discretization grid to the physical dimensions of the repetitive structure of the LHC magnets string. The simulation errors were assessed with respect to reference values being results of simulations using models with higher values of N_x. Thus, the spatial discretization step varies

$$\Delta x_i = \begin{cases} 7.83 \text{ m} & \text{if } i \in I_{MB}, \\ 6.47 \text{ m} & \text{if } i \in I_{SSS}, \end{cases} \tag{6.2}$$

corresponding to half of the length of a cryo-dipole (MB) and full length of an Short Straight Section (SSS), see Fig. 6.1. The magnets arrangement in a standard call and thus the content

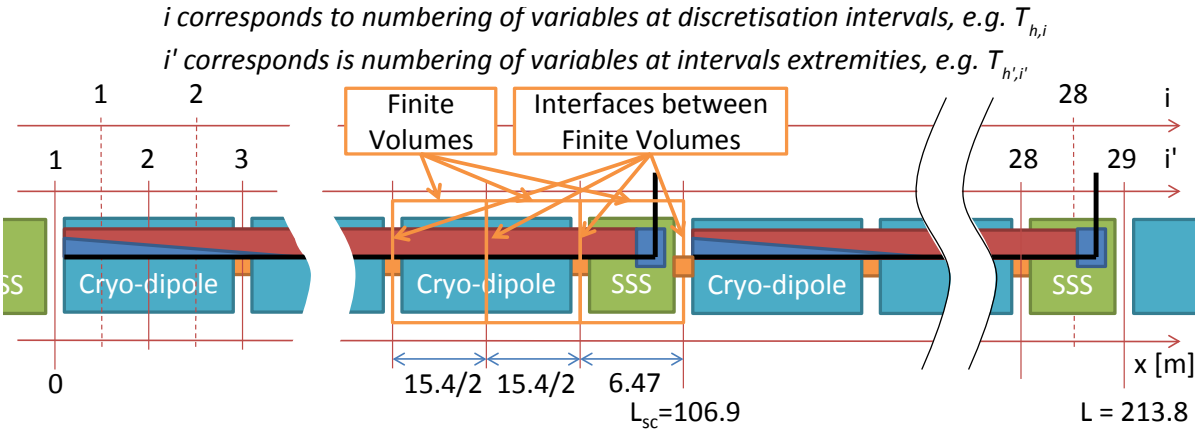

Fig. 6.1 Model discretization scheme

of the sets I_{MB} and I_{SSS} depend on sign of the LHC tunnel slope, varying with a standard cell location along the LHC tunnel. The spatial discretization grid is common for the models of the helium bath, bayonet heat exchanger and the feeding pipe. Please note that Blanco (2001) in his model used spatial discretization step corresponding to each magnet.

6.2.2 Iterative solution of algebraic equations

In order to significantly decrease the computational cost of solving DAE improve the robustness of model simulation, the algebraic equations are solved using iterative approach trading off the solution accuracy against the computing cost. This is done via 1) introduction of artificial dynamics in order to "break" the algebraic loops, replacing the algebraic equations by additional ODE's having the steady-state solution identical with that of the replaced one, ODE's can be simulated more robustly and at much lower computing cost than the original DAEs and 2) introduction of tearing variables, where the original implicit expression is approximated as an explicit using variables from a preceding simulation step, thus allowing to unroll a loop and convert it into a sequence of expressions that can be evaluated explicitly at low computing cost.

6.2.3 Numerically solving stiff ODEs

The cryogenic system dynamics is strongly stiff, because it contains some very slow temperature dynamics of the massive helium bath and some very fast dynamics related to local heat transfer in He II and heat and mass transfers in the system. In fact the, some modes of the bath temperature dynamics approach infinite speed as the temperature gradients approach zero, due to extraordinary heat transport properties of He II.

In order to simulate the system dynamics at low computational cost, I must limit the stiffness altering the description of the physical processes in the way that slows down the dynamics of fastest variables, as explained later in this chapter. Then, an explicit solver may be used to integrate the moderately-stiff dynamics at very low computational cost. This approach is demonstrated by a simple numerical study performed in MATLAB®, presented in Figure 6.2, where the original stiff and altered moderately-stiff dynamics of distributed helium bath temperature are simulated using variable step 2nd order explicit ode23 and implicit ode23s

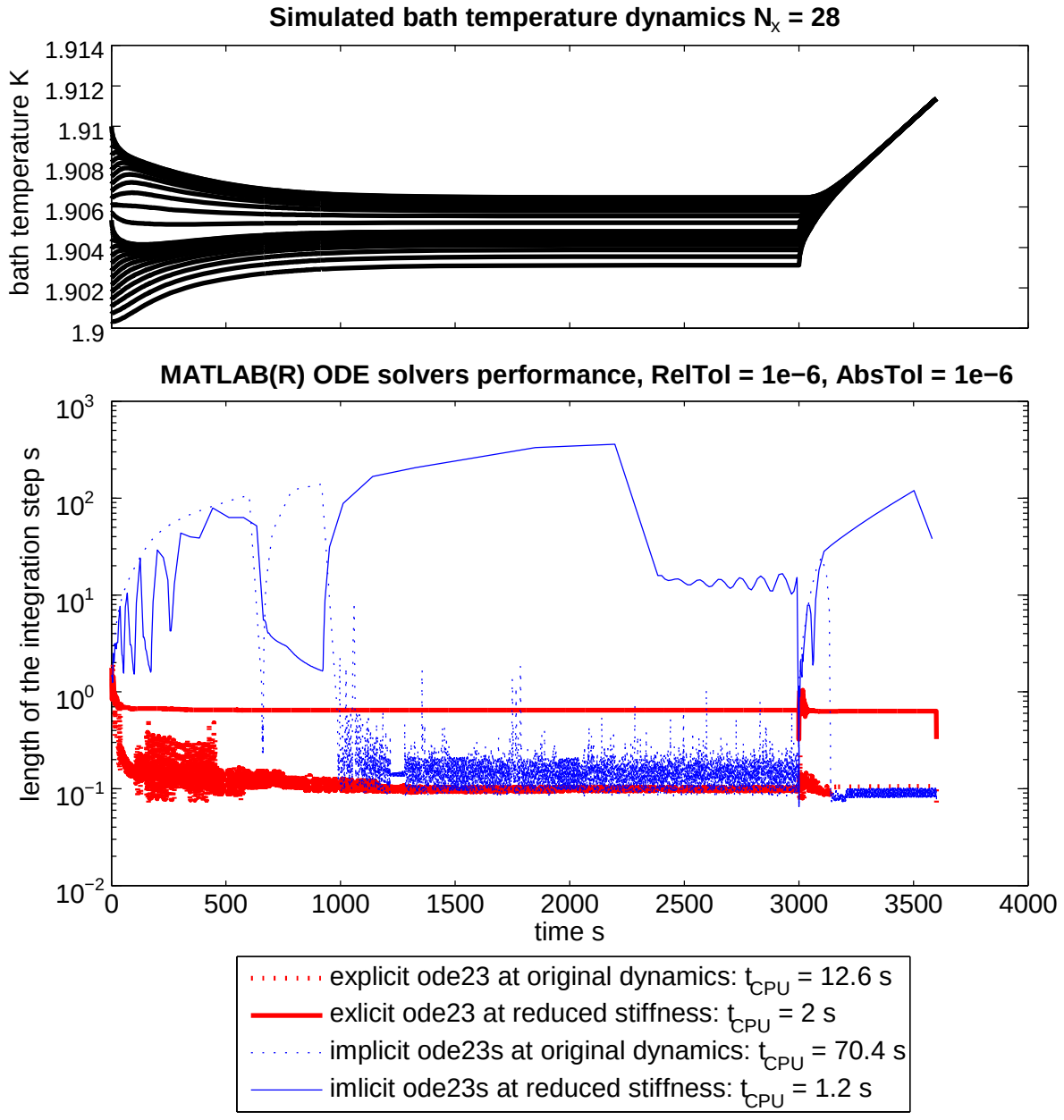

Fig. 6.2 Implicit vs. explicit ODEs integration, with and without stiffness reduction.

solvers, with the same absolute and relative error tolerance of 10^{-6}. In case of the stiff dynamics, the explicit solver is forced to integrate with very small step in order of 0.1 s and needs 12.6 s to perform the simulation. The implicit solver takes steps of strongly variable length ranging from 0.1 s to 100 s. In case of the dynamics after the stiffness reduction, the step length has been increased and thus the computational time has been reduced considerably to 2 s. The implicit solver takes even much larger steps but due to computational complexity related to each step, the simulation takes 1.2 s.

I have decided to use explicit Euler method to integrate the moderately stiff modelled dynamics robustly at very low computational cost. The Euler method is the most basic explicit method for numerical integration of ordinary differential equations and is the simplest Runge-Kutta method. The fixed step method has been chosen as low computing cost is much more valuable than the exact satisfaction of an arbitrary accuracy. However, this implies that the dynamic modes of the model must be precisely analyzed and fastest modes limited in order to achieve fast and convergent simulation. It is a first-order method, where the error per step is proportional to the square of the step size and the global error is proportional to the step size. The suitability of the first order method for the simulation of the moderately stiff dynamics at low computational cost is two fold: 1) for the fastest modes of the stiff dynamics, it is more accurate at relatively coarse time discretization than higher order methods, 2) for slower modes, the time step is relatively very small anyway, resulting in negligible absolute error.

In order to further reduce the computational cost of simulation of the stiff dynamics, the model variables that evolve much slower than others are evaluated much less frequently, i.e. 100 times, than the fast changing ones. Attention has been paid to maximally optimize the computing cost of the frequently evaluated expressions.

6.2.4 Simplifications and approximations

The art of development of a very fast, first principles model, is based on the ability to use as many simplifications as possible, compromising the model accuracy as much as is still acceptable to accurately represent the key aspects of system dynamics. On-line linearization is used if a function is particularity computational costly to evaluate - the linearization is performed during simulation but at much slower rate than the function evaluation, allowing to significantly decrease the computational cost. Precise definition of range of operational conditions in the model validity region is the starting point for the simplifications and thus for the whole modelling process. Careful analysis of the system dynamics in the validity region, allows for model simplifications by neglecting the processes and variables with little impact on model dynamics of interest.

Geometries, physical laws and material properties are also expressed using simplified approximate expressions characterized by low computational cost and valid in a previously defined range of operational conditions. *The key to the model low computing cost is complete absence of computationally expensive on-line interpolation from 2-D or 3-D tables describing the physical properties of materials* like helium. The base for majority of those approximations are the physical properties of helium originating at helium fundamental state equations from the world reference for the helium properties by Arp and McCarty (1989) and taken from HEPAK v3.4, the helium property computer program developed by (CRYODATA INC. (1999)).

6.3 Formulation of dynamic model with 262 state variables

The formulation of numerical model of the magnets temperature dynamics and other variables crucial for the advanced controller is presented in this section. The formulations are derived from the description provided in Chapter 5, frequently approximated or modified to reduce the computational cost of model simulation.

6.3.1 Temperature dynamics of superfluid helium bath

The numerical model of the bath temperature dynamics is a result of spatial discretisation of the PDE describing energy conservation in the bath. Using the interpretation corresponding to finite volume approach, see subsection 6.2.1, the dicretization transforms the PDE it into a set of ODEs describing the energy conservation in a finite volume, with the average temperature dynamics in each of N_x finite volumes

$$\mathrm{d}T_{h,i}(t)/\mathrm{d}t = c_{v,i}^{-1}\ \Delta q_{h,i}/\Delta M_{h,i}, \quad i = \{1...N_{x,h}\}, \tag{6.3}$$

where $\Delta M_{h,i}$ is the helium bath mass and $\Delta q_{h,i}$ is the sum of heat loads over an i-th finite volume. The heat balance over i-th discretisation interval

$$\Delta q_{h,i}(t) = \Delta q_{l,i} - \Delta q_{c,i} + q_{h',s,i} - q_{h',s,i+1}, \quad i = \{1...N_x\}, \tag{6.4}$$

involves transversal heat loads $\Delta q_{l,i}$, cooling power $\Delta q_{c,i}$ and the difference of longitudinal heat transfer in the He II bath at extremities of discretization intervals $q_{h',s,i} - q_{h',s,i+1}$, corresponding to the divergence of the longitudinal heat transfer.

The bath is discretized in

$$N_{x,h} = 28 \tag{6.5}$$

finite intervals of similar but varying length, as described in previous section.

Specific heat capacity of superfluid

The inverse of the specific heat

$$1/c_{v,h,i} = 7.9936 \times 10^{-3}\ T_{h,i}^{-5.7874} + 0.1230 \times 10^{-3}\ (2.15 - T_{h,i})^{0.5234}\ \text{kg K/J}, \quad i = \{1...N_{x,h}\} \tag{6.6}$$

is approximated using simple expression introduced in previous chapter, very closely matching the values from HEPAK.

Mass distribution of superfluid

The superfluid mass distribution along the bath is complex, but since the spatial discretisation grid used in the model is coarse, corresponding to the length of SSS or half of the length of the cryo-dipole and thus precise knowledge of the helium mass distribution along each component is not necessary. The ratio of measured volumes of the helium vessels of cryo-dipole and SSS, see Section 5.2.3

$$V_{SSS,measured}/V_{MB,measured} = 0.62 \tag{6.7}$$

and a reasonable value of estimated mass of helium in the bath based on Table 5.1

$$M_h = 875\ \text{kg}. \tag{6.8}$$

Thus the estimated value of mass in the short straight sections and in the cryo-dipoles

$$M_{h,MB} = 60.428\ \text{kg}, \quad M_{h,SSS} = 37.466\ \text{kg} \tag{6.9}$$

that solve

$$(4\ V_{SSS,measured}/V_{MB,measured}\ + 12)\ M_{h,MB} = M_h. \tag{6.10}$$

The mass of the discrete parts of the modelled helium bath at segments corresponding to SSS $i \in \mathscr{I}_{SSS}$ and cryo-dipoles $i \in \mathscr{I}_{MB}$

$$\Delta M_{h,i} = \begin{cases} M_{h,SSS}, & \text{if } i \in \mathscr{I}_{SSS} \\ M_{h,MB}/2, & \text{otherwise (if } i \in \mathscr{I}_{MB}), \end{cases} \tag{6.11}$$

with the sets of indices I_{SSS}, I_{MB} corresponding to discretized short straight sections and cryo-dipoles, respectively.

6.3.2 Heat transfer in superfluid with stiffness reduction

As discussed in previous chapter, see Eq. (5.21), the heat transfer in superfluid at interfaces between the discretization intervals may be formulated as

$$q_{h',s,i} = -k_{h',s,i}\, A_{h',s,i}\, (\mathrm{d}T/\mathrm{d}x)_{h',i}, \quad i = \{2...N_{x,h}\} \tag{6.12}$$

with the effective heat conductivity

$$k_{h',s,i} = \mathrm{F}_{\mathrm{adjusted}}(T_{h',i})^{1/3.4}\, |(\mathrm{d}T/\mathrm{d}x)_{h',i}|^{1/3.4-1} \tag{6.13}$$

that strongly varies in function of temperature gradients, approaching infinity as they vanish.

During identification tests at higher temperatures smaller temperature gradients are observed than those initially simulated. In order to take this into account, to two model corrections may be introduced, 1) correct the bath heat conductivity if function of the temperature, applied in this model

$$\mathrm{F}_{\mathrm{adjusted}}(T_{h',i}) = (1 + c_{q_{h,s}}\, (T_{h',i} - 1.9))\, F(T_{h',i}), \quad c_{q_{h,s}} = 0.8545, \tag{6.14}$$

or 2) add temperature dependent heat load at to the bath. The value of the correction has been optimized, see Section 6.6. It has no physical meaning and the true reason for the correlation between the magnets temperature gradients and their temperature needs further investigation.

Due to hydraulic plus installed at the extremities of the helium bath

$$q_{h',s,i} = 0, \quad i = \{1, N_x + 1\}, \tag{6.15}$$

representing boundary conditions. At the interface between discrete volumes, the temperature gradient is approximated as

$$(\mathrm{d}T/\mathrm{d}x)_{h',i} = (T_{h,i} - T_{h,i-1})/\Delta x_{h',i}, \quad i = \{2...N_{x,h}\} \tag{6.16}$$

and the bath temperature is approximatively interpolated as

$$T_{h',i} = (T_{h,i} + T_{h,i-1})/2, \quad i = i' = \{2...N_x\}. \tag{6.17}$$

Stiffness analysis

The impact of the thermal conductivity on the dynamics of the magnets temperatures is clear after substitutions and rearranging

$$\begin{aligned} \mathrm{d}T_{h,i}(t)/\mathrm{d}t \sim c_{v,i}^{-1}\ \Delta M_{h,i}^{-1}\ (&T_{h,i-1}\ k_{h',s,i}\ A_{h',s,i}/\Delta x_{i'} \\ &- T_{h,i}\ (k_{h',s,i}\ A_{h',s,i}/\Delta x_{h',i} + k_{h',s,i+1}\ A_{h',s,i+1}/\Delta x_{h',i+1}) \\ &+ T_{h,i+1}\ k_{h',s,i+1}\ A_{h',s,i+1}/\Delta x_{h',i+1}), \quad i = \{2...N_{x,h}-1\}. \end{aligned} \tag{6.18}$$

The linearized temperature dynamics in the matrix form representation

$$\mathrm{d}[T_{h,1}(t)\cdots T_{h,N_x}(t)]^T/\mathrm{d}t = A_{dT/dt}\ [T_{h,1}(t)\cdots T_{h,N_{x,h}}(t)]^T + \ldots \tag{6.19}$$

Now, assuming for a moment for the sake of simplicity of this analysis that $T_{h,i-1}\ k_{h',s,i}\ A_{h',s,i} \approx k_{h',s,i+1}\ A_{h',s,i+1}/\Delta x_{h',i+1}$, the maximal eigenvalue corresponding to the speed of the fastest mode of the linearized temperature dynamics

$$\lim_{N_x\to\infty} \max(eig(A_{dT/dt})) = \max(1/\tau_{dT/dt}) \approx -4\ c_{v,i}^{-1}\ \Delta M_{h,i}^{-1}\ k_{h',s,i}\ A_{h',s,i}/\Delta x_{h',i}. \tag{6.20}$$

Since the speed of fastest mode of the temperature dynamics $\max(1/\tau_{dT/dt})$, with time constant $\tau_{dT/dt}$, is proportional to the heat conductivity, it approaches infinity while the temperature gradients vanish in the bath. Simultaneous presence of the very fast modes and other much slower modes corresponding to very slow average temperature dynamics represent very strong stiffness of the ODE set that makes the numerical simulation costly, because the time step of the simulation must be relatively small to cope with the fastest modes and the simulation length must be sufficiently long to represent the evolution of the slowest modes. In the case of the explicit forward Euler method used to integrate the modelled dynamics, the convergence condition for the numerical solver is that the time constant of the fastest dynamics

$$\min(\tau) \geq \Delta t_{FE}/2 \tag{6.21}$$

with the temporal discretization, or integration step Δt_{FE}.

Stiffness reduction

In order to reduce the computational cost of simulation, I limit the stiffness by limiting the maximal value of effective heat conductivity of superfluid to

$$k_{h',s,i} \leq k_{h',s,max,i}, \quad i \in \{2...N_{x,h}\}, \tag{6.22}$$

$$k_{h',s,max,i}\, A_{h',s,i} = -0.25\ \max(1/tau_{dT/dt})_{design}\, \Delta x_{i'}\ (\ c_{v,i-1}\, \Delta M_{h,i-1} + c_{v,i}\, \Delta M_{h,i}), \tag{6.23}$$

where the speed of fastest mode present in the modelled dynamics

$$\max(1/tau_{dT/dt})_{design} = 1/\Delta t_{FE} \leq 2/\Delta t_{FE} \tag{6.24}$$

is a model design parameter that guarantees the convergence of the explicit solver at a temporal integration interval chosen to express the tradeoff between the the computational cost of simulation and modelling and simulation errors.

This leads to a modified version of the correlation for heat transfer in superfluid, suitable for numerical simulations, that allows to reduce the extreme stiffness introduced by the nonlinearity present in the original correlation

$$q_{h',s,i} = \begin{cases} -k_{h',s,i}\, A_{h',s,i}\, (\mathrm{d}T/\mathrm{d}x)_{h',i}, & \text{if } k_{h',s,i}\, A_{h',s,i} < k_{h',s,max,i}\, A_{h',s,i} \\ -k_{h',s,max,i}\, A_{h',s,i}\, (\mathrm{d}T/\mathrm{d}x)_{h',i}, & \text{otherwise} \end{cases}, \quad i = \{2...N_{x,h}\}. \tag{6.25}$$

Effective cross-section for longitudinal heat transfer in superfluid

In the model, the cross-section of helium bath for the longitudinal heat transfer at a finite volume interface $A_{h',i}$ may take only 4 different values, corresponding to interfaces located at: 1) the interconnections between cryo-dipole and SSS, 2) between SSS and cryo-dipole, 3) between two cryo-dipoles and 4) inside a dipole. Values of these model parameters are presented in Table 5.2 and have been estimated as described in Section 6.6.4.

6.3.3 Heat loads into helium bath

Thus I model the heat load into the bath over i-th spatial discretization interval

$$\Delta q_{h,l,i} = \Delta q_{h,l,s,i} + \Delta q_{h,l,d,i}, \quad i = \{1...N_{x,h}\}, \tag{6.26}$$

with a constant static base load component $\Delta q_{h,l,s,i}$ and a dynamic component $\Delta q_{h,l,d,i}$ accounting for any variation of the static heat load and sum of all dynamic and transient heat loads.

Static heat load component

The base load component is nor equal along the bath due to different static heat loads into the bath at segments corresponding to SSS $i \in \mathscr{I}_{SSS}$ and cryo-dipoles $i \in \mathscr{I}_{MB}$ and to locations exposed to additional heat loads at jumper interconnections $i \in \mathscr{I}_{jumper}$ and vacuum barriers $i \in \mathscr{I}_{barrier}$

$$\Delta q_{h,l,s,i} = \begin{cases} q_{h,SSS} & \text{if } i \in \mathscr{I}_{SSS} \setminus \mathscr{I}_{jumper} \setminus \mathscr{I}_{barrier} \\ q_{h,SSS} + q_{h,jumper} & \text{if } i \in \mathscr{I}_{jumper} \setminus \mathscr{I}_{barrier} \\ q_{h,SSS} + q_{h,jumper} + q_{h,barrier} & \text{if } i \in \mathscr{I}_{barrier} \\ q_{h,MB} & \text{if } i \in \mathscr{I}_{MB} \end{cases}, \quad i = \{1...N_{x,h}\} \tag{6.27}$$

with the model parameters calculated based on the design values of static heat loads

$$q_{h,MB} = 2.60 \text{ W}, \; q_{h,SSS} = 2.05 \text{ W} \tag{6.28}$$

and optimized model parameters

$$q_{h,jumper} = 0.39 \text{ W } (0.12\text{W}), \; q_{h,barrier} = 4.15 \text{ W}(0.42\text{W}), \tag{6.29}$$

with design values in the parenthesis. The optimized heat load at the vacuum barrier is much higher than the design value and needs further investigation.

Dynamic heat load component

Assuming that heat load density of the dynamic component $\partial q_{h,l,d}/\partial x$ is uniform over the bath length, the discretized dynamic heat load component

$$\Delta q_{h,l,d,i} = \partial q_{h,l,d}/\partial x \, \Delta x_i, \quad i = \{1...N_{x,h}\}. \tag{6.30}$$

It represents an unmeasured model input and thus a perturbation to the system. A nonlinear, recursive, numerical filter based on the model is used to estimate the actual value of $\partial q_{h,l,d}/\partial x$ in wide range of operational conditions, as described later.

6.3.4 Cooling power of bayonet heat exchanger

In case of stratified two-phase flow, where the superfluid phase stratifies at the bottom of the heat exchanger, the linear density of cooling power of the heat exchanger averaged over a i-th spatial discretization interval

$$(\partial q_c/\partial x)_i = (\partial q_{h2bs}/\partial x)_i + (\partial q_{h2bv}/\partial x)_i, \text{ with} \tag{6.31}$$

$$(\partial q_{h2bs}/\partial x)_i = \begin{cases} (T_{h,i} - T_{s,b,i})\ (\partial C_{th,h2bs}/\partial x)_i & \text{if } T_{h,i} \geq T_{s,b,i} \\ 0 \quad \text{otherwise.} \end{cases} \tag{6.32}$$

$$(\partial q_{h2bv}/\partial x)_i = (T_{h,i} - T_{v,b,i})\ (\partial C_{th,b,v}/\partial x)_i, \quad i \in 1..N_{x,b}. \tag{6.33}$$

It is the sum of heat transfers from the static He II bath, via the oxygen-free copper wall of the exchanger to the two phases: superfluid He II q_{h2bs} and vapor q_{h2bv}. The heat transfer from the helium bath to the superfluid is one-directional if condensation is neglected and it can onlly be received by the boiling helium. Other variables are: average temperatures of saturated superfluid $T_{s,b,i}$ and vapor $T_{v,b,i}$, average linear densities of the thermal conductances corresponding to the heat flows $(\partial C_{th,h2bs}/\partial x)_i$ and $(\partial C_{th,h2bv}/\partial x)$, respectively.

The heat exchanger is modelled using the same discretization mesh as the one used for the helium bath. Since typically two heat exchangers are installed per each helium bath, the number of discretization points of the heat exchanger

$$N_{x,b} = N_{x,h}/2 = 14. \tag{6.34}$$

The average linear density of thermal conductance between the helium bath and the superfluid flow in the heat exchanger is limited by the Kapitza resistance and thus

$$(\mathrm{d}C_{th,h2bs}/\mathrm{d}x)_i = 0.5\ P_{b,s,i}\ c_{P_{b,s,i}}(P_{b,s,i})\ a_K\ T_{s,b,i}^3, \quad i = \{1...N_{x,b}\}, \tag{6.35}$$

with the approximation using a fit characterized by low computing cost

$$P_{b,s,i}\ c_{P_{b,s,i}}(P_{b,s,i}) = \begin{cases} 0.3077\ A_{b,s,i}^{0.2888} & \text{if } A_{b,s,i} \geq A_{b,s,min,i} \\ 0.3077\ A_{b,s,i}\ A_{b,s,min,i}^{-0.7112} & \text{otherwise,} \end{cases} \tag{6.36}$$

with the variable

$$A_{b,s,min,i} = (2.967 \times 10^{-7}\ a_{K,f,i}\ (0.3\ |T_{h,i} - T_{s,b,i}| + 0.28\ |T_{f,i} - T_{s,b,i}|)\ \Delta t_{INT,max})^{1.4} \tag{6.37}$$

introduced to reduce the stiffness of the corresponding helium mass dynamics, introduced by the ratio between the wetted perimeter, limiting the heat transfer into the superfluid, and the chord, corresponding to free surface of superfluid flow, that increases at vanishing values of $A_{b,s}$.

The heat conductance between helium bath and the helium vapor

$$(\partial C_{th,h2bv}/\partial x)_i = h_{v,b,i}\, P_{b,v,i}, \quad i = \{1...N_{x,b}\}, \tag{6.38}$$

is limited by the the heat transfer coefficient for the forced convection, see Eq. (5.57), that may be approximated at lower computing cost as

$$h_{v,b,i} = c_{q,v,b}\, (1.0198\, T_{s,b,i}^{3.2276} - 2.3191)\, 248.6\, \rho_{v,b,i}^{0.8}\, |W_{v,b,i}|^{0.8} \tag{6.39}$$

with constant correction factor $c_{q,v,b}$ introduced to adjust simulation results with experimental data, presented in Section 6.6, and heat exchanger tube perimeter in contact with the vapor

$$P_{b,v,i} = P_{i,b} - P_{b,s,i}, \quad P_{b,v,i} \geq 0. \tag{6.40}$$

The cross-section of heat exchanger occupied by superfluid helium corresponds to the helium mass distribution and is found using mass, momentum and energy conservation principles. I use a 1-D Saint Venant-type approach - a macroscopic approach based on engineering correlations suitable for the model discretized with large spatial step of few meters. Original Saint Venant equation describes open channel flow. Application of a full first-principles microscopic approach, namely Navier-Stokes equations with an appropriate turbulence models would need a much much finer spatial discretization grid and thus is not suitable for the model aiming at a very small computational cost of simulation.

The mass conservation in the superfluid is described by Eq. (5.58). Discretizing using the Reynolds transport theorem, the dynamics in an i-th finite volume

$$\mathrm{d}A_{b,s,i}/\mathrm{d}t = 1/\rho_s\, (W_{s,b',i} - W_{s,b',i+1})/\Delta x_i - (\mathrm{d}W_{e,b}/\mathrm{d}x)_i, \quad i = \{1...N_{x,b}\}, \tag{6.41}$$

with superfluid mass flow rate at extremities of discretization intervals $W_{s,b',i}$.

The evaporation rate of the saturated helium is proportional to heat input

$$(\mathrm{d}W_{e,b}/\mathrm{d}x)_i = (\mathrm{d}q_e/\mathrm{d}x)_i/\Delta_H, \quad (\mathrm{d}W_{e,b}/\mathrm{d}x)_i \geq 0 \tag{6.42}$$

that must be non-negative if condensation is neglected. With the latent heat of evaporation of He II

$$\Delta_H = 23.4\ 10^3\ \text{J/kg}. \tag{6.43}$$

The evaporation heat input is found based on the static form of energy conservation for the saturated He II flow, neglecting longitudinal heat transfers,

$$(\mathrm{d}q_e/\mathrm{d}x)_i = (\mathrm{d}q_{h2bs}/\mathrm{d}x)_i + (\mathrm{d}q_{f2bs}/\mathrm{d}x)_i \tag{6.44}$$

with the heat loads from the bath q_{h2bs}, Eq. (6.32), and the feeding pipe q_{f2bs}, Eq. (6.102).

Superfluid mass flow rate distribution

The He II mass flow rate distribution along the tube is found using momentum conservation. I neglect most of the terms in the momentum conservation Eq. (5.63), because they have either marginal values or appear in limited conditions range. The latter case corresponds to the shear friction force at the superfluid-vapor interface, that plays no role in most typical operational conditions when the wetted length of the heat exchanger is very small. Momentum flux and part of the hydrostatic force related to the flow depth gradient cannot be simulated at the coarse discretisation grid, thus momentum-based delay of superfluid propagation is not represented. I also neglect the impact of boundary conditions corresponding to the momentum conservation at the heat exchanger inlet and, in case of tunnel slopes corresponding to sub-critical flows, at the outlet. This is justified by the very large factor between the heat exchanger length and depth of the superfluid flow limiting the influence of the boundary conditions on the flow. Anyway, as we will see in the next chapter, due to high thermal conductivity of the heat exchanger tube, it is the slowly changing He II evaporation rate that determines the He II propagation along the heat exchanger and in fact He II penetrates very little inside the heat exchanger at typical operational conditions and thus exact modelling of the momentum is not necessary. The errors are apparent only at lowest bath temperatures when saturation effects promote helium accumulation in the heat exchanger.

The relation between He II mass flow rate and the frictional force

$$W_{s,b',i+1} = ((\mathrm{d}F_{fw,b,s}/\mathrm{d}x)_i\ 8/0.316\ \rho_s\ \mu_s^{-1/4}\ A_{b,s,i}^{7/4}\ D_{h,b,s,i}^{1/4}/S_{b,s,i})^{4/7}, \quad i = \{1...N_{x,b}\}, \tag{6.45}$$

in the model, the gravity force component parallel to the slope driving the flow is compensated by the shear friction force at the superfluid-wall interface

$$(\mathrm{d}F_{fw,b,s}/\mathrm{d}x)_i = -(\mathrm{d}F_{g\parallel,s,i}/\mathrm{d}x)_i = A_{s,b,i}\ \rho_s\ g\ (\mathrm{d}y/\mathrm{d}x)_t. \tag{6.46}$$

Using a fit for the geometrical relations $A_{b,s,i}^{7/4}\ D_{h,b,s,i}^{1/4}/S_{b,s,i})^{4/7}$ valid at He II flow depths $0\text{ m} \leq h_{s,b} \leq 20\ 10^{-3}$ m covering the whole range of the model validity as presented in figure 5.12 I obtain the approximated expression

$$W_{s,b',i+1} = 4.7188 \times 10^4 |(\mathrm{d}y/\mathrm{d}x)_t|^{4/7}\ A_{s,b,i}^{1.4729}, \quad i = \{1...N_{x,b}\}. \tag{6.47}$$

The tunnel slope $\mathrm{d}y/\mathrm{d}x$ is assumed to be constant along a sub-sector and is a model parameter whose value depends on the sub-sector location at the LHC, see Eq. (5.3.3).

The superfluid helium mass flow rate at at final volume extremity corresponding to the heat exchanger inlet is qual to that leaving the feeding pipe

$$W_{s,b',1} = -(1-\chi_{f',1})\ W_{f',1}, \quad W_{s,b',1} \geq 0, \tag{6.48}$$

restricting its sign to express the assumption that only vapor can be sucked into the feeding pipe.

Mass flow rate at the heat exchanger outlet, that is the overflow mass flow rate into the phase separator

$$W_{s,b}(L) = W_{s,b',N_{x,b}}. \tag{6.49}$$

Saturated superfluid helium temperature

In the heat exchanger tube, the He II is in coexistence with the vapor phase and thus the vapor pressure determines the saturated liquid temperature. The vapor pressure distribution inside the heat exchanger tube is approximatively described using the momentum and mass conservation for single phase vapor flow in the heat exchanger, thus neglecting the superfluid-vapor interfacial shear stress force, vapor flow acceleration due to vapor generation and neglecting the very fast vapor pressure and mass dynamics, resulting in the simple expression

Due to very small superfluid holdup, in the model, I neglect the variation of the vapor flow cross-section along the heat exchanger

$$A_{v,b',i} = A_{v,b',i+1} = A_{v,b,i}, \quad i \in \{1...N_{x,b}\} \tag{6.50}$$

to obtain the pressure increment over a finite volume

$$\Delta p_{b,i} = (\Delta F_{g||,v,b,i} - \Delta F_{fw,v,b,i})/A_{v,b,i}, \quad i \in \{1...N_{x,b}\} \tag{6.51}$$

needed to compensate presence of the component of the gravity force parallel to the heat exchanger tube wall

$$\Delta F_{g||,v,b,i} = g\ \rho_v i\ A_{v,b,i}\ \Delta x_i\ (\mathrm{d}y/\mathrm{d}x)_b, \tag{6.52}$$

with approximated vapor density

$$\rho_{v,b,i} \approx 1.6149\ T_{s,b,i} - 2.4448 \tag{6.53}$$

and the shear friction force at the wall

$$\Delta F_{fw,v,b,i} = 0.079/2\ \rho_{v,b,i}^{-1}\ \mu_{v,b,i}^{1/4}\ A_{v,b,i}^{-7/4}\ D_{h,v,b,i}^{-1/4}\ S_{b,v,i}\ W_{v,b,i}^{7/4}\ \Delta x_i. \tag{6.54}$$

that is approximated as

$$\Delta F_{fw,v,b,i} \approx c_{dp_b}\ (-3.7642 \times 10^4\ T_{s,b,i} + 8.8384 \times 10^4)\ W_{v,b,i}\ |W_{v,b,i}|^{0.75}\ A_{v,b,i}\ \Delta x_i, \tag{6.55}$$

with the constant parameter c_{dp_b} optimized to minimize errors between model simulation and the experimental results.

The vapor mass flow rate distribution along the heat exchanger, at interfaces between discrete intervals, is expressed using the static mass conservation in the flow

$$W_{v,b',i+1} = W_{v,b',i} + (\mathrm{d}W_e/\mathrm{d}x)_{b,i}\ \Delta x_{b,i}, \quad i \in \{1...N_{x,b}\}, \tag{6.56}$$

with the boundary condition at the heat exchanger inlet

$$W_{v,b',1} = -W_{f',1} - W_{s,b',1}. \tag{6.57}$$

The corresponding values inside a finite volume are interpolated

$$W_{v,b,i} = (W_{v,b',i} + W_{v,b',i+1})/2, \quad i \in \{1...N_{x,b}\}. \tag{6.58}$$

At helium saturation line, the relation between pressure and saturation temperature may be approximatively expressed as

$$(\mathrm{d}T_s/\mathrm{d}p)_{b,i} \approx -2.6558 \times 10^{-4}\ T_{s,b,i} + 6.4217 \times 10^{-4}, \quad i \in \{1...N_{x,b}\}, \tag{6.59}$$

using the interpolated value of saturation pressure

$$T_{s,b,i}(t) = (T_{s,b',i'}(t) + T_{s,b,i+1}(t))/2, i \in \{1...N_{x,b}\}. \tag{6.60}$$

To solve at low computational cost the two point boundary problem with the saturation temperature and vapor mass flow rates that are strongly coupled and bounded at opposite extremities of the heat exchanger tube, presented in the analysis section, vapor mass flow rate is used as a tearing variable, needed to calculate the reference saturation temperature profile at the finite volume interfaces along the heat exchanger tube,

$$T_{s,b',ref,i} = T_{s,b',ref,i+1} - (\mathrm{d}T_s/\mathrm{d}p)_{b,i}\,\Delta p_{b,i}, \quad i \in \{1...N_{x,b}\} \tag{6.61}$$

starting from the boundary condition at the heat exchanger outlet

$$T_{s,b',ref,N_{x,b}+1} = T_{s,b}(L). \tag{6.62}$$

Then, this reference value is used to calculate evolution of dummy saturation temperature dynamics that converges to the solution of the two-point boundary value problem

$$\mathrm{d}T_{s,b,i}/\mathrm{d}t = 1/\tau_{dT_{s,b}/dt}\,(T_{s,b,ref,limited,i} - T_{s,b,i}), \quad i \in \{1...N_{x,b}+1\}, \tag{6.63}$$

with the time constant of the dummy dynamics

$$\tau_{dT_{s,b}/dt} = 15 \text{ s} \tag{6.64}$$

being a model parameter found by trial and error. The reference values for the sake of numerical robustness

$$T_{s,b,ref,limited,i} = \begin{cases} T_{s,b,ref,i} & \text{if } 1.5 \text{ K} \leq T_{s,b,ref,i} \leq 5.2 \text{ K}, \\ 1.5 & \text{if } 1.5 \text{ K} > T_{s,b,ref,i}, \\ 5.2 & \text{if } T_{s,b,ref,i} > 5.2 \text{ K}. \end{cases} \tag{6.65}$$

Helium vapor temperature

The temperature of vapor in the heat exchanger is approximatively expressed in function of enthalpy of saturated vapor

$$T_{v,b,i} = -4.4265 + 2.5683 \times 10^{-4}\, h_{v,b,i}, \quad i \in \{1...N_{x,b}\}. \tag{6.66}$$

The vapor specific enthalpy dynamics in the heat exchanger tube

$$\begin{aligned} \mathrm{d}h_{v,b,i}/\mathrm{d}t = a_{\mathrm{d}h_{v,b}/dt,i}\ 452.14/\rho_{v,b,i} \\ \times ((W_{v,b',i}\ h_{v,b',i} - W_{v,b',i}\ h_{v,b',i})/\Delta x_{fb,i} + \\ (\mathrm{d}W_{e,b}/\mathrm{d}x)_i\ h_{vs,b,i} + (\mathrm{d}q_{h2bv}/\mathrm{d}x)_i + (\mathrm{d}q_{f2bv}/\mathrm{d}x)_i), \quad i \in \{1...N_{x,b}\} \end{aligned} \tag{6.67}$$

is derived from the energy conservation, including the heat transfers: 1) through the heat exchanger wall, originating at the bath, $(\mathrm{d}q_{h2bv}/\mathrm{d}x)$, already discussed in this section, and 2) through the feeding pipe wall originating at the helium flowing in the pipe $(\mathrm{d}q_{f2bv}/\mathrm{d}x)$, described later.

The dumping factor

$$a_{\mathrm{d}h_{v,b}/dt,i} = \begin{cases} 1/(a_{\mathrm{d}h_{v,b}/\mathrm{d}t,i}\ c_{\Delta t}) & \text{if } a_{\mathrm{d}h_{v,b}/\mathrm{d}t,i} > 1/c_{\Delta t} \\ 1 \quad \text{otherwise,} \end{cases} \tag{6.68}$$

with

$$a_{\mathrm{d}h_{v,b}/\mathrm{d}t,i} = 452.1/\rho_{v,b,i}\ ((|W_{v,b,i}| + |W_{v,b,i+1}|)/\Delta x_{fb,i} + C_{v,b,i}\ (P_{v,b,i} + P_{v,f,i})\ 2.5683 \times 10^{-4}) \tag{6.69}$$

is introduced to reduce the model stiffness and guaranty numerical stability of the solution at a given time integration step length. When the dumping factor is active, it causes loss of energy conservation, and the dynamics corresponds to a dummy dynamics used to find a static distribution of the helium vapor temperature. In fact, the errors in the dynamics representation are negligible and the dynamic version of the energy conservation is used exclusively to avoid introducing additional algebraic expressions into model.

The enthalpy at the interfaces of the finite volumes are calculated taking into account the direction of the vapor flow, as it can be reversed when aspired by the feeding pipe

$$h_{v,b',1} = \begin{cases} h_{vs,b',1} & \text{if } W_{v,b',1} > 0 \\ h_{v,b,1} & \text{otherwise.} \end{cases} \tag{6.70}$$

$$h_{v,b',i} = \begin{cases} h_{v,b,i-1} & \text{if } W_{v,b',i} > 0 \\ h_{v,b,i} & \text{otherwise.} \end{cases}, \quad i \in \{2...N_{x,b}\} \tag{6.71}$$

$$h_{v,b',N_{x,b}+1} = \begin{cases} h_{v,b,N_{x,b}} & \text{if } W_{v,b',N_{x,b}+1} > 0 \\ h_{v,b,N_{x,b}} & \text{otherwise.} \end{cases} \tag{6.72}$$

Enthalpy of the saturated vapor created due to superfluid evaporation

$$h_{vs,b,i} = 4.1903 \times 10^3 \; T_{s,b,i} + 1.6679 \times 10^4, \quad i \in \{1...N_{x,b}\}. \tag{6.73}$$

6.3.5 Coolant mass accumulation in feeding pipe

In this section I model the dynamics of helium mass distribution along the feeding pipe that introduces an important dynamic mode to the magnets temperature dynamics.

Solving two-point boundary value problem

The saturation temperature (de facto pressure) distribution along the pipe that is bounded at the pipe outlet is closely coupled to the distributions of mass flow rate and of specific enthalpy that are bounded at the pipe inlet. Thus in order to solve at low computing cost the complex two-point boundary value problem, I have introduced the dummy dynamic variables for average flow density, saturation pressure and de facto for the specific enthalpy, since the dynamics is reformulated to limit speed of its fastest modes.

Average two-phase flow density distribution

The mass of helium present inside the feeding pipe is related through the pipe geometry to the distribution of the average flow density, found using the homogenous model of two phase flow of superfluid/liquid and vapor. Dummy dynamics of the helium density distribution is introduced to reduce the model stiffness and thus to lower the computational cost of simulation

$$(\mathrm{d}\rho/\mathrm{d}t)_{f,d,i} = 1/\tau_{\rho_f} \; (\rho_{f,ref,i} - \rho_{f,i}), \quad i \in \{1...N_{x,b}\}, \tag{6.74}$$

with time constant

$$\tau_{\rho_f} = 30 \text{ s} \tag{6.75}$$

found by trial and error and the reference distribution of average density of helium

$$1/\rho_{f,ref,i} = 1/\rho_s + \chi_{f,i} \; (1/\rho_{v,f,i} - 1/\rho_s), \quad i \in \{1...N_{x,b}\}, \tag{6.76}$$

with the constant He II density ρ_s and pressure dependent density of saturated vapor

$$\rho_{v,f,i}^{-1} \approx 29.57 \; T_{s,f,i}^{-4.5213}, \quad i \in \{1...N_{x,b}\}, \tag{6.77}$$

approximated as function of the saturation temperature in the pipe $T_{s,f,i}$.

Vapor quality distribution

The vapor quality

$$\chi_{f,i} = (h_{f,i} - h_{s,f,i})/\Delta_h, \quad 0 \leq \chi_{f,i} \leq 1, \quad i \in \{1...N_{x,b}\} \tag{6.78}$$

is a function of enthalpy of the two-phase flow $h_{f,i}$ and enthalpy of saturated liquid He I or superfluid He II $h_{s,f,i}$ at the pressure in the feeding pipe.

To reduce the computational cost of the model, see section 6.2.4, the computationally costly expression for saturated helium enthalpy

$$h_{s,f,i} = h_{s@T_0,f,i} + (T_{s,f,i} - T_{s0,f,i})\ (\mathrm{d}h_s/\mathrm{d}T_s)_{f,i}, \quad i = \{1...N_{x,b}\}, \tag{6.79}$$

with linearization performed during the simulation once every $N_{\Delta t_{slow}/\Delta t}$ simulation steps, using final differences

$$(\mathrm{d}h_s/\mathrm{d}T_s)_{f,i} = (h_s(T_{s,f,i} + \Delta T_{s,f}/2) - h_s(T_{s,f,i} - \Delta T_{s,f}/2))/\Delta T_{s,f}, \quad i = \{1...N_{x,b}\}, \tag{6.80}$$

and the interpolated value

$$h_{s@T_0,f,i} = (h_s(T_{s,f,i} + \Delta T_{s,f}/2) + h_s(T_{s,f,i} - \Delta T_{s,f}/2))/2, \quad i = \{1...N_{x,b}\}. \tag{6.81}$$

Saturation temperature distribution

In order to solve at low computing cost the saturation pressure profile, which is a part of a larger two-point boundary value problem, I introduce dummy dynamic variables

$$\mathrm{d}T_{s,f,d,i}/\mathrm{d}t = 1/\tau_{T_{s,f}}\ (T_{s,f,ref,i} - T_{s,f,d,i}), \quad 1.5\ \mathrm{K} \leq T_{s,f,d,i} \leq 5.2\ \mathrm{K}, \quad i = \{1...N_{x,b}+1\} \tag{6.82}$$

that converge to the reference saturation temperature profile

$$T_{s,f,ref,i+1} = T_{s,f,ref,i} + \mathrm{d}p_{f,i}\ (\mathrm{d}T_{s,f}/\mathrm{d}p_f)_i \quad 1.5\ \mathrm{K} \leq T_{s,f,ref,i+1} \leq 5.2\ \mathrm{K}, \quad i = \{1...N_{x,b}\} \tag{6.83}$$

that is integrated along the pipe with the boundary condition at the pipe outlet

$$T_{s,f,ref,1} = T_{s,b,ref,1}. \tag{6.84}$$

The pressure drop $\mathrm{d}p_{f,i}$ in the two phase flow is found using the steady-state momentum conservation for the flow

$$\mathrm{d}p_{f,i} = 1.6211 \times 10^8 \ (W^2_{f',i}/\rho_{f',i} - W^2_{f',i+1}/\rho_{f',i+1}) + (\rho_{f,i}\ g\ \mathrm{d}y_t/\mathrm{d}x - (\mathrm{d}p_{fw,f}/\mathrm{d}x)_i)\ \Delta x_{f,i} \tag{6.85}$$

and has three components: 1) related to the momentum flux (flow acceleration) with mass flow rate $W_{f',i}$ and helium density $\rho_{f',i+1}$ at finite interval extremities, 2) hydrostatic load due to gravitational acceleration g and 3) due to wall friction shear stress

$$(\mathrm{d}p_{fw,f}/\mathrm{d}x)_i = c_{dp/dx,f}\ v_{1,p_{fw,f},i}\ W_{f,i}\ |W_{f,i}|^{0.75}\ (1+\chi_{f,i}\ v_{2,p_{fw,f},i})\ (1+2.814\ \chi_{f,i})^{-0.25} \tag{6.86}$$

with a constant correction factor $c_{dp/dx,f}$ optimized to reduce model simulation errors, see Section 6.6, and the slowly changing variables

$$v_{1,p_{fw,f},i} = 7.621 \times 10^8\ (1.45 \times 10^{-4} + 5.429 \times 10^{-5}\ T_{s,f,i}), \tag{6.87}$$

$$v_{1,p_{fw,f},2} = 5.231 + 5.17 \times 10^3\ T_{s,f,i}^{-4.842} - 1, \tag{6.88}$$

calculated once every $N_{\Delta t_{slow}/\Delta t}$ simulation steps in order to reduce the computational cost of simulation, together with

$$(\mathrm{d}T_s/\mathrm{d}p)_{f,i} = 204.2 \times 10^{-5}\ T_{s,f,i}^{-4.356} + 1.057 \times 10^{-5}. \tag{6.89}$$

Following values inside discrete interval, are approximatively interpolated

$$W_{f,i} = (W_{f',i+1} + W_{f',i})/2 \tag{6.90}$$

and

$$T_{s,f,i}(t) = (T_{s,f',i} + T_{s,f',i+1})/2, \quad i = \{1...N_{x,b}\}. \tag{6.91}$$

Mass flow rate distribution

According to the mass conservation principle and starting with the boundary condition at the mass flow rate at feeding pipe inlet

$$W_{f',N_{x,b}+1} = W_{f,in} = -W_c, \tag{6.92}$$

is that at the control valve W_c and helium mass flow rate distribution along the tube, at discrete interval extremities,

$$W_{f',i} = W_{f',i+1} + (\mathrm{d}\rho_f/\mathrm{d}t)_i \, \Delta A_{f,i} \, \Delta x_{b,i}, \quad i = \{1...N_{x,b}\} \tag{6.93}$$

is not uniform along the tube due to the dynamics of helium density.

6.3.6 Heat transfers originating at feeding pipe

In this section, I model the heat transfers originating at the feeding pipe that are the origin of the inverse response of the magnets temperature dynamics.

Helium specific enthaply distribution

The specific enthalpy of helium flow doesn't change during expansion at the control valve because the process is adiabatic. Then, section of the pipe placed inside the phase separator. If the level of saturated He II in the separator does not reach the feeding pipe, no heat exchange takes place and the enthalpy of helium entering the section of feeding pipe placed inside the heat exchanger, called here inlet, is equal to that upstream of the control valve. However, at higher levels in the separator, the feeding pipe is in contact with the saturated helium and due to the high conductance at the interface, the specific enthalpy of the flow at the pipe inlet is reduced to the level of saturated superfluid in the separator

$$h_{f',N_{x,b}+1} = \begin{cases} h_c, & \text{if } m_{s,p} < 0.2168 \text{ kg} \\ h_{he}(T_{s,b',N_{x,b}+1}, p_{f',N_{x,b}+1}), & \text{otherwise.} \end{cases} \tag{6.94}$$

with mass of superfluid present in the heat exchanger $m_{s,p}$.

Regarding the specific enthalpy distribution along the pipe, errors related to neglecting its dynamics are negligible, allowing for application of static energy conservation analysis. However in order to provide a computationally efficient solution in presence of the two-point boundary value problem just mentioned, I prefer to use a quasi-dynamic version of the energy conservation formulation, with enthalpy dynamics reformulated to limit its fastest modes and thus to turn it into dummy dynamics if faster modes occur

$$\begin{aligned} \mathrm{d}h_{f,i}/\mathrm{d}t = v_{h,f,i}/\rho_{f,i} \, (-h_{f,i} \, \mathrm{d}\rho_{f,i}/\mathrm{d}t + 1/(\Delta x_{b,i} \, A_{i,f}) \, (W_{f',i} \, h_{f',i} - W_{f',i+1} \, h_{f',i+1} \\ + (-(\mathrm{d}q/\mathrm{d}x)_{f2bv,i} - \mathrm{d}q/\mathrm{d}x_{f2bs,i}) \, \Delta x_{b,i})), \quad i = \{1...N_{x,b}\} \end{aligned} \tag{6.95}$$

with the variable

$$v_{h,f,i}(t) = \begin{cases} 1/(a_{dhdt,f,i}\,\Delta t_{int,max}), & \text{if } a_{dhdt,f,i} > 1/\Delta t_{int,max} \\ 1, & \text{otherwise.} \end{cases} \tag{6.96}$$

used to guarantee the convergence of the dynamics integration, with

$$\begin{aligned} a_{dhdt,f,i} &= 1/\rho_{f,i}\,(\mathrm{d}\rho_{f,i}/\mathrm{d}t) \\ &+ 1/(\Delta x_{f,i}\,A_{i,f})\,(|W_{f',i}| + |W_{f',i+1}| + ((\partial C_{f2bv}/\partial x)_i + (\partial C_{f2bs}/\partial x)_i)\,4.5\times 10^{-4}\,\Delta x_{b,i})) \end{aligned} \tag{6.97}$$

The enthalpy and density at finite volume interfaces depend on the flow direction and thus at the pipe outlet

$$h_{f',1}(t) = \begin{cases} h_{v,b,1}, & \text{if } W_{f',1} > 0 \\ h_{f,1}, & \text{otherwise.} \end{cases} \tag{6.98}$$

$$\rho_{f',1}(t) = \begin{cases} \rho_{v,b,1}, & \text{if } W_{f',1} > 0 \\ \rho_{f,1}, & \text{otherwise,} \end{cases} \tag{6.99}$$

along the feeding pipe

$$h_{f',i}(t) = \begin{cases} h_{f,i-1}, & \text{if } W_{f',i} > 0 \\ h_{f,i}, & \text{otherwise.} \end{cases}, \quad i = \{2...N_{x,b}\} \tag{6.100}$$

$$\rho_{f',i}(t) = \begin{cases} \rho_{f,i-1}(t), & \text{if } W_{f,i} > 0 \\ \rho_{f,i}, & \text{otherwise.} \end{cases}, \quad i = \{2...N_{x,b}\} \tag{6.101}$$

and at the pipe inlet the flow direction cannot be reversed due to density variation and thus the specific enthalpy is described by Eq. (6.94) and the density calculated analogically to the reference density, see Eq. (6.76).

Heat transfer to superfluid in the heat exchanger

The heat transfer from the feeding pipe placed at the bottom of the heat exchanger tube, to the superfluid flowing in the exchanger

$$(\mathrm{d}q_{f2bs}/\mathrm{d}x)_i = \begin{cases} c_{f2bs,i}\,P_{s,f,i}\,h_{K,i}/2\,(T_{f,i} - T_{s,b,i}) & \text{if } T_{f,i} \geq T_{s,b,i} \\ 0 & \text{otherwise.} \end{cases} \tag{6.102}$$

with the feeding pipe temperature $T_{f,i}$ and $c_{f2bs,i}\, h_{K,i}/2$ representing the heat transfer coefficient between helium flow in the feeding pipe and superfluid in the exchanger, correcting for a non-trivial heat flow pattern in the feeding pipe wall using $c_{f2bs,i}$, see Figure 5.14. The product of the outer perimeter of the feeding pipe wetted by the superfluid and the correction factor is approximated based on the geometrical relations

$$c_{f2bs,i}\, P_{s,f,i} = \begin{cases} 0.4101\, A_{b,s,i}^{0.3037} & \text{if } A_{b,s,i} \geq A_{b,s,min,i} \\ 0.4101\, A_{b,s,i}\, A_{b,s,min,i}^{1-0.3037} & \text{otherwise.} \end{cases} \tag{6.103}$$

The variable $A_{b,s,min,i}$, defined in Eq. (6.37), has been introduced to reduce the stiffness of the corresponding helium mass dynamics in the bayonet heat exchanger that appear at small helium flow depths.

The Kapitza heat transfer coefficient solid-liquid interface at feeding pipe inner and outer perimeter

$$h_{K,f,i} = c_{h_K}\, a_K\, (6.859 + 10.83\, (T_{s,b,i} - 1.9)) \tag{6.104}$$

is linearized at 1.9K The constant parameter c_{h_K} has been optimized to minimize the model simulation errors, see Section 6.6.

Heat transfer to vapor in the heat exchanger

The heat transfer from the feeding pipe to the vapor

$$(\mathrm{d}q/\mathrm{d}x)_{v,f2b,i} = C_{v,b,i}\, P_{v,f,i}\, (T_{f,i} - T_{v,b,i}), \tag{6.105}$$

using heat transfer coefficient for turbulent vapor flow inside the exchanger from Eq. (6.39) with the outer perimeter of the feeding pipe in contact with vapor

$$P_{v,f,i} = P_{o,f} - P_{s,f,i}, \quad P_{v,f,i} \geq 0. \tag{6.106}$$

Helium temperature distribution

The temperature of the helium flowing inside the feeding pipe is calculated differently for 1) single phase pure vapor, superfluid or liquid helium flow when it is defined by the flow enthalpy and pressure and 2) for two phase flow when it is equal to the saturation temperature defined by

the pressure distribution

$$T_{f,i}(t) = \begin{cases} T_{he\ I/II}(h_{f,i}), & \text{if } \chi_{f,i} = 0 \text{ (pure liquid/superfluid)} \\ T_{he\ vapor}(h_{f,i}), & \text{if } \chi_{f,i} = 1 \text{ (pure vapor)} \\ T_{s,f,i}, & \text{otherwise (two phase flow)} \end{cases}, \quad i = \{1...N_{x,b}\}. \tag{6.107}$$

Again, to reduce the computational cost linearized expression for the He I/II temperature is used, see section 6.2.4,

$$T_{he\ I/II}(h_{f,i}) = T_{s@h0,f,i} + (h_{f,i} - h_{0,f,i})\ (\mathrm{d}T_s/\mathrm{d}h_s)_{f,i}, \quad i = \{1...N_{x,b}\} \tag{6.108}$$

with the linearization around the temperature of saturated He I/II repeated at the slow pace of slowly changing variables, allowing to reduce the computational cost of simulation, using finite differences

$$(\mathrm{d}T_s/\mathrm{d}h_s)_{f,i} = (T_s(h_{s,f,i} + \Delta h_{s,f}/2) - T_s(h_{s,f,i} - \Delta h_{s,f}/2))/\Delta h_{s,f} \tag{6.109}$$

and approximate interpolation

$$T_s(h_{s,f,i} = (T_s(h_{s,f,i} + \Delta h_{s,f}/2) + T_s(h_{s,f,i} - \Delta h_{s,f}/2))/2. \tag{6.110}$$

The helium gas temperature as function of enthalpy is fitted as

$$T_{v,f,i} = -4.4265 + 2.5683 \times 10^{-4}\ h_{f,i}. \tag{6.111}$$

6.3.7 Helium mass flow rate at control valve

The helium mass flow rate is a model input optimized by the controller, to avoid the non-linearities introduced by the equal-percentage valve characteristics. However, the relation between mass flow rate and valve lift must be calculated each time when the controller manipulates the valves at real system or when experimental data is compared with the simulation results.

The flow at the control valve is always choked, because helium vapor pressure at upstream valve flow

$$p_v(h_c) \approx -0.0245 + 0.0038\ T_c^{3.8879} \tag{6.112}$$

is function of its specific enthalpy and during typical operational conditions it takes values in the range 80 kPa $\leq p_v(h_c) \leq$ 220 kPa that are order of magnitude higher than typical pressure

at feeding pipe inlet, defined as that at the very low pressure in the cryogenic distribution line incremented by the pressure drop in the feeding pipe.

Thus the maximal helium mass flow rate that can be throttled at the valve

$$W_{c,max} = 8.784 \times 10^{-3}\ K_{VS}\ F_L\ \rho_{he,c}^{1/2}\ (\ (p_c - F_F\ p_v))^{1/2} \tag{6.113}$$

with saturation flow coefficient $K_{VS} = 0.11$ m3/h bar , pressure recovery factor for the globe valve $F_L = 0.87$ and liquid critical pressure ratio factor $F_F = 0.96 - 0.28\ p_v/p_c$, the critical pressure $p_c = 227\ kPa$. The square root of helium density at the valve upstream flow is fitted

$$\rho_c^{1/2} \approx 12.433 - 0.0035\ T_{c,in}^{3.7038} + 0.0089\ (p_{c,in} - 3.9)\ T_{c,in}^{2.0498}. \tag{6.114}$$

The control valve has equal-percentage characteristics, thus the mass flow varies in function of the valve lift

$$W_c(x_c) = \begin{cases} c_c(x_c)\ W_{c,max}\ R^{(x_c-1)}, & \text{if } x_c \geq x_{c,min} \\ 0 \quad \text{otherwise.} \end{cases}, \tag{6.115}$$

with valve lift x_c and the valve cutoff position observed during LHC operation

$$x_{c,min} = 3.5 \pm 2\ \%, \tag{6.116}$$

due to finite valve rangeability

$$R = 40. \tag{6.117}$$

However, the installed characteristics seem to deviate from the ideal by few percent and are different for each valve, see Fig. 5.15. Thus a calibration curve $c_c(x_c)$ is identified for each valve.

6.3.8 Dynamics of helium level in phase separator

The circuit is designed to work with partially wetted heat exchanger, so that pure vapor flow leaves the exchanger and the phase separator remains empty. However, helium accumulates in the phase separator during overflow of the bayonet heat exchanger. Modelling of the He II level dynamics allows to deal with the constraints on the maximal helium level in the separator in the case of the heat exchanger overflow and take into account heat exchange with feeding pipe.

Thus, the heat transfer between helium in the pipe and that in the phase separator, see Eq. (6.94)

$$q_{f2p}(t) = \begin{cases} 0, & \text{if } m_{l,ps} < 0.2168 \\ W_c\ (h_c - h_{s,f}(T_{s,b,N_{x,b}+1})), & \text{otherwise.} \end{cases} \tag{6.118}$$

The He II mass dynamics in the separator represents the mass balance between helium overflowing the heat exchanger end entering the separator and that evaporating from the separator, taking into account the heat exchange with the feeding pipe

$$\mathrm{d}m/\mathrm{d}t_{s,p}(t) = W_{s,b,N_{x,b}+1} - (0.2 + q_{f2p})/\Delta_{h,he}. \tag{6.119}$$

Finally, helium level in the separator is related to the accumulated helium mass through the separator geometry

$$l_p = 50\ (1 + 0.5190\ (m_{s,p,i} - 1.3666) + 0.0602\ \tan(m_{s,p,i} - 1.3666)). \tag{6.120}$$

6.4 Model implementation

The model has been implemented as C library, because the resulting code is fast and can be easily integrated into both: 1) Matlab MEX-files used in simulations during model and controller development, see Fig. 6.3, and 2) WinCC OA SCADA CTRL-language through Control Extensions API used in the proof-of-concept implementation at the LHC, presented in Fig. 7.5. The model is subdivided into separate modules that can be simulated separately, corresponding to: 1) the helium bath, 2) the bayonet heat exchanger with the feeding pipe, 3) the control valve and 4) the phase separator.

6.5 Model simulation setup

The system dynamics is integrated using forward Euler method with a relatively small time step $\Delta t = 0.5$ s representing a tradeoff between computational cost of simulation and the simulation errors introduced due to limiting the speed of fastest modes of the stiff system dynamics, related to highly nonlinear heat transfer in superfluid and other mass and heat transfers. Many internal, slowly changing variables are updated each 20 simulation steps corresponding to 10 s of the simulation time. As already mentioned, dynamic variables $T_{s,b,i}$ and $T_{s,f,i}$ do not represent the real very fast pressure dynamics, but a slower dummy dynamics used to solve complex algebraic loops at low computational cost, using continuation approach.

The helium vapor mass flow rate inside the heat exchanger $W_{v,b,i} \in \mathbb{R}^{28}$ affecting the $T_{s,b,i}$ is a tearing variable in another algebraic loop. The algebraic loops are solved over simulation horizon, one iteration per integration step, to lower the computational cost, the and thus its value propagates over the horizon similarly to the state variables.

a) model implementation in C

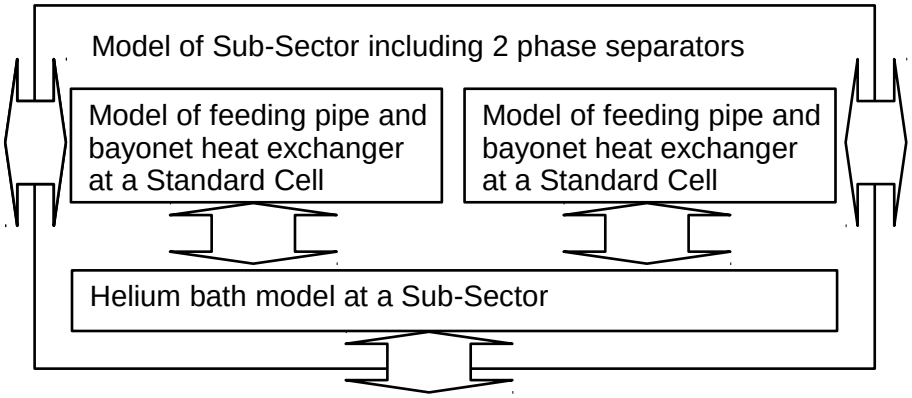

b) model and optimization integration into MATLAB(R) simulation environment

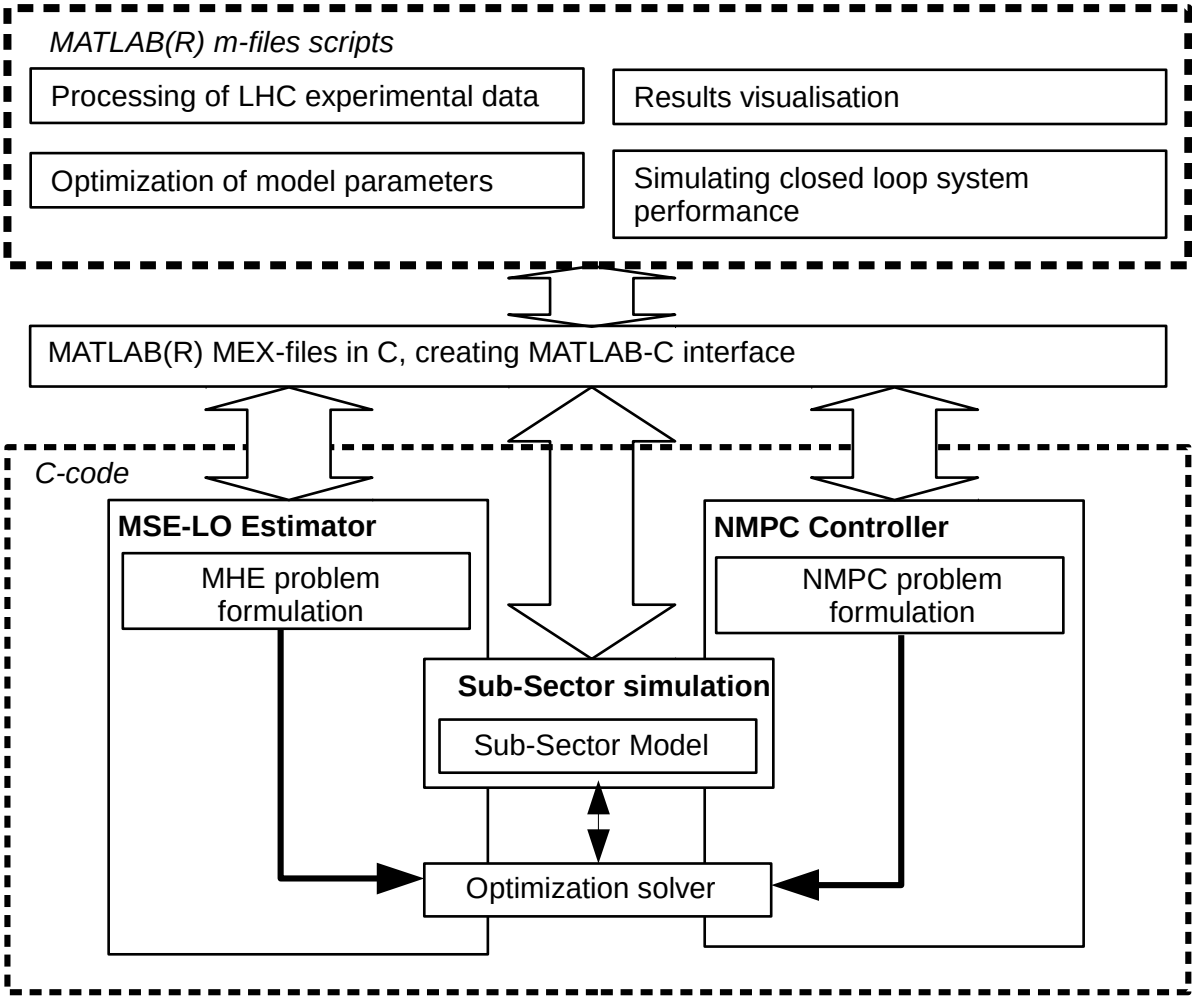

Fig. 6.3 Model implementation and integration in simulation environment.

In the experiments, electric heaters and valves are manipulated in one or multiple PI control closed loops to maintain desired bath temperatures. In simulation, the measured experimental values for the valve positions and power of electric heaters are used. However, unknown mass flow errors and static heat load are estimated in other closed loops - using Luenberger Observer approach, in order to avoid accumulating errors during relatively long simulations of the marginally instable magnets temperature dynamics. Thus, close loops configuration used in in simulations are different from those used in experiments. If experimental data is filtered to remove noise and facilitate model parameters optimization, the same filters are applied to the simulation results to be compared with the experimental data.

The LHC process data has been accessed through Timber - the JAVA data extraction API for the LHC Data Logging system. The row data in form of CSV files, has been processed and re-sampled using Perl and MATLAB scripts to obtain experimental data sets at constant sampling time of 10 s. The measured magnets temperatures and valve lifts are corrected with estimated offsets.

6.6 Identification of model parameters

In the complex first principles model, a number of parameters has to be identified, e.g. corresponding to unknown geometries, flow parameters, material properties or are related to simplified description of physical processes. The identified parameters are summarized in Table 6.1. Due to the fact that 1) the test shave been performed at the LHC in presence of many possible perturbations and 2) that multiple parameters have very similar impact on the observed system output, the confidence intervals for the estimated parameters are not assessed. Thus the meaning of the values is that they represent a set that minimizes the modelling errors of the temperature dynamics. The parameters have been optimized based on 23 identification experiments performed in sub-sectors 19L2 and 23L4, with the total experimental time in order of hundreds of hours.

6.6.1 Non-linearities and parameter sensitivity

In the case of highly non-linear dynamics, impact of the model parameters on model performance depends on operating conditions. Analysis of the dynamics leads to observation that the model parameters may be subdivided into three groups: 1) affecting the model dynamics even when control valve are closed, 2) affecting the model dynamics only when control valves are open, even when wetted length of the exchanger and corresponding saturation effects are negligible and 3) affecting the dynamics only when the valves are open and only when saturation

parameter	value	experiment
Effective bath cross-section $A_{h,mb-sss}$	14.45×10^{-3} m^2	1
Effective bath cross-section $A_{h,sss-mb}$	13.94×10^{-3} m^2	1
Effective bath cross-section $A_{h,mb-mb}$	13.86×10^{-3} m^2	1
Effective bath cross-section $A_{h,mb}$	12.99×10^{-3} m^2	1
Bath heat transfer correction $c_{q_{h,s}}$	0.8545	2
Heat load at vacuum barrier $q_{h,barrier}$	4.15 W	1
Heat load at jumper interconn. $q_{h,jumper}$	0.3873 W	1
Superfluid heat cond. exponent m	3.382	2
Heat exchanger pressure drop corr. c_{dp/dx_b}	1.17	3
Turbulent vapor conductivity corr.$c_{q,v,b}$	3.529	1 & 4
feeding pipe pressure drop corr. $c_{dp/dx,f}$	0.5688	1 & 4
Kapitza cond. correction c_{h_K}	0.6611	3

Table 6.1 Estimated model parameters. Experiment characteristics: 1 - Large temperature gradients, 2- Varying temperature gradients, 3-Pronounced saturation, 4-Valve pulses

effects are pronounced corresponding to non-negligible wetted length of the exchanger. Based on this observation, identification experiments have been designed that amplify the effects of some parameters on the model outputs in conditions where the impact of other parameters is negligible, allowing to reduce propagation of parameters estimation errors.

6.6.2 Parameters identified without model simulation

Parameters that may be identified without model simulation are perfect to start with because their estimation is not influenced by errors related to estimation of other parameters.

Mass of helium bath

Mass of helium bath is estimated independently on other model parameters as described in section 5.2.3.

Control valve mass flow rate calibration

The control valve characteristics, presented in Section 5.5 has been estimated based on bath energy conservation Eq. 5.2, in principle similar to the bath mass and heat load estimation but using specially designed identification tests where constant mean bath temperature has been maintained using electric heaters to compensate for slowly increasing cooling power due to increasing valve lift. The unknown specific enthalpy of vapor at the heat exchanger outlet has been assumed to correspond to that of saturated helium vapor.

In order to refine the characteristics estimation, once other model parameters have been initially identified, the model of the heat exchanger has been simulated to provide better estimated of enthalpy of the vapor flow, that is higher than that of saturated vapor due to the vapor heating provided by the feeding pipe.

6.6.3 Optimization of model parameters based on closed-loop simulation

During the identification of the parameters presented in this section, the model was simulated in a closed loop with Luenberger Observer where heat loads into the bath and valve mass flow rate corrections are calculated and feed to the model in order to reduce the simulation errors of simulated average bath temperature and bath temperature at wetted zones, respectively. The feedback provided by the estimator eliminates errors accumulation over time due to instability of magnets temperature dynamics and thus allows to use significantly longer identification tests than it would be possible in an open loop setup. This is clearly visible when we compare the results of the model identification with those of model validation performed in open loop, presented in Section 6.7. In order to asses the model performance in closed loop, the errors between the model outputs and LHC experimental data is analyzed together with correlations between the outputs and estimated values of the mass flow rate corrections and the heat load. In case of high quality model, the correlations should be negligible.

Thus in the closed loop, the optimal model parameters minimize the cost functional

$$L_{ident} = \sum_{n=1}^{16} \int ((T_{h,@TT,n} - T_{TT,h,n})/0.5 \times 10^{-3})^2 + (((\mathrm{d}\hat{q}/\mathrm{d}x)_{h,l} - mean((\mathrm{d}\hat{q}/\mathrm{d}x)_{h,l}))/2.3 \times 10^{-3})^2 \mathrm{d}t \quad (6.121)$$

and thus minimize errors between simulated $T_{h,@TT,n}$ and experimental $T_{TT,h,n}$ magnet temperatures and minimize the variation of the estimated static heat load into the bath $(\mathrm{d}\hat{q}/\mathrm{d}x)_{h,l}$ since the actual heat load levels should stay constant during the tests.

The Luenberger Observer, provides estimates of heat loads based on errors between measured and simulated mean bath temperature and bath temperature gradients at warmest extremity

$$(\mathrm{d}\hat{q}/\mathrm{d}x)_{h,l} = -6.25 \sum_{n=1}^{16} (T_{h,@TT,n} - T_{TT,h,n}) - 0.05 \sum_{n=13}^{16} ((T_{h,@TT,n} - T_{TT,h,n}) - (T_{h,@TT,n-4} - T_{TT,h,n-4})), \quad (6.122)$$

and estimates of mass flow rate corrections at the valves

$$dW_{c,i} = 0.1\ e_{TT@wetted,i} + 2 \times 10^{-3} \int e_{TT@wetted,i} \mathrm{d}t, \quad i \in \{1,2\} \tag{6.123}$$

that are calculated based on the bath temperature errors at wetted zones,

$$e_{TT@wetted,1} = \begin{cases} \sum_{n=1}^{4} (T_{h,@TT,n} - T_{TT,h,n}), & \text{if } W_{c,1} \geq 0.1 \text{ g/s} \\ 0, \quad \text{otherwise,} \end{cases} \tag{6.124}$$

$$e_{TT@wetted,2} = \begin{cases} \sum_{n=8}^{12} (T_{h,@TT,n} - T_{TT,h,n}), & \text{if } W_{c,2} \geq 0.1 \text{ g/s} \\ 0, \quad \text{otherwise.} \end{cases} \tag{6.125}$$

6.6.4 Parameters identified at quasi-empty heat exchanger

At higher differences between minimal temperature of helium bath and helium saturation temperature in the exchanger, evaporation rates are high and superfluid doesn't penetrate inside the heat exchanger and thus model parameters that affect exclusively the helium penetration have negligible effect on the simulation errors - the simulation results are not sensitive to those parameters. Thus, in this conditions other model parameters that have non-negligible effect may estimated independently, without being affected by eventual estimation errors related to the parameters with negligible impact on simulation results. The model parameters that are estimated in this conditions are related to the heat transfers in the bath and heat transfers originating at the feeding pipe.

An excellent example of an identification test performed in absence of saturation effects is presented in Fig. 6.5. In the plot, the experimental data and simulation results are presented using thick and thin lines, respectively. This experiment consist of three stages. It starts and ends with free warm up that is used to calibrate the static heat loads The main stage of the test in the middle is where 3 custom PI controllers regulate indecently bath temperatures at its extremities and at the wetted zone in the middle of the bath, corresponding to cooling provided by cell #2, as presented in Fig. 6.4. The other control valve is closed. The temperatures are regulated in order to create varying temperature gradients at various bath average temperatures.

In the experiments, the helium flow in a standard cell under test have been turned off and its temperature has been stabilized by heat transfer to the adjacent standard cell. The amount varying of heat introduced at the sub-sector extremity using electric heaters is known. The heat flows through the whole length of the cell under test to the neighbour cell providing cooling, creating varying temperature gradients along the cell under test. The range of magnets

temperature gradients produced during the tests is large, reaching significant significant values far exceeding that occurring at typical operational conditions.

Heat transfers and heat conductivity in superfluid helium bath

Due to the low model spatial resolution and repetitive structure of the magnets string, only four values of effective cross-section for longitudinal heat transfer in are needed in the model, see Section 6.3.2. At given values of estimated heat loads, the parameters have pronounced effect on the magnets temperature gradients. Due to the strong non-linearities of heat transfer in superfluid, the sensitivity of the gradient to the value of this parameter increases with heat fluxes and thus highest possible temperature gradients should be used.

The estimated values of A_h corresponds to roughly 50% of that calculated from dipole magnet geometry Liu et al. (2003), indicating that the interconnections are restricting the heat transfer and/or heat load distribution differs form the estimated. The optimized parameter set gives very good agreement between the experimental data and the model simulation results in the wide range of conditions and at different configurations. Moreover, the variation of the estimated heat load is small indicating that the estimated values may be valid.

Optimized value of the coefficient $c_{q_{h,s}} = 0.8545$, allows to take into account small than expected observed bath temperature gradients at higher bath temperatures.

The exponent at the superfluid heat conductivity, see Eq. (5.18), has been also optimized and the value $m_{opt} = 3.38$ is very close to the reference value $m = 3.4$.

Heat load at the vacuum barrier is also optimized to compensate for detected asymmetry in the observed temperature gradients between cells installed at negative and positive tunnel slopes - where the position of wetted zones with respect to the vacuum barrier is opposite. The estimated value is approx 10 times higher than the design value of 0.4240 W and allows to compensate the asymmetry. However, I have found no source nor explanation for this additional

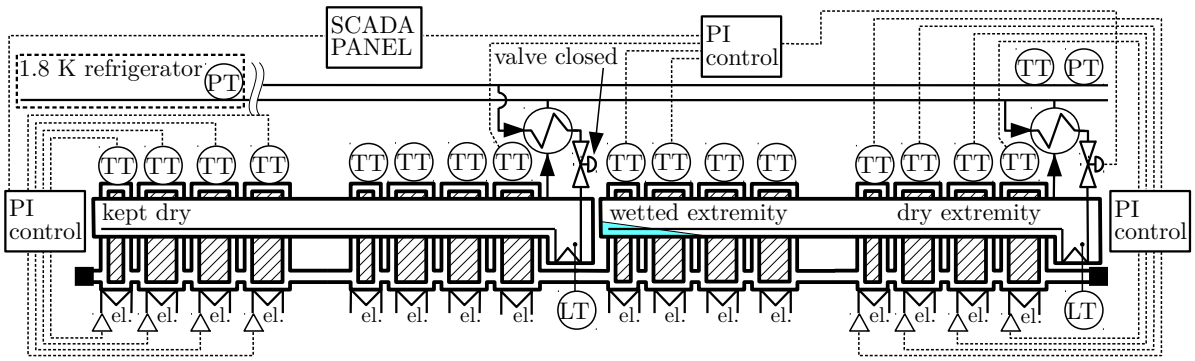

Fig. 6.4 Identification test setup.

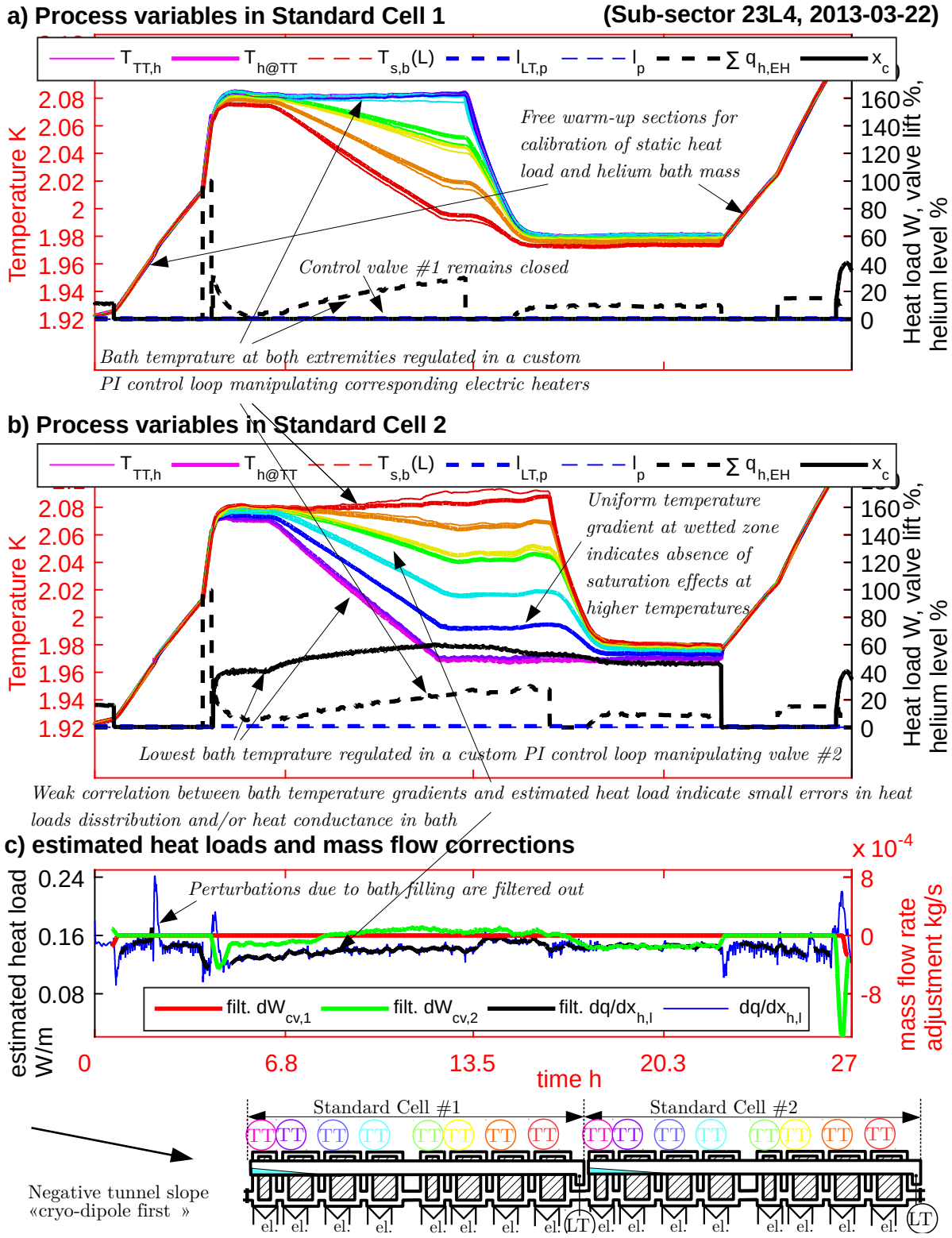

Fig. 6.5 Model identification: large temperature gradients using valve #2.

heat load. One could speculate if this asymmetry is not provoked by a helium convection in the bath, but thus has not been further investigated.

Heat transfers originating at feeding pipe

To estimate the saturation effects independent parameters of the feeding pipe, I use the same tests as for previous parameters in this group but now the cell under test is that with the valve open. At high temperature gradients, the variable heat load into the bath related to the feeding pipe heating that changes with the cooling power is more visible and allows to calibrate the two corresponding model parameters. The existence of this parameters is related to the fact that the heat conductivity of at the vapor - heat exchanger wall and vapor-feeding pipe wall used on a model is an empirical correlation and may differ from reality. In order to adjust the strength and spatial distribution of the vapor heating effect on the helium bath, I have corrected the empirical formula by multiplying the conductivity by a constant coefficient. The optimized value $c_{q,v,b} = 3.529$ is large and probably takes into account another process that is not modelled. Similarly, since the two-phase flow regime in the feeding pipe varies and the homogenous model is a large simplification, I multiply the pressure drop by a constant factor $c_{dp/dx,f} = 0.5688$ to improve the model quality.

Values of these parameters define the strength and distribution of the inverse responde of magnets temperature and thus experimental data at strongly varying mass flow rates is needed to properly asses the value of this parameters. Examples of such test are presented in Figs. 6.6 and 6.7. The correlation between the valve lift and estimated simulated mass flow rate corrections indicate errors in the estimated valve characteristics.

6.6.5 Parameters identified in presence of pronounced saturation effects

The parameters related to the the helium penetration into the heat exchanger tube are the pressure drop correction coefficient $c_{dp/dx_b} = 1.17$ and the Kapitza conductance correction coefficient $c_{a_K} = 0.6611$. The values indicate that the pressure drop in the heat exchanger is 17 % higher than calculated using enginnering correlations, which is a reasonable value taking into account the accuracy of the correlations. The value of the Kapitza coefficient correction indicate that the value of Kapitza coefficient $a_{K,MODEL} = 822$ which in fact corresponds well to the values found in the literature, see Section 5.3.4.

The values have the strongest impact on the bath temperature distribution when the temperature gradients are high but the minimal bath temperatures are sufficiently low to allow superfluid to penetrate inside the exchanger, see Figs. 6.8 and 6.9.

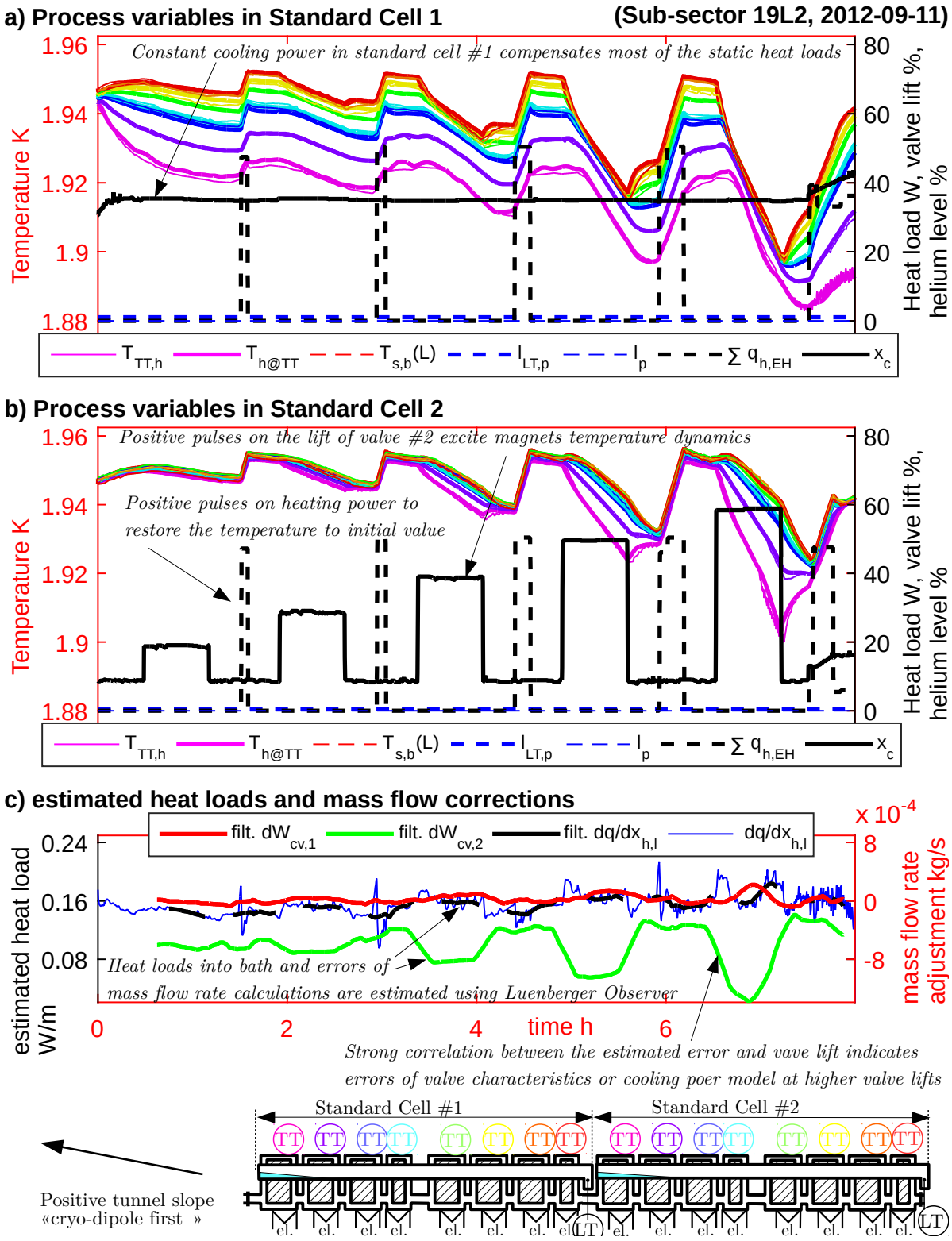

Fig. 6.6 Model identification: valve step response.

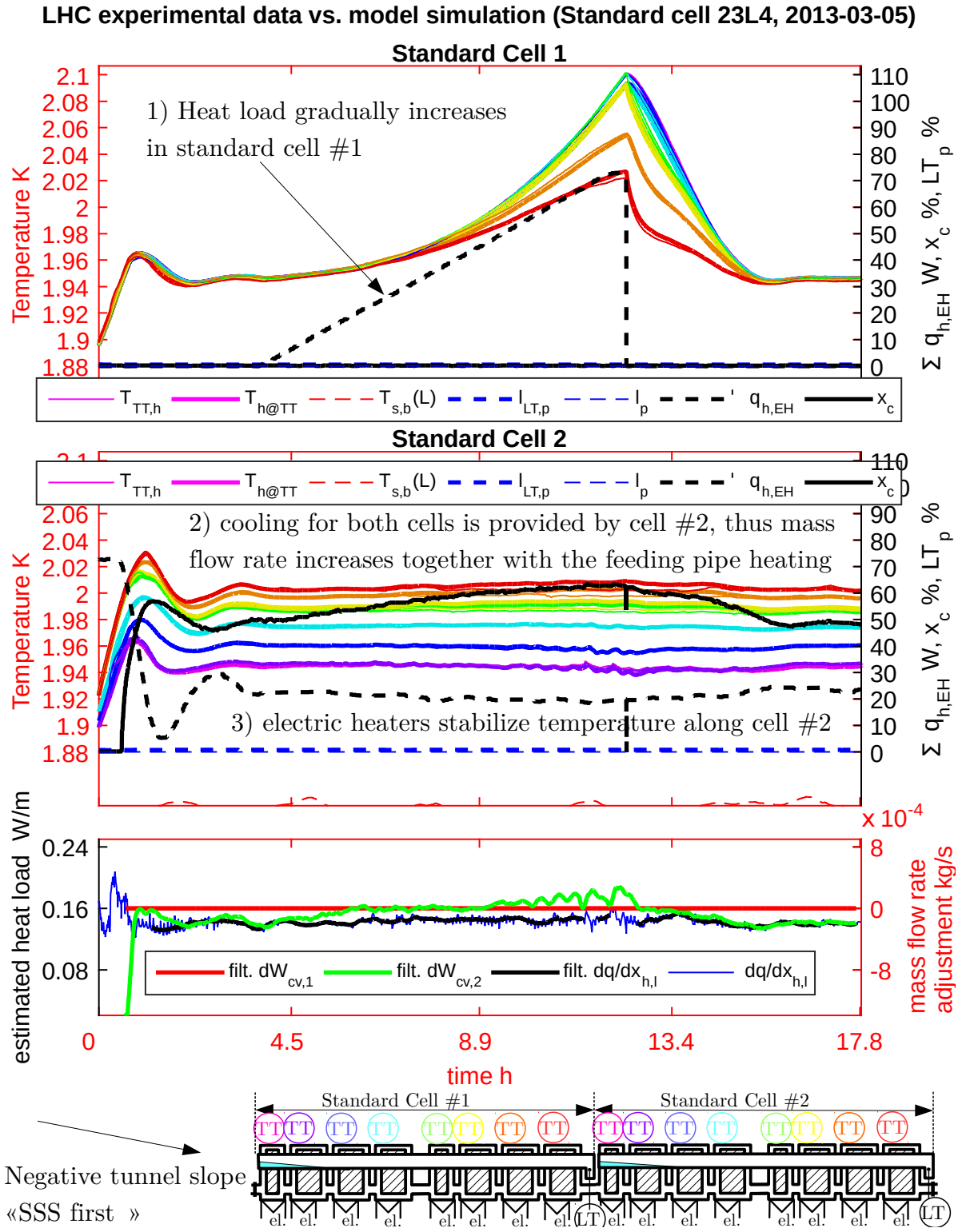

Fig. 6.7 Model identification: feeding pipe identification.

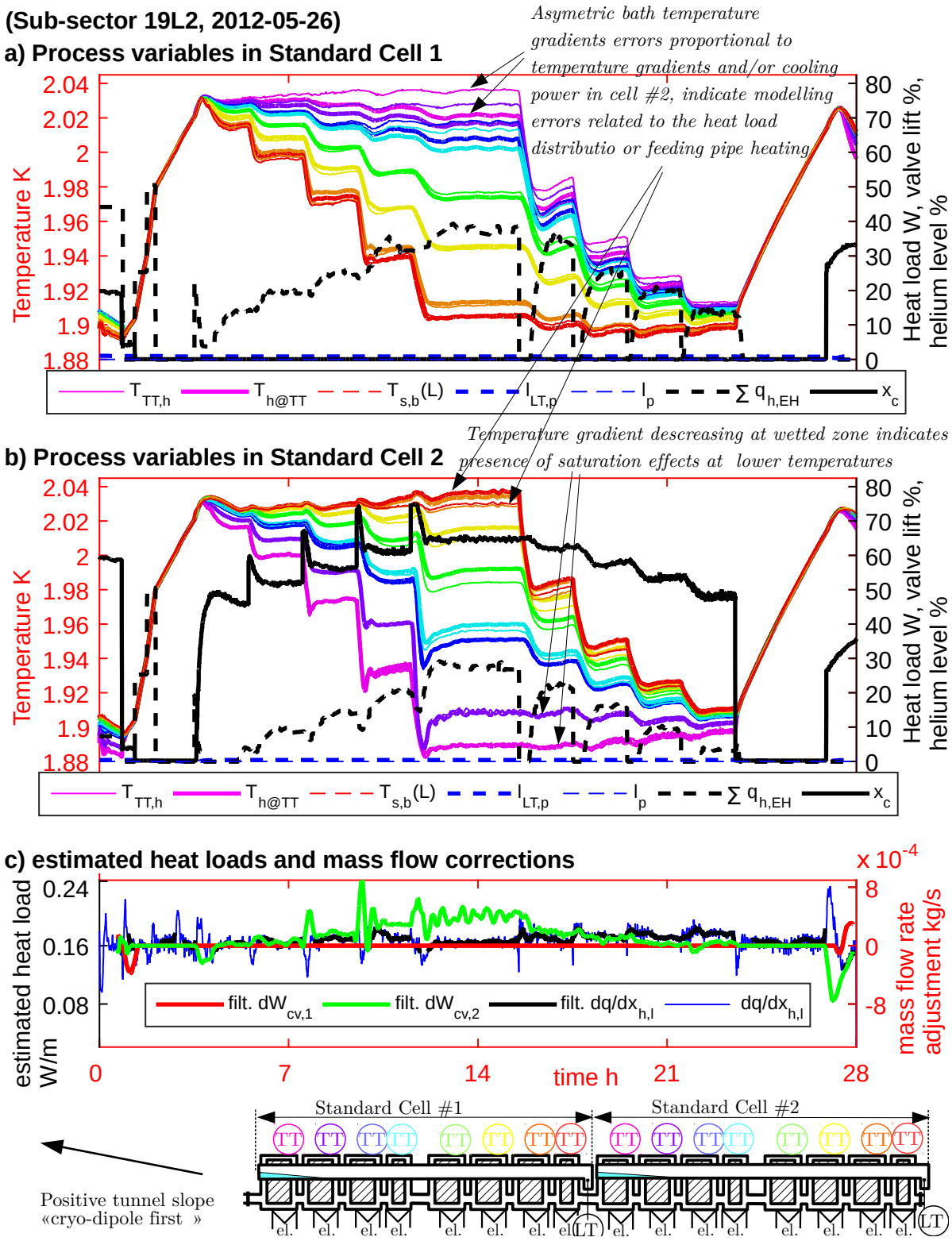

Fig. 6.8 Model identification: large temperature gradients using valve #2, saturated.

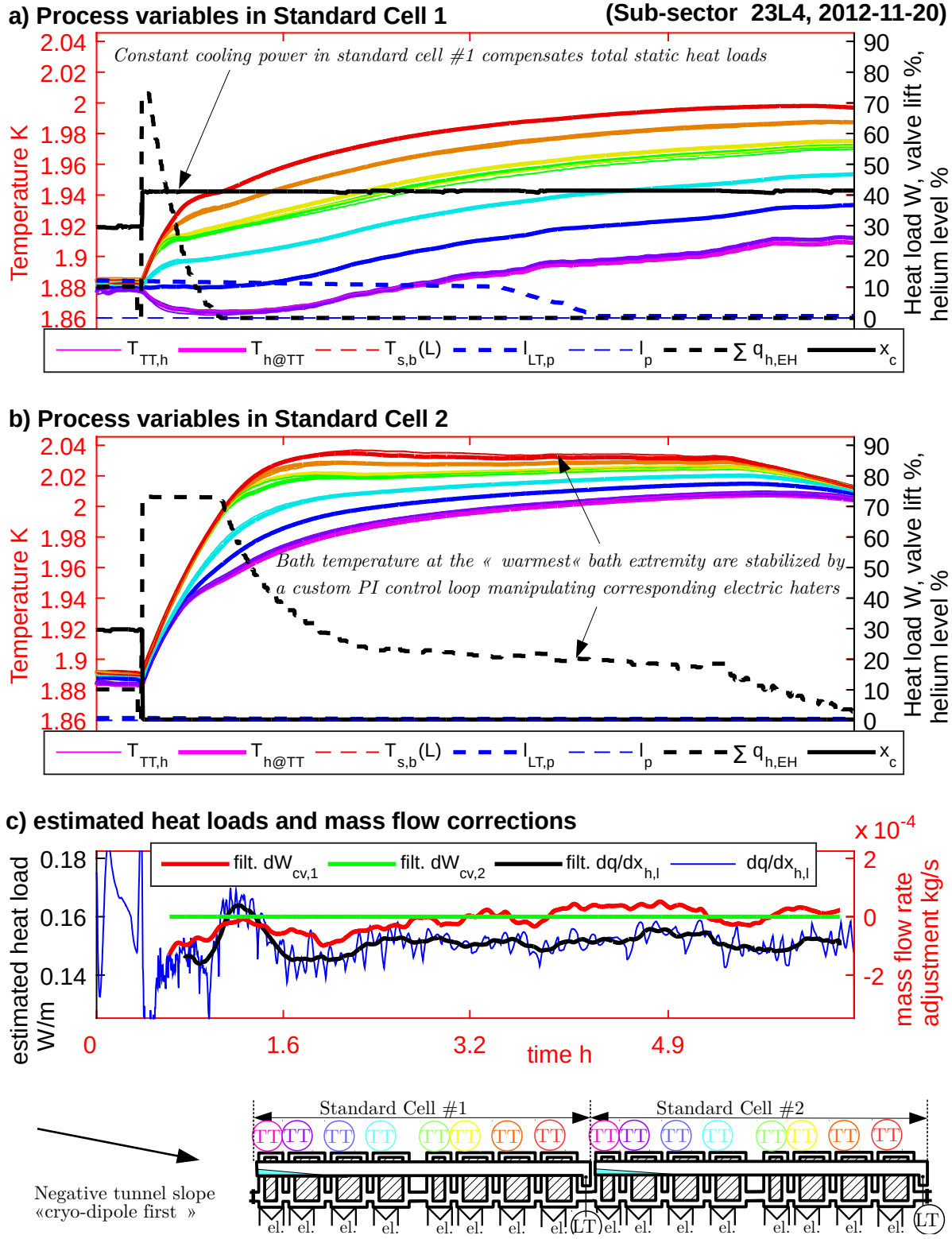

Fig. 6.9 Model identification: large temperature gradients using valve #1.

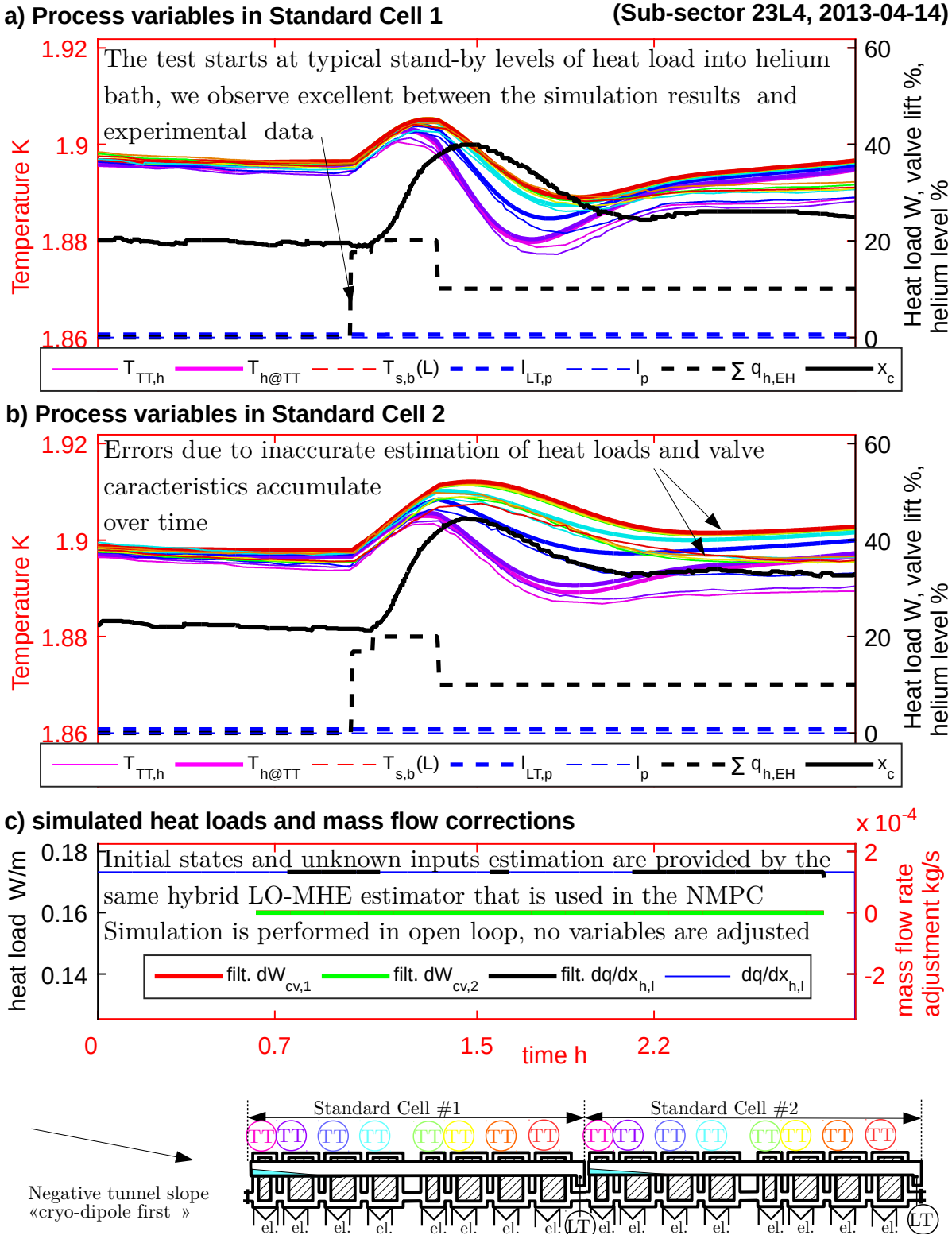

Fig. 6.10 Model validation at heat loads $q_{h,l,\text{stand-by}} \leq q_{h,l,\text{stand-by}} + 40$ W.

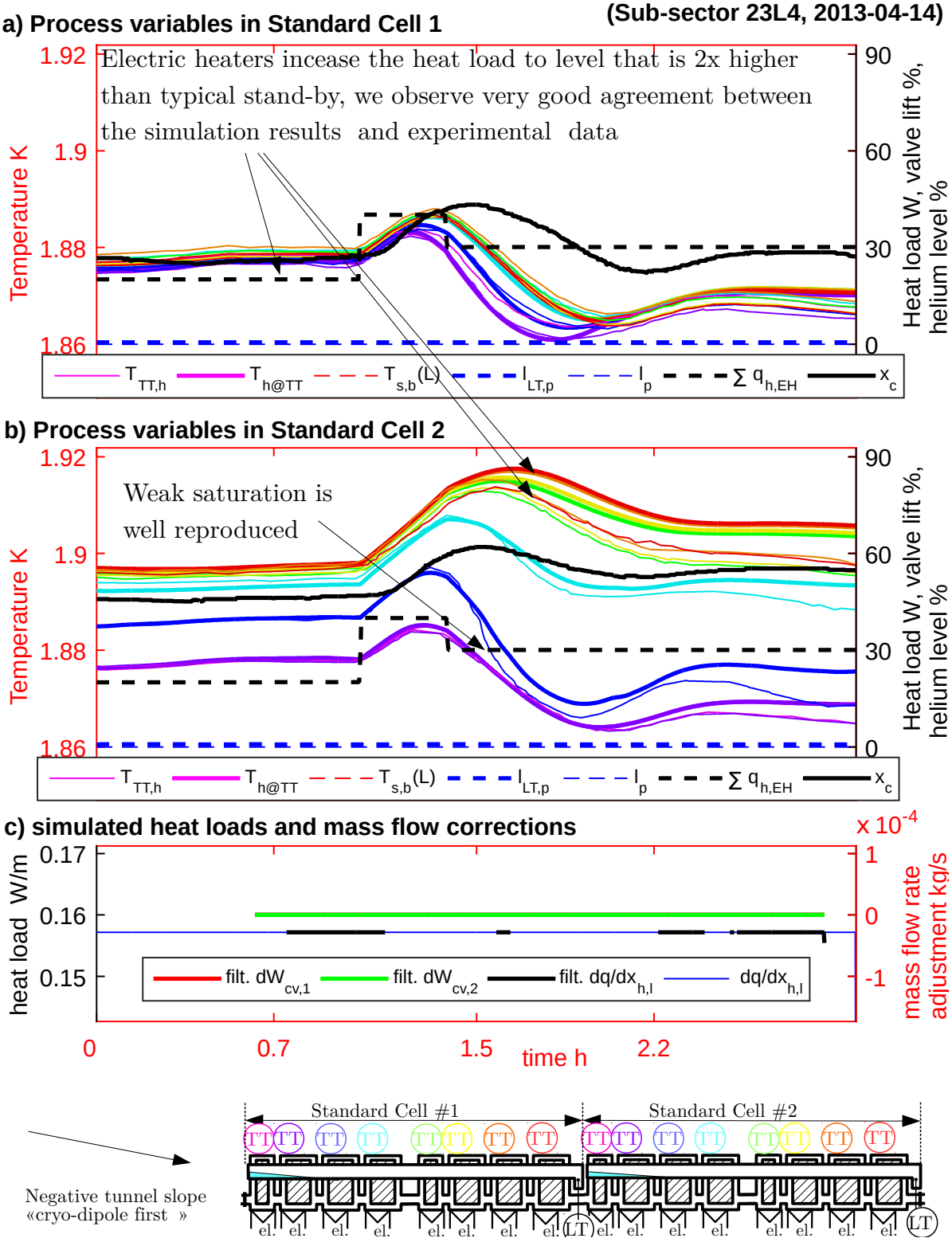

Fig. 6.11 Model validation at heat loads $q_{h,l,\text{stand-by}} + 40\ \text{W} \leq q_{h,l} \leq q_{h,l,\text{stand-by}} + 80\ \text{W}$.

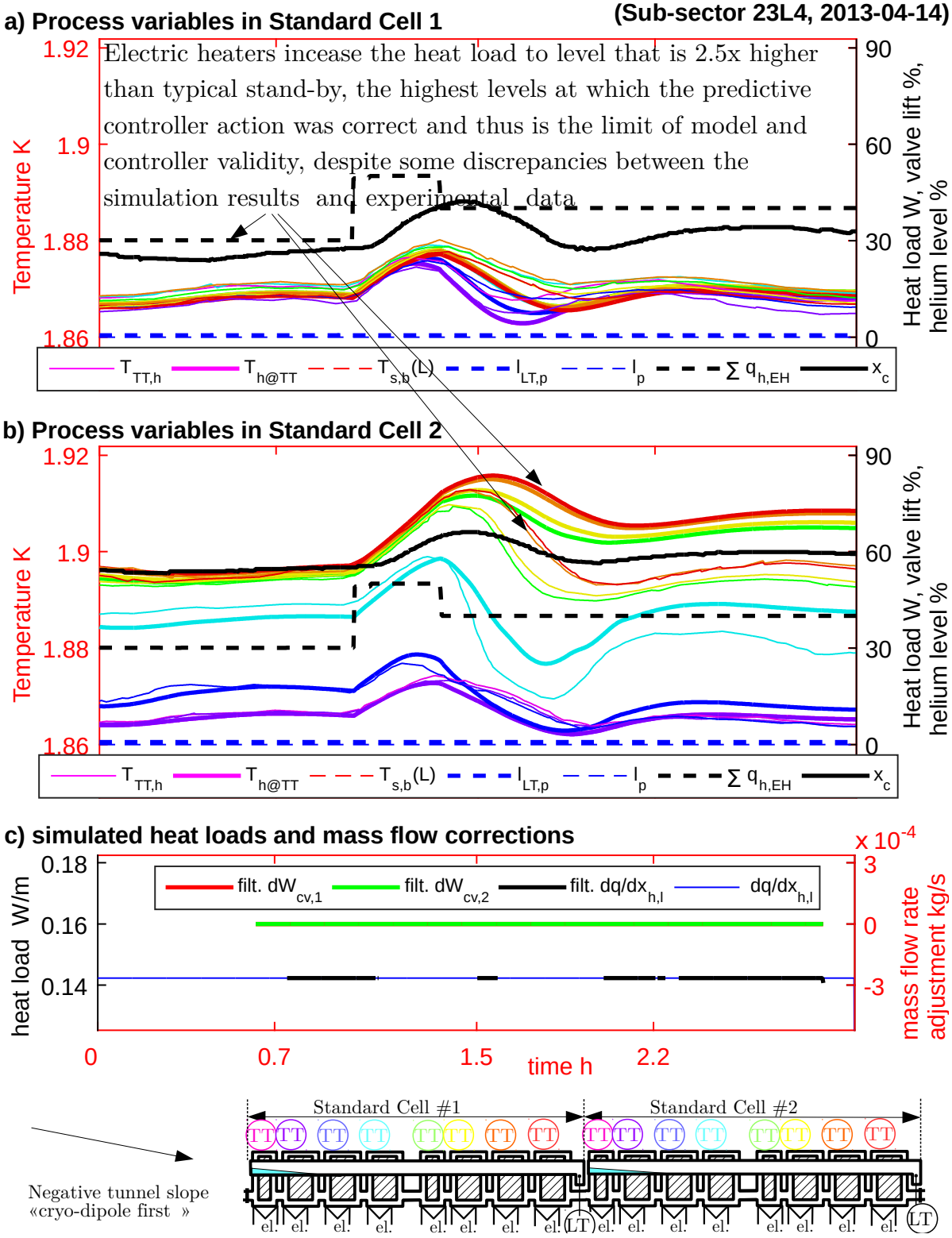

Fig. 6.12 Model validation at heat loads $q_{h,l,\text{stand-by}} + 60\ \text{W} \leq q_{h,l} \leq q_{h,l,\text{stand-by}} + 100\ \text{W}$.

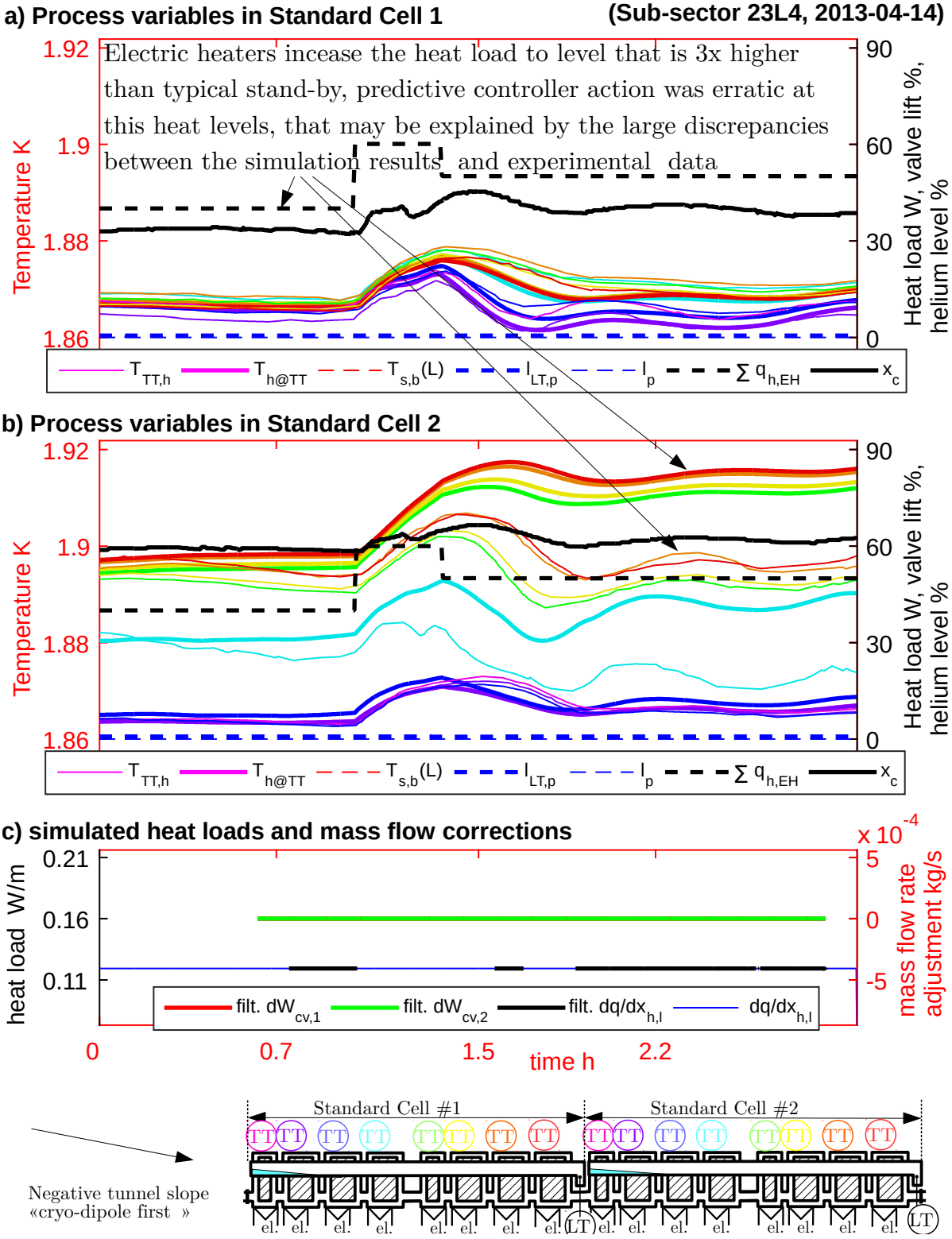

Fig. 6.13 Model validation at heat loads $q_{h,l,\text{stand-by}} + 80\ \text{W} \leq q_{h,l} \leq q_{h,l,\text{stand-by}} + 120\ \text{W}$.

6.7 Model validation

Small temperature distribution errors with negligible correlations between the process variables and both the estimated heat load and mass flow corrections at extreme conditions induced during the identification experiments is the fist step to successful model validation.

The second and final step is the assessment of quality of predictions provided by the model simulation in conditions corresponding to the application in a non-linear predictive controller. This corresponds to an open loop simulation, starting with initial states and using values of unmeasured model inputs provided by the LO-MHE estimator in the same configuration as at the NMPC. The estimator is applied to the experimental data over one hour time period directly preceding the model validation data. Ultimately the model must allow reliable predictions of the system dynamics over the NMPC prediction horizon that is 2 h long.

The scenario of a validation experiments corresponds to a stabilizing action of a NMPC in presence of known heat load perturbations, induced using electric heaters. The same scenario has been repeated in a wide range of heat loads. At heat loads corresponding to the nominal LHC operation with beam, the model performance is excellent, see Fig. 6.10. The performance deteriorates with increasing temperature gradients. It is still very good at heat loads increased by 20 W/sub-sector with respect to nominal, see Fig. 6.11, and the model reaches its validity limit at heat loads increased by 60 W/sub-sector with respect to nominal. The limit is actually defined by the performance of NMPC, that is still acceptable at model performance presented in Fig. 6.12. The model performance beyon its validity range, at heat loads increased by 80 W/sub-sector with respect to nominal, is presented in Fig. 6.13.

The dynamics of the distributed magnets temperatures follows very closely the experimental data, most importantly the dead times are almost identical not only for the maximal magnet temperature but for all measured magnet temperatures clearly validating the concept of delay modelling via distributed parameters model The validation data proves that in absence of perturbations, the prediction are valid over a period longer than 2 h needed in the controller. Moreover, the simulation speed at an Intel i7 3.9 GHz computer is much faster then real time as approx 0.5 s CPU time are enough to perform the 3 h long simulation enabling the advanced control applications.

6.8 Internal variables analysis

One of the most important model applications is in system analysis since a valid first principles model gives insight into process variables that cannot be measured otherwise. Analysis and

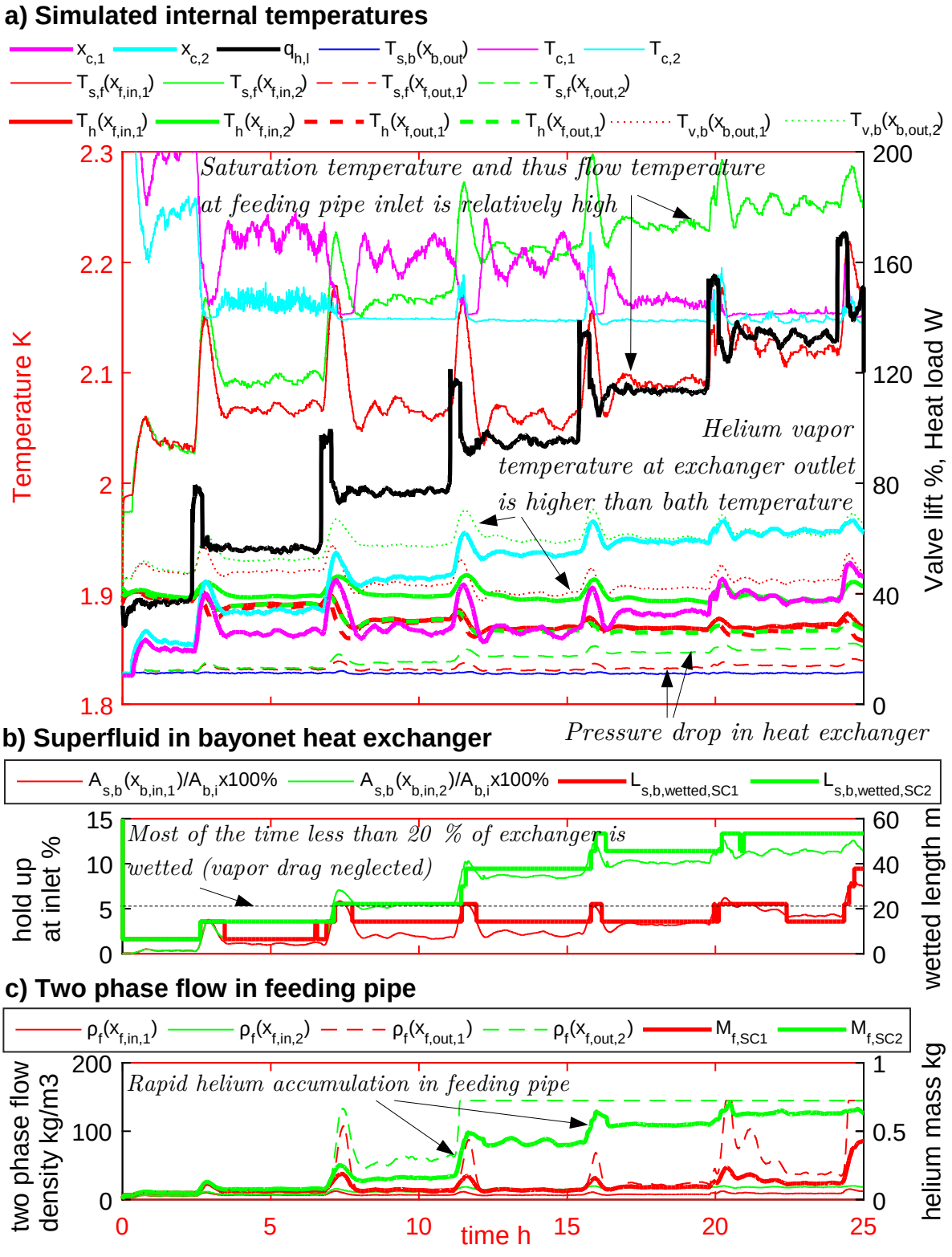

Fig. 6.14 Simulated process internal variables.

better understanding of the processes alow for better operation and improved design of future versions of the cooling system.

6.8.1 Helium distribution in the heat exchanger

Fist of the process variables analysed here is the He II distribution in the bayonet heat exchanger, presented in Fig 6.14b. It may be astonishing to see that the wetted length of the bayonet heat exchanger in normal operational conditions is very low, approx 10 %. This observation is explained the very high thermal conductivity of the copper heat exchanger tube.

6.8.2 Helium mass accumulation in the feeding pipe

On of the main contributions of this thesis is the acknowledgment of importance of the small diameter feeding pipe on the cooling circuit dynamics. Figure 6.14c illustrates the variation of the density of the two phase flow in the feeding pipe and thus the varying He mass accumulated in the pipe. This is phenomenon introduces additional dynamics between the valve position and the cooling power, simply because due to the helium accumulation in this pipe the coolant mass flow rate entering and leaving the pipe are not equal.

Moreover, as the density is always lower than 145 kg/m3, the flow must be a mixture of gas, liquid He I and superfluid He II along the whole length of the tube.

6.8.3 Feeding pipe and the inverse response

Looking at the temperature of the helium flow in the feeding pipe, demonstrated in Figure 6.14a, we see that it is much higher than the temperature of the helium bath and thus heat flows from the feeding pipe into surrounding it the vapour flow in the heat exchanger causing the vapor to warm up and thus creating heat transfer from the vapor to the bath. This mechanism heating up the warm extremity of a cell whose intensity is proportional to the pressure drop in the feeding pipe and thus to the coolant mass flow rate in a cell must be the reason for the strong inverse response characterizing the bath temperature dynamics at higher heat loads.

6.9 Summary

The model dynamics in the state space representation

$$X_m(t+\Delta t) = f\left(X_m(t), U_m(t), P_m\right), \tag{6.126}$$

$$Y_m(t+\Delta t) = g\left(X_m(t), U_m(t), P_m\right). \tag{6.127}$$

with the input $U_m \in \mathbb{R}^{18}$, state $X_m \in \mathbb{R}^{226}$, parameter $P_m \in \mathbb{R}^1$ and output $Y_m \in \mathbb{R}^{20}$

$$U_m = [(\mathrm{d}q/\mathrm{d}x)_{h,l} \quad q_{EH,h} \quad W_c \quad h_c \quad T_{s,b}(L)]. \tag{6.128}$$

$$X_m = [T_h \; \rho_f \; h_f \; A_{l,b} \; h_{v,b} \; m_{l,p} \; T_{s,f} \; T_{s,b} \; W_{v,b}] \tag{6.129}$$

$$P_m = [(\mathrm{d}y/\mathrm{d}x)_t]. \tag{6.130}$$

$$Y_m = [W_{l,b,0} \quad W_{l,b,N_x/2} \quad l_{ps} \quad T_{m,@TT}] \tag{6.131}$$

with the helium bath temperatures interpolated at the thermometers positions $T_{m,@TT}$.

The model performance enables predictions of system dynamics suitable for NMPC in wide range of heat loads, ranging from the LHC nominal to LHC nominal + 60 W/sub-sector, corresponding to approx. 2.5x the nominal stand-by heat loads.

The analysis of internal modeled variables enables better understand the complex circuit dynamics. This understanding may be used to develop new control strategies for the circuit, it may also be helpful in designing future generations of the circuit.

However, high value of one of the optimized model parameters - the correction of turbulent vapor flow conductivity indicated that the modelling of heat transfers involving turbulent vapor flow in the heat exchanger needs to be revised. Also very high estimated heat load at the location of vacuum barrier and the need of the correction of heat transfer in superfluid helium bath in Eq. (6.14) indicates that an important heat load or heat transfer mechanism (convection?) is missing in the model.

Chapter 7

Predictive control for temperature stabilization of long strings of LHC magnets

This chapter presents the first ever output-feedback NMPC for the temperature stabilisation of the LHC main magnets in the LHC arcs.

7.1 Control Problem

7.1.1 System dynamics

As demonstrated in the background Section 2.5 the magnets temperature dynamics changes strongly in function of heat loads, valve actions magnitude and direction and saturation temperature levels. Understanding of the dynamics is crucial for defining an efficient control approach.

Heat-transfer non-linearity

One of the main reasons for this extreme dynamics non-linearity is the non-linear heat transfer in superfluid He II bath that conducts the heat between the magnets and the wetted zone of the heat exchanger, see Section 5.2.4. The temperature gradients in the bath rise strongly with increasing heat transfer through the bath as $\mathrm{d}T/\mathrm{d}x \propto q_{h,s}^{3.4}$. Thus, at sufficiently small heat transfers the temperature gradients are negligible and then a 214 m long helium bath behaves like a lumped parameters system. However, when more cooling power is applied to the bath, the heat transfers increase accordingly provoking very fast growth of bath temperature gradients,

that enable varying dead times and inverse response to appear. This is also why, the system response varies strongly in function of the direction of control valve manipulation: closing the valve decreases the cooling power and thus the gradients, promoting faster system response, while opening the valve increases the gradients that slower the response.

Heating due to feeding pipe

As demonstrated in Sections 5.3.7 and 6.8.3, the bath is heated due to the presence of warm two-phase helium flow in the feeding pipe. Saturation temperature in the pipe grows strongly with increasing helium mass flow rate through the pipe, thus the bath is stronger heated at higher valve openings thus increasing the inverse response. Moreover, the bath heating is stronger at the dry heat exchanger extremity where the helium flows in the feeding pipe after expansion in the phase separator and thus the heat is then transferred all along the helium bath to the wetted zone of the heat exchanger, contribution to increasing of the bath temperature gradients.

Saturation effects

As helium bath approaches the saturation temperature in the bayonet heat exchanger, the cooling power decreases due to decreased temperature difference between the two. In effect, the coolant flow instead affecting the magnets temperature dynamics, it starts to accumulate in the heat exchanger introducing another very strong nonlinearity.

Thermal couplings through helium bath

The heat transfer in helium bath is so efficient, that a heat exchanger effectively provides cooling power to all magnets submerged in the same bath, thus to all cells in a sub-sector. This means that the minimal circuit entity that may be considered separately is a 214 m or 321 m long sub-sector. However, the magnets temperature dynamics may be considered uncoupled between different sub-sectors, allowing for independent simulation of the temperature dynamics in each sub-sector.

7.1.2 Perturbations

Heat loads into the bath are the strongest perturbations during nominal operation. Due to non-linear heat transfer in the superfluid He II the heat loads have strong impact on the operational point of the system.

The control problem

Goals :

G1) stabilize maximal magnets temperature while

G2) minimizing perturbations to vapor flow at 1.8 K refrigerator

Constraints :

C1) maximal helium level in phase separators,

C2) maximal magnets temperature,

C3) maximal and minimal vapor mass flow rate and its change rate at 1.8 K refrigerator,

C4) minimal and maximal control valve lift and

C5) minimal and maximal heaters power

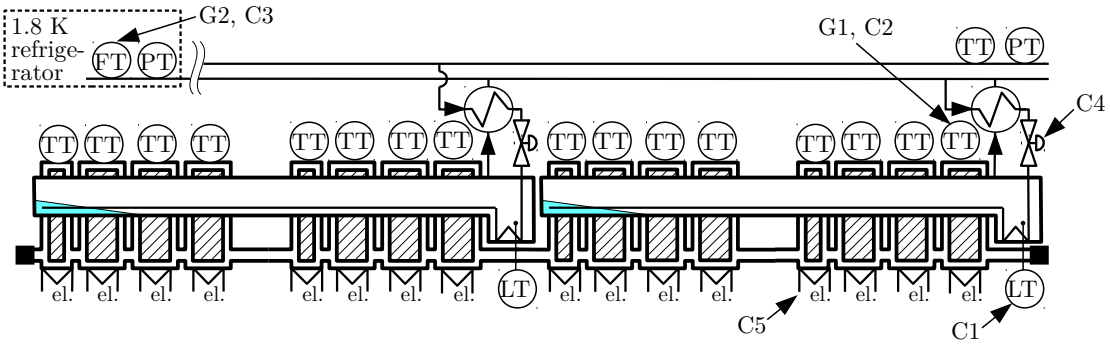

Fig. 7.1 The control problem.

7.1.3 Manipulated and controlled variables

There are 27 standard-cells in an LHC arc, each equipped in one control valve, 6 electric heaters used to control the temperature in 8 magnets and level in 1 phase separator. Thus in an arc there are 27 x 2 = 54 control valves, 27 x 6 = 162 electric heaters, used to control 27 levels in phase separators and 27x8 = 216 magnet temperatures!

7.1.4 Operational constraints

Maximal helium level in phase separators

Maximal helium level in phase separators is an important constraint for two reasons. First is that vapor is sucked away from the bayonet heat exchanger through the separator and when the separator fills up to approx. 60%, there in no free space for the vapor to flow and thus effectively the corresponding heat exchanger is cut off form the 1.8 K refrigerator pumping and thus its cooling power is lost until helium level in the separator falls that may take up to few hours! Opening the control valve while the cooling power is lost - no boiling occurs, only makes helium to accumulate in the separator. However, once the level drops enough to enable the vapor flow again, the warmer helium flow at the feeding pipe placed inside the separator accelerates helium level decrease. The second reason is that the refrigerator may only

work with vapor and thus liquid, or superfluid, phase of helium must not be sucked in by the compressor and thus overflowing the separators must be avoided.

Maximal magnets temperature

Helium in the bath undergoes a phase transition between superfluid and liquid phase at 2.16 K. Thus at bath temperatures $T_h > 2.16$ K the extremely effective heat transfer in superfluid He II vanishes and large temperature gradients appear, making the magnets powering impossible. The temperature level of $T_{h,\max} = 2.1$ K is established as the maximal LHC operational temperature, leaving small margin to the phase transition. During nominal LHC operation with beam this constraint is very unlikely to be violated since typical perturbation to the magnets temperature drive it up to 20-30 mK from the set-point at 1.9 K, much less then the margin to the constraint equal to 200 mK. However, the margin may be strongly reduced if the set-point is increased due to higher pumping pressure at the 1.8 K refrigerator.

1.8 K refrigerator constraints

Cryogenic centrifugal compressors stage at the the 1.8 K refrigerator has well defined operational range due to physical limitations like flow stall or sound barrier. The constraint are on the minimal and maximal mass flow rates

$$W_{v,r,\min} = 0.05\text{kg/s} < W_{v,r} < W_{v,r,\max} = 0.125\text{kg/s} \tag{7.1}$$

and on the mass flow rate change

$$|dW_{v,r}/dt| < (dW_{v,r,}/dt)_{\max} = 8.3\ 10^{-5}\text{kg/s2} \tag{7.2}$$

that corresponds to 5 g/s/min. Electric heaters installed in the helium baths in an LHC sector are used to generate additional heat load and thus demand for cooling power needed to satisfy the minimal helium mass flow rate at the refrigerator. This additional heating should be minimized because providing refrigeration power at 1.8 K is very inefficient and even the World's most efficient LHC refrigeration cycle has the Coefficient of Performance (COP) of only 0.0011. This means that each Watt of unnecessary heating at 1.8 K wastes approx. 1 kW of electric power, needed to generate the corresponding cooling power.

Typically each of the 8 LHC arcs can be controlled separately because the are serviced by a separate refrigerators. However, a redundancy is provided by allowing two arcs to use the same refrigerator. This configuration has been used in some arcs in years 2010-2013 in order to save electric energy in the situation where lower then designed heat loads into the bath allowed in

some cases to safely supply two LHC sectors by one refrigerator, allowing to switch off the other. In this case the magnets stabilisation over two arc should be considered since the arcs share the same refrigerator. This is so, because the essential constraint on the helium mass flow rate at the cold compressor of the 1.8 K refrigeration unit is in fact a constraint on a sum of coolant mass flow rates at all control valves in an arc.

Minimal and maximal valve mass flow rate

Besides the obvious limitation due to valve sizing

$$W_c < W_{c,\max} \approx 2 \times 10^{-3} \text{kg/s} \tag{7.3}$$

there exist a practical limitation on the minimal mass flow rate at the cryogenics valves, that cannot be completely closed during LHC operation as the controlled mass flow rate is necessary to maintain the valve thermalisation, which means to maintain a designed temperatures at various valve cryostat levels. Due to finite valve rangeablility, the constraint on the minimal mass flow rate

$$W_c \geq W_{c,\min} \approx 0.7 \times 10^{-3} \text{kg/s} \tag{7.4}$$

Minimal and maximal heaters power

The maximal heaters power is limited and thus

$$0 \leq q_{h,EH} \leq q_{h,EH,\max} = 25\text{W} \tag{7.5}$$

7.1.5 Goals

The control goal during nominal operation with beams is to stabilize the maximal magnets temperature while minimizing the magnets temperature variation along an arc and minimizing perturbation to the vapor mass flow rate at the 1.8 K refrigerator and respecting the constraints, while minimizing the power of electric heaters used to satisfy the constraint on the minimal mass flow rate at the refrigerator, see Fig. 7.1, thus decreasing the cost of machine operation by operating closer to the constraints. During the transient phase after recovery of refrigeration, the controller should accelerate the final cool-down (below 2.1 K) process, while respecting the constraints, and thus increasing the LHC availability and decreasing the operators workload.

7.1.6 Currently used PI control

The PI controllers currently used to stabilize the magnet temperatures are an excellent example for simple control approach able to deal sufficiently well with all the aspects of the control problem during nominal LHC operation. However, during large transient cool-down phase, occuring after recovery from lost refrigeration, the PI performance is poor, occasionally forcing the interlock system or the operator to adjust the control valves positions.

Control approach

One PI stabilizes the maximal helium bath temperature in every standard cell of the superfluid cryogenic circuit. The mean concept behind the approach is to avoid the operational regions where the dynamics becomes more difficult to control. The controller is conservatively tuned, meaning that the control valve lift at each cell is manipulated slowly and smoothly. This allows to avoid unnecessary large coolant mass flow rates that excite the non-linearities, varying dead times and inverse response related to the appearance of bath temperature gradients. Thus the controller keeps the bath in the region where the gradients vanish and the apparent bath thermal conductivity is very high and thus the dynamics is much easier to control. Moreover, the conservative tuning improves the robustness and thus the controller's capacity of dealing with weaker non-linearities that will appear anyway. The slow controller reaction is also its key property allowing to minimize the perturbation on the vapor flow at the refrigerator. In order to avoid the non-linearities related to saturation effects and respect the constraints on maximal helium level in the phase separators, the set-point of the controller is calculated with respect to the saturation temperature at the refrigerator, assuring that the bath temperature stays well above the saturation temperature in the heat exchanger, avoiding excessive helium accumulation in the exchanger. The minimal valve position constraint is implemented using simple limits on at the controller output.

Limitations

The limitation of the control approach used in the PI controllers are due to its key element - its conservative tuning resulting in very slow closed loop response. It is sufficient for nominal LHC operation around the setpoint, however it is too slow to efficiently handle larger transients, occurring after the refrigeration action recovery. Moreover, in order to respect the constraints on minimal vapor mass flow rate at the refrigerator, electric heaters are used to generate additional heat load and thus coolant flow necessary to maintain a margin to the minimal allowed value. Moreover, the controller performance is strongly affected the thermal couplings between the standard cells, that make the valve to close and the other valve is a sub-sector to take over the

cooling. An important issue not addressed by the PI controller is the valve equal-percentage valve characteristics that causes significant rise of the close loop gain as the valve lift increases - contrary to the intuition that would require the controller to be more conservative at higher mass flow rates when the temperature gradients are higher na the temperature dynamics more complex. Equal percentage valve has been installed in order to provide a large dynamic range of mass flow rates in two extremely different situation - stand by with supercriitical mass flow rates in order of 1 g/s and cool down where higher mass flow rates up of helium at lower density must be precisely throttled at the same valve. During the nominal LHC operation, the flow at the valve is choked and thus the downstream pressure has no effect on the mass flow rate at the valve - country to typical applications of equal percentage valves that compensate to increasing downstream pressure.

7.1.7 Possible control strategies

Maximal magnet temperature stabilisation

Stabilizing the maximal magnets temperature by throttling the coolant mass flow rate, while keeping the bayonet heat exchanger partially wet and the phase separators empty is the control strategy used currently. As showed st the example of current PI control, wisely implemented, the strategy allows even for a simple controller to deliver acceptable closed-loop dynamics. Its limitation is that it requires heat transfer in the helium bath over the distance between the magnets and the wetted zone of the bayonet heat exchanger, and the heat transfer is strongly non-linear making the closed loop dynamics of magnets temperature difficult to control at higher heat loads or fast cool down, when larger temperature gradients appear.

Phase separator level stabilisation

Initially, a control strategy has been considered where the whole length of the bayont heat exchanger is wetted and helium overflows into the phase separator and helium level in the separator is stabilized. This eliminates the limitations due to the non-linear heat transfer in the helium bath, enables the most homogene magnet temperature distribution at lowest possible temperatures. However, the dynamics between the coolant mass flow rate and the helium level is extremely non-linear with large and extremely varying dead times making its implementation using a simple controller impossible. Moreover, the quality of the helium level measurements may not be sufficient for feedback control.

Heat exchanger pressure control

Another possibility studied initially by Andersen (2002) used a control valve at the refrigerator return vapor flow to impact very low pressure in the bayont heat exchanger as additional manipulated variable in order to reduce or remove the inverse response in the temperature that occurs when the temperature is controlled. However, based on the process analysis presented in this thesis, it is difficult to justify this approach because the impact of the pressure on the cooling power is only visible at bath temperatures close to the saturation temperature and currently this operating conditions are avoided in order to decrease the risk of helium accumulation in the phase separator.

7.1.8 Discussion

In order to improve the closed loop temperature dynamics during stable normal operation and during the transient final cool-down phase, the controller must explicitly address the problem of non-linear heat transfer in the helium bath and the saturation effects in the heat exchanger. Thus, a non-linear controller is needed. Moreover, due to strong couplings between cells, the controller must be multivariate, manipulating all the control valves in a sub-sector. Explicit addressing of the constraints related to the refrigerator vapor flow would ask for a controller managing a complete LHC sector that may be too complex to realise.

7.2 Model used in non-linear optimization

The sub-sector model used in the on-line optimization in the controller is the ones with 262 states described in the Chapter 6. The models are relatively complex, however thanks to its optimization for low computational cost of simulation, it assures real-time feasibility of the advanced controller. Initially a much simpler model with 10 state variables has been developed and used in the advanced controller described by Noga et al. (2011). However the experimental validation of that controller at the LHC has failed and gave an impulse to developed of the model presented in this thesis. The additional complexity is related to the representation of the processes responsible for mass accumulation and heat transfers at the feeding pipe.

The model presented in this thesis, has been developed for application in the advanced controller and allows to simulate the dynamics of the controlled variables: the distributed magnets temperature, bayonet heat exchanger helium overflow mass flow rates and the level in the phase separators. The system manipulated variables are the lifts of control valves and the power of electric heaters. However, the lifts are not the model inputs, because corresponding mass flow rates at the control valves are used instead. The reason for this that the mass flow rate

determines the system dynamics and thus can be used by the controller, however the relation between the valve lift and the mass flow rate cannot be found accurately enough using the valve characteristics and thus more accurate vale of mass flow rate a a given valve lift is estimated. Other model inputs correspond to the estimated system variables that have strong impact in the system dynamics: the heat load and the saturation temperature at the heat exchanger outlet.

7.3 Luenberger Observer - Moving Horizon Estimator formulation

7.3.1 Purpose and validity

In order to use a controller based on the model presented in the previous chapter, values of the actual model states Eq. (6.129) and inputs Eq. (6.128) must be available. However, only the power of electric heaters is measured exactly enough and thus 232 other variables have to estimated. Thus, the validity range of the estimator bounds the validity range of the controller. The validity is thus limited by the validity of the model, validity of range of the estimation approach closely related to the observability of the system, discussed at the end of this section. As result, the estimator is valid in whole range of the operational conditions with He II, with an exception of conditions when the bath temperatures are very close to the saturation temperature, when the observability of the system is bad.

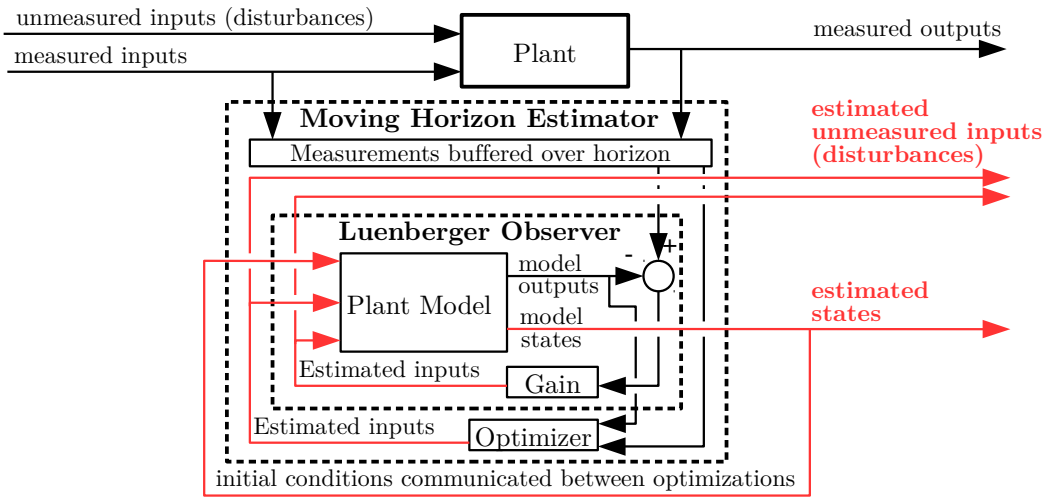

Fig. 7.2 Mixed Luenberger observer - MHE structure

7.3.2 Approach

In case when the bath temperature distribution and thus the saturation effects are neglected and the mass flow rate at the control valves would be accurately known, the heat load into the bath may be estimated using a simple model with two states and an unconstrained non-linear optimization procedure as demonstrated by Blanco (2001). Actually, in this case, the straight-forward relation between the coolant mass flow rate, heat load and the average bath temperature dynamics could be used to estimate the heat load and all model states using a Luenberger-Observer with magnets average temperature error to close the loop.

The difficulty related to the valve mass flow incertitude is that is has the same effect on the average bath temperature dynamics as the unknown heat load and thus the magnets temperature distribution has to be analyzed in order to differentiate the effects of the two and thus enable their estimation. Saturation effects are due to helium accumulation in the heat exchanger tube, that strongly disturbs the relation between the coolant mass flow rate at the valve and the cooling power delivered to the bath - making the estimation of the heat load alone difficult. Estimation of both the heat load and the coolant mass flow rate error at the valve is even more difficult since the saturation effects have strong impact on the bath temperature distribution.

Application of MHE is a tempting option for the challenging estimation problem because it may address all the difficulties just mentioned and it reuses the model and the optimization algorithms developed for the predictive controller. However, 1) the number of estimated variables is relatively high making the problem relatively computationally complex and 2) the estimation related optimization problem is badly posed, as many internal variables may have similar effect to the system outputs. These practically make real-time implementation of the MHE impossible for the complex system.

In order to overcome this problem, a hybrid Luenberger observer - MHE is proposed in this thesis, successfully implemented and is characterized by a very small computing cost, see Fig. 7.2. This is possible by splitting the estimation process into 2 layers: outer MHE layer using computationally costly non-linear model simulations to estimate the variables that have the most complex effect on the measured variables and the inner Luenberger Observer layer, that estimates variables with direct impact on the measured variables and stable internal model variables with very weak direct impact on model outputs.

The estimation is applied to a 214 m long sub-sector of the super-fluid helium cryogenic circuit and uses 1) the model simulation, 2) knowledge about physical constraints on the estimated variables

$$0 \leq W_{c,i_c}, \quad T_{s,\min}(p_{PT,r}) \leq T_{s,b}(L), \tag{7.6}$$

with cell index $i_c = 1..2$ and 3) the measured variables

$$M = [T_{TT,h}\ l_{LT,p}\ x_{CV,c}\ T_{TT,c}\ p_{PT,c}\ p_{PT,r}\ q_{EH,h}], \tag{7.7}$$

with the bath temperatures $T_{TT,h} \in \mathbb{R}^{16}$, levels in the phase separators $l_{LT,p} \in \mathbb{R}^2$, control valve positions $x_{CV,c} \in \mathbb{R}^2$, helium temperatures and pressures at the valves $T_{TT,c} \in \mathbb{R}^2$ and $p_{PT,c} \in \mathbb{R}^2$, respectively, and the very low pressure at the 1.8 K refrigerator $p_{PT,r} \in \mathbb{R}^1$. $T_{s,\min}(p_{PT,r})$ is calculated taking into account the hydrostatic pressure drop in the distribution line.

7.3.3 Moving Horizon Estimation layer

The outer MHE layer optimizes only the variables having pronounced and strongly non-linear and complex impact on the measured variables

$$X_e(t) = [\Delta W_c \quad T_{s,b}(L)], \quad X_e \in \mathbb{R}^3, \tag{7.8}$$

with $\Delta W_c \in \mathbb{R}^2$ representing error of the mass flow rate value calculated using valve sizing equations. We approximate ΔW_c and $T_{s,b}(L)$ with constant values over the MHE estimation horizon length $T_e = 0.5$ h.

7.3.4 Luenberger Observer layer

Other variables, including all model states, are estimated at the inner LO layer, where the model is simulated over MHE estimation horizon in the LO loop closed by the bath heat load

$$(\mathrm{d}q/\mathrm{d}x)_{h,l} = -5\ e_{\Delta T,h,SC2} - 100\ e_{T,h}, \tag{7.9}$$

with errors between measured and simulated bath temperature gradients:

$$e_{\Delta T,h,SC2} = \sum_{n=13}^{16} \left(w_n\ (T_{h,@TT,n} - T_{TT,h,n}) - w_{n-4}\ (T_{h,@TT,n-4} - T_{TT,h,n-4})\right) \tag{7.10}$$

and mean temperatures

$$e_{T,h} = \sum_{n=1}^{16} w_n\ (T_{h,@TT,n} - T_{TT,h,n})/16. \tag{7.11}$$

The values of the weights $w_n \in [0,1]$ depend on sensor position and quality of measurement.

7.3.5 Initial conditions

In a standard MHE formulation using direct single shooting approach, the initial conditions for the model dynamic variables must be optimized to enable model simulation over the MHE estimation horizon. However, the model states are stable in the LO loop, converging to values determined mainly by the valve positions, magnets temperature distribution and the saturation temperature level, meaning that the initial values for most of the internal model variables have little visible impact on the measured variables. Thus, in the estimator presented here, I use a different approach in order to solve the MHE simulation initial conditions at low computing cost, where simulated variables evolve between the consequent MHE executions $j-1$ and j

$$X_m^j(t-T_e) = X_m^{j-1}(t-T_e). \tag{7.12}$$

7.3.6 Optimization problem formulation

The optimization problem is solved each $\Delta t_e = 20$ s involves the model of the state space form Eqs. (6.126) & (6.127)

$$\min_{X_e} J_e, \text{ s.t. } (6.126) \;\&\; (6.127) \;\&\; (7.6) \;\&\; (7.9) \;\&\; (7.12) \tag{7.13}$$

$$J_e = \int_{t-T_e}^{t} (L_{TT} + L_{T_s} + L_{LT} + L_{W_c} + L_{q_l})\, \mathrm{d}t' \tag{7.14}$$

with cost functions representing the optimization objectives: 1) minimizing the error between the measured and simulated temperatures

$$L_{TT} \sim \sum_{i=1}^{N_{TT}=16} w_i\, (T_{h,@TT,i} - T_{TT,h,i})^2, \tag{7.15}$$

2) using approximate values of estimated variables:

$$L_{W_c} \sim \sum_{i=1}^{N_{SC}=2} \left((\Delta W_{c,i})/(W_{c,i} + 10^{-4})\right)^2 \tag{7.16}$$

$$L_{T_s} \sim \left(T_{s,b}(L) - (T_{s,r} + \Delta T_{s,QRL})\right)^2, \tag{7.17}$$

with the approximate saturation pressure drop over the distribution line $\Delta T_{s,QRL}$,

$$L_{dq/dx_l} \sim ((\mathrm{d}q/\mathrm{d}x)_l - 0.1495)^2 \tag{7.18}$$

and

$$L_{LT} \sim \sum_{i=1}^{N_{SC}} L_{LT,i} \tag{7.19}$$

and 3) respecting measurements validity range

$$L_{LT,i} \sim \begin{cases} (l_p - l_{LT})^2 & \text{if } l_{LT,i} > 13\ \% \\ 0 & \text{otherwise.} \end{cases} \tag{7.20}$$

7.3.7 Observability

Observability is a measure for how well internal states of a system can be estimated based on the observation of the system's outputs. In case of the non-linear system, the system observability will change depending on the operational conditions. A valid estimator can only be developed for an observable system.

Lack of valid estimates of some system variables in case of a non-observable system, does not necessary compromise the validity of a non-linear controller, because in some operational conditions the unknown variables may have little or no effect on the controlled variables. In case of the cryogenic system, this is the case when the magnet temperatures are kept sufficiently higher than the saturation temperature in the bayonet heat exchanger - in this case the saturation effects are negligible and the saturation temperature has negligible effect on the measured system variables. Thus, it is impossible to estimate its value based on measured system dynamics, the system is non-observable, however, at the same time, this does not affect the system dynamics and thus the its missing estimate has no impact on performance of the controller, Another example is the impossibility to differentiate between the effects of heat load and the mass flow rate in presence of vanishing bath temperature gradients, thus making the estimation of those variable impossible in these operational conditions. However, the estimation errors have little impact on the controller performance at small bath temperature gradients where the impact of this variables on the system dynamics is negligible.

However, under some conditions high quality estimates may be unavailable due to limited system observability, compromising the performance of controller. This is the case when the variables that cannot be estimated have strong impact on the controlled variables, like when bath temperature gradients vanish completely due extreme saturation effects. In this conditions, impact of two different inputs: the heat load to the bath and the saturation pressure at the heat exchanger outlet have the same effect on the bath temperature that cannot be differentiated - this happens at the bath temperatures close to the saturation temperature while the bath temperature gradients are small and this is the case when most of the measured bath temperatures are at the saturation temperature. In this conditions it is impossible to estimate the variables related to

helium accumulation in the exchanger, compromising the ability of the controller to ensure heat exchanger overflow-free operation. However, one could wonder if this could be improved by operating the circuit with a non-empty phase separator, that could allow to monitor the helium outflow from the heat exchanger, and thus the helium accumulation. However, this would need more helium to be stored in the machine.

a) basic NMPC #1 & MHE

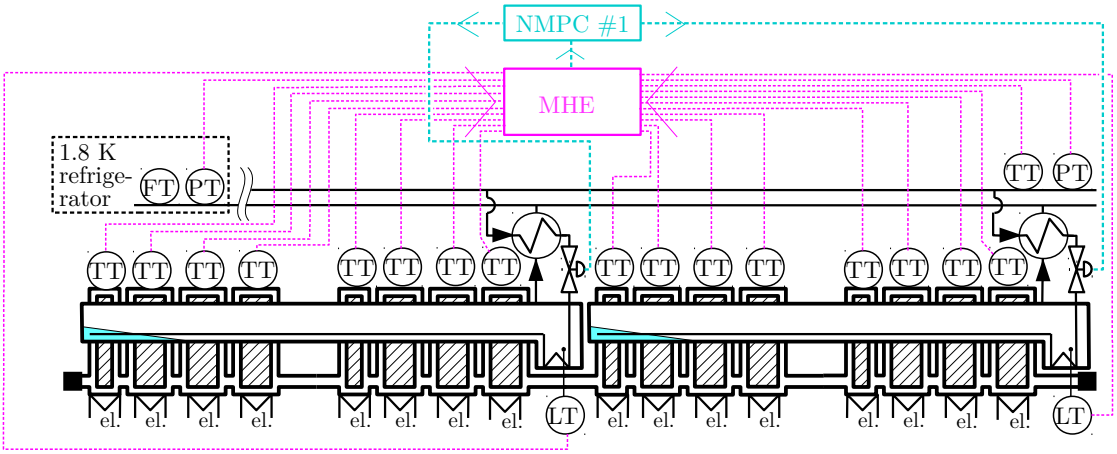

b) extended NMPC #2 & MHE

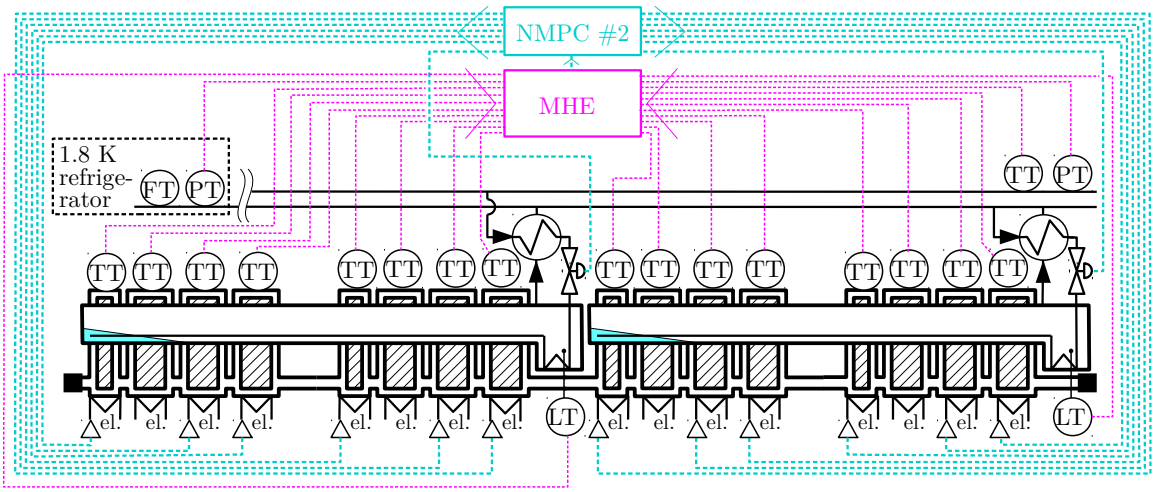

Fig. 7.3 NMPC formulations

7.4 Predictive control formulations

7.4.1 Aproach and validity

NMPC approach using the first-principles, distributed parameters model presented in Chapter 6 has been chosen to explicitly address the complex control goal, constraints and the non-linear bath temperature dynamics, including the problem of non-linear heat transfer in the helium bath and the saturation effects in the heat exchanger. This is possible due to very low computational cost of the model. The controllers presented here stabilize the temperature over a sub-sector of the superfluid helium cryogenic circuit in order to handle the strong thermal coupling between the magnets sharing common superfluid helium bath. This is a valid approach since the thermal coupling between the sub-sectors is negligeable. However, this approach does not allow to explicitly address the constraints related to the refrigerator vapor flow, that would need a much more complex coordinated control action over a complete LHC sector. Instead I started with the much simpler sub-sector wide control and I address this constraint indirectly by imposing corresponding constraints on the flow at each-subsector: limiting the flow rate and its rate of change to a fraction of that at the refrigerator, assuring that a sum of the flows will respect the constraints at the refrigerator.

The controller validity range is limited by the model fidelity and the performance of the state estimator and thus it covers full operation range with superfluid helium, except for the extreme saturation already mentioned case when most of the magnets temperature are equal to the saturation temperature, reducing the systems observability and thus the performance of the estimator. Regarding the validity with respect to the bath heat load, it has been experimentally tested to cover wide range of heat loads into the bath, up to approx. 120 W/sector corresponding to 0.56 W/m, as presented later.

I have developed two NMPC formulations, both are sub-sector wide. First, simpler, using control valves as the only manipulated variables, that does not explicitly address the minimal compressor helium mass flow rate constraint, that can be handled anyway setting the power of the electric heaters without regard on the temperature dynamic behavior, as it is done today. The second formulation dynamically uses manipulates the electric heaters to enforce the constraints on the minimal flow while optimizing the magnets temperature distribution and reducing the "waste" heat introduced into the system.

Both control strategies are formulated as non-linear programming problems with box constraints on the optimized variables, that allows to simplify the optimization and thus decrease its computational cost.

The formulation corresponds to economic NMPC because only the target values for the controlled 16 magnets temperatures are implicitly optimized alongside with the trajectories of

the optimized variables in order to satisfy a number of control objectives, including stabilization of the maximal of the magnet temperatures at the set-point and optimization of the temperature distribution in order to maximize the thermal conductivity of the bath.

7.4.2 Floating temperature strategy

7.4.3 Parametrization of the optimized trajectiories

The optimized trajectories of circuit manipulated variables are parameterized to improve conditioning of the optimization problem and to decrease the number of decision variables to 6 parameters $W^*_{c,i_{SC},i}$, 3 per trajectory, $W_{c,i_{SC}}(t') = \sum_{i=1}^{3} \sigma_i(t')\, W^*_{c,i_{SC},i}(t)$, with $N_b = 3$ basis functions $\sigma_i(t)$ used to approximate the optimal solution, see Figure 7.4. The basis functions have been design to respect constraints on change rate of mass flow rate at the control valve for the parameters values in the controller validity range. The basis functions shape has been chosen to equally redistribute the effect of each parameter on the cost functional that is minimized, in order to improve the numerical properties of the optimization problem. Moreover, the first basis function starts at 1, maintaining the continuity of the manipulated variable trajectory. Parametrisation is especially suitable for models with dynamics integration steps much shorter than the length of the prediction horizon.

7.4.4 Basic NMPC#1 manipulating control valves

The NMPC #1 optimizes trajectories of the manipulated mass flow rates at the two control valves $W_c(t')$ over the future time horizon $t \le t' \le t + T_c$, $T_c = 2$ h.

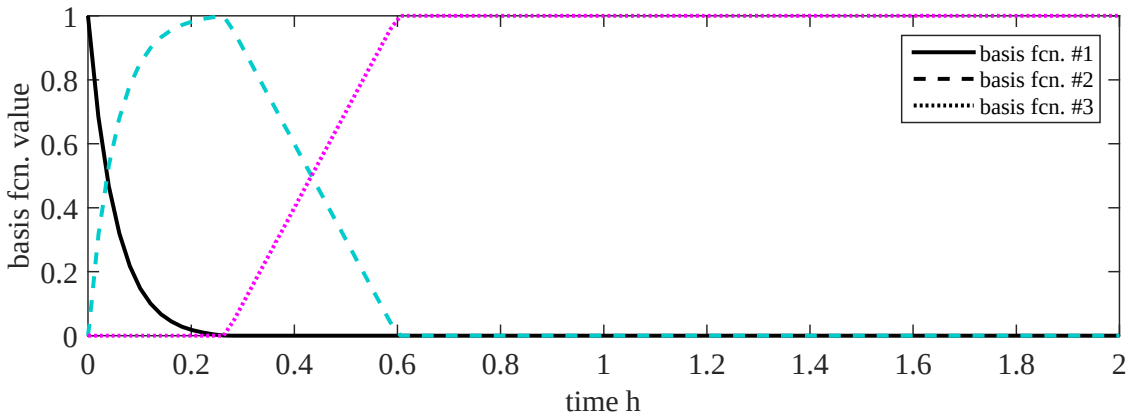

Fig. 7.4 NMPC basis functions

Due to valve rangeability,

$$W_c^* \geq W_{c,\min},\ W_{c,\min} = 0.7\ 10^{-3}\ \text{kg/s}. \tag{7.21}$$

The optimization problem is solved each $\Delta t_c = 20$ s:

$$X_{c\#1}(t) = [W_c^*], \quad X_{c\#1} \in \mathbb{R}^6. \tag{7.22}$$

$$\min_{X_{c\#1}} J_{c\#1} \text{ s.t. } (6.126) \ \& \ (6.127) \ \& \ (7.21), \tag{7.23}$$

$$J_{c\#1} = \phi_c(t+T_c) + \int_t^{t+T_c} (L_{SP} + L_{\Delta T} + L_{\Delta W_c} + L_{(\mathrm{d}W/\mathrm{d}t)_c} + C_{T_{\max}} + C_{(\mathrm{d}W/\mathrm{d}t)_c} + C_{W_c} + C_{W_o})\ \mathrm{d}t', \tag{7.24}$$

with cost functions representing multiple control objectives: stabilizing maximal sub-sector magnets temperature at set-point

$$L_{SP} \sim (\max(T_h) - T_{sp})^2, \tag{7.25}$$

promoting smaller bath temperature gradients

$$L_{\Delta T} \sim (\max(T_h) - \min(T_h))^2 \tag{7.26}$$

and equilibrated cooling power distibution

$$L_{\Delta W_c} \sim\ (W_{c,1} - W_{c,2})^2 \tag{7.27}$$

and penalizing variation of the total coolant mass flow rate

$$L_{(\mathrm{d}W/\mathrm{d}t)_c} \sim \sum_{i=1}^{2} (\mathrm{d}W_c/\mathrm{d}t)^2. \tag{7.28}$$

In order to avoid use of Lagrange multipliers, all constraints other than box constraints on optimized variables are approximatively implemented via the cost functional $J_{c\#1}$ using the non-smooth cost function

$$f_C(x) = \begin{cases} x^2 & \text{if } x > 0 \\ 0 & \text{otherwise.} \end{cases} \tag{7.29}$$

The constraints are: on the maximal magnet temperatures

$$C_{T_{\max}} \sim \sum_{i=1}^{N_x} f_C(T_{h,i} - 2.1 \text{ K}), \tag{7.30}$$

the heat exchanger zero-overflow condition

$$C_{W_o} \sim \sum_{i=1}^{2} W_{s,b,o,i}^2 \tag{7.31}$$

and regarding total sub-sector coolant mass flow rate: on its maximal value

$$C_{W_c} = \sim f_C(W_{c,1} + W_{c,2} - W_{v,ss,\max}) \tag{7.32}$$

and its change rate

$$C_{(\mathrm{d}W/\mathrm{d}t)_c} \sim f_C(|(\mathrm{d}W_{c,1}/\mathrm{d}t) + (\mathrm{d}W_{c,2}/\mathrm{d}t)| - \mathrm{d}W/\mathrm{d}t_{\max}), \tag{7.33}$$

indirectly addressing corresponding refrigerator constraints:

$$W_{v,ss,\max} = W_{v,r,\max}/13.5 = 7.7\ 10^{-3} \text{ kg/s}. \tag{7.34}$$

Note that we do not directly address the separator maximum level constraint but instead we minimize the exchanger overflow, assuring that it stays empty.

The cost at the end of the horizon, approximates the cost functions integral beyond the horizon end

$$\phi_c \sim |max\,(T_h(t+T_c) - T_{sp}(t+T_c))\,|^3, \tag{7.35}$$

representing the quadratic cost on the magnets temperature deviation from the set-point multiplied by the deviation that is proportional to the time needed to correct it.

7.4.5 Extended NMPC #2 manipulating valves and electric heaters

In order to fully address the constraints on the minimal mass flow rate at the 1.8 K refrigerator and further improve the closed loop magnets temperature dynamics another NMPC formulation is proposed. The extended NMPC #2 manipulates the two control valves and additionally 12 electric heaters installed in the bath, grouped by 3. Thus 4 optimized heaters power trajectories are parametrized with $q^*_{EH,h} \in \mathbb{R}^{12}$,

$$q^*_{EH,h} \geq 0. \tag{7.36}$$

The optimization problem is solved each $\Delta t_c = 20$ s:

$$X_{c\#2}(t) = [W_c^* \quad q_{EH,h}^*], \quad X_{c\#2} \in \mathbb{R}^{18}, \tag{7.37}$$

$$\min_{X_{c\#2}} J_{c\#2} \text{ s.t. } (6.126) \ \& \ (6.127) \ \& \ (7.21) \ \& \ (7.36), \tag{7.38}$$

$$J_{c\#2} = J_{c\#1} + \int_t^{t+T_c} (L_{EH} + C_{W_{c,\min}}) \, \mathrm{d}t', \tag{7.39}$$

with the cost functions expressing the additional economic objective of minimizing the artificial heat load

$$L_{EH} \sim \sum_{i=1}^{12} (q_{EH,h,i})^2 \tag{7.40}$$

while assuring a minimal total coolant mass flow rate at sub-sector

$$C_{W_{c,\min}} \sim f_C(-(W_{c,1} + W_{c,2} - 4 \ 10^{-3} \text{ kg/s})) \tag{7.41}$$

thus indirectly addressing the constraint on the minimal mass flow rate at the refrigerator.

7.5 Simple numerical solver

Let us use $X \in \mathbb{R}_X^N$ to represent X_e or $X_{c\#1}$ or $X_{\#2}$ and $J \in \mathbb{R}^1$ for J_e or $J_{c\#1}$ or $J_{c\#2}$ that appear in the optimization problems Eqs. (7.13), (7.23) and (7.38), respectively.

7.5.1 Direct single shooting

In order to simplify the optimization process, direct single shooting is applied to satisfy the constraints related to the model dynamics Eqs. (6.126) and (6.127), meaning that the dynamics is integrated over the estimation or prediction horizon and the simulation results are used to evaluate $J(X)$.

The numerical integrations of ODE's corresponding to state and costate dynamics are performed using explicit Forward Euler method with constant integration step. The method has been chosen despite of the fact that the circuit dynamics is stiff and relatively small time steps of integration are necessary. The maximum length of the time step assuring convergence of the numerical integration. Δt_{max} has been estimated based on eigenvalues analysis of linearized system equation $f(x,u)$.

7.5.2 Simple formulation with box constraints

Box-constraints, Eqs. (7.6), (7.21) and (7.36), are enforced by clipping off an unconstrained iterates of the solution during optimization, thus no Lagrange multipliers are needed, allowing to minimize the number of optimized variables. Some seemingly non-box constraint on manipulated variables can be expressed as such with help of mapping of input trajectories into optimized variables using trajectory parametrisation with basis functions. However, the clippling may only be applied to optimized variables, thus controller manipulated variables and any constraints involving state variables must be treated in a "soft"-way by through corresponding penalty in the cost function.

7.5.3 One-step iterative method

At each control update step j, we use a modified one-step Steepest Descent with Marquardt correction approach to calculate an unconstrained control update

$$X_u^{j+1} = X^j + \alpha^j \, \Delta X_d^j, \tag{7.42}$$

where ΔX_d^j is the search direction and α^j is the line search factor.

7.5.4 Quasi-Newton search direction using Hessian diagonal elements

In a Newton method the search direction, is calculated as $\Delta X_{d,\text{Newton}}^j = -J_{XX}^{-1} \, J_X$, using the Jacobian vector $J_X = dJ/dX$ and inverse of the the Hessian $J_{XX} = \mathrm{d}^2 J/\mathrm{d}X^2$. However, numerical calculation of the Hessian and its inverse is computationally expensive and thus an approximation of the inverse is used in a Quasi-Newton method.

In this Quasi-Newton formulation the search direction is calculated as

$$\Delta X_{d,\text{diag}}^j = -diag(J_{XX})^{-1} \, J_X \tag{7.43}$$

with the diagonal matrix $diag(J_{XX})$ composed of diagonal elements of the Hessian, that is trivial to invert.

7.5.5 Numerical smoothing

We use central finite differences to approximatively calculate the Jacobian and the diagonal elements of Hessian. In order to numerically smoothen the non-smooth model and control

problem formulations, the differences are calculated using the biggest values of the arguments perturbations that do not visibly distort the approximated derivatives.

7.5.6 Globalization

In the optimization, the k-th element of the search direction, $k = 1..N$,

$$[\Delta X_d^j]_k = \begin{cases} -[J_X^j]_k / [J_{XX}^j]_{k,k}, \\ \qquad \text{if } [J_{XX}^j]_{k,k} > |[J_X^j]_k| / [\Delta X_{d,m}]_k \\ -\operatorname{sgn}([J_X^j]_k)\ [\Delta X_{d,m}]_k, \text{ otherwise.} \end{cases} \tag{7.44}$$

This formulation assures that 1) $|[\Delta X_d^j]_k| \leq [\Delta X_{d,m}]_k$, with the maximal step length $\Delta X_{d,m}$ and 2) in case of non-positive $[J_{XX}^j]_{k,k}$, the corresponding direction is calculated using gradient descent method. We use the line search factor $\alpha^j \in \{1, 1/2, 1/4, 1/8, 1/16, 1/32\}$ corresponding to smallest $J(X_u^{j+1})$.

This formulation takes into account that in practical control systems a reasonable solution accuracy is on order of 1% of the operational range of the optimized variable due to limited precision of the actuators. Thus limiting the minimal value of the line search factor won't affect the control system performance, even though the due to the limits on the minimal length of the iterative solution increment, the iterates will oscillate around the solution, the amplitude of this oscillation is much smaller than the accuracy of the actuators.

7.5.7 Clipping to satisfy box constraints

Finally, the unconstrained control update is clipped to satisfy the box constraints, producing X^{j+1}.

7.5.8 Discussion

The minimization of the cost function is performed using a Quasi-Newton method to solve the first order optimality conditions and apply a simple quasi-globalisation method suitable for the accuracy levels needed in advanced control formulations.

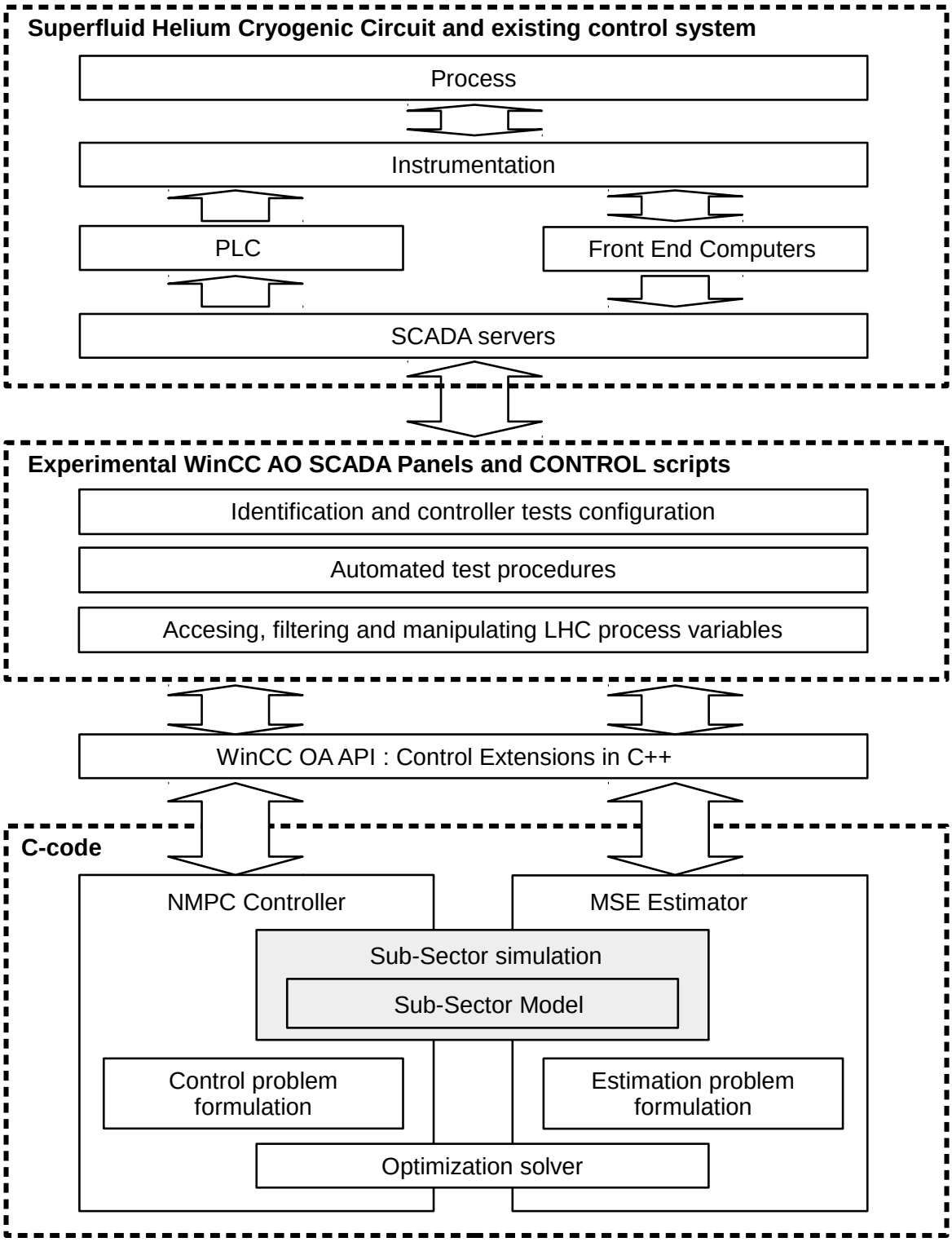

Fig. 7.5 NMPC experimental implementation at the LHC

7.6 Controller implementation and simulation setup

The controller has been implemented in C and is composed of two parts: the application dedicated implementation of the control problem formulation and the application independent optimizer.

The controller simulations have been implemented in MATLAB®, where the C code has been interfaced through MEX-files, see Fig. 6.3.

The LHC experimental proof of concept controller has been implemented as a Siemens SIMATIC WinCC OA SCADA panel, interfacing the C code using control extensions, accessing the process variables and sending values of manipulated variables to the PLC of the process, see Fig. 7.5. Thus the PLC acts as an I/O card. The same control panel type may be used for all sub-sectors and a sub-sector specific data is loaded from a configuration file. All important variables are displayed in real time, including the future system trajectories, see Fig. 7.6.

7.7 Conclusions

The output feedback advanced controller formulations directly and indirectly address all the challenging aspects of the magnets temperature stabilisation at the LHC. Hybrid MHE-LO formulation, optimization problem formulation as one with box-constraints and very simple Quasi-Newton solution method are used solve perform the optimization at lowest computational cost. The implementation has a clear modular structure, allowing to reuse the same code in the NMPC and in MHE and in implementations in simulation and in the experimental validation at the LHC.

Fig. 7.6 Proof-of-concept NMPC implementation as SIEMENS SIMATIC WinCC OA SCADA Panel. The cell specific data is loaded using the panel on the left. The MHE related variables are displayed in the middle and the NMPC predictions are displayed on the right side of the panel.

Chapter 8

Experimental and simulated performance of the predictive controllers

8.1 Introduction

The plant dynamics is strongly affected by the operational conditions defining the operational point: mainly by 1) the stand-by heat load into the bath and the corresponding magnets temperatures distribution and helium mass flow rates at the control valves, but also by 2) the saturation temperature in the heat exchanger and 3) magnets temperature levels.

The circuit has a built in redundancy and thus the machine operation is still possible with faulty redundant instrumentation, like one control valve or multiple bath temperature sensors. The fault-mode operational conditions may be very different from the ones when more instrumentation is available.

There are two principal circuit operational scenarios with superfluid He II: 1) superconducting magnets temperature stabilization at a set-point and 2) final cool-down, large transient phase.

The goal of this chapter is to present the performance of the controllers presented in the previous chapter in wide range of operating conditions and operating scenarios. Due to limited availability of the LHC circuit for tests, the controller performance has been experimentally tested only in tempertaure stabilisation scenario in wide range of heat loads and coolant mass flow rates, at saturation temperatures and magnet temperatures corresponding to LHC nominal operation. Other scenarios have been simulated.

In contrast to the currently used PI controller, where set-point is adjusted as saturation temperature rise in order to avoid helium accumulation in the heat exchanger, the NMPC set-point is always $T_{sp,NMPC} = 1.9$ K and at higher saturation temperature the desired magnets

temperatures are optimized as closest to the set-point that assure no-overflow of the heat exchanger.

8.1.1 Simulations

Simulations of the closed loop NMPC performance have been heavily used during controller development and tuning. In the early simulations, the circuit has been represented using the same model as the one used in simulations. This allows to test the NMPC performance corresponding to the ideal case of no model-plant mismatch and focus on the basic performance of the controller. Later, the robustness of the controller has been tested using different parameters for models used in the controller and that representing the plant, introducing the mismatch.

8.1.2 Experimental validation

All the LHC experimental tests scenarios have been implemented as programs in a SCADA panel and then executed automatically in order to obtain a repetitive test pattern. All test scenarios executed experimentally have been simulated first, in order to reduce to the minimum tuning activities at the LHC.

8.2 Experimental temperature stabilisation at nominal saturation temperature

The basic functionality of the NMPC is its ability to stabilize the magnets temperature at the set-point during nominal LHC operation with beam. Stand-by bath heat loads varying due to insulation vacuum quality or parameters of other LHC circuits have strongest impact the operating point - the magnets temperature distribution and thus the temperature dynamics. Thus, the tests presented here start at various stand-by heat loads into the bath, then a 40 W over sub-sector, 20 min long heat pulse into the bath imitates ramping up of magnet current during particles acceleration to 7 TeV and it is followed by additional 20 W of load corresponding to nominal LHC operation.

8.2.1 NMPC #1

Figures 8.1a and 8.1b demonstrate the experimental NMPC #1 performance, at nominal and five different stand-by heat load levels, respectively. Starting at approx. 35 W over sub-sector (0.17 W/m) corresponding to the LHC nominal, increased to approx 55 W over sub-sector

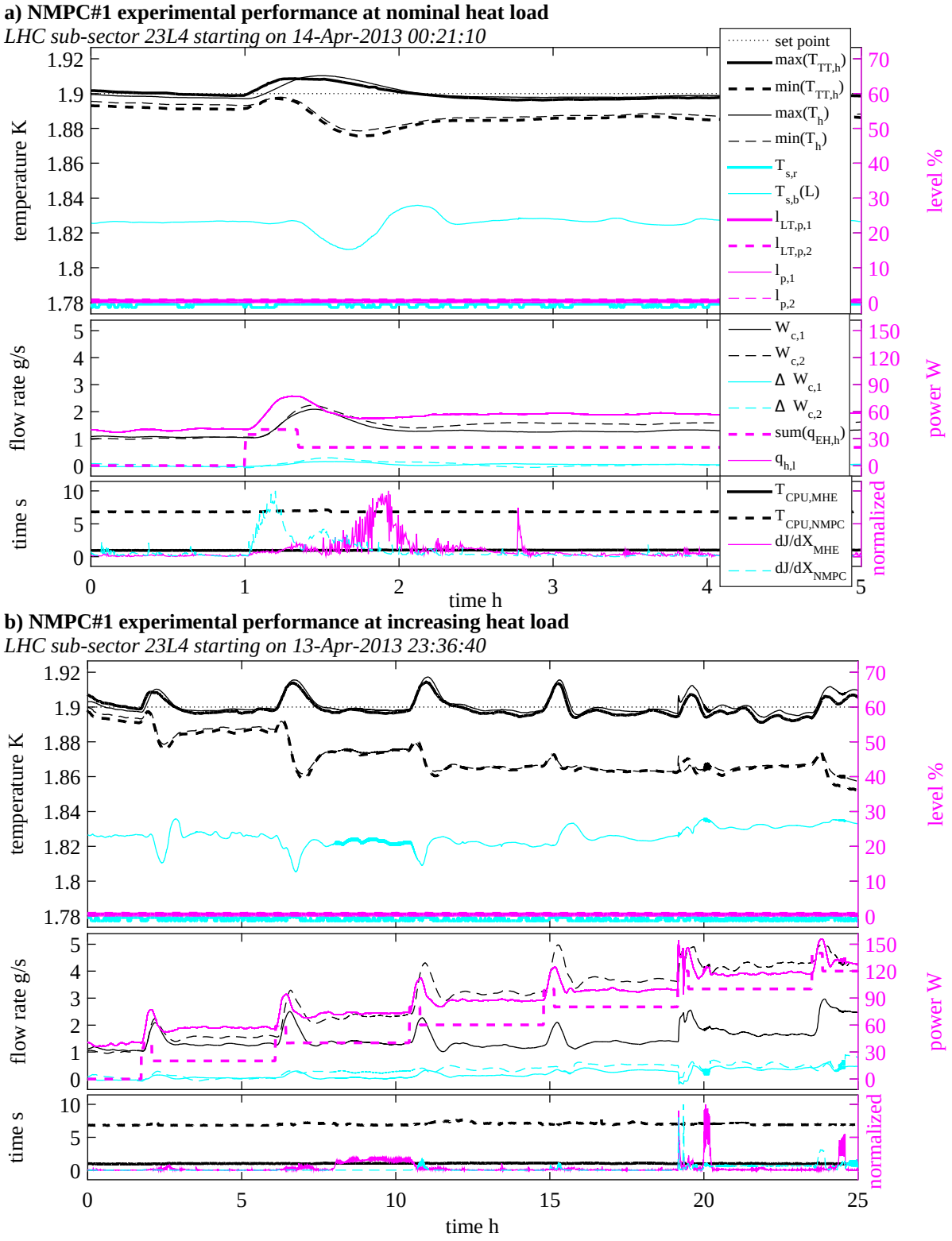

Fig. 8.1 Experimental NMPC #1 performance.

(0.26 W/m), approx. 75 W over sub-sector (0.35 W/m) then approx. 95 W (0.44 W/m) corresponding to the validity limit of the controller and finally to approx. 115 W over sub-sector (0.54 W/m) beyond the validity range. In all cases the maximal magnets temperature has quasi-identical fast closed loop dynamics and reaches the set-point 1 h after perturbation occurs, however then it settles slightly under the set-point. This is despite the fact that the bath temperatures distribution varies strongly between the cases, as indicated by the lowest bath temperature that is quasi-constant at the highest heat loads due to strong saturation effects. All the implemented constraints are respected, however the sum of the coolant mass flow rates at nominal heat load varies between approx 2 g/s and 3 g/s and may be to small to satisfy the constraint on the minimal mass flow rate at the 1.8 K refrigerator. At highest heat loads, beyond the validity range, the observed erratic behavior of the estimator may be one of the reasons for the oscillations of the closed loop controlled maximal magnets temperature.

8.3 Simulated temperature stabilisation at nominal saturation temperature

8.3.1 NMPC #2a

In simulations, presented in Figures 8.2a and 8.2b, the NMPC#2a, which promotes application of electric heaters close to the wetted heat exchanger extremity, stabilized the magnets tempertaure at the setpoint some 3 h after the perturbation and thus its closed loop dynamics is slower than that of the NMPC#1. The reason for that may be higher observed bath temperature and higher coolant mass flow rates at lower bath heat loads, that allow to maintain the sum of coolant mass flow rates above 4 g/s, thus satisfying the corresponding constraint. The electric heaters power introduced into the bath decreases progressively as the heat load increases.

8.3.2 NMPC #2b

Simulation results of the NMPC#2a, which promotes uniform application of electric heaters along the bath is presented in Figure 8.3. At nominal heat loads, the NMPC#2 drives the maximal temperature back to the set-point 0.5 h after the perturbation occurred and the peak temperature perturbation is half of that achieved by the two other NMPC formulations. Moreover, the coolant mass flow rate in a sub-sector is virtually constant equal to the minimal allowed value. The simulated closed loop dynamics is fast, and progressive decrease of electric power s observed as the heat load increase. The bath temperature gradients are larger than

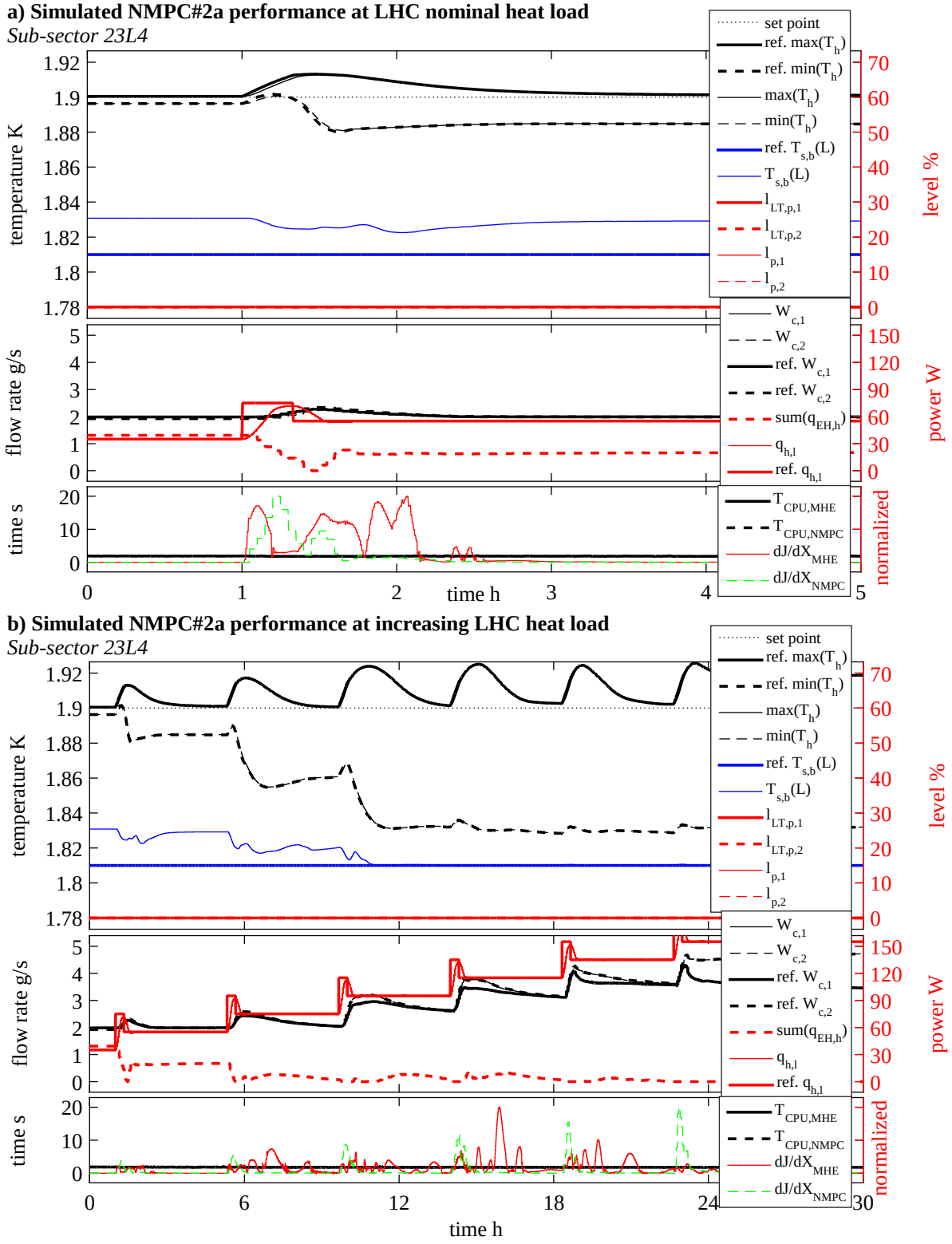

Fig. 8.2 Simulated NMPC #2a performance.

observed in previous cases because all electric heaters are used equally strong and thus more heat is transferred along the helium bath.

8.4 Simulated temperature stabilisation at high saturation temperature

The simulation results of closed loop dynamics of NMPC#2a at high satutarion temperatures are presented in Figure 8.4. As the set-point for the maximal magnets temperature being 1.9 K is impossible to achieve at high saturation temperature at the heat exchanger output of 2.08 K , the controller stabilizes the temperature at the minimal level that allows to avoid helium accumulation in the phase separators. The observed separation between the magnets and saturation temperatures is very small and the maximal magnets temperature stays under the operational constraint of 2.1 K during the whole test, also in presence of perturbations due to heat load.

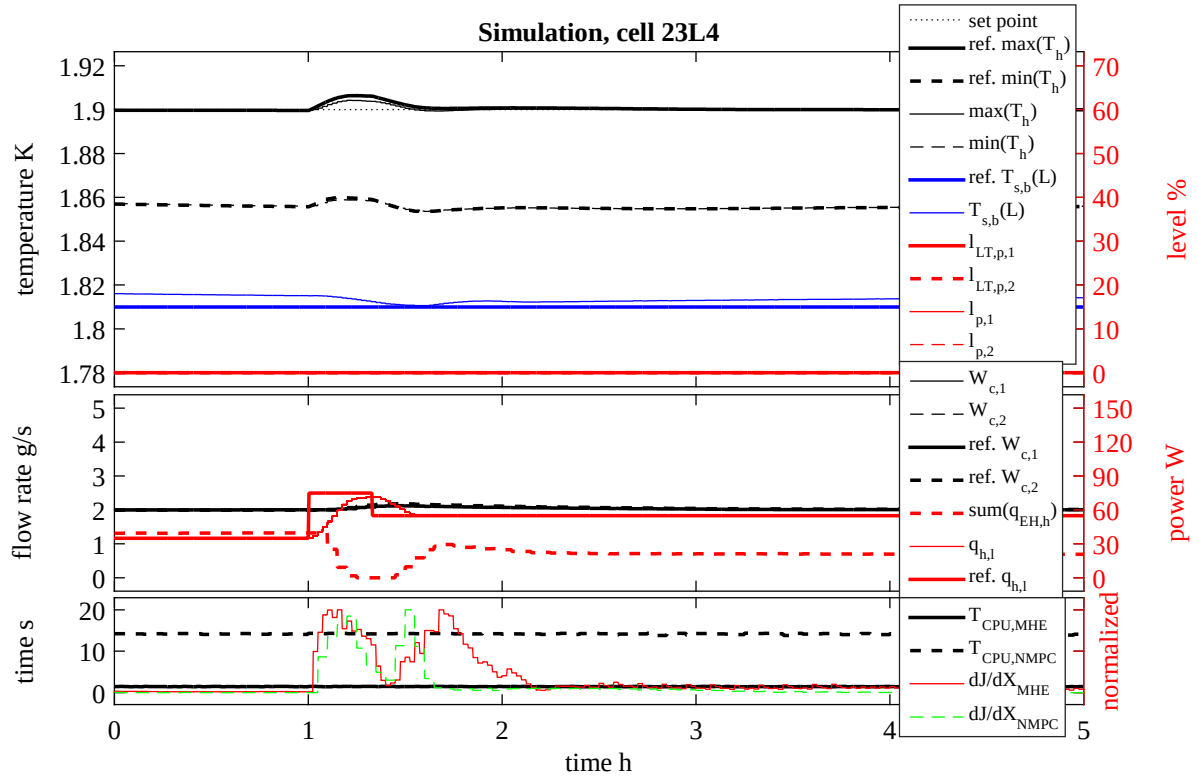

Fig. 8.3 Simulated NMPC #2 performance.

8.5 Simulated large transients during final cool-down

Large transient phase performance of the NMPC#2a has been simulated and the results are presented in Figure 8.5. The state estimator is turned on at time t = 0.5 h and the controller at t = 0.7 h. The controller action is smooth and precise and allows for cool-down from 2.02 K to 1.9 k in approx. 3 h time, while respecting all constraints.

8.6 Simulated instrumentation failure scenarios

Out of two valves, the valve number 2 provides the helium to wetted zone located in the middle of a sub-sector and thus it provides cooling to both cells in a sub-sector. When the valve is unavailable, the valve number 1 provides the cooling power at the extremity of the sub-sector opposite to its warmest end, and thus the distance between the wetted zone and the warmest magnets may reach 200 m, making the PI control very difficult due to large delay times. Simulated controller performance at this failure scenario is excellent, see Fig. 8.6, with 2 h time necessary to bring the temperature back to the set-point after perturbation. However then the temperature slightly undershoots the set-point. All constraints are respected. The

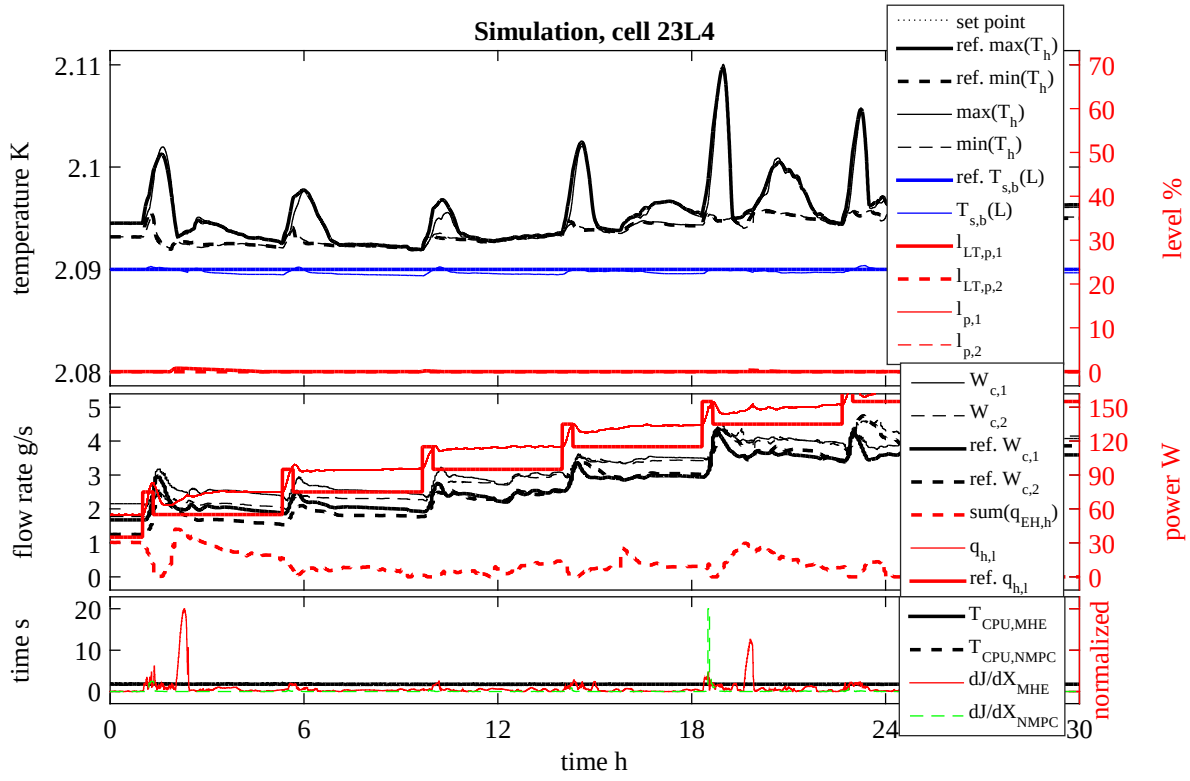

Fig. 8.4 Simulated NMPC #2 performance at high saturation temperature.

magnets temperature gradients are huge even at lowest heat loads, as expected when the heat load corresponding to two standard cells is conducted through the bath.

Performance of the controller in the case of failing sensors is defined by the performance of the LO-MHE estimator, since virtually all of the model state and input variables are estimated.

8.7 Numerical aspects

During all tests, the control update computation (CPU) time on a PC class computers is quasi-constant and approximately equal to: 7 s for the NMPC#1, 14 s for NMPC#2 and 1 s for the hybrid LO-MHE state estimator. The values of first order optimality condition $\|dJ/dX\|$ converge to zero relatively fast after each perturbation in case of both NMPC formulations, however the convergence is much slower in case of the state estimator.

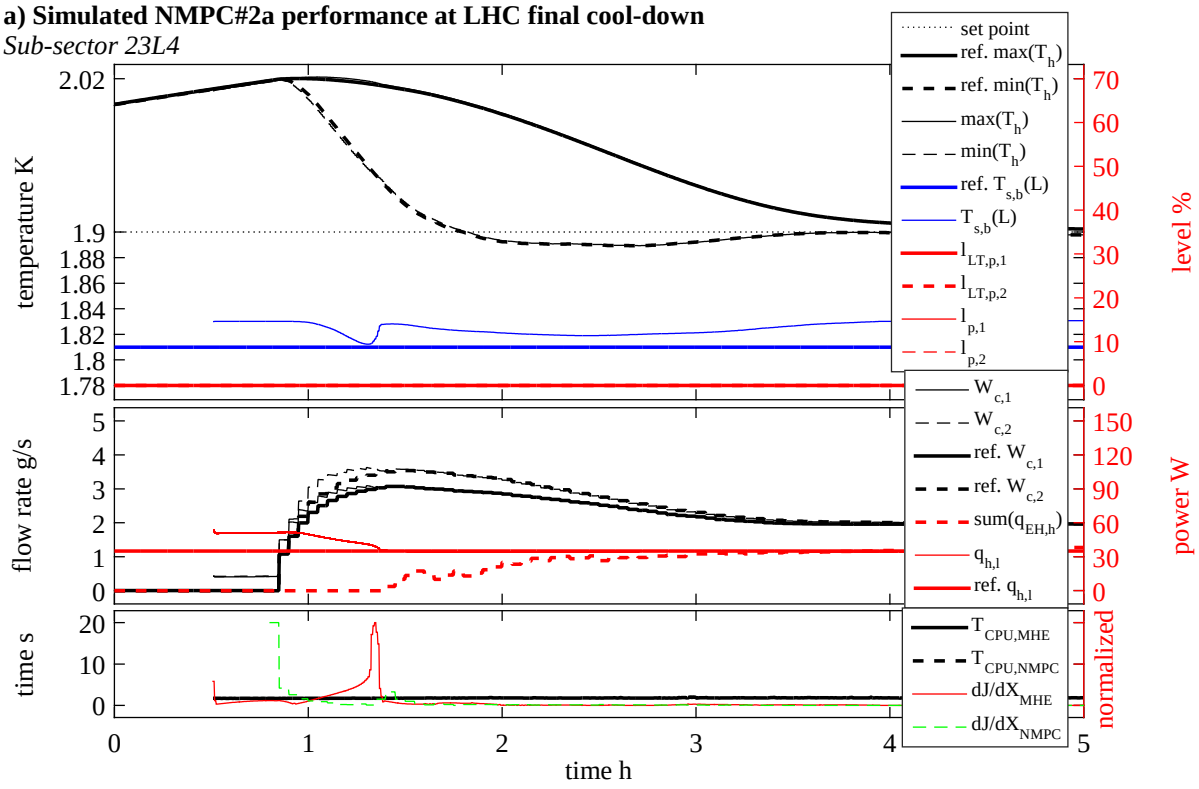

Fig. 8.5 Simulated NMPC #2a large transient performance.

8.8 Conclusions

The experimets performed at the LHC only cover conditions corresponding to operation with beam, however over a wide range of heat loads into the bath. The excellent experimental results validate the model in the control application at wide range of heat loads, providing some credibility for the simulation results. A large number of additional operational scenarios has been simulated at the LHC, covering the whole range of the operational conditions with superfluid He II, including some failure scenarios, all with excellent results.

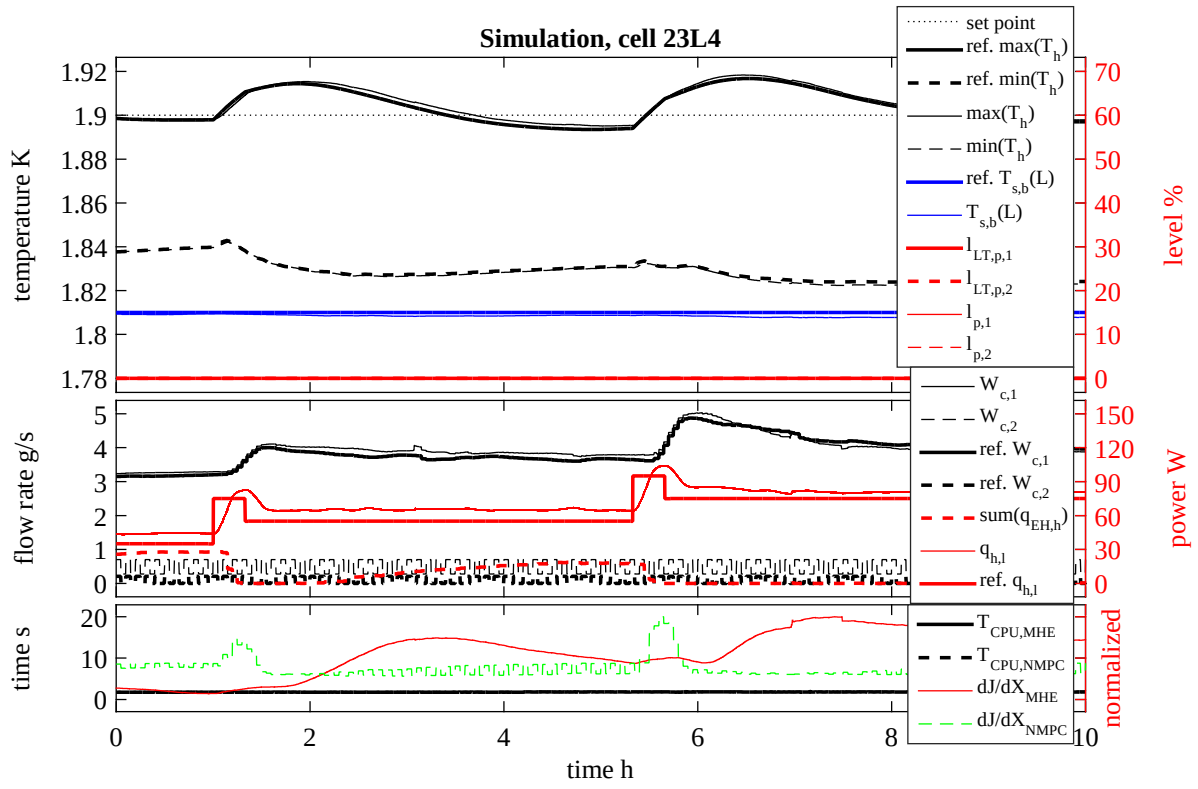

Fig. 8.6 Simulated NMPC #2a CV2 failure performance.

Chapter 9

Conclusions and outlook

In this thesis, I have presented the first ever first-principles model of the superfluid helium cryogenic circuit dynamics that has enabled the proof of concept output feedback NMPC implementation for the superconducting magnets temperature stabilisation in the arcs of the LHC. The real-time feasible output-feedback economic NMPC is based on the rather complicated model and online optimization, both optimized for low computational complexity. Performances of both the model and the controller have been extensively tested at the LHC and in simulations. The model and the controller are valid in a wide range of operational conditions. The NMPC heavily outperforms the currently used PI controllers, introducing new exciting quality of the magnets temperature closed loop dynamics for both temperature stabilisation around the set-point and the large transient final cool-down phase. This application proves that the optimization based advanced control technique may be used to significantly improve the magnets cool-down and temperature stabilization in wide range of operational conditions.

9.1 On-line output feedback NMPC for complex systems

The output-feedback economic NMPCs based on a complex first-principles model are real-time feasible, demonstrating that thoughtful model formulation and implementation, approximated formulation of the optimization problem and application of a very simple solver enable application of on-line NMPC to more complex systems. The formulation allows to trade-off the accuracy against the computational complexity of the model simulation and optimization of control actions. The computing cost efficient hybrid LO-MSE formulation is the key component enabling these output-feedback applications. It allows to greatly reduce the number of MHE optimized variables by assigning most of the estimated variables to the LO, resulting in an extremely computing cost efficient non-linear estimator.

Strongly simplified single-step solver seems to be suitable in this application, where the optimization is repeated continuously and the range of the optimized variables is well defined and relatively small comparing to the relatively low demanded precision of the solution that needs not to exceed that of the manipulated actuators. However, one could argue if the performance of the simple solver is not good enough especially in the case of the estimator, where the convergence of the first-order optimality condition was relatively slow and sometimes erratic.

Similarly, the properties of the MHE-LO formulation should be further investigated, since it is expected that reducing the number of decision variables in the optimal estimation problem must have negative effect on the numerical properties of the algorithm - analogically to the single shooting formulation having worse numerical properties than the multiple shooting formulation.

The real-time feasibility approach using a complex model and simplified optimization algorithms is on contrast to the previously used employing simple models and off the shelf optimization algorithms (Blanco (2001)).

9.2 First principles model performance

The modelling approach used to develop the model, allowed to trade off the model accuracy against its computational complexity. The model is accurate enough to provide valid prediction over the NMPC prediction horizon and its computation complexity is so low that it can be executed approx. 15'000 faster than the real-time evolution of the simulated dynamics. Thus, the model is perfectly suited for the online optimisation based NMPC.

The non-linear model accurately represents the system dynamic over a wide range of operational conditions due to relatively detailed modelling of the key physical processes behind the dynamics. The modelling preceded by the system analysis enabled deeper understanding of the processes and some nuances related to the observed circuit dynamics, allowing to better formulate the control goals for this circuit and to improve similar circuit designs in the future. The analysis was also an unique opportunity to survey all the research work related to the prototype circuit done over last 20+ years.

9.3 Output feedback controller performance

Experimental performance of the NMPC #1 is excellent in wide range of heat loads and represents a new quality with respect to that of the currently used PI controllers. The robust NMPC/MHE closed loop dynamics of the maximal magnets temperature is almost identical at

all the very different heat loads: it is 10 times faster than that of the PIs and the implemented constraints including that on the mass flow rate change are respected, however the temperature stabilizes slightly under the set-point. This has been achieved in presence of strongly varying heat loads and thus temperature distributions in the bath indicated by the lowest bath temperature: with strong saturation effects promoting phase separator overflow in case of the higher heat loads. This remarkable performance is the ultimate validation of the model, designed for this application.

However, the NMPC #1 does not address the important constraint on the minimal vapor mass flow rate at the 1.8 K refrigerator. And thus the problem of uisng the electric heaters to maintain the minimal heat load into the baths and thus the minimal coolant mass flow rate must be handled separately, as it is done today. Operating closer to this constraint has direct economic impact on the LHC operation since generation of cooling power at the extremely low temperatures of 1.8 K is extremely costly and even the World's most efficient LHC 1.8 K refrigeration cycle achieves a coefficient of performance of only 0.0011.

The extended NMPC#2a and NMPC#2b formulations have been developed to address the 1.8 K refrigerator constraint at sub-sector level, manipulating the electric heaters alongside with the valves in order to generate exactly the required minimal coolant mass flow rate. The difference between the two is the pattern of the spatial distribution of the electric heater power over a sub-sector length. The NMPC#2a promotes powering of the heaters installed close to the wetted sub-sector extremity in order to reduce the additional heat transfer through the bath and thus the bath temperature gradients, that have negative effect on the system dynamics. The NMPC#2b promotes more qual powering of heaters along the sub-sector.

Simulations demonstrate that both the of formulations efficiently address the constraint at the sub-sector level. However, at their closed loop performance at nominal heat load is different. In fact NMPC#2a closed loop is much slower than that of the NMPC#2b. Moreover, the maximal magnet temperature perturbation is reduced by half by the NMPC#2b. The reason for this it that the magnets temperature response to the heaters power is instantaneous and thus maintaining heaters powered at the warm sub-sector extremity allows to decrease it when needed and thus immediately compensate for the additional bath heat loads generated due to the LHC operation. In other words, the more equal distribution of electric heaters power results in larger bath temperature gradients that help to evacuate the additional heat load, reducing the need for the gradient increase after perturbation and thus contributing to the maximal temperature stabilisation. That is why the NMPC#2b simulations indicate excellent closed loop dynamics, that could out-perform event the NMPC#1.

Simulation results demonstrate the potential of the NMPC#2b to perform efficiently in wide range of operational conditions and scenarios outside of the temperature stabilisation at varying

heat loads. The controller performs very fast and accurate final cool-down, that is the most challanging operational scenario for the currently used PI controllers. It is capable to stabilize the magnets temperature very close to the saturation temperature in the heat exchanger, which is may be very useful to maintain the LHC operation while the saturation temperature is high due to perturbations of the 1.8 K refrigerator operation. Moreover, the controller maintains its excellent performance even in case of limited availability of manipulated system inputs and outputs due to potential serious instrumentation failures.

Using the single-step solver allowed to achieve constant control update computation time in order of few seconds for the NMPC and one second for the hybrid LO-MHE state estimator, on a PC computer. Of course, the CPU time may vary in function of processor load if the CPU is not exclusively used by the controller. The first order optimality condition that is the norm of the Jacobian vector $\|\mathrm{d}J/\mathrm{d}X\|$ of first derivatives of the cost function has a dynamics that converges to zero relatively fast after each perturbation.

9.4 Future work

This successful model and proof of concept NMPC development opens up a number of interesting future research and development opportunities.

9.4.1 Production implementation

All the LHC experiments were done during the LHC Run 1 and thus before the 1st LHC Long Shutdown (LS1) technical maintenance period, during which all LHC magnets interconnections have been consolidated. Since the interconnection geometry has crucial impact in the heat transfer in the helium bath, both model and controller validation should be repeated at the LHC and eventually the model parameters related to the helium bath cross-section should be updated.

Then, a robust, industrial implementation of the controller could be developed. It could consist of an industrial computer running the advanced controller in a similar manner to the SCADA implementation: sending the values of PI controller outputs kept in the manual mode, that would allow the PI controllers to take over in case of problems wit the advanced controller.

The very low computational cost of model simulation, leaves some room for application of more sophisticated model simulation and optimization algorithms. Their application may be crucial for a robust industrial application of the NMPC.

9.4.2 Soft sensors and other model applications

The state estimator can be implemented independently as an industrial soft sensor providing the estimates of the unmeasured system parameters and allowing to improve the performance of the currently used PI controllers, like actual heat load into the bath, saturation temperature, wetted length of the heat exchanger. This information can be used also to perform on-line diagnostics of the circuit.

Other possible application may be in operators training and optimisation of the machine operation.

9.4.3 Improvements of model formulation

There are at least to aspects of the modelling description with significant impact on model performance at the limits of its validity range that may be improved.

Heat transfer in superfluid helium bath

Very high estimated heat load at the location of vacuum barrier and the need of the correction of heat transfer in superfluid helium bath in Eq. (6.14) indicates that a non-negligible heat load or heat transfer mechanism (convection?) is missing in the model and process analysis.

Shear drag force at superfluid-vapor interface in heat exchanger

In order to improve the model accuracy in presence of strong saturation effects and thus extend its validity range to higher heat loads that could be useful in future more powerful designs, the frictional shear force at the superfluid-vapor phase boundary could be implemented into the model. In this case, appropriate model identification experiments should be developed that cover the extreme operational range with strong saturation effects and significant wetted length of the heat exchanger. This operational range is of interest because it corresponds to operation at much higher heat load loads and lower bath temperature gradients, where the full potential of NMPC could be exhibited.

Heat transfer coefficient of feeding pipe

In order to remove some of the modelling errors observed at higher bath temperature gradients, the description of heat transfer in the feeding pipe presented in this thesis could be possible refined. This may be related to the fact that description of the heat transfers originating at the feeding pipe is limited to the case when superfluid is present in the pipe, while simulation results indicate that at high mass flow rates at the valve, the flow temperature may exceed

the super-fluid - liquid phase transition temperature and thus the description is incomplete. Moreover, the approach to identification of corresponding model parameters could be improved by deeper analysis of the impact of model parameters on the simulated dynamics and better choice of experimental reference data.

9.4.4 Extended controller formulations

True sector- or double-sector-wide control

An extension of the control scheme over a complete LHC sector in order to fully control the coolant flow at the 1.8 K refrigerator using a distributed NMPC or parallel computing approach would definitely be a challenge. In this case, a dynamics model of the very low suction pressure distribution in the cryogenic distribution line could be used to improve the control.

Feed-forwarding magnet currents information

Implementation of feed-forward control taking into account the planned magnets current ramp during particles acceleration seems to be a desired extension of the predictive controllers. It should be straight forward to implement, adding magnet currents as model inputs corresponding to important measured perturbations. The impact of the current on the heat loads has been analyzed in this thesis. However, it would also involve a stronger integration with the LHC powering system, to obtain the magnet ramping information sufficiently in advance, which would also need deeper analysis of the LHC magnets powering procedures.

9.4.5 Alternative control formulations

Other control strategy that could be possibility realized using the model is aiming at stabilization of certain helium level in the phase separators, allowing to work with the heat exchanger wetted along its full length and keep the magnets temperature uniformly at the saturation temperature. However, this would probably need more model validation experiments at the range where the heat exchanger is full and subsequent model tuning.

Alternative control problem formulations may be investigated too. An batch control approach could be studied to take advantage of the repetitive nature of the perturbations related to the magnets current ramping. Another possibility is to reformulate the sub-sector wide NMPC optimized variables to be the sum of the mass flow rates at the valves and their ration, that would allow to apply the constraints on the minimal and maximal sum of mass flow rates simply by clipping off the the optimized variables. In this case suitable basis functions for the ratio trajectory parametrization should be developed.

9.4.6 Application of multi-thread based computing

The single shooting approach used in the controller is suitable for implementation using parallelization techniques, where part of the code is executed simultaneously using multiple cores to further accelerate the speed of optimisation. In fact each of the simulations performed to numerically evaluate the Jacobians and Hessians of the cost functional at each Newton-method iteration may be performed independently as separate thread.

References

Andersen, J. (2002). Temperature control at the CERN Large Hadron Collider. Master's thesis, NNTU, Trondheim.

Arp, V. D. and McCarty, R. D. (1989). Thermophysical properties of helium-4 from 0.8 to 1500 K with pressures to 2000 MPa. Technical report, US. Nat. Bureau Stand. Technol. Div.

Arpaia, P., Blanco, E., Girone, M., Inglese, V., Pezzetti, M., Piccinelli, F., and Serio, L. (2015). Proof-of-principle demonstration of a virtual flow meter-based transducer for gaseous helium monitoring in particle accelerator cryogenics. *Review of Scientific Instruments*, 86(7):–.

Balle, C., Casas-Cubillos, J., Vauthier, N., and Thermeau, J. (2007). Calibration of Cryogenic Thermometers for the LHC. Technical report, CERN. LHC-PROJECT-Report-1077.

Baudouy, B., Bessette, A., and Four, A. (2013). Modeling of a horizontal circulation open loop in two-phase helium. *Cryogenics*, 53:2 – 6.

Bézaguet, A.-A., Casas-Cubillos, J., Lebrun, P., Marquet, M., Tavian, L., and Van Weelderen, R. (1993). The superfluid helium model cryoloop for the CERN large hadron collider (LHC). Technical report, CERN. CERN-AT-93-21-CR. CERN-LHC-Note-233.

Blanco, E. (2001). *Nonlinear Model-based Predictive Control Applied To Large Scale Cryogenics Facilities*. PhD thesis, U. of Valladolid.

Blanco, E., de Prada, C., Cristea, S., and Casas, J. (2009). Nonlinear predictive control in the LHC accelerator. *Control Eng. Pract.*, 17(10):1136–1147.

Blanco, E (2003). Supefluid Helium Cooling Loop on String 2. Technical report, CERN.

Bourcey, N., Nielsen, L., Parma, V., Rohmig, P., Roy, E., and Bergot, J. B. (2002). Thermal performance of the LHC short straight section cryostat. In *Particle accelerator. Proceedings, 8th European Conference, EPAC 2002, Paris, France, June 3-7, 2002*, pages 2526–2528.

Bradu, B. (2010). *Modélisation, simulation et contrôle des installations cryogéniques du CERN*. PhD thesis, University Paris-Sud 11.

Brunet, J. C., Parma, V., Peón-Hernández, G., Poncet, A., Rohmig, P., Skoczen, B., and Williams, L. R. (1997). Design of the second series 15 m LHC prototype dipole magnet cryostats. Technical report, CERN. CERN-LHC-Project-Report-133.

Brüning, O. S., Collier, P., Lebrun, P., Myers, S., Ostojic, R., Poole, J., and Proudlock, P., editors (2004). *LHC Design Report*. CERN.

Burla, P., King, Q., and Pett, J. G. (1999). Optimization of the Current Ramp for the LHC. In *Particle accelerator. Proceedings, 18th Biennal Conference, PAC'99, New York, USA*. CERN-LHC-PROJECT-REPORT-281, LHC-PROJECT-REPORT-281.

Burnod, L., Leroy, D., Szeless, B., Baudouy, B., and Meuris, C. (1994). Thermal modelling of the LHC dipoles functioning in superfluid helium. Technical report, CERN. CERN-AT-94-21-MA. CERN-LHC-Note-281.

Camacho, D., Chevassus, S., Policella, C., Rieubland, J. M., Vandoni, G., and Van Weelderen, R. (1998). Thermal Characterization of the HeII LHC Heat Exchanger Tube. Technical report, CERN. CERN-LHC-Project-Report-232.

Carlson, D., Haurie, A., and Leizarowitz, A. (1991). *Infinite Horizon Optimal Control*. Springer Verlag.

Casas, J. and Van Weelderen, R. (1993). Modèle de simulation de la dynamique du transfert de chaleur dans une boucle cryogénique d'hélium superfluide. Technical report, CERN.

Casas-Cubillos, J., Chorowski, M., Claudet, S., Ganni, R., Klebaner, A., Parma, V., Peterson, T., Riddone, G., Rode, C., Rousset, B., Serio, L., Tavian, L., Theilacker, J., Vullierme, B., Van Weelderen, R., and Weisend, J. (2007). Baseline Configuration of the Cryogenic System for the International Linear Collider. Technical report, CERN. CERN-AT-2007-002-ACR.

CERN (2013). The Large Electron-Positron Collider. CERN website.

CERN Press Office (2013). About CERN. CERN Press Release.

Chen, H. and Allgöwer, F. (1998). A Quasi-Infinite Horizon Nonlinear Model Predictive Control Scheme with Guaranteed Stability. *Automatica*, 34(10):1205 – 1217.

Claudet, G. (1993). The Tore Supra He II cryogenic system. *Fusion Engineering and Design*, 20:485–490.

Claudet, S. (2005). Recent Progress in Power Refrigeration below 2 K for Superconducting Accelerators. Technical report, CERN. CERN-AT-2005-012-ACR.

Claudet, S., Ferlin, G., Millet, F., and Tavian, L. (2004). 1.8 K Refrigeration Units for the LHC: Performance Assessment of Pre-series Units. Technical report, CERN. CERN-LHC-Project-Report-797.

Collier, J. (1972). *Convective boiling and condensation. 2nd ed. London*. McGraw-Hill.

Conn, A. R., Gould, N. I. M., and Toint, P. L. (2000). *Trust-region Methods*. Society for Industrial and Applied Mathematics.

CRYODATA INC. (1999). User's Guide to HEPAK Version 3.4.

Cyvoct, A., Lebrun, P., Marquet, M., Tavian, L., and Van Weelderen, R. (1991). Heated two-phase flow of saturated helium II over a length of 24 m. Technical report, CERN. CERN-AT-91-28-CR. CERN-LHC-Note-169.

Diehl, M., Ferreau, H., and Haverbeke, N. (2009). Efficient numerical methods for nonlinear MPC and moving horizon estimation. In Magni, L., Raimondo, D., and Allgöwer, F., editors, *Nonlinear Model Predictive Control*, volume 384 of *Lecture Notes in Control and Information Sciences*, pages 391–417. Springer Berlin Heidelberg.

Dufay, L., Perin, A., and Van Weelderen, R. (1999). Characterization of Prototype Superfluid Helium Safety Relief Valves for the LHC Magnets. Technical Report LHC-Project-Report-318. CERN-LHC-Project-Report-318, CERN, Geneva.

Ekin, J. W. (2006). *Experimental Techniques for Low-Temperature Measurements: Cryostat Design, Material Properties, and Superconductor Critical-Current Testing*. Oxford Univ. Press, Oxford.

Evans, L. and Bryant, P. (2008). LHC machine. *Journal of Instrumentation*, 3(08):S08001.

Ferlin, G., Claudet, S., Tavian, L., and Wagner, U. (2010). 1.9 K Heat Inleak and Resistive Heating Measurements on LHC Cryomagnets. Technical report, CERN. CERN-ATS-2010-016.

Findeisen, R. and Allgöwer, F. (2002). An introduction to nonlinear model predictive control. In *21st Benelux Meeting on Systems and Control*.

Flemsaeter, B. (1995). Contribution to the dynamic analysis and optimal control of the Superfluid Helium Cooling Loop for the LHC Magnet String. Master's thesis, NNTU, Trondheim.

Flemsaeter, B., Blanco, E., Casas, J., De Prada, C., and Saelid, S. (1998). Applying Advanced Control Techniques for Temperature Regulation of the LHC Superconducting Magnets. In *Proceedings of the 17th International Cryogenic Engineering Conference*.

Flemseater, B. (2000). *Investigation, Modelling and Control of the 1.9 K Cooling Loop for Superconducting Magnets for the Large Hadron Collider*. PhD thesis, NNTU, Trondheim.

Gomes, P., Anastasopoulos, K., Antoniotti, F., Avramidou, R., Balle, C., Blanco-Viñuela, E., Carminati, C., Casas-Cubillos, J., Ciechanowski, M., Dragoneas, A., Dubert, P., Fampris, X., Fluder, C., Fortescue, E., Gaj, W., Gousiou, E., Jeanmonod, N., Jodlowski, P., Karagiannis, F., Klisch, M., López, A., Macuda, P., Malinowski, P., Molina, E., Paiva, S., Patsouli, A., Penacoba, G., Sosin, M., Soubiran, M., Suraci, A., Tovar, A., Vauthier, N., Wolak, T., and Zwalinski, L. (2008). The Control System for the Cryogenics in the LHC Tunnel. Technical report, CERN. CERN-LHC-PROJECT-Report-1169.

Grancharova, A., Johansen, T., and Tøndel, P. (2007). Computational aspects of approximate explicit nonlinear model predictive control. In Findeisen, R., Allgöwer, F., and Biegler, L., editors, *Assessment and Future Directions of Nonlinear Model Predictive Control*, volume 358 of *Lecture Notes in Control and Information Sciences*. Springer Berlin Heidelberg.

Heat Load Working Group (2001). Heat loads on Arc cell in nominal operation. CERN website. Accessed: 2015-09-30.

Huang, R. (2010). *Nonlinear model predictive control and dynamic real time optimization for large-scale processes*. PhD thesis, Carnegie Mellon University Pittsburgh, PA.

IEC (1998). INTERNATIONAL STANDARD IEC 60534-2-1.

IEC (2013). ILC Technical Design Report.

Kano, M. and Ogawa, M. (2010). The state of the art in chemical process control in Japan: Good practice and questionnaire survey. *Journal of Process Control*, 20(9):969–982. {ADCHEM} 2009 Special Issue.

Kowalczyk, P., Poncet, A., and Skoczen, B. (2000). Layout and design of the auxiliary bus-bar line for the LHC arc main cryostat. In *Particle accelerator. Proceedings, 7th European Conference, EPAC 2000, Vienna, Austria, June 26-30, 2000. Vol. 1-3*, pages 2456–2458. CERN-LHC-PROJECT-REPORT-413.

Kuhn, H. W. and Tucker, A. W. (1951). Nonlinear programming. In *Proc. Second Berkeley Symp. on Math. Statist. and Prob.*, volume 11.

Lebrun, P., Mazzone, L., Sergo, V., and Vullierme, B. (1992). Investigation and qualification of thermal insulation systems between 80 K and 4.2 K. Technical report, CERN. CERN-AT-92-12-CR. LHC-NOTE-189. CERN-LHC-Note-189.

Lebrun, P., Serio, L., Tavian, L., and Van Weelderen, R. (1997). Cooling Strings of Superconducting Devices below 2 K: the Helium II Bayonet Heat Exchanger. *Adv. Cryog. Eng., A*, 43:419–426.

Lebrun, P. and Tavian, L. (2002). The technology of superfluid helium. In *CAS - CERN Accelerator School on Superconductivity and Cryogenics for Accelerators and Detectors*.

Lebrun, P. and Tavian, L. (2014). Cooling with Superfluid Helium. In *CAS-CERN Accelerator School: Superconductivity for Accelerators*.

Leyffer, S. and Mahajan, A. (2010). *Software For Nonlinearly Constrained Optimization*. John Wiley & Sons, Inc.

Liu, L., Riddone, G., and Tavian, L. (2003). Numerical analysis of cooldown and warmup for the Large Hadron Collider. *Cryogenics*, 43(6):359–367.

Liu, L., Riddone, G., and Tavian, L. (2004). Numerical Study of the Final Cooldown from 4.5 K to 1.9 K of the Large Hadron Collider. Technical report, CERN.

Maglioni, C. and Parma, V. (2007). Estimate of Helium quantity in LHC magnets. CERN Powerpoint Presentation.

Maglioni, C. and Parma, V. (2008). Calculation of Helium Inventory in LHC Arcs from Geometry and Comparison with Observations. Technical report, CERN. LHC-Project-Note 408.

Maglioni, C. and Parma, V. (2010). Static Heat Loads in the LHC Arc Cryostats: Final Assessment. Technical report, CERN. CERN-ATS-2010-003.

Michalska, H. and Mayne, D. (1995). Moving horizon observers and observer-based control. *Automatic Control, IEEE Transactions on*, 40(6):995–1006.

Nikitina, L., Sahner, T., Skoczen, B., and A, P. (2003). Cryodipole downstream extremity MB-MB type AR4. CERN Engineering Specification. LHC_LI.ES.0001.

Noga, R. (2007). Modeling and control of the String2 LHC Prototype at CERN. Master's thesis, Gdansk University of Technology, University of Karlsruhe, Grenoble Institute of Technology.

Noga, R., de Prada, C., Ohtsuka, T., Blanco, E., and Casas, J. (2014). Non-linear Moving Horizon Estimation and Control for the Superfluid Helium Cryogenic Circuit at the Large Hadron Collider. In *Decision and Control (CDC), 2014 IEEE 53rd Annual Conference on*.

Noga, R. and Ohtsuka, T. (2011). Nmpc for stiff, distributed parameter system: Semi-automatic code generation and optimality condition evaluation. In *Proceedings of the 18th International Conference on Process Control*.

Noga, R., Ohtsuka, T., de Prada, C., Blanco, E., and Casas, J. (2010). Nonlinear Model Predictive Control for the Superfluid Helium Cryogenic Circuit of the Large Hadron Collider. In *Proceedings of the 2010 IEEE Int. Conference on Control Applications*.

Noga, R., Ohtsuka, T., de Prada, C., Blanco, E., and Casas, J. (2011). Simulation Study on Application of Nonlinear Model Predictive Control to the Superfluid Helium Cryogenic Circuit. In *Proceedings of the 18th IFAC World Congress*.

Noga, R., Ohtsuka, T., de Prada, C., Blanco, E., and Casas, J. (2015). Nmpc for superfluid helium cryogenics. In *Proceeding of the 5th IFAC Conference on Nonlinear Model Predictive Control*.

Ödlund, E. (2007). Virtual instrumentation: Introduction of virtual flow meters in the LHC cryogenics control system. Master's thesis, LinkÖpings universitet.

Ohtsuka, T. (2004). A continuation/GMRES method for fast computation of nonlinear receding horizon control. *Automatica*, 40(4):563–574.

Poncet, A. and Parma, V. (2007). Series-produced Helium II Cryostats for the LHC Magnets: Technical Choices, Industrialisation, Costs. Technical report, CERN. CERN-LHC-PROJECT-Report-1075.

Prashant, K. A. and Bangalore, A. (2004). Introduction To Cryogenic Instrumentation in SM18.

Qin, S. J. and Badgwell, T. A. (2003). A survey of industrial model predictive control technology. *Control engineering practice*, 11(7):733–764.

Quesnel, J.-P. (1999). Geometrie theorique du tunnel du LEP.

Rao, C. V., Rawlings, J. B., and Lee, J. H. (2001). Constrained linear state estimation - a moving horizon approach. *Automatica*, 37(10):1619–1628.

Riddone, G. (1997). *Theoretical Modeling and Experimental Investigation of the Thermal Performance of the LHC Prototype Lattice Cryostats*. PhD thesis, TU Torino.

Riddone, G., Gilbert, N., Roussel, P., Moracchioli, R., and Tavian, L. (2006). Performance Assessment of 239 Series Sub-cooling Heat Exchangers for the Large Hadron Collider. Technical report, CERN. CERN-LHC-Project-Report-860.

Rousset, B., Gauthier, A., Jäger, B., and Van Weelderen, R. (1999). HE II Two Phase Flow in an Inclinable 22 m Long Line. Technical report, CERN. CERN-LHC-PROJECT-REPORT-328.

Rousset, B., Gauthier, A., Jäger, B., van Weelderen, R., and Weisend II, J. (1998). Hydraulic Behaviour of He II in Stratified Counter-Current Two-Phase Flow. Technical report, CERN. LHC Project Report 217.

Rousset, B., Grimaud, L., and Gauthier, A. (1997). Stratified two-phase superfluid helium flow: I. *Cryogenics*, 37(11):733–737. The {DESY} Workshop on {HE} {II} Two-phase Flow.

Salerno, L. J.and Kittel, P. S. A. L. (1983). Thermal conductance of pressed contacts at liquid helium temperatures. *AIAA Journal*, 22:1810–1816.

Sato, A., Maeda, M., and Kamioka, Y. (2005). Chapter 201 - normalized representation for steady state heat transport in a channel containing he {II} covering pressure range up to 1.5 {MPa}. In Zhang, L., Lin, L., and Chen, G., editors, *Proceedings of the Twentieth International Cryogenic Engineering Conference (ICEC20)*, pages 849–852. Elsevier Science.

Seguchi, H. and Ohtsuka, T. (2003). Nonlinear receding horizon control of an underactuated hovercraft. *Internat. J. Robust Nonlinear Control*, 13(3 - 4):381–398.

Seki, H., Ogawa, M., Ooyama, S., Akamatsu, K., Ohshima, M., and Yang, W. (2001). Industrial application of a nonlinear model predictive control to polymerization reactors. *Control Engineering Practice*, 9(8):819–828. Advanced Control of Chemical Processes.

Srinivasan, R. and Hofmann, A. (1985). Investigations on cooling with forced flow of He II. Part 2. *Cryogenics*, 25(11):652–657.

Tavian, L. (2000). Large Cryogenics Systems at 1.8 K. In *EPAC 2000*.

Tavian, L. (2012). Performance limitations of the LHC cryogenics: 2012 review and 2015 outlook. In *In e-proceedings of LHC beam operation workshop, Evian, 2012*.

Tzotzi, C. and Andritsos, N. (2013). Interfacial shear stress in wavy stratified gas-liquid flow in horizontal pipes. *International Journal of Multiphase Flow*, 54(0):43–54.

Van Sciver, S. (2011). *Helium Cryogenics*. Springer.

Waltz, R., Morales, J., Nocedal, J., and Orban, D. (2006). An interior algorithm for nonlinear optimization that combines line search and trust region steps. *Mathematical Programming*, 107(3):391–408.

White, F. (1998). *Fluid Mechanics*. Mcgraw-Hill College.

Würth, L., Rawlings, J. B., and Marquardt, W. (2009). Economic dynamic real-time optimization and nonlinear model-predictive control on infinite horizons. In *In proceedings of ADCHEM 2009*.